



**HAL**  
open science

# Ab initio simulation of extended defects of $\alpha$ -Ti in presence of interstitial atoms H & O

Liang Liang

► **To cite this version:**

Liang Liang. Ab initio simulation of extended defects of  $\alpha$ -Ti in presence of interstitial atoms H & O. Material chemistry. Université Paris Saclay (COMUE), 2016. English. NNT : 2016SACLX009 . tel-01355132

**HAL Id: tel-01355132**

**<https://pastel.hal.science/tel-01355132>**

Submitted on 22 Aug 2016

**HAL** is a multi-disciplinary open access archive for the deposit and dissemination of scientific research documents, whether they are published or not. The documents may come from teaching and research institutions in France or abroad, or from public or private research centers.

L'archive ouverte pluridisciplinaire **HAL**, est destinée au dépôt et à la diffusion de documents scientifiques de niveau recherche, publiés ou non, émanant des établissements d'enseignement et de recherche français ou étrangers, des laboratoires publics ou privés.

NNT : 2016SACLX009

THÈSE DE DOCTORAT  
DE L'UNIVERSITÉ PARIS-SACLAY  
préparée à l'ÉCOLE POLYTECHNIQUE

ÉCOLE DOCTORALE N° 573  
Interfaces : approches interdisciplinaires / fondements, applications et innovation

Spécialité : **PHYSIQUE**

par

**Liang LIANG**

**Simulation *ab initio* des défauts étendus du  
Ti  $\alpha$  en présence d'interstitiels H et O**

Thèse présentée et soutenue à Palaiseau, le 18 mars 2016

**Composition du jury :**

M.	Hichem DAMMAK	Président
M.	Joseph MORILLO	Rapporteur
M.	Laurent CAPOLUNGO	Rapporteur
Mme.	Anna SERRA	Examinatrice
M.	Emmanuel CLOUET	Examinateur
M.	Adrian SUTTON	Examinateur
Mme.	Véronique DOQUET	Invitée
M.	Olivier HARDOUIN DUPARC	Directeur de thèse



Thesis presented to obtain the degree of  
**DOCTOR OF UNIVERSITÉ PARIS-SACLAY**  
prepared at the **ÉCOLE POLYTECHNIQUE**

DOCTORAL SCHOOL No. 573

Interfaces : approches interdisciplinaires / fondements, applications et innovation

Speciality: **PHYSICS**

by

**Liang LIANG**

***Ab initio* simulation of extended defects of  
 $\alpha$ -Ti in presence of interstitial atoms H & O**

Thesis presented and defended at Palaiseau, the 18th of March 2016

**Thesis committee:**

Prof.	Hichem DAMMAK	President
Prof.	Joseph MORILLO	Referee
Prof.	Laurent CAPOLUNGO	Referee
Prof.	Anna SERRA	Examiner
Dr.	Emmanuel CLOUET	Examiner
Prof.	Adrian SUTTON	Examiner
Dr.	Véronique DOQUET	Invited
Dr.	Olivier HARDOUIN DUPARC	Supervisor



*à mes parents et à Yijiao.*



# Remerciements

En un premier temps, je tiens à remercier mon directeur de thèse Monsieur Olivier Hardouin Duparc. Sa disponibilité et sa patience, ses compétences scientifiques à la fois profondes et étendues, et ses conseils constructifs m'ont permis de réaliser cette thèse sur un sujet difficile mais fortement intéressant. Grâce à lui, j'ai beaucoup appris, non seulement des connaissances et des compétences scientifiques mais aussi une bonne attitude sur la recherche scientifique, qui me servira certainement tout au long de ma vie.

Je remercie M. Joseph Morillo et M. Laurent Capolungo qui ont accepté d'être rapporteurs de ma thèse. Merci pour leurs relectures profondes d'un manuscrit pas toujours facile à lire. Je remercie aussi Mme Anna Serra, Mme Véronique Doquet, M. Adrian Sutton, M. Emmanuel Clouet et M. Hichem Dammak qui ont accepté d'être membres de mon jury. J'ai beaucoup apprécié leurs questions précises et constructives.

Je remercie les deux directeurs successifs du LSI durant ma présence dans ce laboratoire, Mme Martine Soyer et M. Kees van der Beek. Ils m'ont tous deux fortement aidé, pour commencer et pour terminer cette thèse. Je remercie Mmes Sylvie Michèle, Isabelle Taquin et Marylène Raclot pour leur aide administrative indispensable.

Je remercie Mme Nathalie Vast, chef du groupe TSM : Sans le projet de mutualisation informatique LLR/LSI initié et piloté en grande partie par elle côté LSI, je n'aurais pas pu effectuer les nombreux calculs de ma thèse. Je remercie M. Andrea Cucca et M. Andrea Sartinara, ingénieurs informaticiens des laboratoires LSI et LLR à l'école polytechnique. Ils m'ont beaucoup aidé pour l'installation et l'optimisation des codes et pour l'utilisation de clusters locaux Zaubefloete/JollyJumper en calcul parallèle.

Je remercie Mme Sylvie Lartigue, M. Marc Hayoun, M. Marc Torrent, M. Jean-Claude Crivello et Mme Michèle Gupta pour m'avoir appris tant de connaissances



importantes liées aux sujets de ma thèse. Je remercie M. Emmanuel Clouet avec qui j'ai eu l'occasion d'échanger des idées sur des méthodes importantes utilisées dans cette thèse.

Je remercie Mme Véronique Doquet qui a piloté le projet ANR blanc Fluti qui a permis mon premier stage au LSI. Je remercie toutes les personnes associées au projet ANR Blanc Fluti pour les excellentes présentations et les discussions très constructives tous les six mois pendant ma thèse : M. Samuel Forest, M. Jérôme Crépin, M. Matthieu Mazière, M. Ivan Guillot, M. Jean-Philippe Couzinié, Arina, Bassem, ...

Je remercie bien sûr toutes les personnes de mon groupe et les doctorants du LSI : Jelena, Michèle, Iurii, Antoine, Hai Yen, Maksim, Sabuhi, Oleksandr, Sky et ZhengXuan, mes compatriotes, pour plein de discussions enrichissantes et leur soutien tout au long de ma thèse.

Je remercie aussi tous ceux et celles qui m'ont aidé et que j'ai connus au laboratoire et sur le campus et qui ne sont pas dans cette liste.

Je remercie aussi bien sûr le CEA qui m'a financé, l'École polytechnique et le CNRS ainsi que l'IDRIS-GENCI pour les moyens de calculs nationaux.

Finalement, je remercie très sincèrement mes parents, qui sont en Chine, et ma fiancée Yijiao, pour leur soutien et leurs sacrifices. Sans eux, je n'aurais pas pu aller si loin.

# List of (some) abbreviations

hcp: hexagonal closed packed

SF: Stacking Fault

SFE: Stacking Fault Energy

GSF: Generalised Stacking Fault

TB: Twin Boundary

TD: Twinning Disconnection or Twinning Dislocation

DFT: Density Functional Theory

VASP<sup>TM</sup>: Vienna *ab initio* Simulation Package

GGA: Generalised Gradient Approximation

PBE: Perdew-Burke-Ernzerhof

PAW: Projector Augmented Wave

ZPE: Zero Point Energy

NEB: Nudged Elastic Band

MEP: Minimum Energy Path

DDmap: Differential Displacement map

EC: Elastic Constant

CRSS: Critical Resolved Shear Stress



# Contents

<b>General introduction</b>	<b>1</b>
<b>1 Literature Review</b>	<b>5</b>
1.1 Some general facts about of $\alpha$ -titanium . . . . .	6
1.1.1 Preliminaries about phases in Ti . . . . .	6
1.1.2 Slip in $\alpha$ -Ti . . . . .	7
1.1.2.1 Slip systems . . . . .	7
1.1.2.2 Stacking-faults . . . . .	9
1.1.2.3 Dislocation cores . . . . .	10
1.1.2.3.1 Dislocation core atomistic models . . . . .	10
1.1.2.3.2 $\langle \mathbf{a} \rangle$ screw dislocation core . . . . .	11
1.1.2.3.3 $\langle \mathbf{c} + \mathbf{a} \rangle$ screw dislocation core . . . . .	13
1.1.2.4 Dislocation glides . . . . .	14
1.1.2.4.1 Peierls energy barrier and Peierls stress . . . . .	14
1.1.2.4.2 $\langle \mathbf{a} \rangle$ screw dislocation glide . . . . .	16
1.1.2.4.3 locking-unlocking mechanism . . . . .	16
1.1.3 Twinning in $\alpha$ -Ti . . . . .	17
1.1.3.1 Twin boundaries . . . . .	17
1.1.3.2 Twinning disconnections . . . . .	18
1.2 Effects of H and O on $\alpha$ -Ti . . . . .	20
1.2.1 H and O position in Ti . . . . .	20
1.2.2 Solubility of H and O in Ti . . . . .	21
1.2.3 H and O diffusion in Ti by DFT+Phonon calculation . . . . .	23
1.2.3.1 H diffusion . . . . .	23
1.2.3.2 O diffusion . . . . .	23
1.3 Effects of H and O on extended defects in $\alpha$ -titanium . . . . .	24
1.3.1 Effects of O on dislocation cores . . . . .	24
1.3.2 Effects of H on dislocation cores . . . . .	28
1.3.3 Effects of H and O on Twin boundaries . . . . .	30
1.3.4 Effects of H and O on Twinning disconnections . . . . .	31
<b>2 Theory &amp; Tools and Techniques</b>	<b>33</b>
2.1 Theory & Tools . . . . .	34
2.1.1 Density Functional Theory with VASP code . . . . .	34
2.1.1.1 Density Functional Theory . . . . .	34

2.1.1.2	Exchange-correlation functional: PBE-GGA . . . . .	35
2.1.1.3	Pseudopotentials: the PAW method . . . . .	37
2.1.1.4	Plane wave bases . . . . .	39
2.1.1.5	Calculation of ground state in VASP . . . . .	41
2.1.2	Vibrational Energy Calculations via PHON . . . . .	43
2.2	Techniques . . . . .	44
2.2.1	Solutes interactions in Ti . . . . .	46
2.2.2	Elastic constant calculations . . . . .	46
2.2.3	Stacking faults . . . . .	48
2.2.4	Screw dislocation cores . . . . .	49
2.2.5	$\langle \mathbf{c} + \mathbf{a} \rangle$ screw dislocation core construction . . . . .	49
2.2.6	$\langle \mathbf{a} \rangle$ screw dislocation core construction . . . . .	51
2.2.7	Twin boundaries and deformation tests . . . . .	53
2.2.8	A new twinning disconnection dipole model . . . . .	54
2.2.9	Solute Segregation . . . . .	55
<b>3</b>	<b>Results I: Titanium and H &amp; O in <math>\alpha</math>-Ti</b>	<b>57</b>
3.1	About $\alpha$ and $\omega$ phases of Ti at 0 K and 0 Pa . . . . .	58
3.2	H and O interstitial positions in $\alpha$ -Ti . . . . .	60
3.3	H and O interactions with $\alpha$ -Ti . . . . .	64
3.3.1	Structures and Energies . . . . .	64
3.3.2	Electronic Structures . . . . .	67
3.3.3	solute-solute interactions in $\alpha$ -Ti . . . . .	68
3.4	Effects of H and O on the stiffness elastic constants . . . . .	70
3.5	Migration of H and O in $\alpha$ -Ti . . . . .	76
<b>4</b>	<b>Results II: H and O effects on stacking faults and on dislocation cores</b>	<b>79</b>
4.1	Stacking-Faults in $\alpha$ -Ti . . . . .	80
4.1.1	Vitek's method for $\gamma$ -surface calculations . . . . .	80
4.1.2	New stacking faults and twinning-assisted SF formation . . . . .	83
4.1.3	Discussion . . . . .	84
4.2	$\langle \mathbf{c} + \mathbf{a} \rangle$ screw dislocation core dissociation . . . . .	86
4.3	H and O interaction with SFs . . . . .	88
4.3.1	Segregation of H and O to stacking faults . . . . .	89
4.3.2	Effects of H and O on stacking fault energies . . . . .	91
4.4	$\langle \mathbf{a} \rangle$ screw dislocation core . . . . .	93
4.5	H and O effects on $\langle \mathbf{a} \rangle$ screw dislocation core . . . . .	94
4.5.1	H and O effects on prismatic plane spreading $\langle \mathbf{a} \rangle$ screw dislocation core . . . . .	94
4.5.2	H and O effects on $\pi_1$ plane spreading $\langle \mathbf{a} \rangle$ screw dislocation core . . . . .	97
4.6	H and O effects on $\langle \mathbf{a} \rangle$ screw dislocation glide . . . . .	99
4.6.1	$\langle \mathbf{a} \rangle$ screw dislocation glide in pure Ti . . . . .	99
4.6.2	$\langle \mathbf{a} \rangle$ screw dislocation glide with H and O solute . . . . .	101

---

<b>5</b>	<b>Results III: H and O effects on TB and on TD</b>	<b>105</b>
5.1	Twin boundaries in $\alpha$ -Ti . . . . .	106
5.2	H and O effects with TBs . . . . .	108
5.2.1	Segregation . . . . .	108
5.2.2	Atomic and electronic structures . . . . .	109
5.3	TBs under deformation in presence of H/O . . . . .	112
5.3.1	Twin boundary $c$ -axis deformations . . . . .	112
5.3.2	Twin boundary $c$ -axis deformations in presence of O/H . . . . .	115
5.3.3	Twin boundary deformations perpendicular to $K_1$ . . . . .	118
5.4	H and O effects on twinning disconnection $\{10\bar{1}2\}$ . . . . .	122
5.4.1	Conclusions . . . . .	123
	<b>Conclusions</b>	<b>125</b>
	<b>Bibliography</b>	<b>129</b>
	<b>List of Figures</b>	<b>145</b>
	<b>List of Tables</b>	<b>151</b>



# General Introduction

Titanium is a relatively recent light metal, by metallurgical history standard. It is very important and much used both as pure and allied in the aeronautic industry and in biomedical applications as well as for transport of some corrosive products at very low temperatures for instance [1, 2, 3, 4].

It is much used in its hexagonal close packed (hcp)  $\alpha$ -phase under mechanical constraints and it is therefore important to study the elementary mechanisms of its deformation behaviour which will be influenced by the presence of impurities. The two principal plastic deformation modes in hexagonal materials are dislocation gliding and deformation twinning [5, 6]. It is well known that the room-temperature plastic deformation of titanium is controlled by the motion of screw dislocations [7], whose non-planar core structure induces a large Peierls stress. Because of the insufficient number of independent slip systems in hcp metals, like  $\alpha$ -titanium, deformation twinning is also activated, all the more so for deformations along the  $c$ -axis, and/or at low temperature.

Titanium alloys always contain some residual solute impurities such as oxygen, hydrogen, nitrogen and carbon. Oxygen is an interstitial impurity with a solubility limit of perhaps 1 at.% ( $\sim 3400$  weight ppm) at room temperature. Oxygen has a clear strengthening effect [8, 9, 10]. It is known to increase titanium and its alloys yield stress by changing the structure of dislocation cores and by reducing the mobility of screw dislocations. It is also supposed to be responsible for the dynamic strain ageing phenomena [8, 11]. An oxygen diffusion controlled twinning during low-temperature creep has been proposed [12]. Hydrogen, with a solubility limit as small as about 0.1 at.% ( $\sim 20$  weight. ppm) at room temperature, has a complicated, yet important role. It softens titanium in some cases [13, 14, 15] and hardens it in other cases [17, 18]. For example, one softening effect is the fact that the sustained load cracking resistances are increased with the increase of hydrogen concentration. The hydrogen enhanced localized plasticity mechanism is used to explain this phenomena. It suggests that hydrogen facilitates the dislocation



emission and glide at crack tips and can thus accelerate the creep in this region and prevents the attainment of the high localized stresses necessary for fracture [19, 20]. The non-monotonic effect of H on low temperature creep in titanium is also observed [21]. Furthermore, different H/O concentration ratios also affect the creep phenomena and other mechanical properties of  $\alpha$ -Ti [11, 16, 20]. As suggested by analysing of compression test on commercial-purity titanium, the presence of hydrogen decreases the extent of dynamic strain ageing in titanium [22]. This phenomenon can be explained by assuming that hydrogen in solid solution prevents other solute atoms from segregating to mobile dislocations thanks to the high mobility of hydrogen.

Thus, accurate atomistic level simulations of the interactions of oxygen and hydrogen with extended defects on  $\alpha$ -titanium are key points to understand the strong effect of oxygen and the complex role of hydrogen on the plasticity of  $\alpha$ -titanium. Thanks to the development of high performance computing clusters and advanced atomistic models [23, 24], density functional theory based *ab initio* calculations can now be performed to study solute-extended defects interactions.

I shall not try to explain in this manuscript how titanium nuclei were first synthesized in stars, see [25], whether it happened in supernovae or in neutron mergers. I shall not either try to explain why titanium is the ninth most abundant element by weigh in Earths rocky crust, nor shall I recall when and how titanium was discovered, in its dioxide form, in the late eighteenth century by William Gregor and Martin Heinrich Klaproth, who still knew nothing about it, and only fully exploited much later on thanks to very important technological progresses, e.g. with Guillaume/William Kroll. I shall concentrate on titanium, in its low temperature  $\alpha$ -phase, on its extended defects, and on the influence of O and H by using density functional theory based *ab initio* calculations.

Chapter 1 presents a literature review of previous studies in three parts: i) extended defects in  $\alpha$ -titanium (stacking-faults, dislocation cores, twin boundaries and twinning disconnections) and the small scale plasticity; ii) interstitial solutes H and O in  $\alpha$ -titanium and iii) the effects of H and O on such extended defects.

Chapter 2 presents the theories and the simulation tools and techniques and models used in this work. Density functional theory via VASP program and the zero point energy calculations are rapidly introduced. Different simulation models are presented for solutes interactions in Ti; this chapter 2 also presents elastic constant calculations, extended defects and the effects of H and O on them.

In chapter 3, the main goal is to study the effects of H and O in  $\alpha$  titanium. It addresses the problem of the preferred interstitial positions of H and O in  $\alpha$ -Ti, the interaction of H and O with  $\alpha$ -Ti, the effects of H and O on the elastic constants of  $\alpha$ -Ti and the migration of H and O in  $\alpha$ -Ti. These studies constitute first steps before studying the effects of H and O on extended defects in  $\alpha$ -Ti.

In chapter 4, I study the effects of hydrogen and oxygen on various stacking faults and dislocation cores. Various stacking faults are first built in  $\alpha$ -Ti on the basal, prismatic,  $\pi_1$  and  $\pi_2$  plane. I also study various generalised stacking faults, ie. I get several Vitek's gamma surfaces. The  $\langle \mathbf{a} \rangle$  and  $\langle \mathbf{c} + \mathbf{a} \rangle$  screw dislocation cores are built and studied. The effect of H and O on the stacking faults, and on the  $\langle \mathbf{a} \rangle$  screw core and its glide is eventually carried out in that chapter.

In Chapter 5, I study the effects of hydrogen and oxygen on four important twin boundaries and on the  $\{10\bar{1}2\}$  twinning disconnection. The four TBs,  $\{10\bar{1}2\}$ ,  $\{10\bar{1}1\}$ ,  $\{11\bar{2}1\}$ ,  $\{11\bar{2}2\}$ , are first built and relaxed, and the effects of H and O on their structures and on their behaviour under deformation along  $\langle \mathbf{c} \rangle$ -axis or along the direction perpendicular to their twin plane  $K_1$  are investigated. A new Twinning disconnection (TD) dipole model is proposed and built. The effects of hydrogen and oxygen on the  $\{10\bar{1}2\}$  TD is briefly studied.



# Chapter 1

## Literature Review

This chapter presents a literature review of studies done on three parts: extended defects in  $\alpha$ -titanium; interstitial solutes H and O in  $\alpha$ -titanium and the effects of H and O on such extended defects.

In the first part, I started by the discussion of phases of titanium. The slip systems, stacking-faults, dislocation cores and their glides are summarised. Twin boundaries and twinning disconnection are then presented in this part.

In the second part, different interstitial sites containing H and O are summarised. The solubilities of H and O are then discussed. Some results of H and O diffusion obtained from DFT+Phonon calculations are also presented.

In the third part, the effects of H and O on dislocation core are presented, much less studied compared to dislocation-interstitial solute interaction, their effects on twinning and twinning dislocation are briefly discussed .

## 1.1 Some general facts about of $\alpha$ -titanium

### 1.1.1 Preliminaries about phases in Ti

In pure titanium, three phases are mainly known:  $\alpha$ ,  $\beta$  and  $\omega$  [1, 2, 3, 26]. The  $\alpha$  phase has a hexagonal close-packed (hcp) structure. It exists at ambient pressure and temperature. The  $\beta$  phase has a body centred cubic (bcc) structure with one atom per primitive cell. It exists at high temperature and ambient or high pressure. The  $\omega$  phase, hexagonal structure with three atoms per primitive cell, is generally formed under high pressure.

A  $\gamma$  and a  $\delta$  phases have also been observed under high pressure [27, 28, 29]. A non-observed face centred cubic (fcc) phase has also recently been proposed by density functional theory (DFT) calculation [30] as well as a  $\delta'$  phase [31]. The  $\gamma$  and  $\delta$  phases have respectively a distorted hcp and a distorted bcc structure. They are obtained from the  $\omega$  phase under pressures of around 120 GPa and 140 GPa respectively [27, 28]. The structures of  $\alpha$ -Ti and  $\omega$ -Ti are shown in figure 1.1. The pressure-temperature phase diagram of titanium established by Zhang et al. [33] is presented in figure 1.2. The stability of the Ti phases at 0 K and 0 Pa

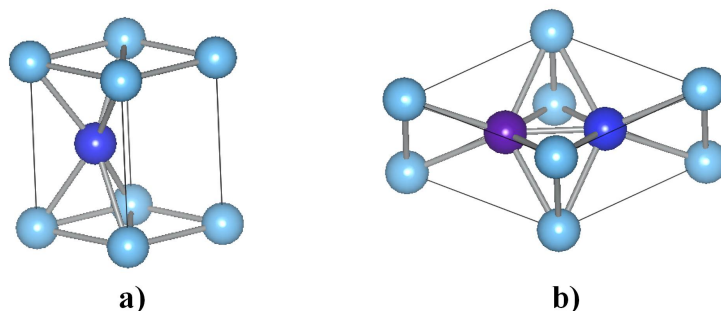


Figure 1.1: a) The conventional hexagonal cell of the  $\alpha$ -Ti structure; b) The primitive cell of the hexagonal  $\omega$ -Ti structure. In figure b, all balls should have the same size (in first approximation). The 'sticks' have no physical meaning.

has been widely studied by first-principles calculations. Except for the calculation of Nishitani et al. [34] in which the hexagonal  $c/a$  ratio is not allowed to relax, all other DFT calculations give the  $\omega$  phase as the more stable one compared to the  $\alpha$  phase, by several meV per atom in terms of electronic total energy. From the extrapolation of the experimental values shown in figure 1.2, Tonkov's 1992 results [35] give the  $\omega$  phase more stable while Zhang's 2008 results [33] give  $\alpha$  phase more stable at 0 K with a transition pressure around 5 GPa. Both  $\alpha$  and  $\omega$  phases may well be metastable at 0 K under 0 Pa. The atom quantum vibrational

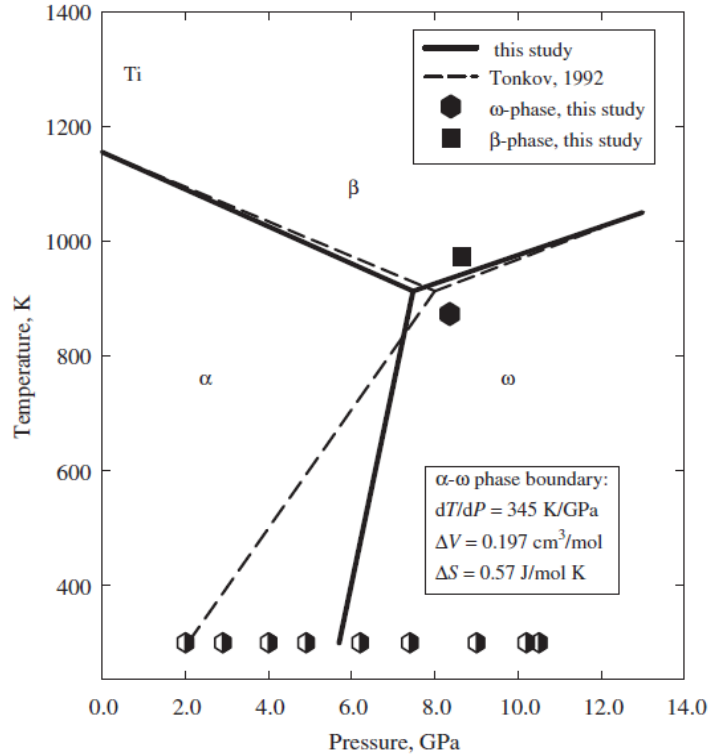


Figure 1.2: Phase diagram of titanium, determined by Tonkov in 1992 [35] and by Zhang et al. in 2008 [33]

contribution at zero K, namely the so-called zero point energy (ZPE) contribution can play an important role on phase stability at very low temperatures. It may reverse energy differences between phases, as known long from a long time in studies of molecular crystals. The  $\alpha$  and  $\omega$  phase stability should thus be checked with explicit consideration of ZPE (see section 3.1).

## 1.1.2 Slip in $\alpha$ -Ti

### 1.1.2.1 Slip systems

Possible slip modes, or slip systems, are presented in figure 1.3. They are also summarised per families in table 1.1 together with their respective numbers of independent modes. Independent modes within one family may not be independent with respect to modes of other families [36, 37, 38]. The first three families (with  $\langle \mathbf{a} \rangle$ ) only provide four independent slip systems, so that a  $\langle \mathbf{c} + \mathbf{a} \rangle$  associated slip is required to fulfill the von Mises criterion of five independent modes for easy plastic deformation, or, since such a slip system may be difficult to activate, a twinning mode may be activated instead. [6]

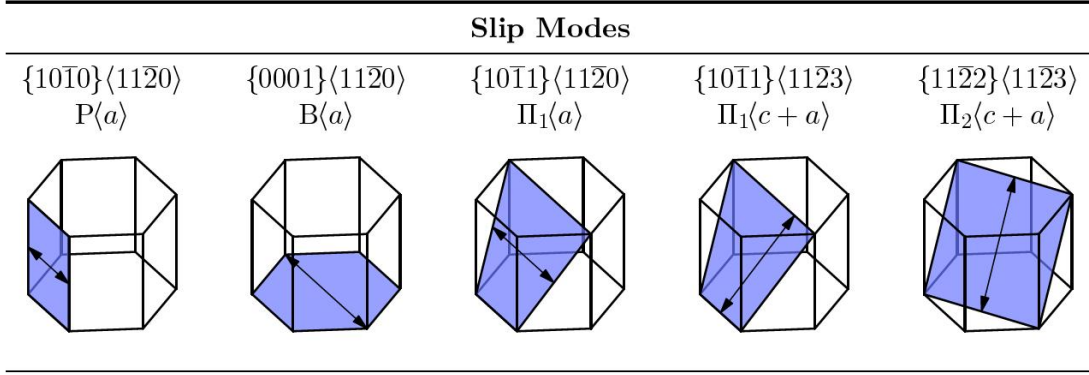


Figure 1.3: Slip systems. The arrow in a given plane indicates a slip direction [39].

Table 1.1: Deformation modes of  $\alpha$ -Ti.

Direction	Plane	Crystallographic elements	Number of independent modes
$\langle a\rangle$	Prismatic Slip	$\{1\bar{1}00\}\langle 1\bar{2}10\rangle$	2
	Basal Slip	$\{0001\}\langle 1\bar{2}10\rangle$	2
$\langle c+a\rangle$	$\pi_1$ Slip	$\{10\bar{1}1\}\langle 1\bar{2}10\rangle$	4
	$\pi_1$ Slip	$\{10\bar{1}1\}\langle 11\bar{2}3\rangle$	5
$\langle c+a\rangle$	$\pi_2$ Slip	$\{11\bar{2}2\}\langle 11\bar{2}3\rangle$	5
Twinning modes		$\{K_1\}\langle \eta_1\rangle$	5

where  $K_1$  and  $\eta_1$  are the twinning plane and twinning direction of a given twinning mode (see section 1.1.3).

The activated slip systems for a T60 grade titanium sample ( $\alpha$ -Ti with a oxygen concentration of 3200 wt.ppm) under a transverse tensile test are shown in figure 1.4. It clearly shows that, for a deformation less than 0.43%, the prismatic plane glides dominate the plasticity. When deformation is larger than 0.43%, the  $\langle a\rangle$  dislocation and  $\langle c+a\rangle$  dislocation associated  $\pi_1$  plane glides become important. The basal plane glides and twinning are not observed in that T60 sample, was observed in a T40 sample (with 1155 wt.ppm for oxygen) [40].

In table 1.2, the normalised critical resolved shear stress (CRSS) compared with the prismatic CRSS. These results are consistent with the slip mode activation frequencies shown in figure 1.4.

Table 1.2: Critical resolved shear stress (CRSS) in two  $\alpha$ -Ti samples, normalised to their prismatic CRSS, Barkia's PhD thesis 2014 [11].

Material	Prism $\langle a\rangle$	Basal $\langle a\rangle$	$\pi_1$ $\langle a\rangle$	$\pi_1$ $\langle c+a\rangle$
T40	1	$1.52 \pm 0.08$	$1.24 \pm 0.04$	$2.01 \pm 0.30$
T60	1	$1.48 \pm 0.08$	$1.18 \pm 0.05$	$1.82 \pm 0.15$

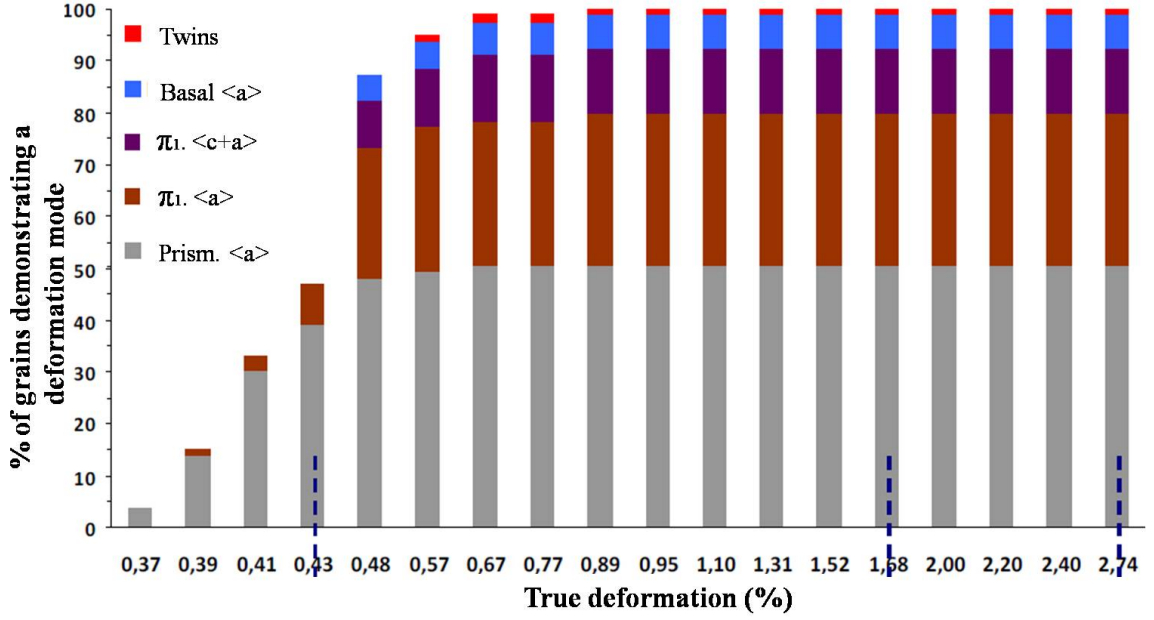


Figure 1.4: Frequency of slip modes under a transverse tensile for a T60 sample. Barkia's PhD thesis 2014 [11].

### 1.1.2.2 Stacking-faults

The stacking-faults (SFs) in  $\alpha$ -titanium, a hcp metal, can be divided into two categories: the  $\langle \mathbf{a} \rangle$  dislocation associated SFs and the  $\langle \mathbf{c} + \mathbf{a} \rangle$  dislocation associated SFs. Note that the  $\frac{1}{4}[\bar{1}012]$  SF in the  $\pi_1$  plane, fifth line in table 1.3, is not associated to a dislocation in the literature.

Table 1.3: Stacking-faults studied in the literature.  $\mathbf{b}_{TD}$  is the twinning dislocation associated to the  $\{10\bar{1}1\}$  twin.

Slip Plane	Associated dislocation	SF vector	SFE(mJ/m)
Basal $\{0001\}$	$\langle \mathbf{a} \rangle$	$\frac{1}{3}\langle 10\bar{1}0 \rangle$	292 [41], 287 [42], 259 [43]
Prism $\{10\bar{1}0\}$	$\langle \mathbf{a} \rangle$	$\frac{1}{6}\langle \bar{1}2\bar{1}0 \rangle$	220 [41], 250 [43]
$\pi_1 \{10\bar{1}1\}$	$\langle \mathbf{a} \rangle$	$\frac{1}{6}\langle \bar{1}2\bar{1}0 \rangle$	689 [41]
$\pi_1 \{10\bar{1}1\}$	$\langle \mathbf{a} \rangle$	$\frac{1}{6}\langle \bar{1}2\bar{1}0 \rangle - \frac{1}{2}\mathbf{b}_{TD}$	227 [44]
$\pi_1 \{10\bar{1}1\}$		$\frac{1}{4}\langle 10\bar{1}\bar{2} \rangle$	(240-Zr [45])
$\pi_1 \{10\bar{1}1\}$	$\langle \mathbf{c} + \mathbf{a} \rangle$	$\frac{1}{6}\langle \bar{1}\bar{1}23 \rangle$	409 [46]
$\pi_2 \{11\bar{2}2\}$	$\langle \mathbf{c} + \mathbf{a} \rangle$	$\frac{1}{6}\langle \bar{1}\bar{1}23 \rangle$	(388-Zr [47]), 399 [46]

The  $\langle \mathbf{a} \rangle$  dislocation associated prismatic and basal  $I_2$  SFs are well known. Several numerical studies have been carried out to investigate the  $\langle \mathbf{c} + \mathbf{a} \rangle$  dislocation in hcp [46, 47, 48, 49, 50, 51, 52, 53, 54, 55]. The edge dislocation on  $\{11\bar{2}2\}$  was found to dissociate into two  $\frac{1}{2}\langle \mathbf{c} + \mathbf{a} \rangle$  partial dislocations or into three partial dislocations as  $\frac{1}{9}[\bar{1}\bar{1}26] + \frac{1}{9}[14\bar{5}3] + \frac{1}{3}[10\bar{1}0]$ . The screw dislocation was found to dissociate into two



$\frac{1}{2}\langle\mathbf{c}+\mathbf{a}\rangle$  in  $\{10\bar{1}1\}$  or  $\{11\bar{2}2\}$  pyramidal planes also called  $\pi_1$  and  $\pi_2$ , respectively. Calculations of stable  $\frac{1}{2}\langle\mathbf{c}+\mathbf{a}\rangle$  stacking faults found on the two pyramidal planes were also used to support these dissociation mechanisms. These calculations, however, were based on pair potentials, so that both the SF energies (SFEs) and the core dissociation configurations may be suspect. A recent work, [44], showed the failure of an advanced semi-empirical  $n$ -body potential to predict a stable  $\langle\mathbf{a}\rangle$  associated SF on the  $\{10\bar{1}1\}$  plane. Moreover, the stable SFs are usually found with the traditional Vitek's method [56]. It has been shown, however, that such a restricted  $\gamma$ -surface approach can fail to detect more stable SFs, such as the  $\langle\mathbf{a}\rangle$  associated SF on the  $\pi_1$  plane, due to the prohibition of all-atom relaxations [41]. Previous simulations [57] revealed a dissociation of the  $\langle\mathbf{a}\rangle$  screw dislocation core in the prismatic plane, in connexion with the prism SF. However, a more stable  $\pi_1$  dissociation configuration has recently been found [41, 24], clearly related to the new  $\pi_1$  SF just mentioned [44]. The landscape of the  $\langle\mathbf{c}+\mathbf{a}\rangle$  associated SF deserves to be re-examined.

### 1.1.2.3 Dislocation cores

#### 1.1.2.3.1 Dislocation core atomistic models

For the atomistic simulation of dislocation cores, three major methods exist. The first method is called the cluster method and is illustrated in figure 1.5. A screw dislocation core is created with its atoms positioned according to the elasticity theory. An outer cylindrical layer of atoms, more or less thick, is kept fixed and surrounded by vacuum. Only the atoms within that cylinder are allowed to relax [45]. The application of this method is rather straightforward but its drawback lays in the presence of a fixed surface and its possible effect on the dislocation core, especially in DFT simulation where the number of atoms one can simulate is still rather limited.

The second method is the so called flexible boundary condition method where a lattice Green's function couples the atomistic core to the far-field harmonically responding medium, thus eliminating the spurious effects of the surfaces in insufficiently large cells in the cluster approach [41]. It can be used either with periodic or non-periodic boundary conditions. It is presented in figure 1.6.

The third method is the dipole dislocation core method which is discussed in details in Bulatov and Cai's book [58]. It uses periodic boundary conditions with the

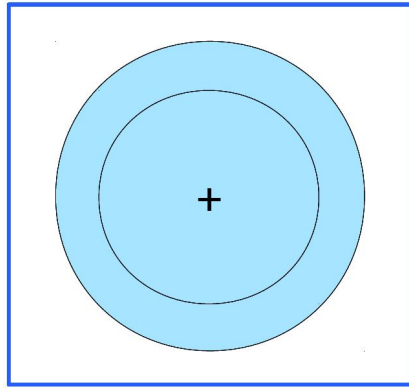


Figure 1.5: The fixed boundary method

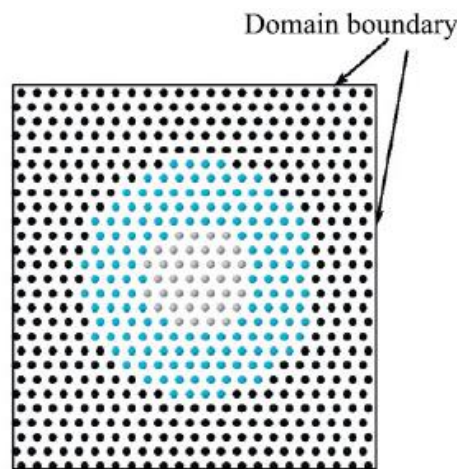


Figure 1.6: The flexible boundary method

atomic displacements created by a screw or edge dislocation core being counter-balanced by an opposite direction dislocation core. For the  $\langle \mathbf{a} \rangle$  screw dislocation core construction, Clouet orients the dipole to a diagonal direction or adjusts the supercell transition vectors in order to create a quadrupolar model [23], see figure 1.7. Since each core is placed at the geometric centre of surrounding opposite cores in the quadrupolar model, the stress of other dislocations cores at each core position is minimal.

### 1.1.2.3.2 $\langle \mathbf{a} \rangle$ screw dislocation core

Many atomistic simulations of the  $\langle \mathbf{a} \rangle$  screw dislocation core structure can be found in the literature. Using tight-binding method in a pioneering way, Legrand found that the  $\langle \mathbf{a} \rangle$  screw dislocation core mainly spreads in prismatic plane with secondary spreading in basal plane [59, 60], giving a non-planar character to the core. Liang & Bacon used pair-wise potentials and also showed a metastable

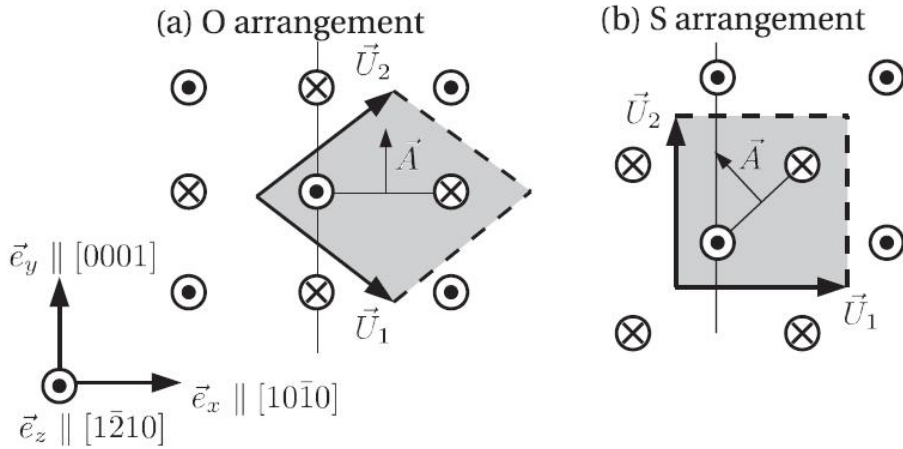


Figure 1.7: Clouet's quadrupolar configuration [23]: an extended dipole method. (a) and (b) represent two quadrupolar configurations with different periodic dislocation arrangements.

prismatic plane extended  $\langle \mathbf{a} \rangle$  screw dislocation core structures when using large numbers of atoms [52].

Recent simulations by Tarrat et al. with a DFT method showed that the prismatic core dissociates into two partial dislocations in the same or in neighbouring prismatic planes, depending on the initial core central position (line position) [57, 61], see figure 1.8. These simulations use the cluster model.

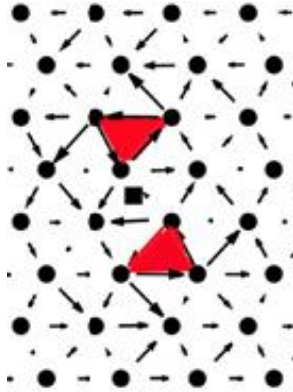


Figure 1.8:  $\langle \mathbf{a} \rangle$  screw dislocation core structure with one specific dislocation line position, only the screw components are shown with DD map [61]

With the flexible boundary condition method in DFT calculation, Ghazisaeidi and Trinkle confirmed Tarrat et al.'s point with different initial positions. A pure prismatic spreading or a combination of prismatic and  $\pi_1$  spreading can be obtained [41], see figure 1.9.

Clouet et al. [24], using their quadrupolar method, confirmed the existence of the prismatic and  $\pi_1$  plane spreading of the  $\langle \mathbf{a} \rangle$  screw dislocation core. They showed

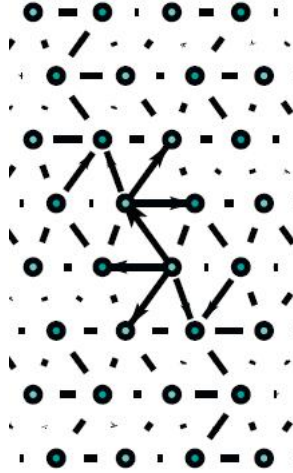


Figure 1.9:  $\langle \mathbf{a} \rangle$  screw dislocation core spreads to the  $\pi_1$  plane [41].

that the  $\pi_1$  plane spreading core is more stable than the prismatic plane spreading core with, a  $\Delta E \sim 5 \text{ meV}/\text{\AA}$ . With nudged elastic band method (NEB), they obtained a Peierls energy barrier of  $8 \text{ meV}/\text{\AA}$  for the prismatic to pyramidal plane cross-slip, see figure 1.10 ( $\xi=0$  to 1). They related their results to the locking-unlocking mechanism proposed by Farenc, Caillard and Couret [62], see section 1.2.2.4.3.

### 1.1.2.3.3 $\langle \mathbf{c} + \mathbf{a} \rangle$ screw dislocation core

The  $\langle \mathbf{c} + \mathbf{a} \rangle$  screw dislocation core structures has been much less studied than the  $\langle \mathbf{a} \rangle$  screw dislocation core. Minonishi et al. simulated the  $\langle \mathbf{c} + \mathbf{a} \rangle$  screw dislocation core with a Lennard-Jones potential (lj56) and showed that the core structure dissociates into two  $\frac{1}{2}\langle \mathbf{c} + \mathbf{a} \rangle$  partial dislocations in  $\{10\bar{1}1\}$  or  $\{11\bar{2}2\}$  pyramidal planes. The final core structure depends on the initial dislocation line position and the initial state of dislocation (perfect or pre-extended), see figure 1.11.

Using various pair-wise potentials, labelled na56, ti12 and be134, Liang and Bacon [52] showed that the  $\langle \bar{1}\bar{1}23 \rangle$  screw dislocation has a variety of stable forms in every material (na56, ti12 and be134). The disregistry is concentrated on combinations of  $\{10\bar{1}1\}$  ( $\pi_1$ ),  $\{11\bar{2}2\}$  ( $\pi_2$ ) and  $\{10\bar{1}0\}$  (prismatic) planes with the na56 and ti12 potentials. However, the be134 potential did not reveal a prismatic dissociation character, so that the disagreement between these empirical potentials results needs to be elucidated by ab initio DFT calculations.

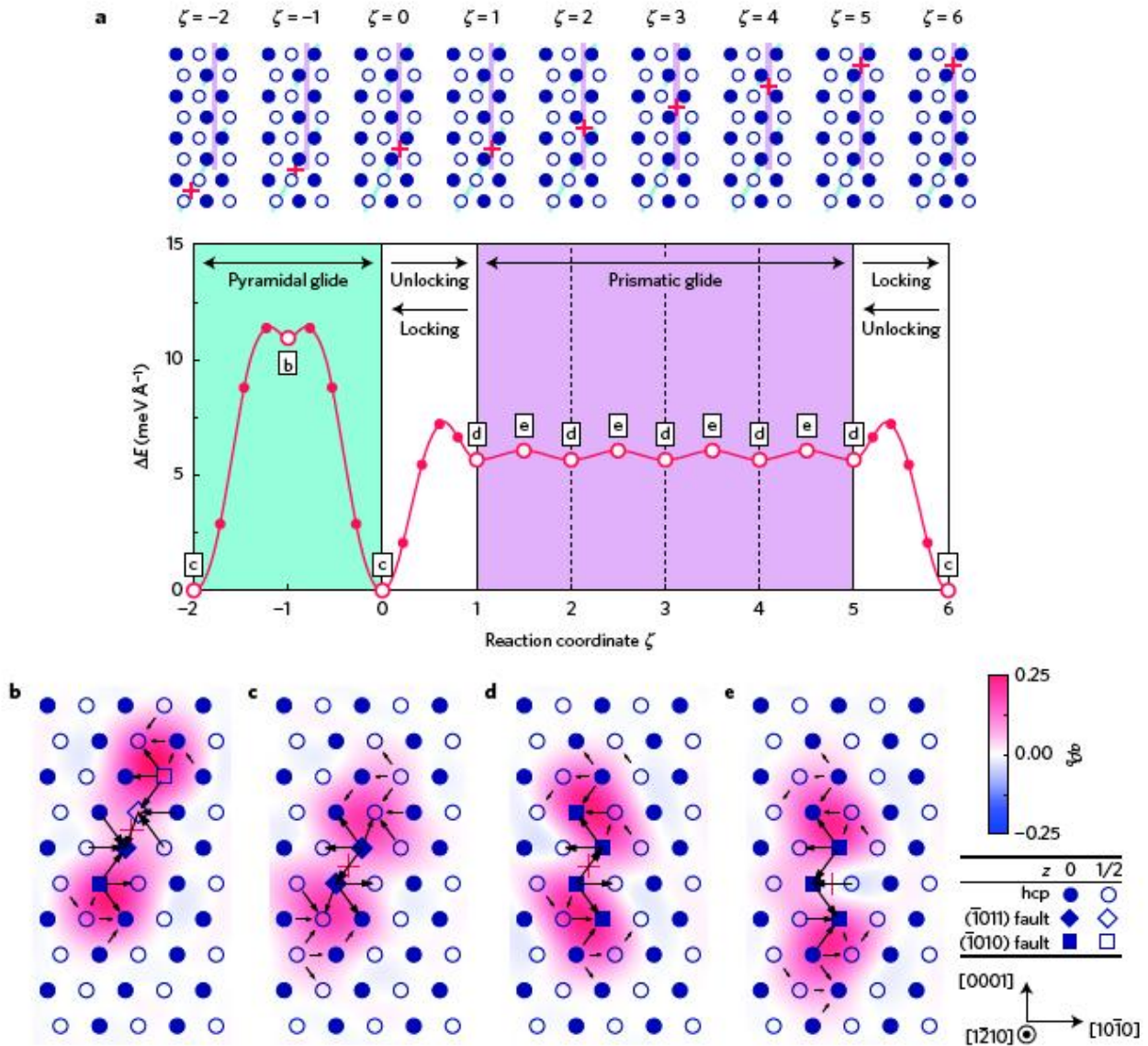


Figure 1.10: **(a)** screw dislocation core gliding on  $\pi_1$  plane ( $\xi = -2 \sim 0$ ), on prismatic plane ( $\xi = 1 \sim 5$ ) and the cross slip ( $\xi = 0 \sim 1$ ) [24]. The various dislocation core structures are shown in the bottom part of the figure, b, c, d, e.

### 1.1.2.4 Dislocation glides

#### 1.1.2.4.1 Peierls energy barrier and Peierls stress

In order to move a dislocation, it is necessary to 'move atomic bonds' at the core of the dislocation in a crystal with lattice periodicity, against the so-called lattice friction. The model of Orowan-Peierls [63] and Nabarro [64] takes into account this discretisation and periodicity. The Peierls' potential images and describes the lattice friction, see figure 1.13.  $\Delta E_p$ , the maximal value of the Peierls potential profile is called the Peierls energy barrier. The minimal value represents the

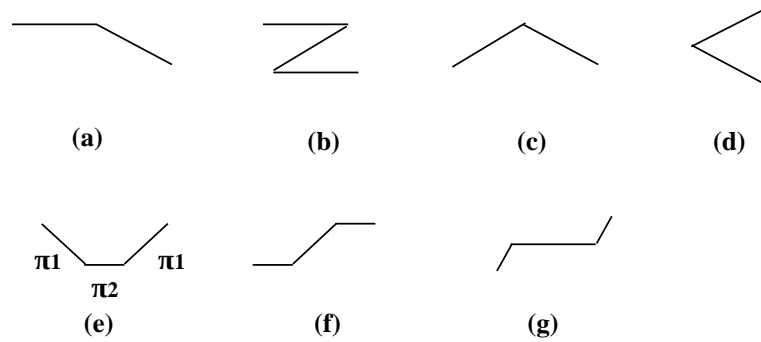


Figure 1.11: Possible  $\langle \mathbf{c} + \mathbf{a} \rangle$  screw dislocation core dissociation proposed by Minonishi et al. [50] in which the 1.11c and 1.11e are actually observed in their simulations. The figure 1.11c corresponds to the relaxed core structure from a initially perfect dislocation core and the 1.11e are obtained from a pre-extended  $\langle \mathbf{c} + \mathbf{a} \rangle$  screw dislocation core

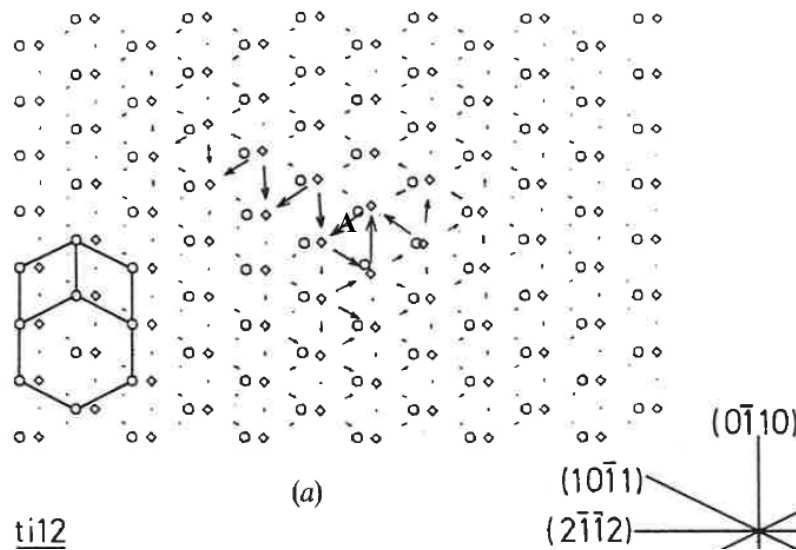


Figure 1.12:  $\langle \mathbf{c} + \mathbf{a} \rangle$  screw dislocation core dissociation in  $\pi_1$ ,  $\pi_2$  and prismatic planes obtained using a  $t_{112}$  potential with a dislocation line position at A [52].

equilibrium state of the dislocation and corresponds to the Peierls valleys. The Peierls stress, which allows a dislocation motion from one Peierls valley to another without thermally-activation process, can be obtained from the maximal slope of the Peierls potential profile.

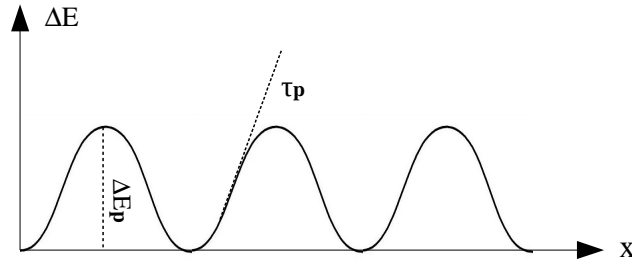


Figure 1.13: Peierls potential profile.  $\Delta E_p$  is the Peierls energy barrier and  $\tau_p$  is the Peierls stress.

#### 1.1.2.4.2 $\langle a \rangle$ screw dislocation glide

The  $\langle a \rangle$  screw dislocation glide is intensively studied in literature. As concluded by Caillard and Martin [65], two thermally activated mechanisms may operate below and above a given temperature (around 300 K for Ti) for the prismatic glide, which leads to a discontinuity of the activation enthalpy. Above 373 K, straight screw dislocations move steadily with an average velocity depending more on their intrinsic mobility between visible obstacles than on their interactions with obstacles. This behaviour corresponds to a kink-pair mechanism. Below 300 K, the same dislocation move jerkily. They stay immobile and then jump very quickly to the next position. This phenomenon is related to the locking-unlocking mechanism presented in the next paragraph.

A dislocation glide in prismatic plane at 150 K [24] is presented in figure 1.14. The white arrows in figure 1.14c represent the dislocation glide during 0.4 second. The barrier potential corresponding to this prismatic slip is presented in figure 1.10 for  $\xi = 1 \sim 5$ .

#### 1.1.2.4.3 locking-unlocking mechanism

The locking-unlocking mechanism [62] was proposed by Farenc, Caillard and Couret to explain the jerky and immobile dislocation behaviours observed in  $\alpha$ -Ti for temperatures below 300 K. In this mechanism, screw dislocations have a sessile (i.e. sitting, immobile) core in their ground state and suddenly transform to activated metastable glissile (i.e. sliding) core states and move rapidly (jerkily) in a prismatic plane. This proposition was confirmed by Clouet et al. in 2015 [24] with

ab initio calculations of the  $\langle \mathbf{a} \rangle$  screw dislocation core. Their results have been shown in figure 1.10.

The locking-unlocking mechanism starts from  $\xi = 0 \sim 1$  where the energy barrier is  $8 \text{ meV}/\text{\AA}$ , twenty times larger than the Peierls energy barrier for the prismatic glide ( $0.4 \text{ meV}/\text{\AA}$ , very small). The prismatic plane spreading core (figure 1.10d) is transitioned to a more stable pyramidal plane ( $\pi_1$ ) spreading core (figure 1.10c). Since the Peierls energy barrier for a  $\pi_1$  plane glide is about  $12 \text{ meV}/\text{\AA}$ , thirty times higher than the Peierls energy barrier for the prismatic glide. The dislocation motion is slowed down after locking. The process in the reverse direction leads to the unlocking of the  $\langle \mathbf{a} \rangle$  screw dislocation glide, hence a quick dislocation motion in prismatic plane.

### 1.1.3 Twinning in $\alpha$ -Ti

#### 1.1.3.1 Twin boundaries

Because of the insufficient number of independent slip systems in hcp materials (see section 1.1.2.1), deformation twinning is also activated, all the more so for deformations along the  $\mathbf{c}$ -axis, and/or at low temperature. Deformation twinning has an important impact on mechanical properties such as material formability [66], texture development [67, 68], strain hardening [69] and ductility [6] in titanium. The three most common twins observed in titanium, as well as in zirconium which also has a low axial  $c/a$  ratio, are the  $\{10\bar{1}2\}$ ,  $\{11\bar{2}1\}$ , and  $\{11\bar{2}2\}$  twins [2]. The  $\{10\bar{1}1\}$  twin is observed under high compression, e.g. 25% strain at room temperature [70], and under low compression along the  $\mathbf{c}$ -axis at high temperature, above  $400^\circ\text{C}$ , [71]. The  $\{10\bar{1}2\}$  twin boundary (TB) has been intensively studied by ab initio calculations [72, 73, 74], as well as the  $\{11\bar{2}1\}$  [75], the  $\{11\bar{2}2\}$  [76, 72], and the  $\{10\bar{1}1\}$  TB [76]. The  $\{10\bar{1}1\}$  TB has been correctly observed and analysed at the atomic level with high resolution transmission electron microscopy (HRTEM) in titanium in 1996, after a series of erroneous analyses [77]. The  $\{10\bar{1}2\}$  TB was first observed with HRTEM in zinc ( $c/a = 1.856$ ) in 1994 [78], then in titanium [79], also see [70] for a review in 1999. These observations agreed with the previously established atomic models with semi-empirical interatomic potentials [80, 81]. Other, rarer, twins can appear in  $\alpha$ -Ti, such as  $\{10\bar{1}3\}$ ,  $\{11\bar{2}3\}$ ,  $\{11\bar{2}4\}$  [82]. I do not consider them in this work. Different types of twins can form within the same grain [83], double twinning phenomena are observed [84]. Detwinning [85] could be induced with a reverse direction load applied.



The crystallographic elements of twinning presented in figure 1.1 and are listed in table 1.4 for the four most important deformation twins observed in  $\alpha$ -Ti.

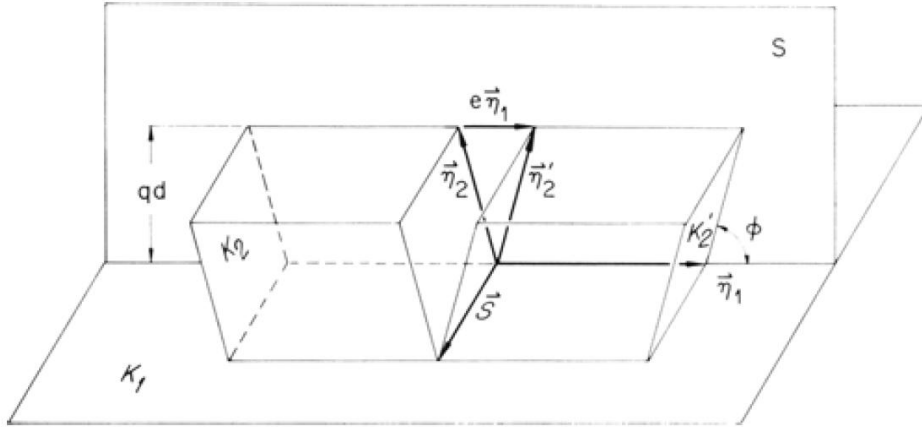


Figure 1.14: Crystallographic elements of twinning. The unit cell defined by  $\eta_1$ ,  $\eta_2$  and  $S$  is homogeneously sheared to the unit cell in twin defined by  $\eta'_1$ ,  $\eta'_2$  and  $S$ . Figure from [6].

Note: The determination of the crystallographic elements and parameters of twins can be obtained with Kihô and Bilby&Crocker's theory [86, 87, 88]. Other descriptive elements  $\eta_2$  (then  $(K_2, \eta_1)$ ) than those given for each  $K_1$  in table 1.4 can be obtained. One usually chose the most reasonable ones, see section x.x.x.x)

Table 1.4: Twinning crystallographic elements  $K_1$ ,  $\eta_2$ ,  $K_2$ ,  $\eta_1$ ,  $S$ , shear magnitude  $s = \frac{1}{2} |e\vec{\eta}_1| / |\vec{\eta}_2|$ , Kihô, Bilby and Crocker's index  $q$ , and  $c$ -type (Tension or Compression, along  $c$ ) for the  $\{10\bar{1}2\}$ ,  $\{11\bar{2}1\}$ ,  $\{11\bar{2}2\}$  and  $\{10\bar{1}1\}$  TBs (with  $\gamma=c/a(1.633)$ ).

$K_1$	$\eta_2$	$K_2$	$\eta_1$	$S$	$s$	$q$	$c$ -type
$\{10\bar{1}2\}$	$\langle 10\bar{1}1 \rangle$	$\{\bar{1}012\}$	$\langle \bar{1}011 \rangle$	$\{1\bar{2}10\}$	$\frac{3-\gamma^2}{\gamma\sqrt{3}}$	4	T
$\{11\bar{2}1\}$	$\langle 11\bar{2}0 \rangle$	(0001)	$\langle \bar{1}\bar{1}26 \rangle$	$\{\bar{1}100\}$	$\frac{1}{\gamma}$	2	T
$\{11\bar{2}2\}$	$\langle 22\bar{4}3 \rangle$	$\{11\bar{2}4\}$	$\langle 11\bar{2}3 \rangle$	$\{\bar{1}100\}$	$\frac{2(\gamma^2-2)}{3\gamma}$	6	C
$\{10\bar{1}1\}$	$\langle 30\bar{3}2 \rangle$	$\{10\bar{1}3\}$	$\langle 10\bar{1}2 \rangle$	$\{1\bar{2}10\}$	$\frac{4\gamma^2-9}{4\gamma^2+3}$	8	C

### 1.1.3.2 Twinning disconnections

The mechanical twins we study are generated during plastic deformations. The formation of such twins can be divided into two parts: twin nucleation and twin growth (see figure 1.15). Twinning disconnection or twinning dislocation (TD) is the key concept for twinning development. It is presented in figure 1.16.  $\mathbf{t}(m)$  and

$\mathbf{t}(t)$  are respectively the translation vector of the matrix part and twin part. The twinning disconnection vector is  $\mathbf{b}_p = \mathbf{t}(t) - \mathbf{t}(m)$ . The TDs step height  $h_p$  is equal to  $\mathbf{n} \cdot \mathbf{t}(m) = \mathbf{n} \cdot \mathbf{t}(t)$ . It is also equal to  $p \cdot d$ , where  $p$  is the number of crystallographic planes (interplanar distance  $d$ ) affected by TD. The TD is characterized by  $(\mathbf{b}_p, h_p)$ .

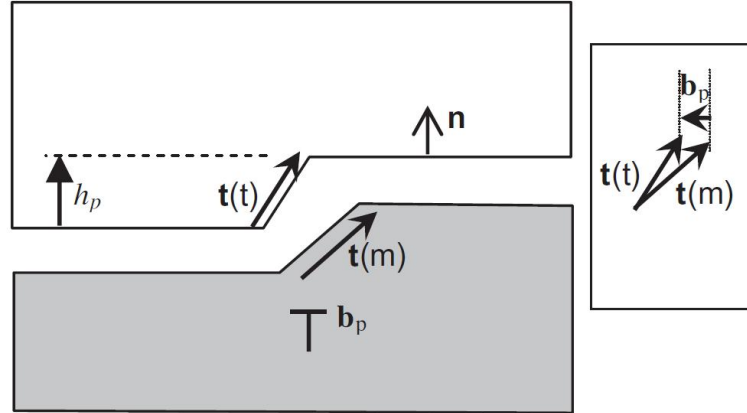


Figure 1.15: Schematic presentation of a TD [89].

Two twin nucleation models exist: homogeneous nucleation [90] and heterogeneous nucleation [91] mechanisms. The first one assumes that the nucleation process can happen without any defect. This model requires a high stress and has little experimental support. The second model proposes that the nucleation process starts from defects such as dislocations, grain boundaries and twin boundaries. As discussed for instance by Wang et al. for hcp metals [92], the instability of a monolayer twin fault suggests that the pole mechanism for twin nucleation in HCP metals, first proposed by Thompson & Millard [93], is not possible. Apart of a few exceptions, the non-coincidence of slip-twinning plane in HCP makes the dissociation-of-dislocation caused twin nucleation unfavourable. A pure-shuffling mechanism has been proposed by Lann and Dubertret [94]. MD simulations by Wang et al. [95] showed a pure-shuffling mechanism.

Generally, the deformation twin growth includes propagation and thickening processes. The propagation process is mainly due to the TD glide in  $K_1$  plane under stress. The thickening process could be explained by: the repeated nucleation process, the entering of matrix dislocations in the twin part, the generation of TDs by dissociation and the rebound of a TD off a boundary onto an adjacent atomic plane [82]. For hcp crystals, since a single TD is stable on pre-existing TB, layer-by-layer glide of TDs is a possible mechanism for twin growth and thickening [81, 96]. The importance of the low energy prismatic/basal interface for the  $\{10\bar{1}2\}$  twin growth has been established [97, 98]. Capolungo et al. pointed that the  $\{10\bar{1}2\}$  twin thickening in Mg is independent of slip-assisted mechanism [99].

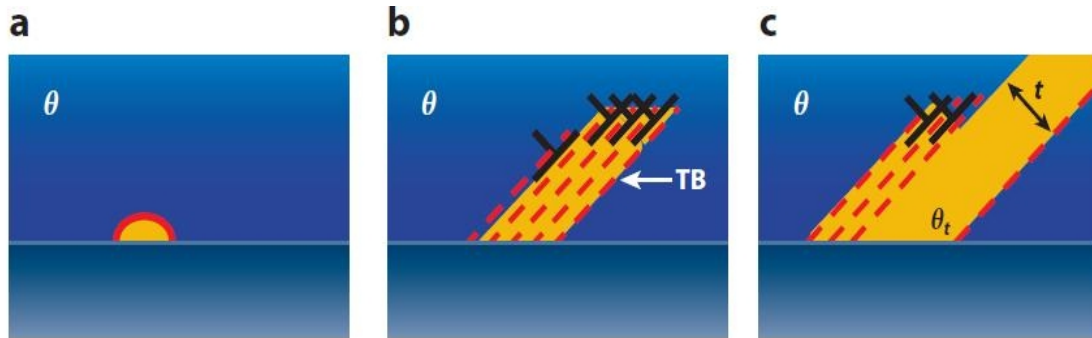


Figure 1.16: Basic processes for twin development: a) nucleation, b) propagation and c) thickening (yellow regions). The twin thickness  $t$  is the spacing between two adjacent twin boundaries (TBs). The bottom blue region is one grain, and the top blue region is another grain with a different crystallographic orientation.  $\theta$  corresponds to the orientation of the parent grain, and  $\theta_t$  is the orientation of the twin. The red dashed lines are the glide planes. The bold black symbols represent twinning dislocations [82].

Numerous studies of the four TD core structures [100, 101], TD generation and growth [102, 96], TD mobilities [81, 103, 89], and TB-dislocation interactions [104, 105] in hcp materials have been carried out by Bacon, Pond, Serra and their collaborators, based on TD constructions using empirical potentials.

Because of the limited accuracy of these potentials and the lack of reliable hcp metal-solute potentials for defect-solute interaction, the ab initio DFT method is also needed. To our knowledge, only Ghazisaeidi, Hector and Curtin [106] simulated with DFT a  $\{10\bar{1}2\}$  TD, with a simple model in which surfaces with fixed borders are used. In that 2014 work, 858 atoms were used for a TD construction, which is at the limit of current (2015-2016) DFT calculations.

## 1.2 Effects of H and O on $\alpha$ -Ti

### 1.2.1 H and O position in Ti

When oxygen (O) and hydrogen (H) are present in  $\alpha$ -Ti as solutes, i.e. not forming as oxides or hydrides, they stay at interstitial sites. There are two main types of interstitial sites in hcp metals [8]: the octahedral (Octa) and tetrahedral (Tetra) sites. They are shown in figure 1.17.

Eight possible self-interstitial atom sites in hcp Ti or Zr have been studied [45, 107, 108]. For oxygen, Henning et al. found the hexahedral site more stable than the

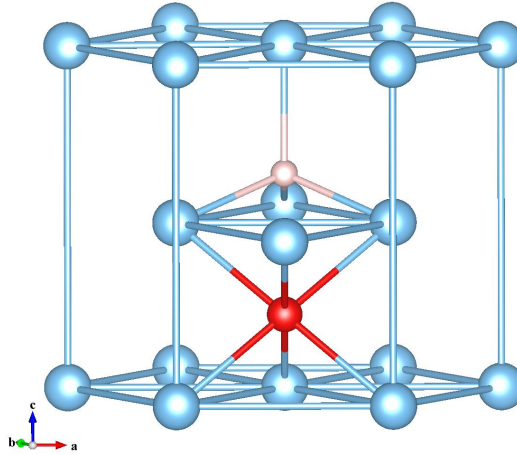


Figure 1.17: The octahedral interstitial atom is shown in red and the tetrahedral interstitial atom is shown in pink. One has  $\mathbf{a} = [2\bar{1}10]$ ,  $\mathbf{b} = [\bar{1}2\bar{1}0]$  and  $\mathbf{c} = [0001]$ .

tetra site [109]. The octahedral site proves to be the most stable one, in agreement with experimental results [110, 8].

The site is, by far, the larger in size compared with the tetrahedra site. Although it is tempting to consider the sizes of these sites and compare them with sizes of oxygen and hydrogen atoms, it would not make much sense with respect to DFT calculations. Besides, the quantum mechanical considerations by Clementi et al. ascribe an atomic radius of 0.48. Albeit in disagreement with experimental analyses at finite temperatures [111, 112], DFT calculations find hydrogen to be more stable in an octahedral site at zero K in  $\alpha$ -Ti [113, 114, 115].

### 1.2.2 Solubility of H and O in Ti

In this work, H and O are put in an octahedral site for a series of supercells of different sizes. The largest box used is 768 atoms ( $8 \times 8 \times 6$ ) for H and 96 atoms ( $4 \times 4 \times 3$ ) for O, corresponding to a H concentration of 27 wt.ppm or 0.13 at.% and 3480 wt.ppm or 1.04 at.% for O. To the best of my knowledge, the Ti-O phase diagram does not seem to be known below 400°C [116]. The maximum solubility of oxygen in  $\alpha$ -titanium is about 33 at.% at elevated temperature, above 600°C. As a stable surface oxide ( $\text{TiO}_2$ , rutile) forms at the titanium surface (with a thickness very slowly growing in time between 3-7 nm at room temperature), oxygen can be kept within titanium even at room temperature, up to 1 at.% ( $\sim 3400$  wt.ppm). The maximum solubility of hydrogen in the  $\alpha$  phase is of the order of 8 at.% (at high temperatures like 600°C for instance), that of nitrogen 19 at.% and carbon

2 at.% [8]. At any given temperature, hydrides may form for H concentrations above the corresponding solubility limit. The solubility limit of H as interstitial atoms of  $\alpha$ -Ti at ambient temperature measured by Paton [118] is 21 wt.ppm ( $\sim 0.1$  at%), in good agreement with the work of Vitt and Ono [119] and K $\ddot{o}$ ster et al. [121]. Vitt and Ono summarised several works with a solubility limit for H in  $\alpha$  Ti (purity  $> 99.7\%$ ) which follows a Sieverts law.

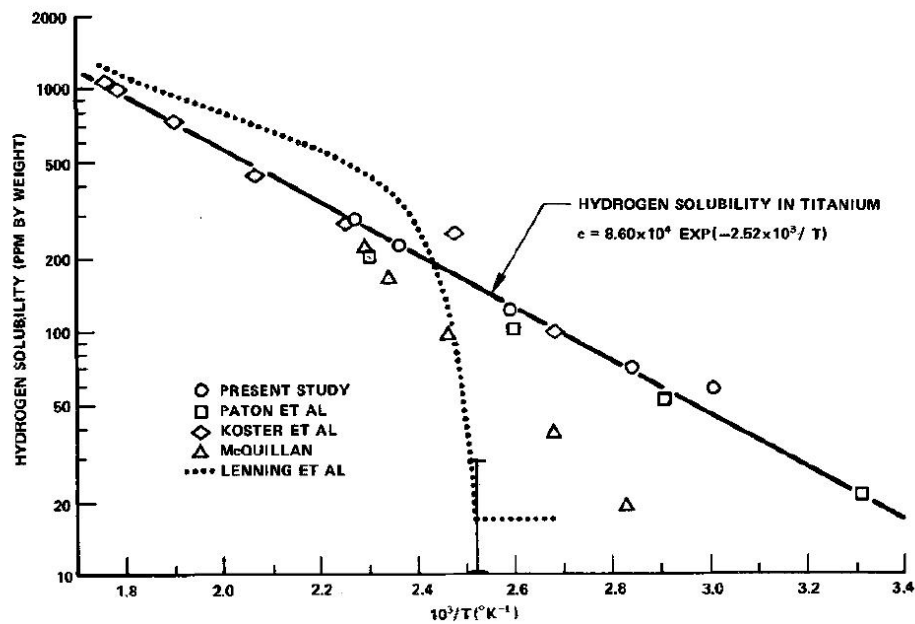


Figure 1.18: H's limit of solubility in the Octa interstitial site [119].

In the Industrial and in the experimental academic world, labels grades 1 to 4 are used for titanium considered as commercially pure (CP), corresponding to various preparations, thermally and mechanically, and various contents of oxygen and other impurities (H, C, N, Fe). The samples can also be qualified according to the US/International ASTM nomenclature, the British (UK) BS nomenclature, the French AFNOR nomenclature (T40, T60, ...), or the German DIN nomenclature, not to mention titanium producers own commercial designations, see, for instance, Cardarelli's Materials Handbook [120].

In the case of oxygen, at ambient temperature, a T40 (with 1600 wt.ppm or 0.51 at.%) and a T60 (with 3200 wt.ppm or 1.02 at.%) materials have been intensively used in the framework of the FluTi ANR project.

### 1.2.3 H and O diffusion in Ti by DFT+Phonon calculation

#### 1.2.3.1 H diffusion

Coupling DFT-NEB calculation with phonon calculation, Lu and Zhang estimated the H, deuterium and tritium diffusivity in Ti [122]. They also reported experimental results for comparison in a figure which we reproduce as figure 1.19. They obtained diffusion pre-factors  $2.5 \times 10^{-6} \text{ m}^2/\text{s}$  and  $1.3 \times 10^{-6} \text{ m}^2/\text{s}$  for the  $D_{0\perp}$  and  $D_{0\parallel}$  directions for temperatures varying from 280 to 1000 K, in pretty good agreement with experimental results which give  $3.0 \times 10^{-6} \text{ m}^2/\text{s}$  and  $1.7 \times 10^{-6} \text{ m}^2/\text{s}$ , respectively [122].

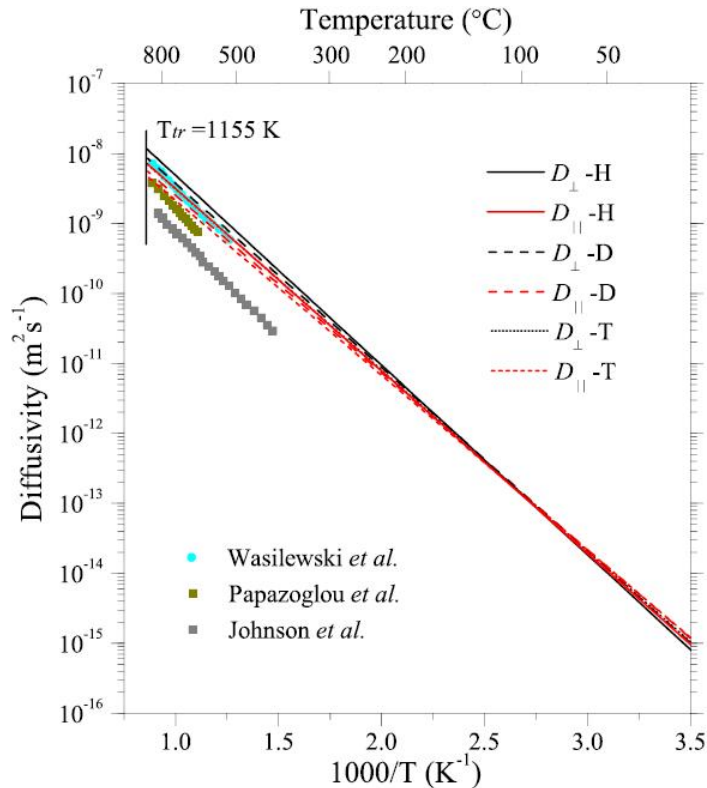


Figure 1.19: Basal and perpendicular diffusivities of H (and of deuterium (D) and of tritium (T)), functions of temperature  $T$ , in  $\alpha$ -Ti, figure from [122].

#### 1.2.3.2 O diffusion

For oxygen diffusion study, the activation energy obtained by Wu and Trinkle in 2011 [110] matches well the experimental results while their calculated absolute diffusion coefficient is ten times smaller than the experimental one. This may be due to their inaccurate energy barriers because only one intermediate image was

used in their the NEB calculations. The comparison with experimental results are shown in figure 1.20.

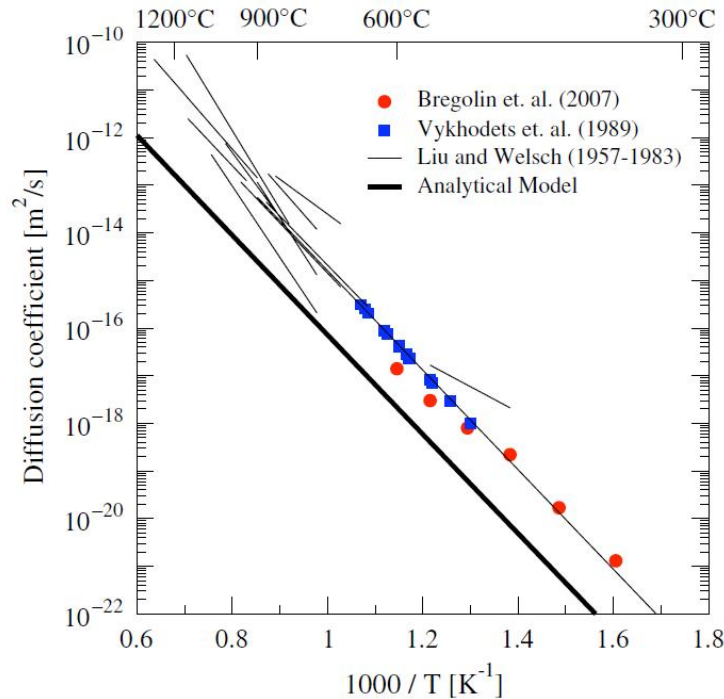


Figure 1.20: Diffusion of O in  $\alpha$ -Ti by Wu and Trinkle [110] (Analytical Model) vs. experimental results.

## 1.3 Effects of H and O on extended defects in $\alpha$ -titanium

### 1.3.1 Effects of O on dislocation cores

Oxygen is an  $\alpha$  phase stabilizer and presents a strong strengthening effect. Its effect on flow stress becomes larger as its concentration increases or as the temperature is lowered in both single and polycrystalline titanium [11, 8, 123], see figure 1.21. The strengthening effect of oxygen is usually explained by its supposed effects on  $\langle a \rangle$  screw dislocation.

According to Conrad [8], the dislocation kinetic aspects can be divided into three temperature regimes:

(a) A low or ambient temperature regime where moving dislocations interact with stationary solutes.

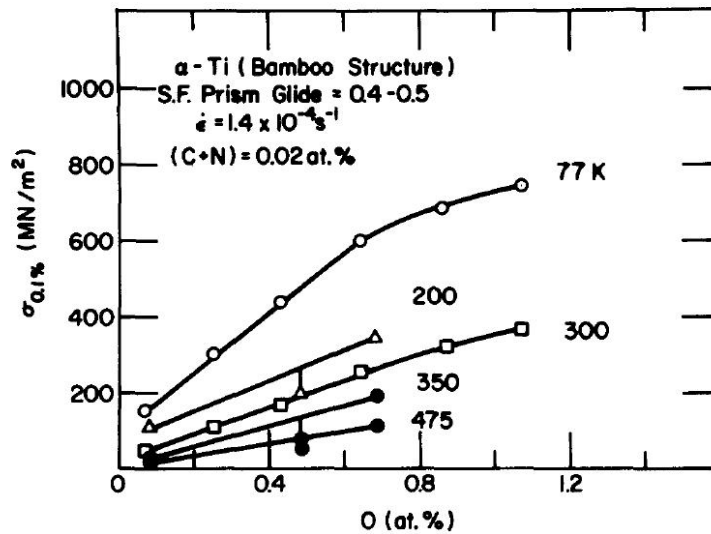


Figure 1.21: Effect of oxygen on the yield stress of Ti wire specimens with a ‘bamboo’ structure. Data from Elssner, Krohn and Ruano [124].

(b) An intermediate temperature regime where moving dislocations interact with slowly moving solutes and where the dynamic strain ageing behaviour appears (in the PhD thesis work of Barkia, the dynamic strain ageing (serration) is also observed in the ambient temperature)

(c) An high temperature regime where the solutes move rapidly.

First tentative explanations were related to the elastic strain field interactions since the presence of O creates a non-spherical distortion of Octa sites, which meets the Fleischer criterion for rapid hardening [125]. The solute is assumed to act as a “thermal” obstacle for the prismatic dislocation motion. Several models exist for the solute strengthening phenomena. There are at least two models for the solute interaction with a non-dissociated core: 1) the Friedel-Fleischer model where the obstacles to the dislocations are individual solute atoms at low concentration, 2) the Mott-Nabarro-Cottrell model where the obstacles reflect the collective action of groups of solute atoms at high concentrations.

A model by Šob, Kratochvil and Kroupa [126, 127] proposed that the core structure of screw dislocations in the hcp, lattice of  $\alpha$ -Ti can be described by a sessile splitting on the prism plane and on the first order pyramidal plane simultaneously and that slip can proceed after its transformation into a glissile configuration on the prism plane. The strengthening by interstitial solutes is considered as a barrier (through an elastic interaction between the interstitial atoms and the partial on the first-order pyramidal planes) for this these thermal activated sessile-glissile transformations.



The work of Tyson, Kratochvil and Conrad suggests that the strengthening effect cannot be simply explained by elastic interaction. A chemical interaction is likely to be involved. The breaking of Ti-O directed bonds may change dislocation core structure.

A recent study of Yu et al. [10] showed a dramatic strengthening effect of oxygen. The dislocations before and after deformation in the  $\alpha$ -Ti with an oxygen concentration of 0.1 wt.% and 0.3 wt.% are shown in 3D in figure 1.22. After deformation, the dislocation array with 0.3% of oxygen is tangled and moved to different planes. The dislocation array breaks up into groups, each containing several dislocation lines with defined pinning points (red arrows in figure 1.22B).

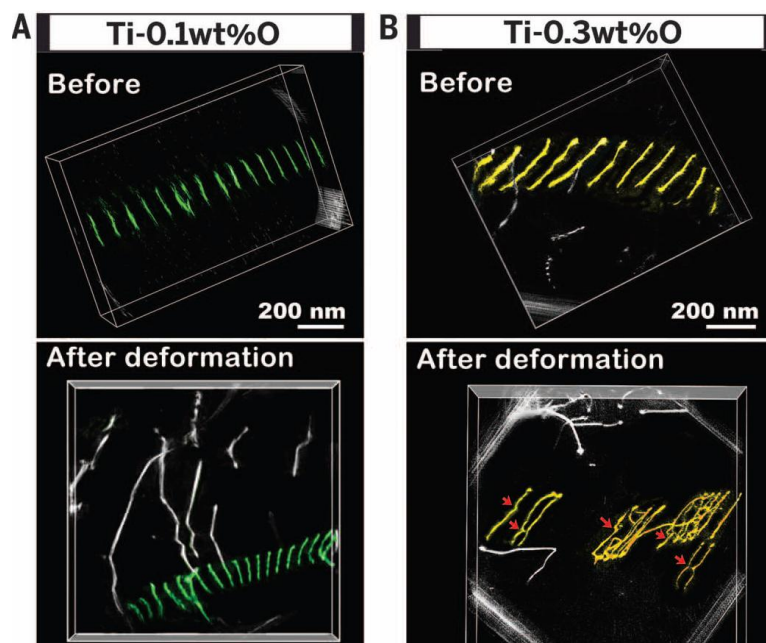


Figure 1.22: A) dislocations in 3D before and after deformation in Ti-0.1wt%O, B) dislocations in 3D before and after deformation in Ti-0.3wt%O.

Yu et al. also performed a DFT-based  $\langle a \rangle$  screw dislocation core simulations. They only found the metastable prismatic plane spreading core. When an oxygen is put into the small core region and in the prismatic plane where the dislocation line is located, they obtained a large repulsive “interaction” between the core and the oxygen. They observed a partial cross-slip of the prismatic plane spreading core to an adjacent prismatic plane and proposed a possible cross-slip mechanism of  $\langle a \rangle$  screw dislocation induced by oxygen. However, the proposed cross-slip mechanism implies the appearance of two partial edge dislocations connected with the screw segment, see figure 1.23, which is very different from Šob’s proposition.

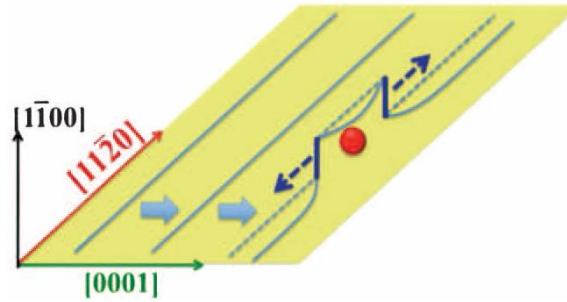


Figure 1.23: The cross-slip mechanism of an  $\langle \mathbf{a} \rangle$  screw dislocation induced by an oxygen, as proposed by Yu et al. [10]

In 2015, in her PhD thesis work, Chaari, together with her supervisor(s), showed a strong effect of oxygen on the prismatic core structure. Three different sites near central core position were tested with prismatic or pyramidal plane spreading core configuration. They found that the presence of such an oxygen favours a combination of mixed prismatic-pyramidal plane core spreading when started from either a prismatic or a pyramidal plane spreading core, see figure 1.24.

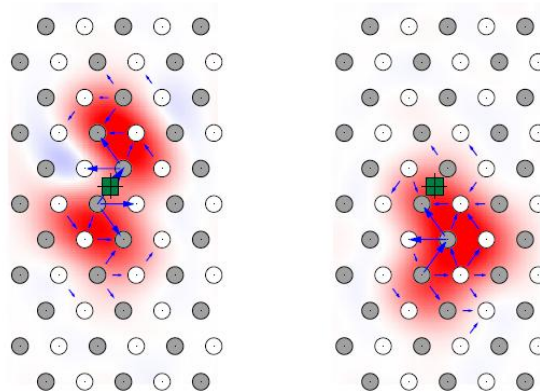


Figure 1.24: a) Initial DD map with a oxygen is placed in central core position; b) DD map after relaxation [128].

Some of my works on oxygen-core interaction have been done in parallel.

The presence of oxygen near  $\langle \mathbf{a} \rangle$  screw dislocation cores may be also responsible for other phenomena, such as dynamic strain ageing (serration). Figure 1.25 shows a mechanical jump test of  $\alpha$ -Ti, where serration is clearly found.

Abnormal peaks at the front of transversal direction (TD) strain-stress curves were observed in the PhD thesis work of Barkia [11], see figure 1.26. Since  $\langle \mathbf{c} + \mathbf{a} \rangle$  dislocation were observed only in TD direction, the abnormal peak, considered as a static ageing phenomena, was attributed to the interaction of oxygen with  $\langle \mathbf{c} + \mathbf{a} \rangle$  dislocation, see figure 1.26.

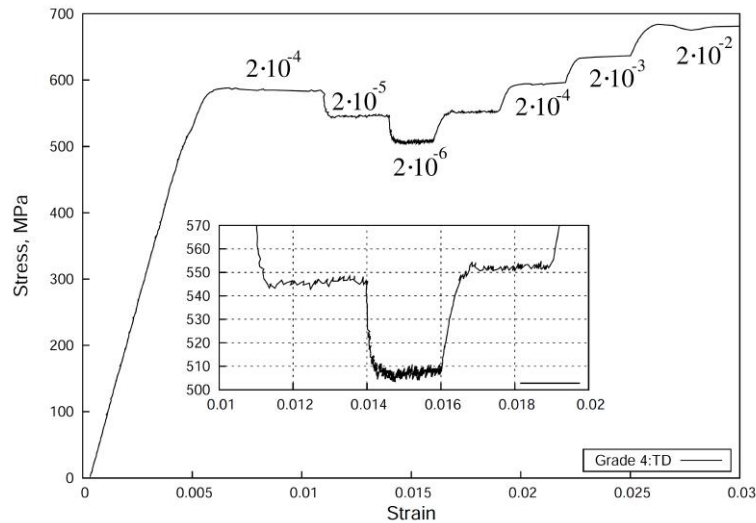


Figure 1.25: Serration on Stress-Strain curve under a mechanical jump test [11]

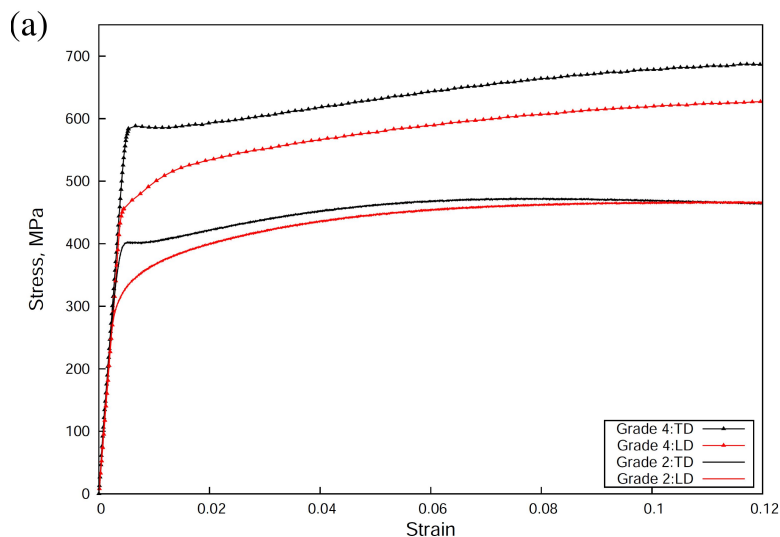


Figure 1.26: Abnormal peaks at the front of two TD direction strain-stress curves related to  $O-\langle c+a \rangle$  interaction [11].

### 1.3.2 Effects of H on dislocation cores

Hydrogen is a  $\beta$  phase stabilizer. It has a low solubility limit (21 wt.ppm) in  $\alpha$ -Ti at ambient temperature, see section 1.2.2. It presents a more complex role with respect to the mechanical properties of  $\alpha$ -Ti. Beck's experiments (figure 1.27) showed a slight increase of the prismatic CRSS [17]. It seems that even its small strengthening effects depend on the concentration of other major solutes in Ti, such as O, Fe, N, C.

However, it weakens titanium in other cases [13, 14, 22, 15]. The recent study done by Marchenko (and her supervisor(s)) in her PhD thesis work [20] showed a

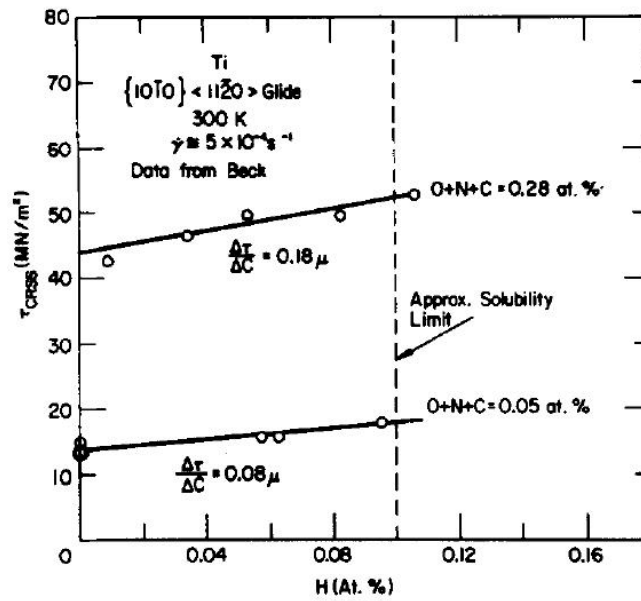


Figure 1.27: Effect of hydrogen content on the critical resolved shear stress for prism slip of Ti. [17]

decrease of fracture toughness (“softening effect”) with the increase of H concentrations tested in T40 and T60 samples, see figure 1.28. A non-monotonic effect of H on Ti creep at ambient temperature was observed by Mignot et al. [21]. Furthermore, both Barkia and Marchenko observed that different H/O concentration ratios affect the creep phenomena and other mechanical properties of  $\alpha$ -Ti [11, 20].

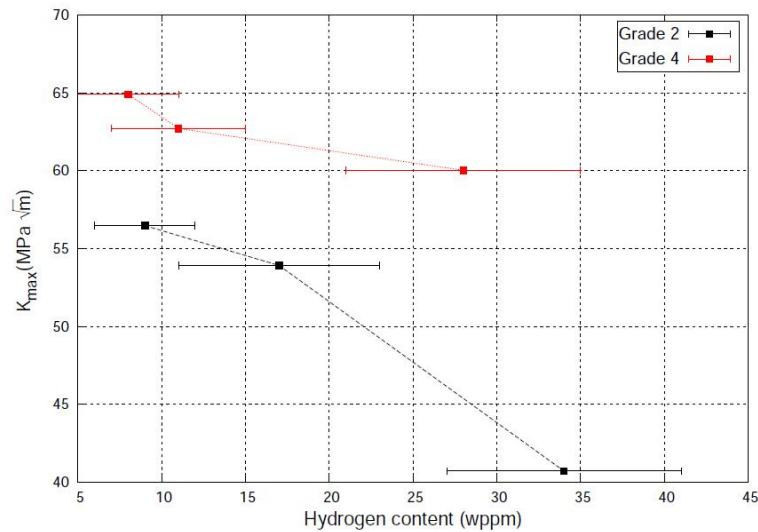


Figure 1.28: Fracture toughness  $K_{max}$  for T40 and T60 as a function of H concentration [20].

### 1.3.3 Effects of H and O on Twin boundaries

The effects of interstitial solute on twinning are much less studied compared to solute-dislocation interaction study. Periodic segregation of substitutional solutes has recently been observed in magnesium [129] to three coherent twin boundaries, accompanied by pinning and strengthening effects. The presence of oxygen in twin boundaries of  $\alpha$ -Ti has recently been studied by ab initio calculations [74] (see figure 1.29), as well as the solubility of many impurities in TBs in several hexagonal metals [72], but a complete segregation study of H or O on the three most common TBs in  $\alpha$ -titanium has not yet been done. In view of the increasing interest for ab initio calculations of mechanical properties (see [130] for a recent review), it may also be useful to investigate at the atomistic level the behaviour of these TBs under strain along a uniquely chosen crystallographic axis, e.g. the  $c$ -axis, for the sake of comparisons, without and with solutes.

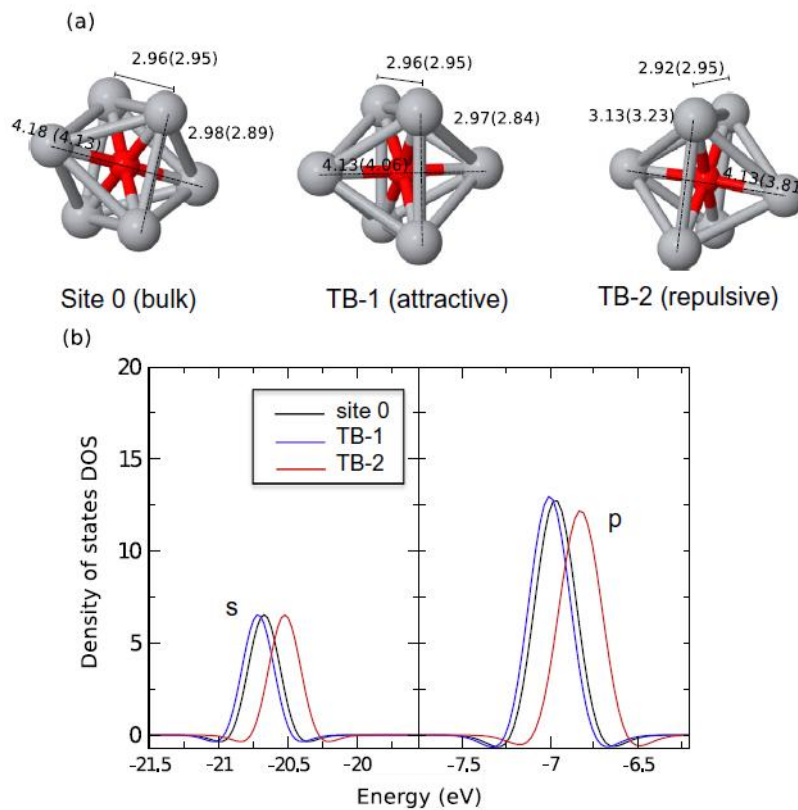


Figure 1.29: a) Geometric analysis of O in a bulk site or two near  $\{10\bar{1}2\}$  TB sites. Values in parenthesis are distances before relaxation in Å. After relaxation, octahedral site in TB1 and TB2 approach those in bulk environment. b) electronic density of states for oxygen s and p states at each site. Site 0 is the bulk octahedral site. Attractive and repulsive sites show shifts in the oxygen states, but not changes in broadening [74].

### 1.3.4 Effects of H and O on Twinning disconnections

Oxygen diffusion controlled twinning mechanism during low-temperature creep has been proposed [12]. They explained that, since oxygen diffuses very slowly compared with the twin growth speed during creep, the presence of oxygen in the octahedral sites near TB act as barrier for new twin layer formation, the schematic twinning formation in presence of oxygen is presented in figure 1.30.

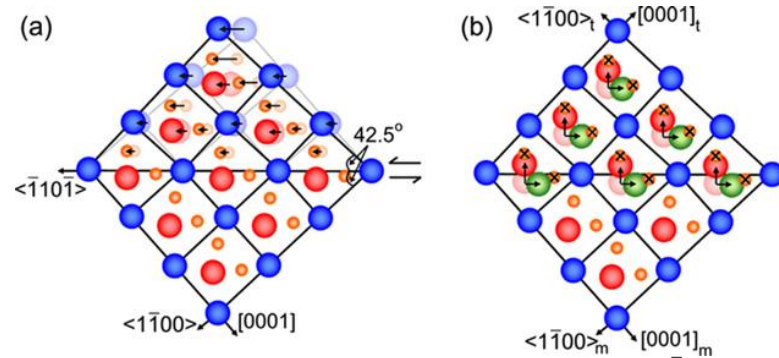


Figure 1.30: a) Shear added to perfect crystal to form a  $\{10\bar{1}2\}$  twin in  $\langle \bar{1}10\bar{1} \rangle$  direction; b) Arrows give the shuffles required to move the atoms in B-type sites (red) to either the B-(red) or C-type sites (green) in the twinned lattice. Reorientation of the lattice will eliminate the octahedral sites (marked with an X) where an oxygen atom could reside. [12].



# Chapter 2

## Theory & Tools and Techniques

This chapter presents the theories, the simulation tools and the techniques and models used in this work.

The theories and the corresponding simulation tools are presented in the first part, including the *abinitio* calculations via Vienna Ab initio Simulation Package (VASP<sup>TM</sup>), the Zero Point Energy (ZPE) calculations coupled with PHON program.

In the second part, different simulation models are presented for solutes interactions in Ti, elastic constant calculations, stacking faults, screw dislocation cores; twin boundaries and twinning disconnection and solute segregation.



## 2.1 Theory & Tools

### 2.1.1 Density Functional Theory with VASP code

#### 2.1.1.1 Density Functional Theory

In this PhD work, the density functional theory (DFT) is used to study the solute-defect interactions in  $\alpha$ -Ti. I use the Vienna Ab initio Simulation Package (VASP<sup>TM</sup>) in its 5th version [131, 132].

Although DFT is very well described in several good books, such as, among others, Martin's book [133], I still want to say a few words about it in order to introduce what still are its main approximations in its (practical) actual applications, for which I rely on VASP<sup>TM</sup>.

Among the different electronic structure calculation methods with wave-function-based approaches, the Hartree-Fock method is one of the simplest. It uses the Born-Oppenheimer, or adiabatic, approximation to decouple the motion of electrons from the motion of atomic nuclei. For the electrons, it only considers some limited, approximated, effects between them. They can only "feel" the effect of other electrons as an average, expressed by the Hartree potential term. This method does not take the so-called correlation effects between the electrons but it takes the electron exchange effects into account via the use of rapidly heavy Slater determinants.

The density functional theory also uses the Born-Oppenheimer approximation. The main differences with previous approach is the consideration of the ground state electronic density as the fundamental notion instead of the electron wave-functions.

The use of the electronic density relies on two fundamental theorems provided by Pierre Hohenberg and Walter Kohn [134].

The first theorem is: the electronic ground-state energy of a system described by a from Schrödinger's equation is a unique functional of the electron density assuming the so-called  $v$ -representability, when " $v$ " is the external potential applied onto the electrons. It rigorously proves that a functional of the electron density exists that can be used to solve the Schrödinger equation, but it says nothing about what the functional actually is.

The second theorem is: the electron density that minimises the energy of the overall functional is the true electron density corresponding to the full solution of the Schrödinger equation. That theorem still says nothing about what the functional actually is even if it provides, in principle, a way to get its variational minimisation.

In order to offer a constructive way to actually progress in the finding of the electron density problem in some nuclei environment, Walter Kohn and Lu-Jeu Sham [135] considered in 1965 that the electronic density  $n(\mathbf{r})$  can be expressed as corresponding to a set of  $N$  fictitious Kohn-Sham electrons with fictitious Kohn-Sham orbitals  $\varphi(\mathbf{r})$ , via  $n(\mathbf{r}) = \sum |\varphi(\mathbf{r})|^2$ , so that the kinetic energy functional  $T[n]$  is exactly  $\sum_i^n -\frac{\hbar^2}{2m} \nabla^2 \varphi_i(\mathbf{r})$

$$\left[ -\frac{\hbar^2}{2m} \nabla^2 + \nu_{ext}(\mathbf{r}) + \nu_H(\mathbf{r}) + \nu_{XC}(\mathbf{r}) \right] \varphi_i = \varepsilon_i \varphi_i \quad (2.1)$$

for  $i=1, N$ .  $-\frac{\hbar^2}{2m} \nabla^2 \varphi_i$  is the kinetic part of electron  $i$ ,  $\nu_{ext}(\mathbf{r})$  is the external Coulomb potential due to the atomic nuclei,  $\nu_H(\mathbf{r})$  is the Hartree-Coulomb potential between the electrons, and  $\nu_{XC}(\mathbf{r})$  is the exchange-correlation part of the effective external potential.

Note that for heavy atoms this approach can be extended to the consideration of the Dirac equation, rather than the Schrödinger equation.

The main problem is to get some good approximation of the exchange and correlation description. This problem is addressed (alluded to) in the next section. Another problem is related to the fact that is usually numerically very difficult to actually consider all  $N$  electrons where  $N$  is the total number of electrons at stake in the many atom problem considered. It is numerically very difficult and may not be necessary for the study of many properties. This will be addressed in the ‘pseudopotentials’ section (2.1.1.3).

### 2.1.1.2 Exchange-correlation functional: PBE-GGA

Several approximations can be used to define the exchange-correlation functional. Among them, we have: the local density approximation (LDA) and the generalized gradient approximation (GGA). The LDA considers that it is possible and numerically efficient to simply carry out a spatial integration over locally homogeneous

electron gas.

$$E_{XC}^{LDA}[n] = \int \varepsilon_{XC}(n)n(\mathbf{r})d\mathbf{r} \quad (2.2)$$

where  $\varepsilon_{XC}(n)$  is the one electron exchange-correlation energy of a homogeneous electron gas, which has been obtained by Ceperley and Alder [136] using a heavy quantum mechanical Monte-Carlo simulation.

For system where the electron density is too far from being uniform, even ‘locally’, information on the spatial variation in the electron density, should be included. The GGA approximation is then usually used although it is not perfect and may even prove worse than LDA in some cases such as vacancy problems. One has:

$$E_{XC}^{LDA}[n] = \int f(n, \nabla n)n(\mathbf{r})d\mathbf{r} \quad (2.3)$$

where  $f(n, \nabla n)$  is a an effective one electron exchange-correlation energy.

The Perdew-Burke-Ernzerhof GGA functional (PBE-GGA) [137] is used in this work, via VASP. According to its authors, it integrates many of the best features of the local spin density approximation (LSDA). The improvements over the Perdew-Wang GGA [138] include an accurate description of the linear response of the uniform electron gas, a correct behaviour under uniform scaling, and a smoother potential. It is divided into a correlation  $E_C^{GGA}$  and an exchange  $E_X^{GGA}$  part.

$$E_C^{GGA}[n \uparrow, n \downarrow] = \int d^3r n[\epsilon_C^{unif}(r_s, \zeta) + H(r_s, \zeta, t)] \quad (2.4)$$

where  $n \uparrow, n \downarrow$  represent the electron spin densities.  $\epsilon_C^{unif}(r_s, \zeta)$  is the correlation energy per particle of a uniform electron gas.  $H$  is the gradient contribution from three conditions.  $r_s$  is the local Wigner-Seitz radius ( $n = 3/4\pi r_s^3$ ,  $\zeta = (n \uparrow - n \downarrow)/n$  is the relative spin polarization, and  $t$  is a dimensionless density gradient. For the exchange  $E_X^{GGA}$  part:

$$E_X^{GGA} = \int d^3r n\epsilon_X^{unif}(n) + F_X(r_s, \zeta, s) \quad (2.5)$$

where  $F_X$  is the spin-polarized enhancement factor,  $s$  is the reduced gradient. See Perdew et al. [137] for a detailed description. The PBE-GGA functional is a very widely used functional for metals.

### 2.1.1.3 Pseudopotentials: the PAW method

The chemical bonding and other physical properties of materials are mainly defined by the so-called valence electrons. The so-called core electrons have generally small influences on these properties. Thus, instead of explicitly calculating all electron interactions between all electrons (as in the full-potential linear muffin-tin orbital (FP-LMTO) Method, for example, which implies some linearisation procedure), a frozen core approximation is used in the so-called pseudopotential method. Rigorous arguments are provided in many good books and I only want to give here some flavour of the method. A core region is defined by a cut radius  $r_c$ . Inside that core region, the true electronic wavefunction with its large variations is replaced by a smoothly varying wavefunction. The part outside the core region keeps the same dispersion character. This treatment decreases significantly the size of a plane wave basis needed for a given accuracy. Furthermore, compared with the norm-conserving pseudopotential (NCP) and the ultrasoft pseudopotential (USPP), the projector-augmented-wave (PAW) method originally introduced by Blöchl [139] provides a way to calculate almost all-electron like properties from the smooth wavefunctions. The PAW method keeps the full all-electron wavefunction in a form similar to the general orthogonalized-plane-wave (OPW) method used in NCP or USPP, and the augmented-plane-wave (APW) approach is used with muffin-tin spheres for describing the rapid variation of full wavefunction near the nucleus.

A linear transformation  $\tau$  relates the smooth functions  $\tilde{\Psi}^v(\mathbf{r})$  to the all-electron wavefunctions  $|\Psi^v\rangle$  by:

$$|\tilde{\Psi}^v\rangle = \tau^{-1} |\Psi^v\rangle \quad (2.6)$$

$\tau$  implies a set of projectors within a core region defined by a chosen parameter  $r_c$ , so that, beyond  $r_c$ , one has  $|\Psi\rangle = |\tilde{\Psi}\rangle$ .

With respect to previous pseudization schemes, the PAW method ensures in an automatic way that the valence wavefunctions are initially built in an exact, full-electron, way. Yet, of course, only these valence wave functions are explicitly considered in the many atom density functional optimisation. The core functions below  $r_c$  remain frozen. The accuracy of the PAW potential modelling thus still depends on the number of electrons considered as valence electrons, e.g. 4 or 12 in the case of titanium. Besides, even for a given number of valence electrons, the PAW construction involves  $r_c$  as a parameter. This is probably what distinguishes

VASP PAW 12 electrons 2000 and 2005. From inspection of the VASP POTCAR input files, the main difference is the use of an RCLOC=1.7 (cutoff of potential) in the version of 2000, replaced by a variable ICORE=3 (Local potential) in 2005. Reducing the  $r_c$  is important for the study of very high pressure phases, see [31]. It should not be important in this work which is carried out at zero pressure.

If X is a given transition metal with  $d$  and  $s$  valence electrons, one has in VASP X-potentials which only consider valence electrons, and  $X_{pv}$ -potentials which also consider the six  $3p$  electrons in the underlying layer (so-called semicore electrons). In VASP guide, it is said that: “when to switch from  $X_{pv}$  potentials to the X potentials for metal with  $3d$  electrons, even the Ti, V and Cr potentials give reasonable results, but should be used with uttermost care”.

Most calculations done in this work are performed with X-potential (4 electrons in Ti with  $3d4s$ . Recall that isolated Ti atoms have the following electronic structure:  $1s^22s^22p^63s^23p^63d^24s^2$ ). X and  $X_{sv}$  potentials (two more  $3s$  electrons compared to  $X_{pv}$  potential) are compared versus several physical properties in the following table 2.1.  $X_{sv}$  considers 12 electrons in Ti with  $3s^23p^63d4s$ . We used the version PAW-PBE 12e-2005 (the 2000 version gives similar results).

For the plane wave cut-off energies (see definition in eq. (2.9)), I use 300 eV for the 4e PAW potential (i.e. about 70% larger than the corresponding VASP ENMAX value which is 178 eV), and 500 eV for the 12e PAW potential (more than 80% larger than the VASP ENMAX=275 eV). Kpoint=14x14x10 for both cases. A Methfessel-Paxton method of order one or two is used for smearing with a smearing width of 0.02-0.1 eV [132, 149]. Some calculated properties are given in table 2.1. The last column should be complemented by direct comparisons with experimental values when available, as it is the case for the elastic constants. This is done in Table 3.10 (in Chapter 3). With respect to these elastic constants, the 12e PAW potential is not much more superior to the 4e PAW potential. It is actually worse for some. And whereas  $C_{44}$  and  $C_{66}$  (as  $(C_{11} - C_{12})/2$ ) are the linear responses to shear modes,  $C_{12}$  and  $C_{13}$  are not autonomous elastic responses:  $C_{12}$  is obtained as  $C_{12}=(C_{11} + C_{12})/2 + C_{66}$ , and  $C_{13}$  as  $C_{13}=[9B-2(C_{11} + C_{12})-C_{33}]/4$ . Some discussions about the other physical properties are provided in section 2.2.

The partial density of states (DOS) of one Ti atom with 4e and 12e potential are presented in figure 2.1. The  $s, p, d$  orbital of both potential have the same variation profiles, but differences can be easily observed. For example, the  $3d$  orbital with 12e potential is less smooth than the one with 4 potential. Band structures between the two potentials are very similar (figure 2.2).

Table 2.1: Comparison between 4e and 12e PAW-PBE potential for various properties in  $\alpha$ -Ti. Also see section 3.4 and table 3.10 for the elastic constants.

	4e	12e-2005	Expt.	$ \frac{12e-4e}{12e} $
<b>Lattice parameter</b>			[140]	
a	2.924 Å	2.937 Å	2.946 Å	0.4%
c/a	1.581	1.582	1.587	0.4%
<b>Elastic constants</b>	(GPa)	(GPa)	(GPa)[141]	
$C_{11}$	186	185	176	0.53%
$C_{12}$	88	81	87	8.6%
$C_{13}$	84	76	68	10.5%
$C_{33}$	191	189	191	1.1%
$C_{44}$	47	49	45	4.1%
$C_{66}$	49	52	45	5.8%
$C_{66}/C_{44}$	1.04	1.06		2.0%
<b><math>E_f</math> of H in Ti 3x3x2</b>	(eV)	(eV)		
Octa	-2.705	-2.702		0.1%
Tetra	-2.624	-2.627		0.1%
Octa-Tetra	-0.081	-0.075		7.4%
<b>SFE</b>	(mJ/m <sup>2</sup> )	(mJ/m <sup>2</sup> )	(mJ/m <sup>2</sup> )	
Prism. $\frac{1}{2}\langle a \rangle$	213	244	155±25 [142]	12.7%
Basal $I_2$	309	307		0.7%
$\pi_1 \frac{1}{2}\langle a \rangle$	738	803		8.1%
$\pi_1 \frac{1}{2}\langle c + a \rangle$	513	543		5.5%
$\pi_2 \frac{1}{2}\langle c + a \rangle$	626	664		5.7%
<b>Disloc. core <math>E_{excess}</math></b>	(eV/Å)	(eV/Å)		
Prism.	0.403	0.413		4.1%
$\pi_1$	0.387	0.401		3.0%
$E_{prism} - E_{\pi_1}$	0.016	0.012		25%

#### 2.1.1.4 Plane wave bases

Any one-electron wavefunction can be described by a finite or infinite set of plane waves. A supercell periodically repeated in space allows to define a series of relevant wavefunctions:

$$\varphi_{nk} = u_{nk}(\mathbf{r})e^{i\mathbf{k}\cdot\mathbf{r}} \quad (2.7)$$

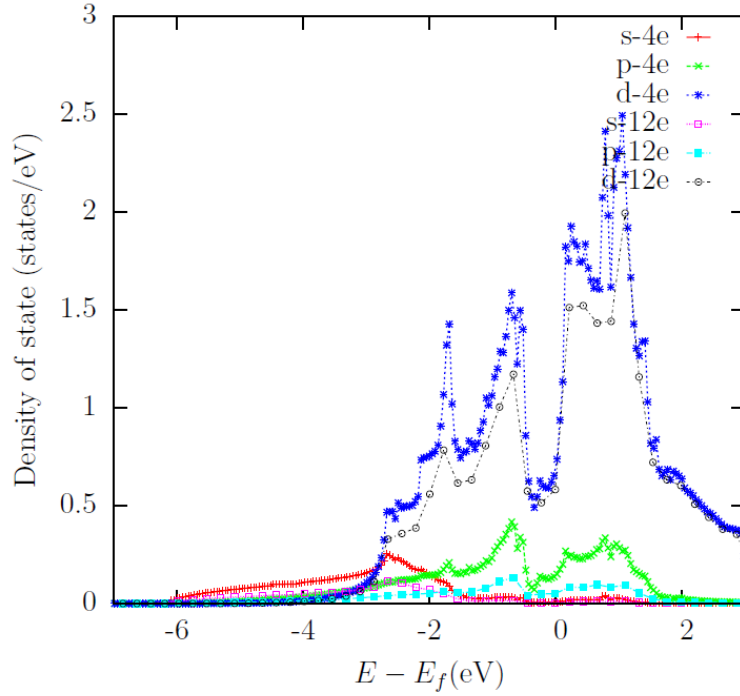


Figure 2.1: DOS of Ti with 4e or 12e

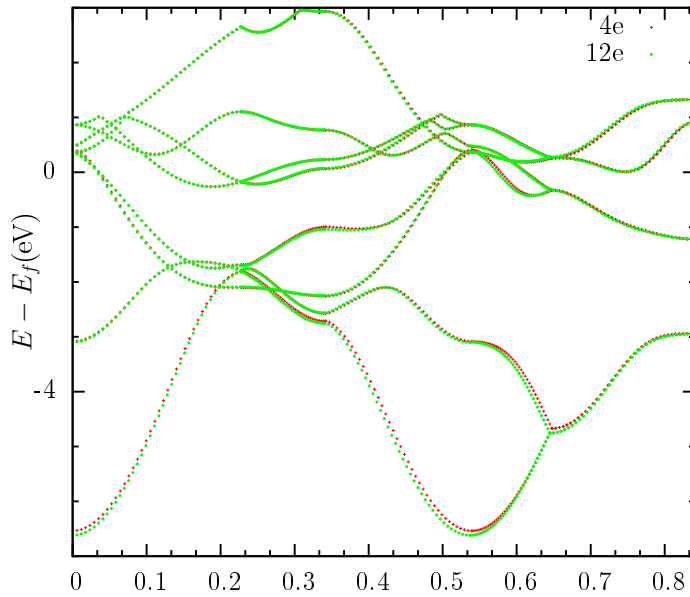


Figure 2.2: Band structures of Ti with 4e or 12e

where  $\varphi_{n\mathbf{k}}$  is the wavefunction associated with band  $n$  and the wave vector  $\mathbf{k}$ . The  $u_{n\mathbf{k}}(\mathbf{r})$  are functions with the periodicity of the supercell. They can thus be Fourier expanded in terms of plane waves involving  $\mathbf{G}$  vectors of the form  $m_1 \cdot \mathbf{b}_1 + m_2 \cdot \mathbf{b}_2 + m_3 \cdot \mathbf{b}_3$  where the  $m_i$  span all possible integers and the  $\mathbf{b}_i$  are reciprocal lattice vector of the supercell lattice vector  $\mathbf{a}_i$ , defined by  $\mathbf{a}_i \cdot \mathbf{b}_j = 2\pi\delta_{ij}$ .

Thus, the wavefunctions can be described as:

$$\varphi_{n\mathbf{k}} = \sum_{\mathbf{G}} C_{n,\mathbf{k}+\mathbf{G}} e^{i(\mathbf{k}+\mathbf{G})\cdot\mathbf{r}} \quad (2.8)$$

One obviously has  $\varphi_{n\mathbf{k}+\mathbf{G}'} = \varphi_{n\mathbf{k}}$ . The  $\mathbf{k}$  vectors of all the relevant  $\varphi_{n\mathbf{k}}$  functions can thus be restricted to the first Brillouin zone. The previously mentioned Fourier expansions of the  $u_{n\mathbf{k}}(\mathbf{r})$  are in principle infinite. In practice they can be limited as soon as one considers that the physical properties obtained from a sufficiently large set of  $\varphi_{n\mathbf{k}}$  are converged. That limitation on the  $\mathbf{G}$  is, for a given  $\mathbf{k}$ , on all the  $\mathbf{G}$  such that:

$$|\mathbf{k}+\mathbf{G}|^2 < \frac{2mE_c}{\hbar^2} \quad (2.9)$$

Where  $E_c$  is called a cut-off energy and is determined together with a satisfying sampling in  $\mathbf{k}$  of the first **BZ** until convergence of the physical properties.

High symmetrical  $\mathbf{k}$  points are naturally chosen for an efficient sampling of the First BZ. The Monkhorst-Pack method [144] can be used to get these points. The MP method is optimised for cubic crystals. It is not so for hexagonal crystals for which a Gamma centred grid is a better choice.

In VASP, in the INCAR file, the cutoff energy (ENCUT) needed for convergence is 300 eV for 4e and 500 eV for 12e PAW-PBE potential. In the KPOINTS file, parameter  $n_{k1} \times n_{k2} \times n_{k3}$  is set to determine the  $k$ -grid generation. After the convergence test, a 14x14x10  $k$ -grid is applied to a  $\alpha$ -Ti primitive cell containing 2 atoms for both the 4e and 500 eV for 12e PAW-PBE potential.

The choice of a larger cell decreases the volume of corresponding BZ and thus reduces the number of  $k$  points needed to achieve convergence. For a slab, the number for  $k$  point is set to one in the slab direction since it is considered as a supercell with an infinitely large dimension in that direction (infinitely large in principle, numerically finite in practice).

### 2.1.1.5 Calculation of ground state in VASP

The procedures to obtain the ground states are visualised in figure 2.3.

Four files are needed for a VASP calculation, the INCAR, POSCAR, KPOINTS, POTCAR file. POSCAR contains the information about the three lattice vectors of the supercell, the atoms species and the atomic positions. KPOINTS contains



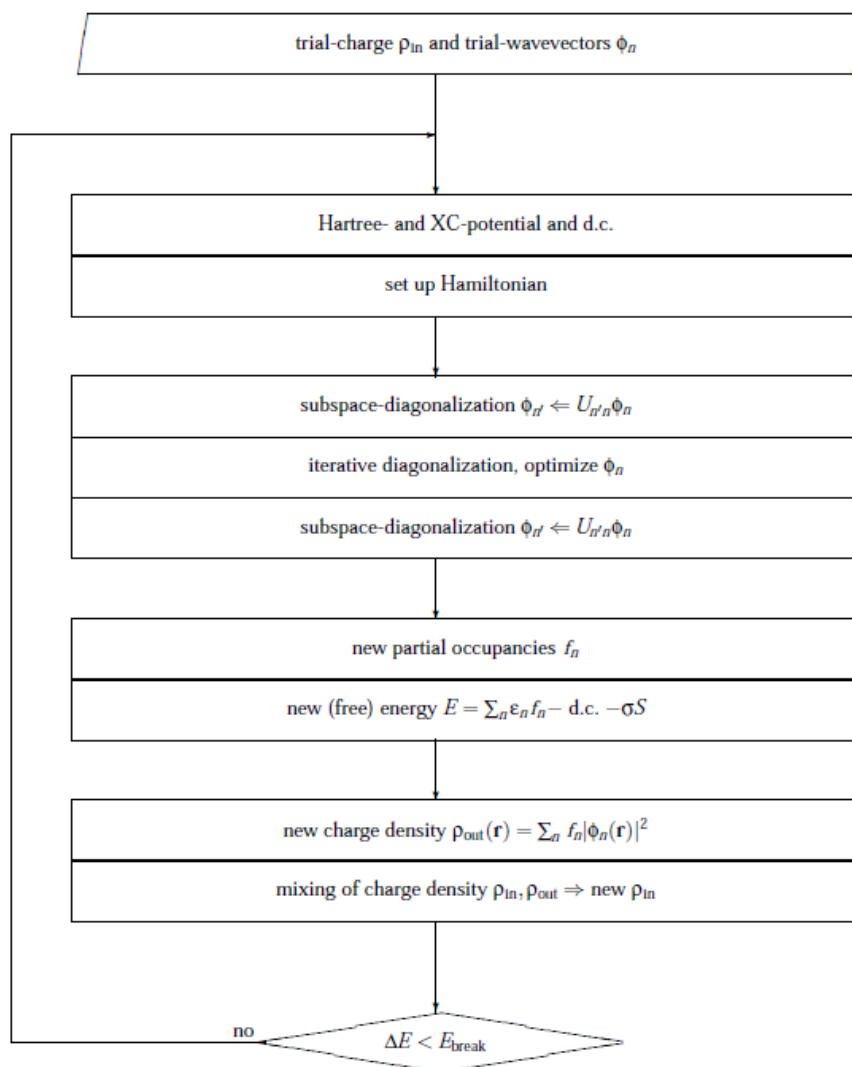


Figure 2.3: Procedures of a self-consistent calculation to obtain the KS ground state in VASP [145]

the information for the  $k$ -grid generation. POTCAR is the file describing the ion-electron interaction potential. INCAR is the file which defines the options to be taken to carry out the *abinitio* DFT calculation which implies various optimization algorithms.

Note that another way than Kohn-Sham exists, which is orbital free, and computationally much more efficient for some materials (no matrices to diagonalise, up to 1 million atoms of Al in simulation box for example [146]). Unfortunately it implies other limits and it is not efficient for transition metals.

### 2.1.2 Vibrational Energy Calculations via PHON

From the Gibbs free energy  $G=F+PV$ , the Helmholtz energy  $F$  part can be approximated at volume  $V$  and temperature  $T$  can be approximated by the following equation [147]:

$$F(V, T) = E_{el}(V) + F_{vib}(V, T) + F_{TEC}(V, T) \quad (2.10)$$

where  $E_{el}(V)$  is the 0 K electronic total energy,  $F_{vib}(V, T)$  the lattice vibrational free energy of the ions under the quasi-harmonic approximation.  $F_{vib}(V, T)$  is:

$$F_{vib}(V, T) = k_B T \sum_{\mathbf{q}} \sum_j \ln \left\{ 2 \sinh \left[ \frac{\hbar \omega_j(\mathbf{q}, V)}{2k_B T} \right] \right\} \quad (2.11)$$

where  $\omega_j(\mathbf{q}, V)$  represents the frequency of the  $j$ th phonon mode at wave vector  $\mathbf{q}$ . When possible magnetic contributions and electron - phonon interactions are neglected, the thermal electronic contribution  $F_{TEC}(V, T)$  is composed by the energy and entropy parts, equal to  $E_{TEC} - TS_{TEC}$ . The bare electronic entropy is expressed by :

$$S_{TEC}(V, T) = -k_B \int n(\varepsilon, V) [f \ln f + (1 - f) \ln(1 - f)] d\varepsilon \quad (2.12)$$

where  $n(\varepsilon, V)$  is the electronic density of states and  $f$  is the Fermi distribution  $f(\varepsilon_F, \varepsilon, T)$  where  $\varepsilon_F$  is the Fermi energy. The electronic excitation part is expressed by:

$$E_{TEC}(V, T) = \int n(\varepsilon, V) f \varepsilon d\varepsilon - \int_0^{\varepsilon_F} n(\varepsilon, V) f \varepsilon d\varepsilon \quad (2.13)$$

The electronic total energy  $E_{el}(V)$  at 0 K is directly obtained with VASP program. For the  $F_{vib}(V, T = 0)$ , the phonon frequencies  $\omega_j(\mathbf{q}, V)$  are obtained from the Born force constant matrix. The phonon frequencies at wave-vector  $\mathbf{q}$  are the eigenvalues of the dynamical matrix  $D_{s\alpha, t\beta}$ , expressed as:

$$D_{s\alpha, jt\beta}(\mathbf{q}) = \frac{1}{\sqrt{M_s M_t}} \sum_i \Phi_{is\alpha, jt\beta} \exp[i\mathbf{q} \cdot (\mathbf{R}_j^0 + \tau_t - \mathbf{R}_i^0 - \tau_s)] \quad (2.14)$$

and the force constant matrix elements  $\Phi_{is\alpha, jt\beta}$  are calculated with the force components  $F_{is\alpha, jt\beta}^{u_{jt\beta}}$  on atom  $is$  when atom  $jt$  moved by  $u_{jt\beta}$  with respect to its perfect

position.

$$\Phi_{is\alpha,jt\beta} = -\frac{F_{is\alpha,jt\beta}^{u_{jt\beta}} - F_{is\alpha,jt\beta}^{-u_{jt\beta}}}{2u_{jt\beta}} \quad (2.15)$$

where  $i, j$  are cell numbers,  $s, t$  atom numbers,  $\alpha, \beta$  Cartesian directions.  $\mathbf{R}_i^0$  is a lattice vector which gives the position of the primitive cell  $i$  and  $\tau_s$  is the position of the atom  $s$  in the primitive cell.

The forces are calculated with VASP with the Hellmann-Feynman theorem, using for the electronic occupancies a smearing procedure adapted to metallic systems.

$F_{vib}(V, T)$  is then obtained from the related above. These calculations are actually done by and with Alfè's PHON program [148]. The thermal electronic contribution  $F_{el}$  is zero since we work at 0 K.

## 2.2 Techniques

The 5th version of VASP<sup>TM</sup> is used with MPI parallel programming mainly on  $k$  points and on electronic bands. Simulations were mainly performed using HPC resources from local clusters at École Polytechnique through the LLR-LSI project (672 cores on LLR-LSI Jollyjumper; 128 cores on LLR-LSI Rantanplan and 128 cores on LSI Zauberfloete) where I have been one of the major users so that the LLR-LSI project must be gratefully acknowledged. 0.43 million CPU hours are also consumed via equally gratefully acknowledge projects on GENCI-CINES/IDRIS. Generally, 24-256 cores are used for one calculation during 1~2 days. About 2-2.5 million CPU hours were consumed during my PhD work.

The needs of diagonalisation of Kohn-Sham Hamiltonians for DFT calculations cause an extremely calculation time increase with the increase of number of electrons per simulated cell. A calculation with 12e potential is more than ten times heavier than the one with a 4e potential in  $\alpha$ -Ti.

For  $\alpha$ -Ti, the energy is converged to  $10^{-6}$  eV on a primitive cell containing two atoms with a plane-wave energy cut-off of 300 eV and  $14 \times 14 \times 10$   $k$  points generated in a Gamma centred grid. For further simulations, the number of irreducible  $k$  points times the number of simulated atoms product is maintained as much as possible for larger boxes. The metallic electronic partial occupancies are taken care of with the tetrahedron method with Blöchl corrections for small boxes when

forces are not required. Otherwise a Methfessel-Paxton method of order one or two is used for smearing with a smearing width of 0.02-0.1 eV [132, 149]. The Kohn-Sham Hamiltonian is diagonalised with the residual minimisation method direct inversion in the iterative subspace [132, 133]. Conjugate gradient method is used to optimise the atom positions by minimising the Hellmann-Feynman forces.

For convergence criterion of electronic relaxation (labelled EDIFF in VASP INCAR file), I most usually chose a value of 0.01 meV. For the convergence criterion of subsequent atom position relaxation, so-called ionic relaxation (labelled EDIFFG in VASP INCAR file). I generally chose a value of 1 meV (EDIFFG positive) on the energy where only energy minimisations are required. I also occasionally carried out convergence on forces rather than on energy (using negative value of EDIFFG in VASP) to check the validity of some atomic position relaxations. For the calculations with dislocation cores where relaxations may be difficult to achieve with only energy minimisation convergence, the convergence on forces are chosen. In this work, I consider that the core relaxation in pure  $\alpha$ -titanium is converged within 2 meV/Å. The solute segregation calculations and the Peierls energy barrier calculations performed with CI-NEB method of three intermediate images are converged to 10 meV/Å (See Sections 3.5 and 5.1).

Seen from table 2.1, the comparison between 4e and 12e potential shows that: lattice parameters of  $\alpha$ -titanium are nearly the same; elastic constant values change less than 10%; anisotropy of  $\alpha$ -Ti changes by 2%; Stacking-fault energy changes are less than 13%; Formation energy of Ti-H bond within a  $Ti_{36}H$  system is nearly the same, which indicates the solute effects on Ti bulk or with defects should be very limited when passing its potential from 12e to 4e.

Larger differences (in %) can be obtained if one considers differences of differences. This is the case when calculating the energy difference between a prismatic plane spreading core and a pyramidal plane spreading core: the difference between 4e and 12e goes up to 25%. Yet the important point is that both PAW versions give a larger  $E_{prism}$  than  $E_{\pi_1}$ . The some remark must be done for the Octa-Tetra difference.

For Ti-H and Ti-O system calculations, oxygen is modelled with its six  $2s2p$  electrons. Hydrogen is modelled with a potential in which the number of electrons is not exactly one. All potentials (Ti,H,O) are provided by VASP. Cutoff energies of 300 eV and 400 eV have been tested for Ti-H and Ti-O system. Differences are less than 2% for the Ti-solute bond formation energy when the solute is in an octahedral or in a tetrahedral site. The differences of formation energy between

the octahedral and the tetrahedral site is less than 0.5%. I thus chose 300 eV for ENCUT, consistent with the cutoff perviously chosen for pure  $\alpha$ -Ti.

### 2.2.1 Solutes interactions in Ti

In this section, I first introduce the equation for the formation energy of of Ti-solute bond, with one solute in an Octa or a Tetra interstitial site. The formation energy is calculated as the difference between the total energy of supercell containing Ti+solute and the sum of energy of the pure titanium cell and one half of the energy of the solute under the form of a molecule.

$$E_f = E_{Cell+solute} - [E_{Cell} + 1/2E_{molecule}] \quad (2.16)$$

When there are two solutes in a cell of  $\alpha$ -titanium and each solute is in a different interstitial site, the interaction energy between the two solutes is calculated in equation 2.17. Possible configurations for interstitial-interstitial atom interaction are shown in figure 2.4 with **c** direction projection (a) and **a** direction projection (b). In total, 15 possible configurations are found. The interaction energy is calculated by the difference between the sum of total energy of supercell containing Ti+A+B plus a pure titanium supercell and the sum of total energy of two supercell each containing one solute in interstitial site.

$$E_{Interaction} = E_{Cell+A+B} + E_{Cell} - [E_{Cell+A} + E_{Cell+B}] \quad (2.17)$$

### 2.2.2 Elastic constant calculations

The elastic stiffness constants (EC) of a material characterise the strain-stress relations in the elastic domain. A symmetric Voigt matrix of 6x6 is used to describe these relations. For a hexagonal material, crystalline symmetry reduces number of independent elastic constants to only five [150, 151]. The Voigt matrix is presented below. In its standard way,  $x$  and  $y$  are orthogonal directions in the isotropic basal plane,  $z$  is along **c** axis.

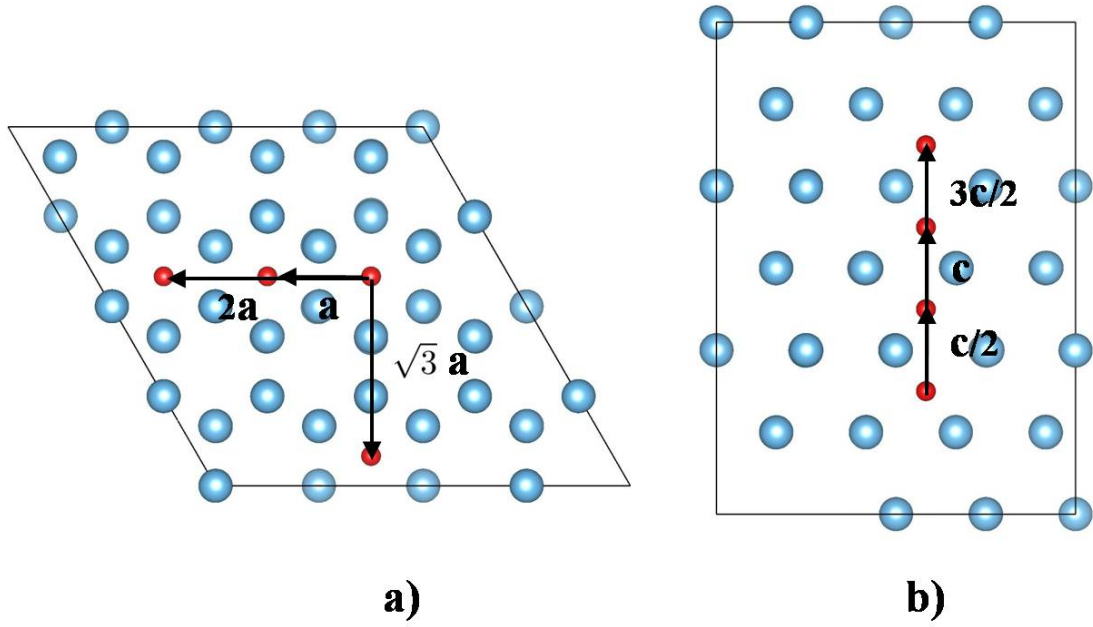


Figure 2.4: Possible configurations for the study of interstitial-interstitial atom interaction. a)  $c$ -axis projection; b)  $a$  direction projection

$$[C_{ij}]_{\text{Hex}} = \begin{bmatrix} C_{11} & C_{12} & C_{13} & 0 & 0 & 0 \\ C_{12} & C_{11} & C_{13} & 0 & 0 & 0 \\ C_{13} & C_{13} & C_{33} & 0 & 0 & 0 \\ 0 & 0 & 0 & C_{44} & 0 & 0 \\ 0 & 0 & 0 & 0 & C_{44} & 0 \\ 0 & 0 & 0 & 0 & 0 & C_{66} \end{bmatrix}$$

with  $C_{66} = \frac{(C_{11}-C_{12})}{2}$

From these elastic constants, three important moduli can be obtained, The bulk modulus  $B$  (module of compressibility, noted  $B$  in this work, yet noted  $K$  by other good authors, Feynman included!), the Euler-Young modulus  $E$  (elastic modulus), and the Coulomb shear modulus  $G$  (modulus of rigidity).

One can estimate these moduli for isotropic polycrystals under the Voigt assumption of uniform strain within the polycrystal [150] rather than under the Reuss assumption of uniform stress (cf., for instance, [152]) because the results are almost the same for Ti (This would not be true for Zn). The formulas are:

$$B = \frac{1}{9}[2(C_{11} + C_{12}) + C_{33} + 4C_{13}] \quad (2.18)$$

$$G = \frac{1}{30}[7C_{11} - 5C_{12} + 2C_{33} - 4C_{13} + 12C_{44}] \quad (2.19)$$

$$E = \frac{[(2C_{11} + 2C_{12} + 4C_{13} + C_{33})(7C_{11} - 5C_{12} + 2(-2C_{13} + C_{33} + 6C_{44}))]}{3[9C_{11} + 5C_{12} + 4(3C_{13} + C_{33} + C_{44})]} \quad (2.20)$$

The three-dimensional distribution of the directional Young modulus characterizes its elastic anisotropy [153]. It is obtained by the following equation:

$$E(l_1, l_2, l_3) = [(1 - l_3^2)S_{11} + l_3^4 S_{33} + l_3^2(1 - l_3^2)(2S_{13} + S_{44})]^{-1} \quad (2.21)$$

where the  $S_{ij}$  are the elastic compliance constants and  $l_3$  is the  $z$ -cosine direction. The  $[S_{ij}]$  matrix is the inverse of the  $[C_{ij}]$  matrix.

Five independent deformation modes are used to get the 5 independent  $C_{ij}$  of the hexagonal symmetry [32, 154]. Series of deformations [-2%, -1%, -0.5%, 0.5%, 1%, 2%] are applied for each deformation mode in order to obtain the corresponding elastic constants, see section 3.4.

### 2.2.3 Stacking faults

In this method, the rigid translation is applied to the upper half block of super-cell in order to create a Generalised-SF (GSF) in the middle (See figure 2.5). The atoms are allowed to relax only in the direction perpendicular to the fault plane. We use the slab model with two surfaces. The form and the volume of the supercell are fixed. The excess energies for each GSF are then obtained on each slip plane by the following equation:

$$\gamma = \frac{E_{slab}^{GSF} - E_{slab}}{A} \quad (2.22)$$

Working out the corresponding this  $\gamma$ -plot, we identified some possible meta-stable SFs which are revealed by local energy minima on the surface.

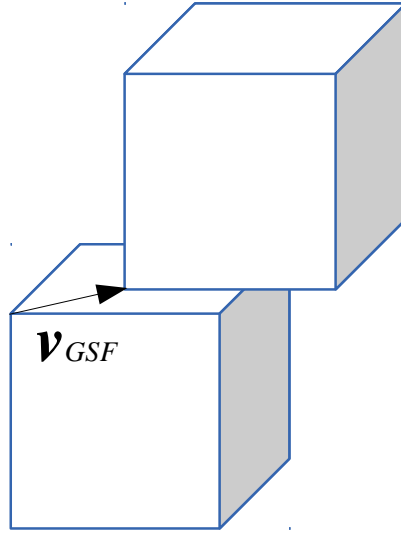


Figure 2.5: Schematic presentation of a GSF characterized by the fault vector  $\mathbf{v}_{GSF}$ .

## 2.2.4 Screw dislocation cores

### 2.2.5 $\langle \mathbf{c} + \mathbf{a} \rangle$ screw dislocation core construction

Three models for dislocation core construction are introduced in the first chapter. Since the second method (flexible boundary condition method) is difficult to control and the plane perpendicular to  $\langle \mathbf{c} + \mathbf{a} \rangle$  screw dislocation direction is not periodic in the direction perpendicular to  $\pi_2$  plane  $[11\bar{2}\frac{2}{\Lambda^2}]$  with  $\Lambda^2 = (2/3)(c/a)^2$ , the first method is chosen.

The initial condition for relaxation is the isotropic elasticity solution for the perfect screw dislocation displacement field which is applied to all atoms.

$$u_z = \frac{b}{2\pi} \cdot \tan^{-1}\left(\frac{y}{x}\right) \quad (2.23)$$

A quasi-cylinder with 8 periods of  $[\bar{1}100]$  vector length, see figure 2.6 and 32 atomic layers in the direction perpendicular to  $\pi_2$  plane are built. The unrelaxed  $\langle \mathbf{c} + \mathbf{a} \rangle$  screw dislocation core is presented in figure 2.6. Two central core positions, A and B in figure 2.6, are tested as centres for the atomic displacements imposed in the outer cylinder according to elasticity theory. My systems contain about four



hundred atoms (412 with A and 413 with B). A vacuum layer of 15 Å surrounds the cylinder. The cut-off is also chosen to separate the light blue zone where the atoms are allowed to a three direction relaxation while the atoms in the dark blue zone are allowed to relax only in the  $\langle \mathbf{c} + \mathbf{a} \rangle$  direction.

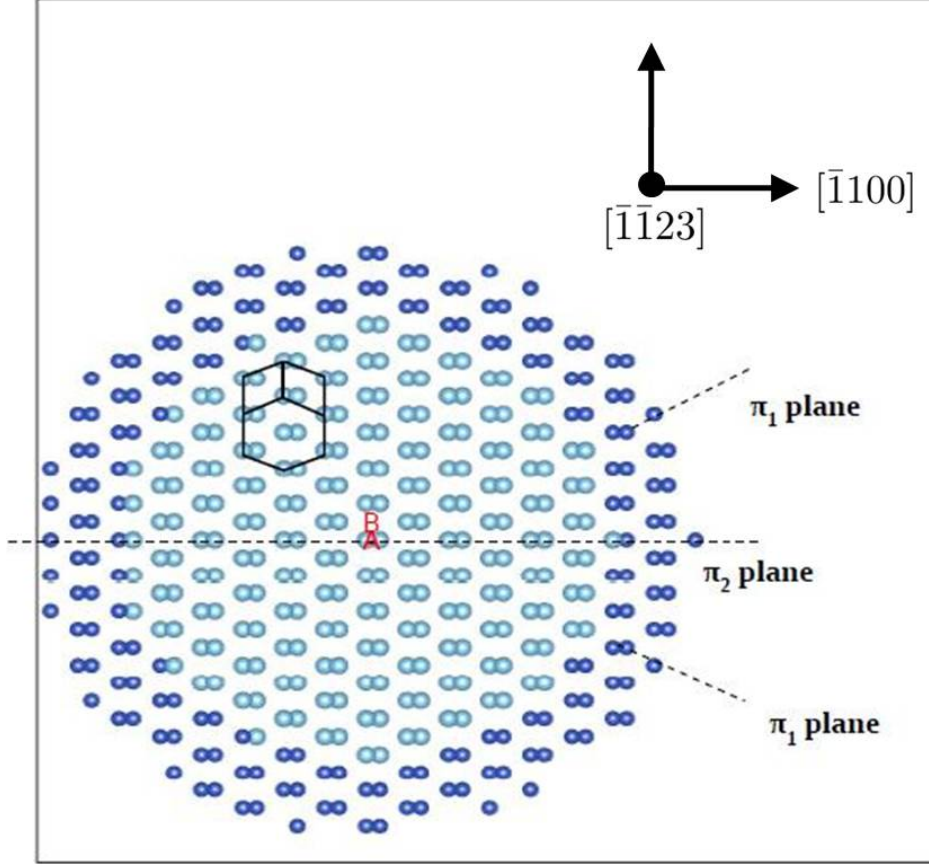


Figure 2.6: The  $\langle \mathbf{c} + \mathbf{a} \rangle$  screw dislocation visualised with two central core positions A and B for the application of  $u_z$  [eq. 2.22]. Direction perpendicular to  $\pi_2$  plane is  $[\bar{1}\bar{1}\bar{2}\frac{2}{\Lambda^2}]$  with  $\Lambda^2 = (2/3)(c/a)^2$ .

After DFT relaxation, Vitek's difference displacement maps (DDmap) of the relaxed configuration are drawn. What the DDmaps show are pair difference displacements  $u_z[i, j]$ : The arrows are from the smaller to the larger displacement between atoms. The arrow lengths represent the displacement differences. Only arrows with a magnitude larger than  $0.1 | \langle \mathbf{c} + \mathbf{a} \rangle |$  are presented in the DDmap.

$$u_{z[ij]} = (u_z^{final_i} - u_z^{initial_i})_{max} - (u_z^{final_j} - u_z^{initial_j})_{min} \quad (2.24)$$

Since  $u_z$  in equation 2.24 depends only the distance from the core position from screw dislocation, pairs of close atoms as visible in figure 2.6 can be considered as single entities and the DDmap procedure is applied on these pair entities.

### 2.2.6 $\langle a \rangle$ screw dislocation core construction

The quadrupole dislocation model applied by Clouet on Zr [23] uses a 3D periodic method, thus without free surface problems. The centrosymmetry property of the quadrupole configuration minimise the stress added by one core of the dipole to the other. This allows the use of a relative small box to calculate the Peierls Stress by imposing a NEB method. Compared with O arrangement, the S arrangement avoids the annihilation of two prismatic direction orientated dislocation dissociation [23]. We will thus use the S arrangement to simulate our  $\alpha$ -Ti  $\langle a \rangle$  screw dislocation core.

Once a bulk structure is built, the anisotropic elasticity of a straight dislocation is applied to the box, see Eschelby et al., Stroh, Hirth & Lothe 1982 section 13-3, Balluffi section 3 [37, 155, 156, 157, ?, ?]. In the equilibrium state, one has

$$c_{i\alpha k\beta} \frac{\partial^2 u_k}{\partial x_\alpha \partial x_\beta} = 0 \quad i = 1, 2, 3 \quad (2.25)$$

where Einstein summation is assumed on the indices  $\alpha, k, \beta$  which together with  $i$ , represent orthogonal directions.  $c_{i\alpha k\beta}$  are the elastic stiffness constants in their four indices tensorial notation,  $u_k$  is the elastic field displacement along  $k$  within the stroh et al. formalism. The solutions of these equations are :

$$u_k = A_k f(\eta) \quad (2.26)$$

where

$$\eta = x_1 + px_2 \quad (2.27)$$

and where  $p$  and  $A_k$  are constants. Solving the sextic equation for a screw dislocation, one gets:

$$u_k = Re \left[ \frac{-1}{2\pi i} \sum_{n=1}^3 A_k(n) D(n) \ln \eta_n \right] \quad (2.28)$$

when  $x_3$  is parallel to the screw dislocation direction line. The basic requirement for a simple solution of the pure edge-pure screw type is that the  $x_1x_2$  plane be a reflection plane. This is true in our case.

For the pure screw dislocation,  $A_1(1) = A_2(1)=0$  and  $A_3(1)$  can be chosen equal 1. One finds that the displacement is (see, [37], eq. 13-128)

$$u_z = -\frac{b_z}{2\pi} \tan^{-1} \frac{(C'_{44}C'_{55} - C'^2_{45})^{\frac{1}{2}} y}{C'_{44}x - C'_{45}y} \quad (2.29)$$

Where the  $C'_{ij}$  are the Voigt elastic constants with respect to the relevant  $(x_1, x_2, x_3)$  orthogonal frame.  $C'_{44}$ ,  $C'_{45}$  and  $C'_{55}$  must thus be obtained from the standard  $C_{ij}$ . In the case of our  $\langle \mathbf{a} \rangle$  screw dislocation, two Bond-rotations are needed [?]. The first corresponds to a clockwise  $90^\circ$  rotation and the second to an anti-clockwise rotation of  $42^\circ$ .

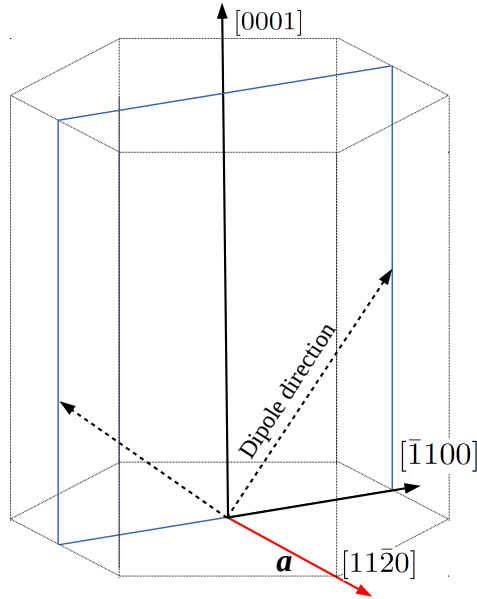


Figure 2.7:  $\langle \mathbf{a} \rangle$  screw dislocation core construction.

Table 2.2: Titanium elastic constants (GPa) in the standard and in the new Cartesian frames.

	$C_{11}$	$C_{12}$	$C_{13}$	$C_{33}$	$C_{44}$	$C_{45}$	$C_{55}$	$C_{66}$
standard	186	88	84	191	47	0	47	49
new	184	90	84	186	48	2	48	51

Since the  $\tan^{-1}(\frac{y}{x})$  is discontinuous at  $x \sim 0$ , correct  $+\pi$  or  $-\pi$  constants must be added in the computer program (written in Fortran).

A dipole is then constructed in several steps using the method of Cai [58]. The dipole is visualised in figure 2.8 with a continuous analytic model in the left which is without error adjustment and a discontinuous model with 800 atoms in the right in which the adjustment has been done .

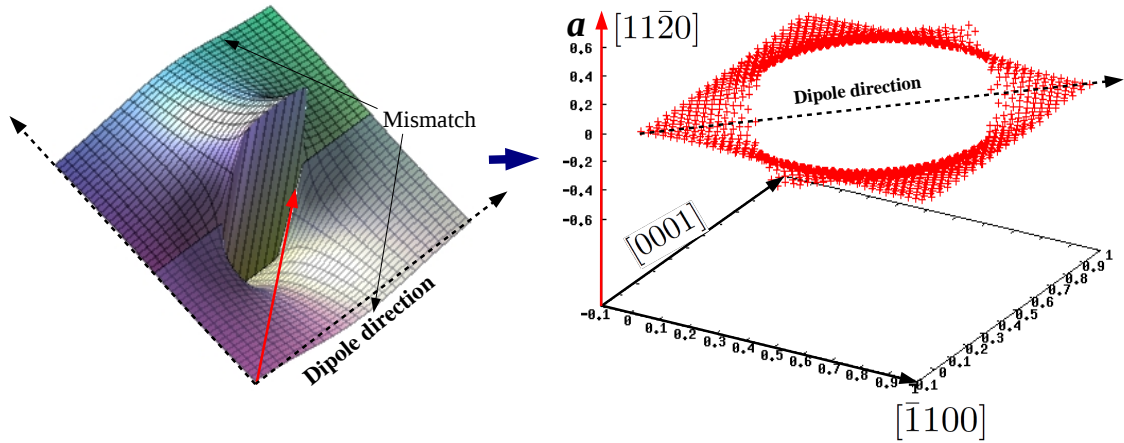


Figure 2.8: (a) screw dislocation core dipole model. Continuous model and atomic model.

### 2.2.7 Twin boundaries and deformation tests

The  $\{10\bar{1}2\}$ ,  $\{10\bar{1}1\}$ ,  $\{11\bar{2}1\}$  and  $\{11\bar{2}2\}$  TBs can be built in the Haüy-Bravais hemitropic (half-turn) way by rotating one part of a crystal by a half turn about either the axis normal to the twin plane (Mügge's type I twin) or about an axis contained in the twin plane (Mügge's type II twin). The  $\{11\bar{2}1\}$  TB requires a pre-opposite direction displacement (shuffle) of  $\frac{1}{12}\langle\bar{1}100\rangle$  on to the alternate basal planes so as to relax to its minimum energy state [158, 80, 89]. It eventually proves to be strictly type II. that if originally built as a type II twin, the atomic relaxations for the  $\{11\bar{2}1\}$  TB are actually pretty small. Conversely, the relaxed  $\{11\bar{2}2\}$  TB is strictly type I, because of its in depth  $z$  structure. Because we use bulk 3D periodic boundary conditions with a code which utilizes the Bloch theorem (VASP), there are two boundaries per simulated box, instead of one if la Möbius periodic conditions were allowed along  $z$  [159].

After relaxation to a stable twin structure, one layer on the top and two layers on the bottom of the bi-crystal twin structure are fixed for H & O segregation calculations. Thus 3 layers in each supercell boundary are fixed to maintain the twin structure.

For the deformation tests on such structures, two directions are chosen. They are respectively the direction perpendicular to each  $K_1$  plane (figure 2.9a) and the  $c$ -axis direction of  $\alpha$ -Ti of the matrix (figure 2.9b).

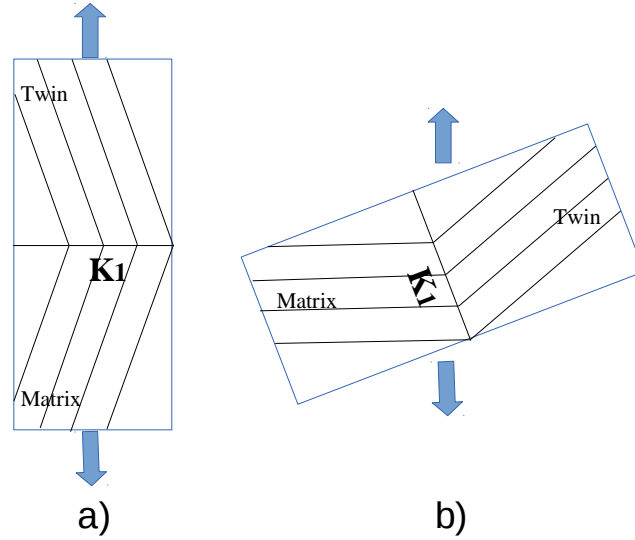


Figure 2.9: Schema of deformation tests done on twin structures. a) deformation direction is perpendicular to each  $K_1$  plane; b) deformation direction is the  $c$ -axis direction of the matrix part.

## 2.2.8 A new twinning disconnection dipole model

We propose a disconnection dipole model with a pair of opposite disconnections in the box for the sake of ab initio studies with size limited boxes. The disconnections to be studied are twinning disconnections so that our model can be called a TD dipole model. However ab initio studies in solid state systems are still mostly static studies, and not dynamical studies even if DFT molecular dynamics is possible, in principle (its just a question of CPU time). We will not be able to study the twinning in itself. According to results by Wang et alii since 2009, taking magnesium as a prototype hcp metal, a stacking fault near a partial dislocation can dissociate into multiple location dipoles, thus forming a twin nucleus [92, 160]. Barrett and El Kadiri [161, 162] and Ostapovets and Serra [98] proposed a model of twin growth with disclinations situated in basal-prismatic (BP, or PB) facets, creating superimposed interfacial disconnection (ID) dipoles whose conservative motion can mediate the motion of the facets[98]. These dynamical and large size dipole models are different from the static TD dipole model we are going to describe. In our model, see figure 2.11, the left-right boundaries are periodic because the "+TD"/"-TD" dipole suppresses the horizontal mismatch. Since the vertical mismatch induced by the TDs cannot be suppressed, a three

atomic layer thick twin boundary (TB) is fixed at the top-bottom junction. Two vertical atomic layers are also fixed in the middle of the dipole in order to prevent the likely interaction between the "+TD" and the "-TD" in a small box. The fixed boundaries are coloured in dark blue in figure 2.11. The validity of this tentative approach has not been fully checked in this preliminary study. Yet, the segregation energies on the TB obtained within the TD dipole model are in good agreement with the ones obtained with a simple TB model (actually with two TBs for vertical periodicity), see the result parts.

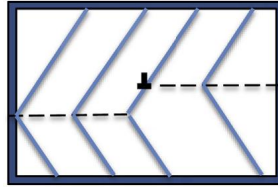


Figure 2.10: TD model by Ghazisaeidi et al. for Mg-solute interaction [106].

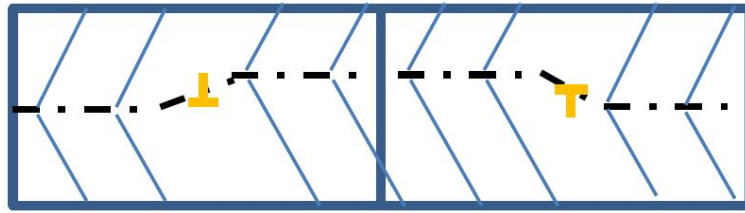


Figure 2.11: The TD dipole model.

## 2.2.9 Solute Segregation

The segregation energy is defined as the energy difference between a super-cell containing a solute at a given interstitial site  $i$  at the extended-defect and the same supercell with the solute in the bulk-like environment. With the following equation, segregation is favored at site  $i$  if  $E_{seg}(i)$  is negative.

$$E_{seg}(i) = E_{solute}^i - E_{solute}^{bulk}$$

Taking the example of a solute segregation energy calculation on stacking-fault (see figure 2.12), all deformed octahedral sites on or near the SFs are investigated. According to their distances to the SFs, they are named site 1 (closest to SF), site 2 and site3 (far from SF), site2 are closer than site3, except for the site 2 of the prism fault for which it is also a on-SF-site. Their positions with respect to SFs are shown in figure 2.12.

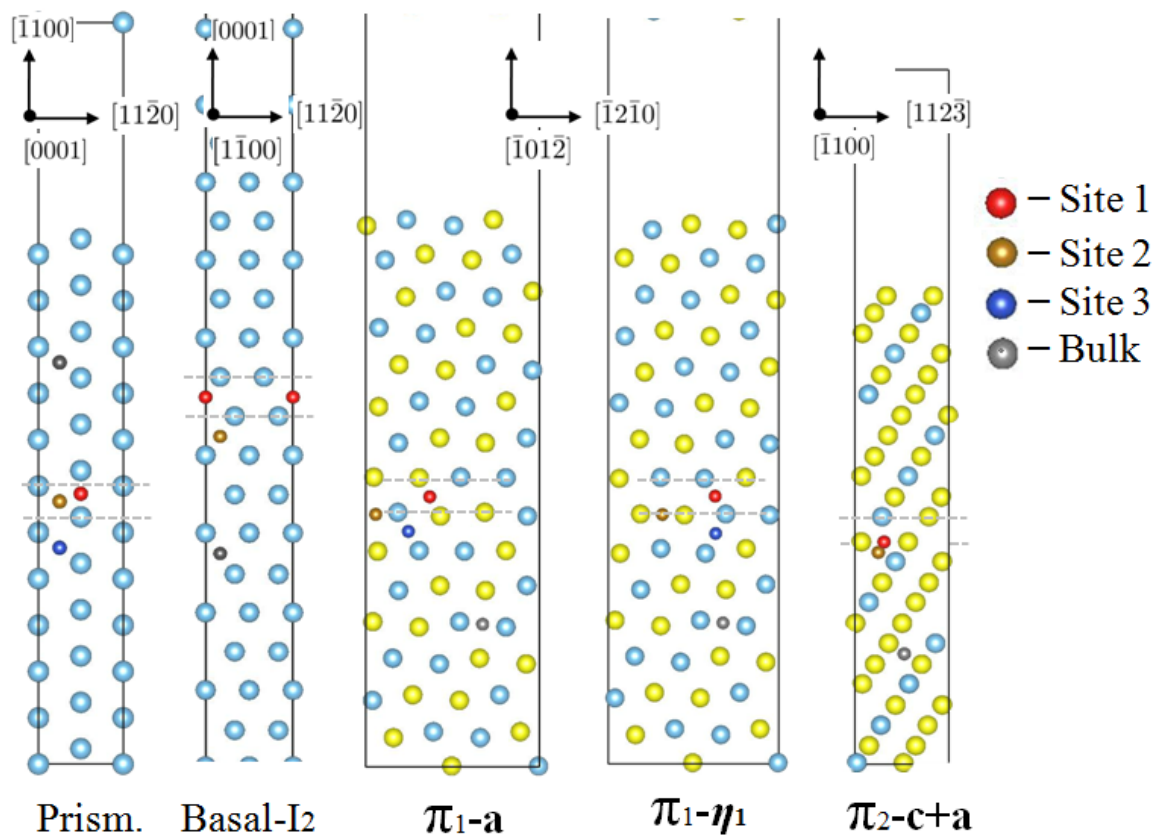


Figure 2.12: Segregation sites for H and O near SFs

# Chapter 3

## Results I: Titanium and H & O in $\alpha$ -Ti

Although the main goal of this chapter is to study the effects of H and O in  $\alpha$  titanium, I first start by studying the stability problem between the  $\alpha$  and  $\omega$  phases of Ti at 0 K and zero pressure.

I then study:

- the question of the preferred interstitial positions of H and O in  $\alpha$ .
- the interaction of H and O with  $\alpha$ -Ti and of two solutes H/O in  $\alpha$ -Ti.
- the effects of H and O on elastic constants of  $\alpha$ -Ti.
- the migration of H and O in Ti.

These studies constitute first steps before studying the effects of H and O on stacking-faults, on dislocation cores, on twin boundaries and on twinning dislocations in  $\alpha$ -Ti.



### 3.1 About $\alpha$ and $\omega$ phases of Ti at 0 K and 0 Pa

Three different PAW potentials of Ti with the GGA-PBE exchange and correlation function are used to calculate the total free energies  $F$  at 0 K: A four electron  $3d4s$  potential (2002 version) and two 12 electron  $3s3p3d4s$  potentials (2000 and 2005 versions). For the phonon calculations, I used  $E_{\text{cut}} = 500$  eV for  $4e-02$  potential and  $E_{\text{cut}}=700$  eV for the two  $12e$  potentials. Kpoints are equivalent to a  $25 \times 25 \times 15$  grid in a primitive cell of 2 atoms of the  $\alpha$  phase.

The optimised lattice parameters and the free energies of the  $\alpha$ ,  $\omega$  and  $\beta$  phases obtained by DFT calculations are given in tables 3.1- 3.4 for Ti and Zr. Since the energy differences between  $\alpha$  and  $\omega$  are very small, ZPE calculations will be carried out to get the complete  $\Delta F$  at zero K.

Table 3.1: Lattice parameters and electronic total energies of  $\alpha$ ,  $\omega$  and  $\beta$  phases of Ti, calculated at 0 K and 0 Pa, with experimental values

Potentials	$\alpha$			$\omega$			$\beta$	
	a ( $\text{\AA}$ )	c/a	$E_{el}$ (eV)	a ( $\text{\AA}$ )	c/a	$E_{el}$ (eV)	a ( $\text{\AA}$ )	$E_{el}$ (eV)
4e	2.924	1.582	-7.762	4.552	0.619	-7.776	3.236	-7.662
12e-00	2.938	1.583	-7.946	4.581	0.618	-7.952	3.254	-7.837
12e-05	2.937	1.582	-7.8357	4.579	0.618	-7.8407	3.252	-7.725
Expt.	2.946	1.587	[140]	4.614	0.608	[163]	3.263	[164]

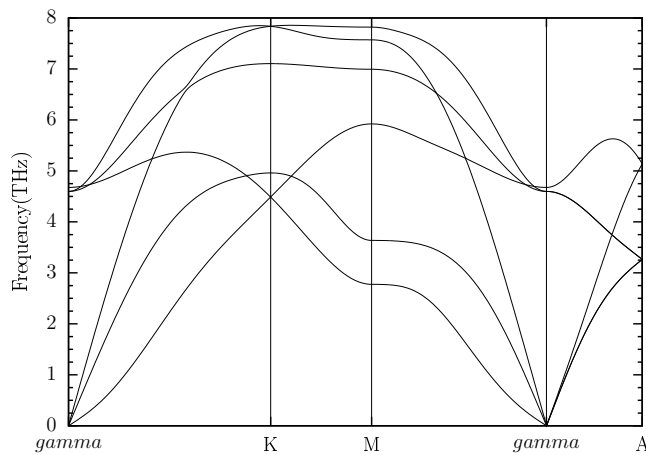


Figure 3.1: The phonon dispersion curves of  $\alpha$ -Ti. 12e-05 used for the PAW potential.

The  $\Delta E_{el}$  between the  $\alpha$  and  $\omega$  phases of Ti are presented in table 3.2. The ZPEs calculated with different box sizes and the total free energy differences at 0 K are

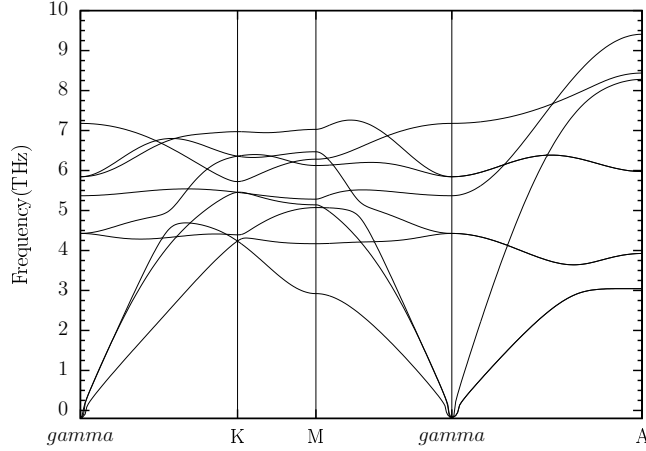


Figure 3.2: The phonon dispersion curves of  $\omega$ -Ti.  $12e-05$  used for the PAW potential.

also given in that table. Phonon dispersion curves of the  $\alpha$  phase calculated with a  $12e$  potential are shown in figure 3.1. Only experimental data measured by Stassis et al. at 295 K are available [165]. Phonon dispersion curves of the  $\omega$  phase are shown in figure 3.2.

Table 3.2: Energy differences (in meV) between the  $\alpha$  and the  $\omega$  phases of Ti, not including and including  $\Delta ZPE$ s

Potentials	$\alpha$		$\omega$		$\Delta E_{el}$	$\Delta F$
	Size	ZPE	Size	ZPE		
4e	2x2x2	33				
	3x3x2	33	2x2x3	34	-14	-13
	4x4x3	32	3x3x4	34	-14	-12
12e-00	2x2x2	36				
	3x3x2	34	2x2x3	33	-6	-7
	4x4x2	34	3x3x4	36	-6	-4
12e-05	3x3x2	35	2x2x3	36	-5	-4
	4x4x3	35	3x3x4	34	5	-6

From table 3.2, we can see that the ZPE difference between  $\alpha$  and  $\omega$  is very small, 1 or 2 meV, and not sufficient to reverse the  $\omega$  phase stability at 0 K obtained with pure electronic total energies for Ti. The energy difference remains very small in all cases. In the literature review, see section 1.1.1, we wrote that both  $\alpha$  and  $\omega$  phases may well be metastable at 0 K and 0 Pa.

A similar study can be done for Zr which is also a group IV B transition metal. The values are shown in tables 3.3-3.4. The ZPE differences can change the  $\alpha/\omega$  phase stability of Zr deduced from  $\Delta E_{el}$  differences although these calculations

seem to be at the current DFT limits for Zr, probably because Zr has altogether more electrons than Ti (40 vs. 22).

Table 3.3: Lattice parameters and electronic total energies of  $\alpha$ ,  $\omega$  and  $\beta$  phases of Zr

Potentials	$\alpha$			$\omega$			$\beta$	
	a (Å)	c/a	$E_{el}$ (eV)	a (Å)	c/a	$E_{el}$ (eV)	a (Å)	$E_{el}$ (eV)
4e	3.235	1.599	-8.478	5.037	0.626	-8.486	3.574	-8.340
12e-00	3.232	1.597	-8.5469	5.055	0.624	-8.5473	3.579	-8.468
12e-05	3.234	1.598	-8.5197	5.042	0.625	-8.5194	3.574	-8.435
Expt.	3.228	1.592[167]		5.037	0.622[168]		3.573[166]	

Table 3.4: Energy differences (in meV) between the  $\alpha$  and  $\omega$  phases of Zr not including and including ZPEs

Potentials	$\alpha$		$\omega$		$\Delta E_{el}$	$\Delta F$
	Size	ZPE	Size	ZPE		
4e-02	3x3x2	23	2x2x3	23	-8	-8
12e-05	3x3x2	24	2x2x3	21.6	-4	-2.8
	4x4x3	23	3x3x4	24.1	-4	+0.7
12e-05	3x3x2	24.5	2x2x3	21.6	+0.3	-2.6

## 3.2 H and O interstitial positions in $\alpha$ -Ti

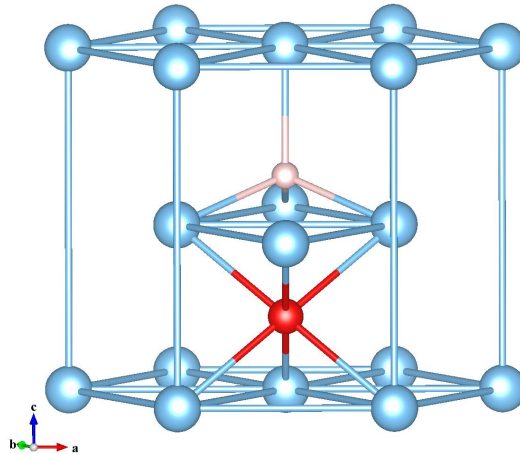


Figure 3.3: The octahedral interstitial atom is shown in red, the tetrahedral interstitial atom is shown in pink.  $\mathbf{a} = [2\bar{1}10]$ ,  $\mathbf{b} = [\bar{1}2\bar{1}0]$  and  $\mathbf{c} = [0001]$

Octahedral and tetrahedral sites are shown in figure 3.3. For an octahedral site, with 4e potential, the distance of a H and O with their six first neighbour Ti atoms is 2.04 Å before structural relaxation. It turns to 2.08 Å after relaxation, both for H and O. For a tetrahedral site, the distances with its four first neighbour Ti atoms are 1.73 Å for three of them in the bottom and 1.78 Å of fourth one which is on the top. They turn to respectively 1.87 Å and 2.00 Å after relaxation for H and 1.96 Å and 2.19 Å for O. The tetrahedral site has thus a larger change compared to the octahedral site in presence of a H and O. When O is put in a tetrahedral site, it moves to the basal plane.

I now calculate the formation energies of Octa and Tetra sites with H or O. The results are shown in table 3.5. Potentials with 4e and 12e are used. We give the results for several box sizes and different relaxation condition to explicitly provide an idea, in this PhD work, of the convergence and reliability of the results.

*Table 3.5: Formation energy differences between Octa and Tetra sites for H and O in Ti. ISIF=3 means that the form and volume of supercell are relaxed, and they are fixed when ISIF=2. The octahedral site is favoured if  $E_{Octa} - E_{Tetra}$  is negative:*

$$E_{Octa} < E_{Tetra}$$

	Box size	$E_f$ -Octa (eV)	$E_f$ -Tetra (eV)	$\Delta E_f(Octa - Tetra)$
H-4e	2x2x1 ISIF 3	-2.696	-2.498	-0.198
	2x2x2 ISIF 3	-2.718	-2.535	-0.183
	3x3x2 ISIF 3	-2.706	-2.624	-0.081
	4x4x3 ISIF 3	-2.685	-2.560	-0.124
	2x2x1 ISIF 2	-2.689	-2.500	-0.191
	2x2x2 ISIF 2	-2.713	-2.535	-0.178
	3x3x2 ISIF 2	-2.705	-2.624	-0.081
	4x4x3 ISIF 2	-2.680	-2.560	-0.120
H-12e	3x3x2 ISIF 2	-2.702	-2.627	-0.075
	4x4x3 ISIF 2	-2.701	-2.627	-0.074
O-4e	3x3x2 ISIF 2	-5.688	-4.459	-1.230
	4x4x3 ISIF 2	-5.675	-4.408	-1.267

Since the formation energy difference between octahedral and tetrahedral sites  $\Delta E_f$  is small for H, the ZPE is also be calculated. Seen from table 3.6, the 0 K phonon contribution to  $E_f$  difference is 31 meV with the 4e potential. It is in the same trends as of  $E_{el}$ : The octahedral site is even more stable when the vibrational energy is taken into account. ZPE calculation needs no be done

with 12e potential. O and H will thus be put in octahedral sites in subsequent simulations.

Table 3.6: Stability of interstitial sites for H in  $\alpha$ -Ti.  $\Delta F_f$  is the free energy difference with ZPE taken into account.

	Method	Box	$\Delta E(\text{Octa} - \text{Tetra})$
4e	$\Delta E_f$	3 3 2	-81
	$\Delta ZPE$	3 3 2	-31
	$\Delta F_f$	3 3 2	-112
12e	$E_{el}$	3 3 2	-75

The same procedures are applied to Zr. Two literature papers give the Tetra site as the more stable one compared to Octa site for both H and O[45, 171].

Table 3.7: Formation energy differences between Octa and Tetra site for H and O in Zr

	Box size	$E_f$ -Octa (eV)	$E_f$ -Tetra (eV)	$\Delta E_f(\text{Octa} - \text{Tetra})$	$\Delta F_f$
H-4e	3x3x2	-2.664	-2.693	0.029	-0.059
	4x4x3	-2.704	-2.728	0.023	
H-12e	3x3x2	-2.283	-2.345	0.062	-0.026
O-4e	3x3x2	-2.922	-1.931	-0.991	

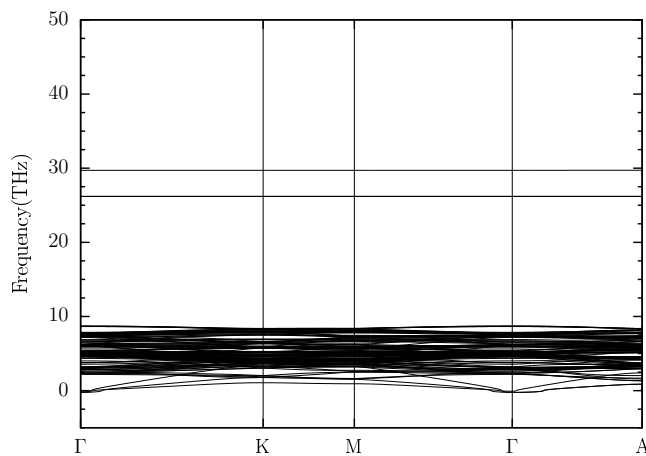


Figure 3.4: The phonon dispersion curves of the supercell  $Ti_{36}H$  with H in the octahedral interstitial site. In figure 3.4-3.7, following a usual mode of representation, the ‘negative’ frequencies correspond to imaginary frequencies coming from negative eigenvalues.

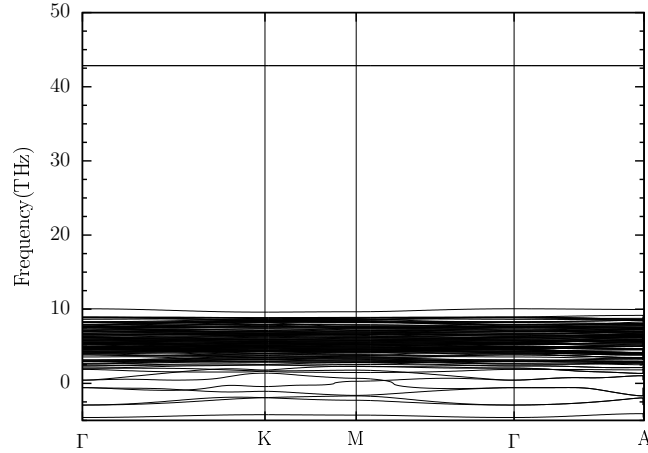


Figure 3.5: The phonon dispersion curves of the supercell  $Ti_{36}H$  with H in the tetrahedral interstitial site (see note at the end of this 3.2 section).

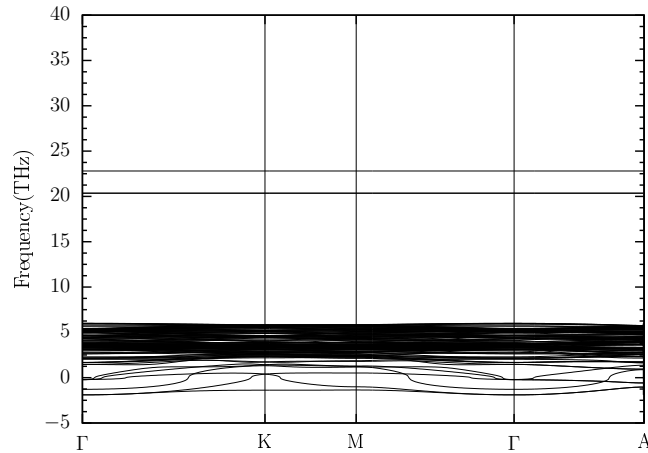


Figure 3.6: The phonon dispersion curves of the supercell  $Zr_{36}H$  with H in the octahedral interstitial site.

The results in table 3.7 confirmed that the Tetra site in Zr is slightly more stable than the Octa site in terms of total electronic energy  $E_{el}$ . However, the ZPEs are relatively important and finally change the Tetra site stability.

Phonon band structures of the  $Ti_{36}H$  and  $Zr_{36}H$  systems with a H in an octahedral or a tetrahedral site are presented in figure 3.4-3.7. They are developed over the  $\Gamma - K - M - \Gamma - A$  lines in the usual Brillouin zone of the hexagonal lattice as originally defined by Herring in 1942. For the  $Ti_{36}H$  system, we clearly see that the vibration energy of a H in a tetrahedral site (figure 3.5), corresponding to the phonon band at 43 THz, is higher than in octahedral site where the phonon bands of H are located between 25 and 30 THz. This means that hydrogen is more energetic (less stable) in a tetrahedral site than in an octahedral site. Since these phonon calculations are done with 4e potential and with a large accuracy

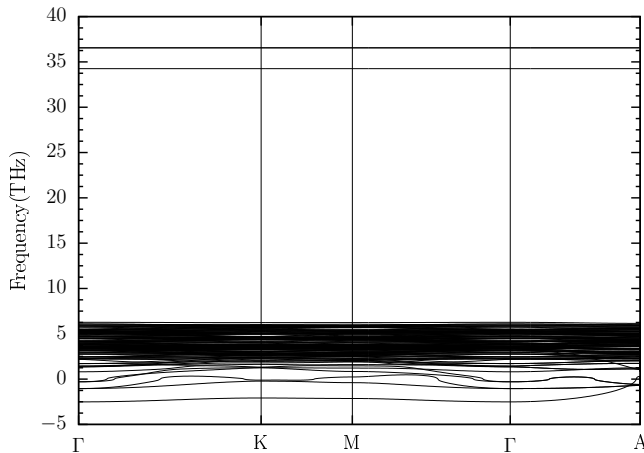


Figure 3.7: The phonon dispersion curves of the supercell  $Zr_{36}H$  with H in the tetrahedral interstitial site.

on structure optimisation and convergence (on force:  $0.1 \text{ meV/\AA}$ ), the imaginary phonons shown in tetrahedral site (figure 3.5) indicate a dynamical instability of the hydrogen in the tetrahedral site configuration for H.

Similar phenomena are found for Zr except for the appearance of negative phonons for H in the octahedral site. In this case, it is likely due to the rather low energy convergence. I used (1 meV) with the 12e potential on  $Zr_{36}H$ .

Note : I should have got two extra horizontal (dispersionless) bands with PHON for the  $Ti_{36}H$  system with H in the tetrahedral site (figure 3.5), as for the  $Zr_{36}H$  system (figure 3.7). Lu and Zhang [122] obtain only one extra dispersionless band and say it is threefold degenerate. Given the isotropy of the planar hexagonal plane opposed to the  $\mathbf{c}$ -axis direction, it seems to us that one should obtain two extra dispersionless modes, as we do in three of our four cases, one of these two modes being twofold degenerate.

### 3.3 H and O interactions with $\alpha$ -Ti

#### 3.3.1 Structures and Energies

With the supercells which can be used in this DFT work, the H concentrations are largely beyond any reasonable solubility limits (see section 1.2.2 in the introduction, Conrads paper). However, with only one H or one O per supercell with N titanium atoms, nothing else can exist than a (probably rather artificial)  $Ti_nH$

or  $Ti_nO$  compound. This is because, a  $Ti_{36}H$  supercell, for instance, is not equivalent to a  $Ti_{3600}H_{100}$  supercell within which possibilities to generate local hydride would exist. Garcés and Vajda were able to generate chain-like configurations with H-Ti-H pairs in a  $Ti_{24}H_3$  supercell (2x2x3 hcp cell) which they considered as the seed for hydride formation [172]. I only consider  $Ti_nH$  and  $Ti_nO$  cells in this work.

Table 3.8: Effects of one H and one O in various hcp titanium cells. The  $\delta X$  values are relatively  $\Delta X/X$  variations, given in %, see text. Atomic position optimisations are converged to 0.1 meV, with the 4e PAW potential with Encut=300 eV.

	Box size	$E_f$ (eV)	$\delta d_{nn}$	$\delta V$	$\delta Lx$	$\delta Lz/Lx$
H	1x1x1	-2.702	2.89	+4.10	+0.80	+2.46
	2x2x1	-2.696	3.09	+1.18	+0.32	+0.53
	2x2x2	-2.718	2.75	+0.57	+0.10	+0.37
	3x3x2	-2.706	2.30	+0.19	+0.06	+0.06
	4x4x3	-2.684	2.21	+0.15	-0.03	+0.22
O	1x1x1	-5.458	2.55	-1.91	-1.35	+0.79
	2x2x1	-5.724	2.06	-0.98	-0.74	+0.50
	2x2x2	-	2.11	-0.57	-0.30	+0.04
	3x3x2	-5.692	2.11	-0.28	-0.20	+0.12
	4x4x3	-5.682	2.16	-0.09	-0.16	+0.23

I now consider several  $nx \times ny \times nz$  Ti hcp cells with one H or one O in an octahedral site, corresponding to  $Ti_nH$  or  $Ti_nO$  cells with  $N = 2 nx \times ny \times nz$ . As usual, the x and y directions are in the hexagonal plane and z corresponds to the c-axis. These cells are DFT optimized with respect to atomic positions and cell size/shape. I thus get the formation energies  $E_f$ , calculated with  $E_{H_2} = 2.233$  eV and  $E_{O_2} = -9.855$  eV. The global volume variations  $\Delta V/V$  which can be decomposed in  $\Delta Lx/Lx$  in the hexagonal plane and  $\Delta Lz/Lz$  along the c-axis. I can also measure locally the  $d_{nn}$  nearest Ti neighbour distances to the solute and get the relative  $\Delta d_{nn}/d_{nn}$  variations. All these information are given in table 3.8 where I give the relative  $\Delta(Lz/Lx)/(Lz/Lx)$  variations in the last column because  $Lz/Lx$  is reminiscent of the c/a ratio. In that table, in order to save space, the  $\Delta X$  symbols correspond to  $\Delta X/X$  relative variations, given in %. The negative formation energies indicate that the formation of these systems is always favoured. It is twice as much favoured for oxygen than for hydrogen, indicating stronger Ti-O bonds than Ti-H bonds. A hydrogen induces a global expansion



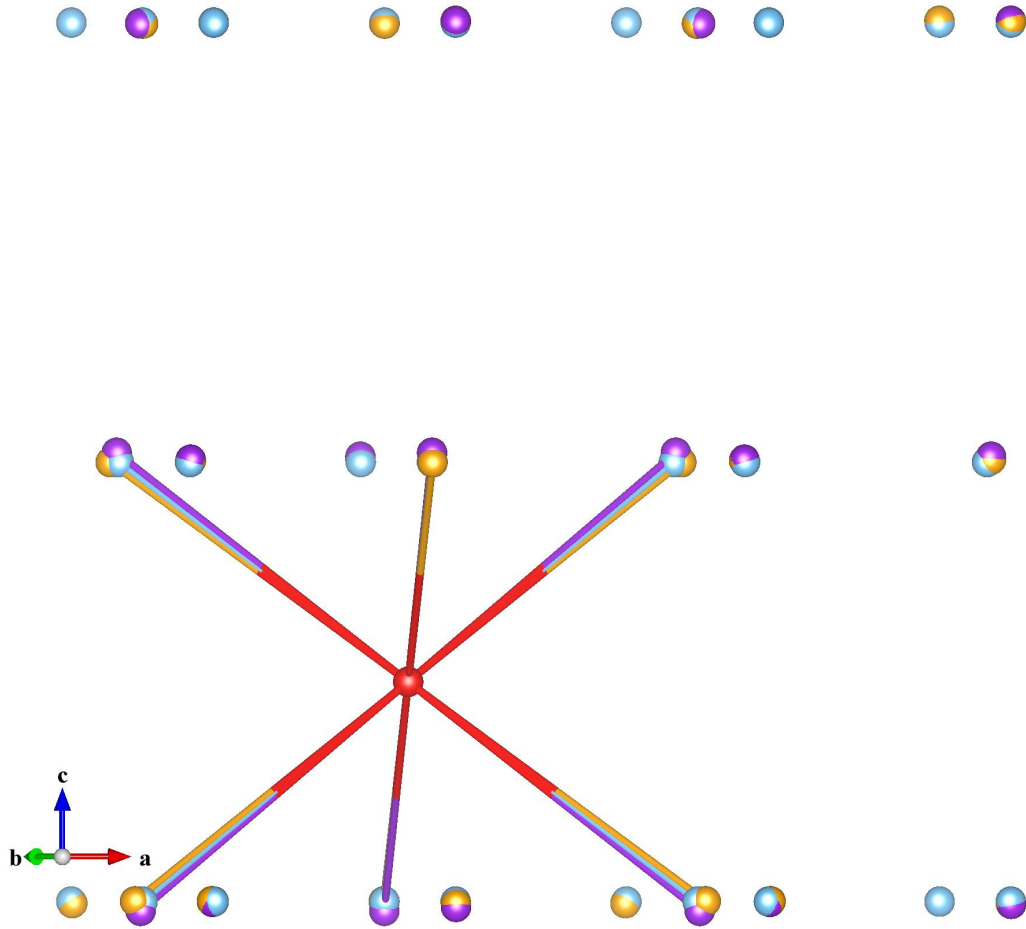


Figure 3.8: Local titanium position changes induced by (yellow titanium) or by O (purple titanium) in octahedral site, compared with original positions (blue). The solute, H or O, is in red. Configuration with a  $4 \times 4 \times 3$  supercell.

of its environment, the cell volumes, both  $L_x$  and  $L_z/L_x$  while oxygen globally reduces the cell volumes, to a less extent and with a global decrease in  $L_x$  but a global increase in  $L_z/L_x$ . This shows that a simple reasoning from assumed atomic sizes of hydrogen and oxygen, with hydrogen being assumed to be smaller than hydrogen, would be much too naive. It would lead to opposite conclusions. Naive atomic size reasoning neglects possible chemical effects. Besides, the quantum mechanical considerations by Clementi et al. ascribe an “atomic radius” of 0.48 Å, clearly counter intuitively smaller than for hydrogen (0.53 Å) [173]. It is noteworthy that the global  $\Delta V$  are negative when an O is inserted, the local  $\Delta d_{nn}$  are always positive. The local atomic displacements are visualised in figure 3.8 relative to a  $4 \times 4 \times 3$  box (one solute interstitial atom within 96 titanium atoms). The solute atom, whether H or O, is in red, at the octahedral site. The yellow,

purple, balls represent the positions of the titanium atoms after relaxation in presence of a H (yellow titanium), an O (purple titanium), respectively. The original titanium positions are in blue. Although the radial  $\Delta d_{nn}$  is the same for all six Ti nearest neighbour of the solute, the directional displacements are not isotropic especially in the case of O which induces a more pronounced pushing of its Ti neighbours in the c-direction than in the basal directions. H has an almost isotropic effect.

### 3.3.2 Electronic Structures

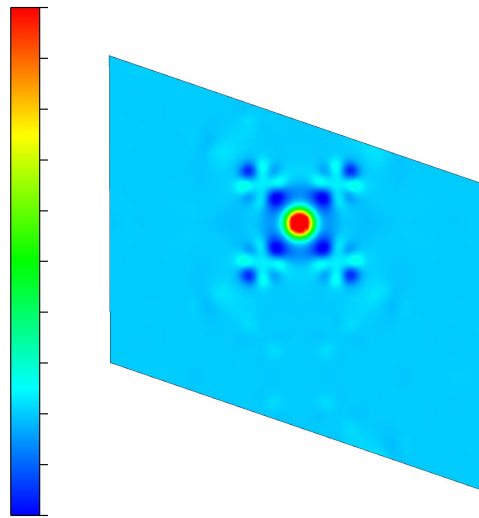


Figure 3.9: Charge transfer between Ti and H atom in the plane containing four nearest Ti atoms and one H. The scale is from -0.005 (deep blue) to 0.02 (red)  $e/\text{Bohr}^3$

When one H is put in a Ti box of  $4 \times 4 \times 3$ , charge transfer between Ti and H atom in the plane containing four nearest Ti atoms and one H are showed in figure 3.9. The scale is from -0.005 to 0.02  $e/\text{Bohr}^3$ , idem for O in figure 3.10 (Bohr is the Bohr radius  $a_B=0.5292 \text{ \AA}$ ). More charges are transferred for Ti to H as shown in figure 3.9 compared with O in figure 3.10. The Ti-H bond has thus a more ionic character than the Ti-O bond. Dark blue areas are formed only in the Ti-H bond direction compared with the more homogeneous distribution in the Ti-O system. This corresponds to a more polarised bond between Ti and H than between Ti and O. The radius of the light green circle surrounding oxygen core is larger than in the case of H, this means a larger influence of oxygen atom on the electronic structures on Ti atoms in the supercell than hydrogen.

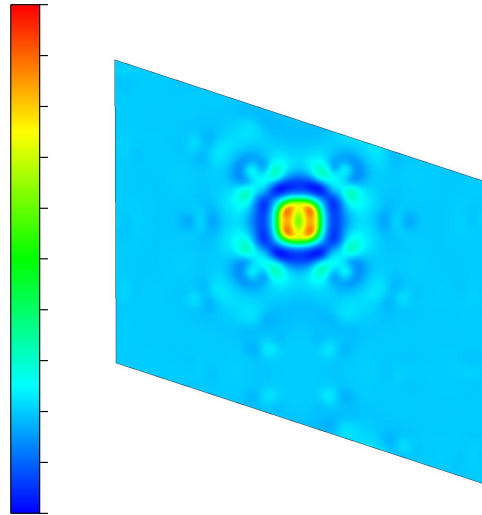


Figure 3.10: Charge transfer between Ti and O atom in the plane containing four nearest Ti atoms and one O. The scale is from  $-0.005$  to  $0.02$   $e/\text{Bohr}^3$

When one H or one O is put in a Ti box of  $4 \times 4 \times 3$ , the partial DOS of a nearest neighbour (nn) Ti of H/O is calculated and presented in figure 3.11. The Ti near H has a DOS comparable to the case of pure Ti. Even the a 2nd nn Ti of O is more affected by Ti compared to that of 1st nn Ti of H. A small peak around  $-7$  eV appears in the case of 1st nn Ti of O, which means a hybridization of orbitals between the  $3d$  of Ti and the orbitals of O. This could correspond to the decrease of the  $3d$  orbital DOS profile.

### 3.3.3 solute-solute interactions in $\alpha$ -Ti

The O-O, H-H and O-H interactions have been calculated in a  $4a \times 4a \times 3c$  supercell of 96 atoms of  $\alpha$ -Ti. Possible configurations for solute-solute interaction in two different interstitial sites are shown in figure 3.12.

The O and/or H atoms are put in two different interstitial sites A and B. The interaction energies thus obtained by the following equation are shown in table 3.9.

$$E_{Interaction} = E_{Box+A+B} + E_{Box} - [E_{Box+A} + E_{Box+B}]$$

The interaction energies depend on the vectorial distance between the occupied interstitial sites A and B, thus implying a scalar distance and an orientation as

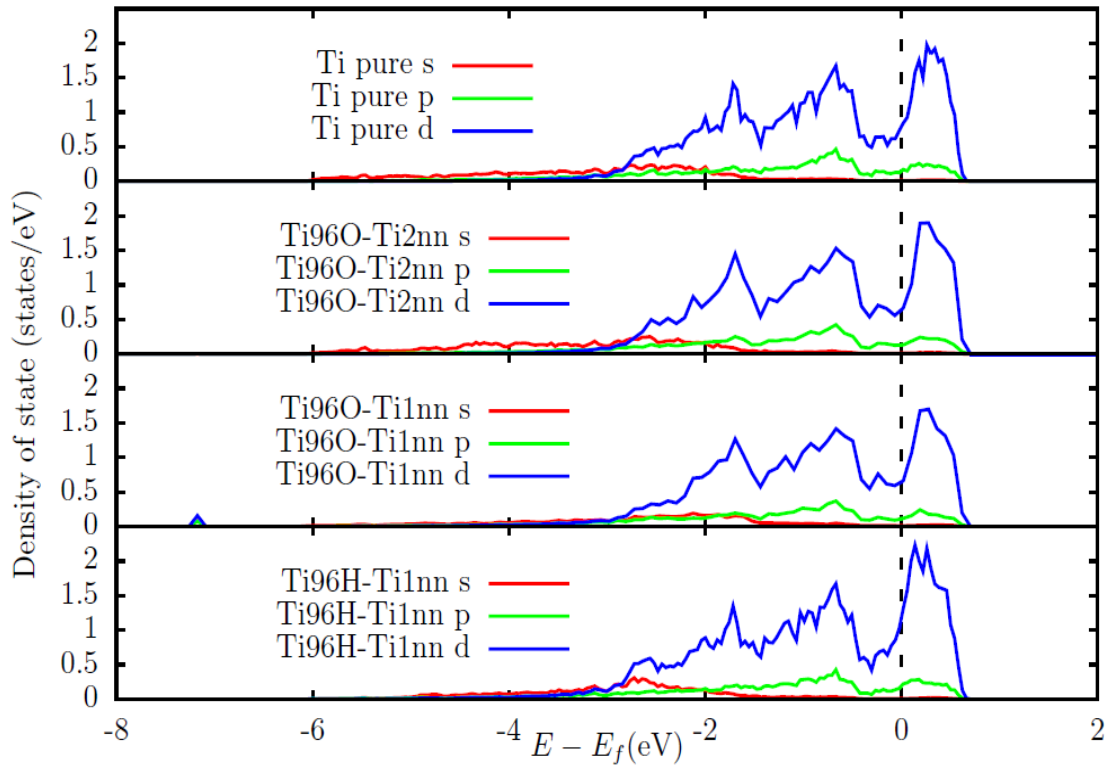


Figure 3.11: DOS of Ti in presence of H or O

indicated in table 3.9. The O-O interaction is repulsive when the O atoms are very close. It is attractive for distance cases from 4.62 to 5.85 Å. It becomes very small afterwards. The O-H and H-H interactions are smaller than O-O interactions. The O-H interaction is always attractive while the H-H one is mainly attractive under 6.86 Å and repulsive beyond. We can safely conclude that the interaction between two interstitial O or H atoms in  $\alpha$ -Ti becomes very small when the distance is more than  $\sim 3a$  (or  $2c$ ). These results are presented in the table 3.9.

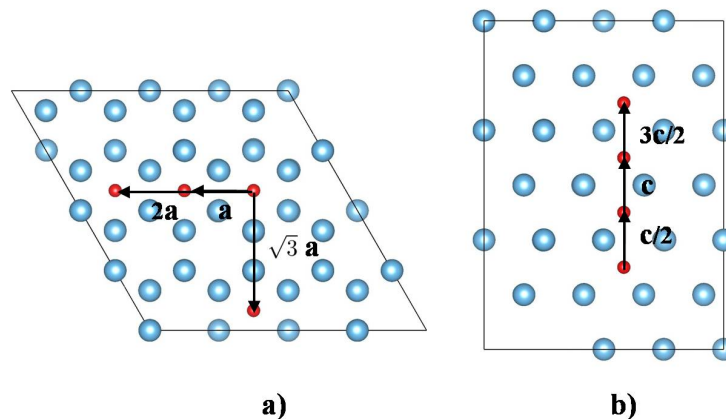


Figure 3.12: Possible configurations for solute-solute interaction in two different interstitial sites a)  $c$ -axis projection; b)  $a$  direction projection.

Table 3.9: O-O, H-H and O-H interaction energies (in meV). Distances are in ( $\text{\AA}$ ).  
Box size is  $4 \times 4 \times 3$ .

<b>c</b> -axis Dis.	Basal plane Dis.	Total Dis.	Orientation	O-O	H-H	O-H
0	<b>a</b>	2.92	$[\bar{1}210]$	64	7	-28
	$\sqrt{3}\mathbf{a}$	5.06	$[1\bar{1}00]$	-72	-5	-21
	<b>2a</b>	5.85	$[\bar{1}210]$	-55	-21	-31
$\frac{1}{2}\mathbf{c}$	0	2.31	$[0001]$	545	-20	-23
	<b>a</b>	3.73	$[2\bar{4}23]$	6	-5	-22
	$\sqrt{3}\mathbf{a}$	5.57	$[2\bar{2}01]$	-9	-3	-10
	<b>2a</b>	6.29	$[4\bar{8}43]$	2	-6	-11
<b>c</b>	0	4.62	$[0001]$	-59	23	-17
	<b>a</b>	5.47	$[\bar{1}213]$	-55	-5	-24
	$\sqrt{3}\mathbf{a}$	6.86	$[1\bar{1}01]$	0	1	-5
	<b>2a</b>	7.45	$[2\bar{4}23]$	-20	3	-12
$\frac{3}{2}\mathbf{c}$	0	6.93	$[0001]$	-26	20	-8
	<b>a</b>	7.53	$[2\bar{4}29]$	-5	-1	-12
	$\sqrt{3}\mathbf{a}$	8.59	$[2\bar{2}03]$	-1	0	-9
	<b>2a</b>	9.07	$[4\bar{8}49]$	3	6	-2

### 3.4 Effects of H and O on the stiffness elastic constants

Five independent deformation modes are used to get the 5 independent  $C_{ij}$  of the hexagonal symmetry [32, 154]. A series of deformations [-2%, -1%, -0.5%, 0.5%, 1%, 2%] are applied for each deformation mode in order to obtain the corresponding elastic constants, see figures 3.14 and 3.15 for the Ti-H system and Ti-O system, respectively.

The results for pure Ti, Ti-H and Ti-O systems are presented in tables 3.10-3.12.

The values given in the first line of table 3.10, the '4e VASP' line, have been obtained with the nice VASP elastic constant facility. According to inspection of the corresponding VASP OUTCAR output files, this VASP option apparently uses deformations as large as 10%. This sounds rather large for elastic constants and the values subsequently indicated have been obtained via series of deformations for each deformation mode, as said at the beginning of this section. I obtained the  $C_{44}$  constants from series of double shear deformations (XX-XZ and YY-YZ). This should give a better numerical estimation than with a series of single shear

Table 3.10: Elastic Constants (GPa) of pure Ti: comparison

PAW potential	$C_{11}$	$C_{12}$	$C_{13}$	$C_{33}$	$C_{44}$	$C_{66}$	B	G	E
4e VASP	169	84	81	187	41	43	113	44	116
4e	186	88	84	191	47	49	119	49	130
12e <sub>00</sub>	183	81	76	188	49	51	113	51	134
12e <sub>05</sub>	185	81	76	189	49 (45)	52	114	52	135
12e [154]	182	83	76	192	45	50	114	49	130
Expt.4K [141]	176	87	68	191	51	45	110	51	132
$ \frac{4e-Expt.}{Expt.} $ (%)	5.7	1.2	23.5	0.0	4.4	10.1	8.2	3.9	1.5
$ \frac{12e_{05}-Expt.}{Expt.} $ (%)	5.1	6.9	11.8	1.0	8.9	16.9	3.6	2.0	2.3

deformations. In the '12e-05' line in table 3.10, corresponding to the 12 electrons PAW (PBE\_GGA) potential provided by VASP, I give in parentheses the  $C_{44}$  value obtained with single shear deformations. Kwasniak also used single shear deformations [154]. Double shear deformation  $C_{44}$  values are closer to the experimental value obtained by Fisher and Renken [141] in 1964 at 4 K, using an ultrasonic wave interference technique (measurement of acoustic wave velocities in three independent crystallographic directions of the hexagonal lattice).

The results for the Ti-H systems, viz.  $Ti_nH$  cells with  $N = 2 \times nx \times ny \times nz$  are given in table 3.11 with elastic constants deduced from curves such as those given in figure 3.14. For the 1x1x1 and 1x1x2 boxes ( $Ti_2H$  and  $Ti_4H$  respectively), one gets negative  $C_{66}$  ( $= (C_{11} - C_{12}) / 2$ ) values. Since  $C_{66}$  correspond to a fundamental shearing mode of hexagonal lattice, that means that these two systems are elastically unstable. The 2x2x1 box, corresponding to  $Ti_8H$ , seems to have a positive  $C_{66}$ . Yet, from the corresponding  $\Delta E$  curve for the  $(C_{11} - C_{12})$  shearing mode, this small positive value probably corresponds to inaccurate fitting. Only larger systems,  $Ti_{16}H$ ,  $Ti_{36}H$  and  $Ti_{96}H$ , can be considered as elastically stable (I also checked that all eigenvalues of the corresponding Voigt matrices are indeed positive). For these systems, the bulk compressibility B is not much changed with respect to the pristine  $\alpha$ -Ti B value (120 and 118 GPa vs. 119 GPa). By contrast, the averaged Coulomb shear value G (rigidity modulus) is significantly decreased (38 and 45 GPa vs. 49 GPa). This is an opposite conclusion with respect to Liang and Gongs calculations in 2010 [114] but in agreement with experimental measurements for B and G extrapolated at 0 K for  $TiH_{0.04}$  [175], which corresponds to  $Ti_{25}H$ , in between our  $Ti_{16}H$  and  $Ti_{36}H$  boxes

All Ti-O systems I studied are elastically stable, see table 3.12. Oxygen clearly

Table 3.11: Elastic Constants (GPa) of Ti-H system

	$C_{11}$	$C_{12}$	$C_{13}$	$C_{33}$	$C_{44}$	$C_{66}$	B	G	E
1x1x1- $Ti_2H$	-355	267	85	232	-109	-311	44	-167	1845
1x1x2- $Ti_4H$	93	200	43	370	32	-54	125	20	57
2x2x1- $Ti_8H$	168	140	63	287	44	12	127	45	120
2x2x2- $Ti_{16}H$	164	110	83	194	41	27	120	38	103
3x3x2- $Ti_{36}H$	164	89	92	185	37	37	118	38	112
4x4x3- $Ti_{96}H$	180	95	84	198	43	43	120	45	121
Pure Ti	186	88	84	191	47	49	119	49	130
Pure Ti [114]	177	81	180				112		
2x2x2 [114]							115	51	
$TiH_{0.04}^{Exp}$ [175]							119		

has a stiffening effect, in relative agreement with Kwasniak's 12 electrons calculations [154] and experimental knowledge according to which oxygen clearly has a strengthening effect on titanium.

Knowing that Pugh used the polycrystalline B/G ratio in 1954 to define an empirical criterion according to which a polycrystalline material with a larger than 1.75 is ductile [176], and brittle otherwise, it is tempting to draw the polycrystalline B/G ratio for our (limited) Ti-H and Ti-O systems, see figure 3.13. Our systems are always ductile, but they are artificial systems which cannot locally form hydride or oxides. One can notice the non-monotonic influence of O and H for our 'low' concentration boxes, especially so for the Ti-H systems. The slight increase of the polycrystalline B/G ratio deduced from the  $Ti_{96}H$  system may be put in parallel with the beneficial influence of O at approximately 1 at% on mechanical properties of  $\alpha$ -Ti as recently observed by Firstov et al. [178] and by Sun et al. [177]. It is probably more audacious to put in parallel the strong but highly non monotonic influence of the H concentrations in our artificial systems with the different, and opposite, beneficial or not, effects of H on Ti which have been experimentally observed [21].

Considering the directional Young's modulus  $E(\vec{l})$  whose formula for hexagonal crystals has been given in section 2.2.2 of chapter 2, I can draw its surfaces for pure Ti, Ti-H and Ti-O systems as shown in figure 3.16. Its anisotropy is clearly enhanced for the  $Ti_{36}O$  system, not so for the  $Ti_{36}H$  system.

Table 3.12: Elastic Constants (GPa) of Ti-O system

	$C_{11}$	$C_{12}$	$C_{13}$	$C_{33}$	$C_{44}$	$C_{66}$	B	G	E
1x1x1-Ti <sub>2</sub> O	423	129	191	408	146	147	253	137	348
1x1x2-Ti <sub>4</sub> O	227	164	111	300	84	31	170	64	171
2x2x1-Ti <sub>8</sub> O	245	170	96	244	71	64	150	70	181
2x2x2-Ti <sub>16</sub> O	201	115	86	230	57	43	134	55	144
3x3x2-Ti <sub>36</sub> O	207	106	81	228	56	51	131	57	150
4x4x3-Ti <sub>96</sub> O	186	95	83	207	47	45	122	49	129
Pure Ti	186	88	84	191	47	49	119	49	130
2x2x2 [154]	196	100	80	218	58	48	125	57	147
4x4x3 [154]	187	84	82	196	47	51	118	50	133

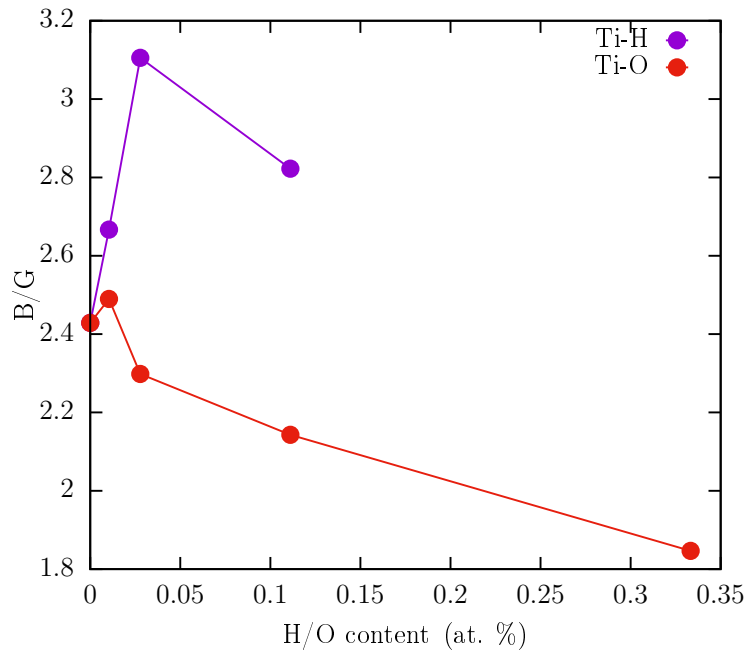


Figure 3.13:  $B/G$  ratio of Ti-H and Ti-O system. The polycrystalline Ti is intrinsically brittle for a  $B/G$  value less than 1.75 according to Pugh's plasticity criterion.



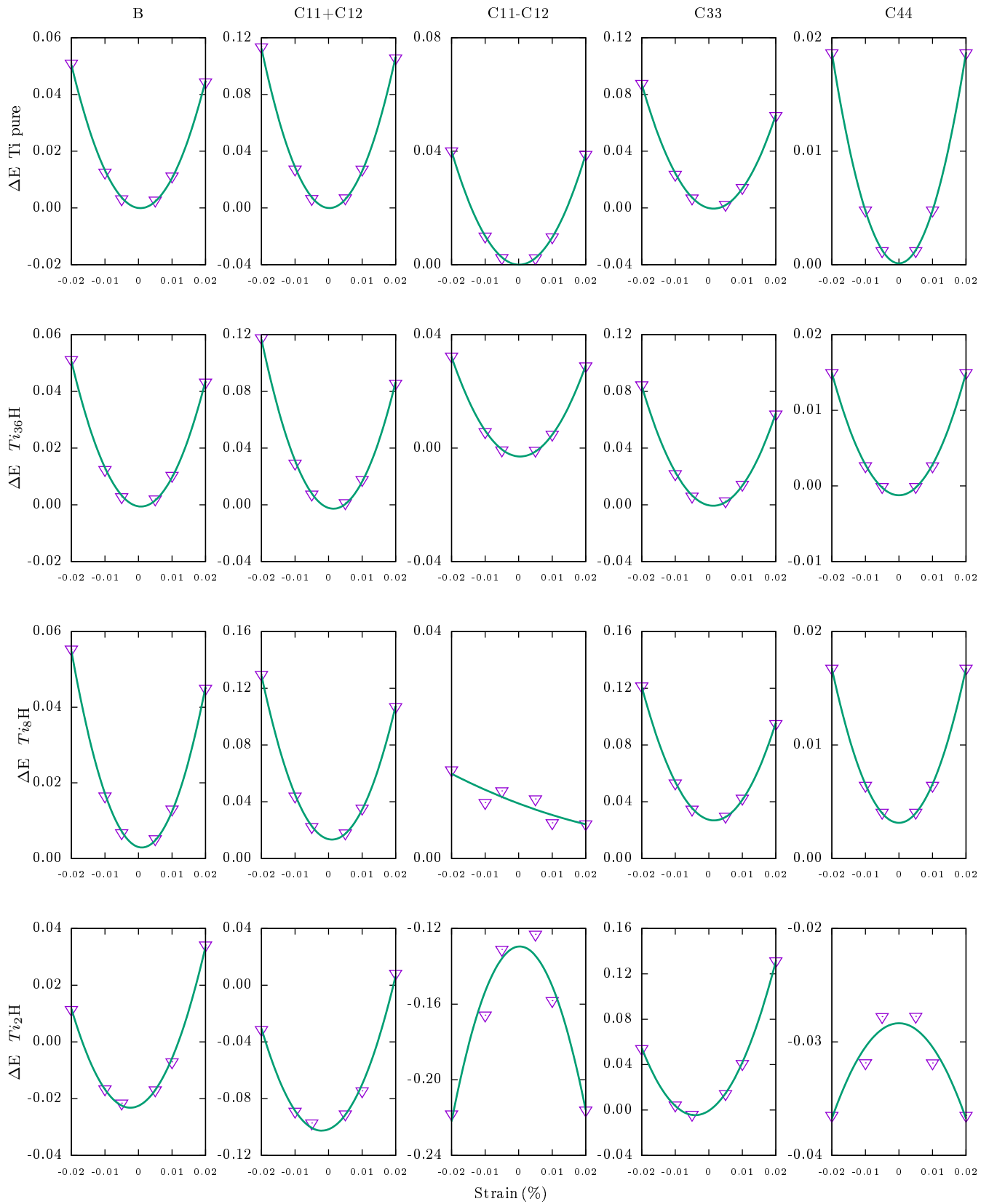


Figure 3.14: Elastic constant calculation for Ti-H system

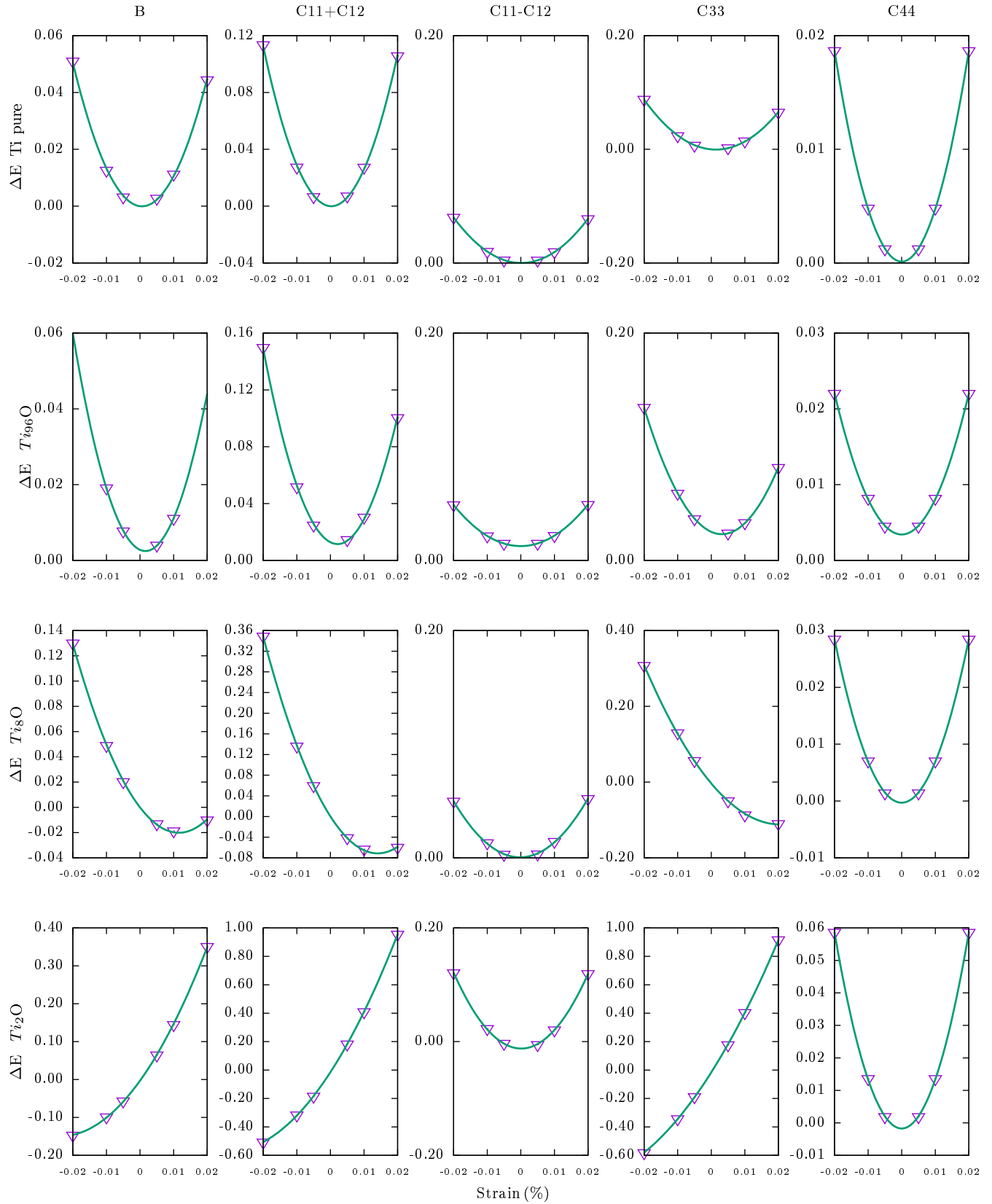


Figure 3.15: Elastic constant calculation for Ti-O system

### 3.5 Migration of H and O in $\alpha$ -Ti

Because of the controversy between the experimental conclusions and the DFT calculations for the hydrogen interstitial site stability and as a preliminary step for solute segregation study, the climbing image nudged elastic band (NEB) method [179] is used with three linearly interpolated intermediate to calculate a minimum energy pathway (MEP) during the Octa to Tetra site migration process. The results obtained with a H in a 4x4x3 supercell are shown in figure 3.17

One can see that the conjugate gradient algorithm (IBRION=2) fails to predict a good energy pathway, compared to the quasi newton algorithm (IBRION=1). However both methods give a similar energy barrier which is 514 meV for IBRION=1 and 479 meV for IBRION=2. The calculation of Lu and Zhang. [122] gives 504 meV for this energy barrier, in excellent agreement with this work.

For the O migration in  $\alpha$ -Ti, our results for a migration along the  $c$ -axis give 3.34 eV compared to the 3.25 eV found by Wu and Trinkle [110]. The basal plane migration barrier is 1.71 eV given by our calculation. This indicates an easier migration in basal plane for oxygen.

Coupling with our phonon calculations and using the transition state theory [122, 180, 181], one can calculate the jump frequencies for micro-diffusion processes and the diffusion coefficients depending on the temperature. Further works are required for this part.

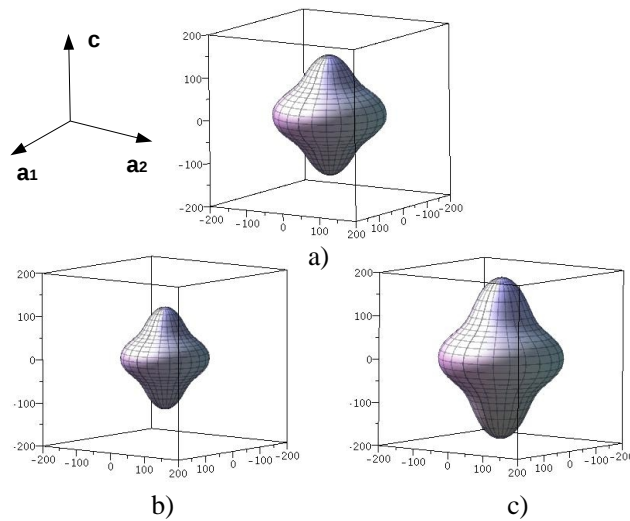


Figure 3.16: Elastic modulus surface of a) pure Ti; b)  $Ti_{36}H$ ; c)  $Ti_{36}O$ . The unit for the three box axis is GPa.

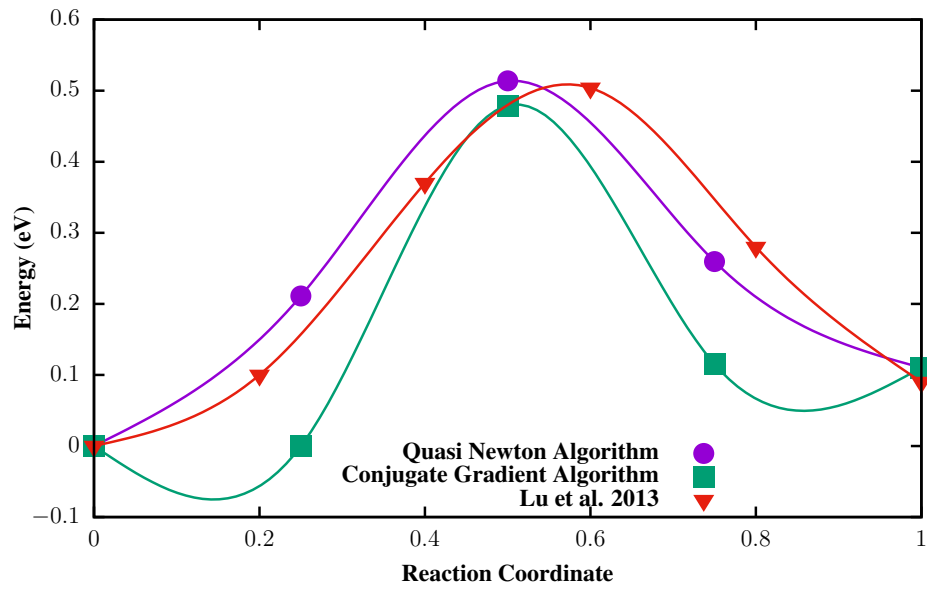


Figure 3.17: The Octa to Tetra site migration of H in  $\alpha$ -Ti

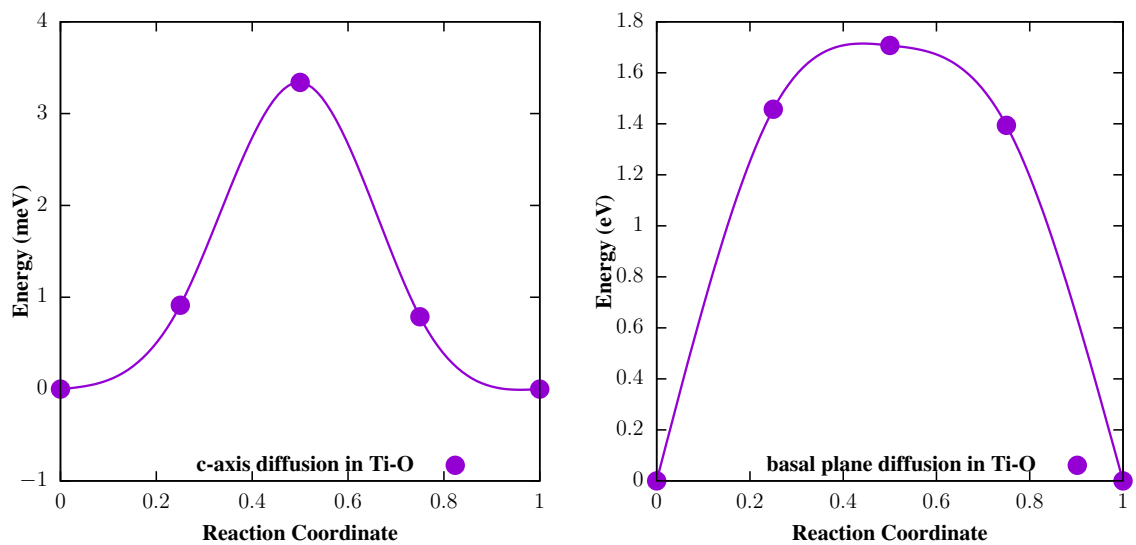


Figure 3.18: The c-axis and basal plane migration of O in  $\alpha$ -Ti



# Chapter 4

## Results II: H and O effects on stacking faults and on dislocation cores

This chapter is to study the effects of hydrogen and oxygen on the stacking faults and dislocation cores.

It is divided into six parts:

- stacking faults calculations in  $\alpha$ -Ti
- $\langle \mathbf{a}+\mathbf{c} \rangle$  screw dislocation core simulation
- H and O effects on stacking-faults
- $\langle \mathbf{a} \rangle$  screw dislocation core simulation
- H and O effects on dislocation core
- H and O effects on  $\langle \mathbf{a} \rangle$  screw dislocation glide.

## 4.1 Stacking-Faults in $\alpha$ -Ti

In this part, we first introduce our computational techniques, and, in the result part, we present the  $\gamma$ -surfaces for the four main slip planes of  $\alpha$ -Ti, viz. basal, prismatic, and pyramidal  $\pi_1$  and  $\pi_2$  planes, thus providing a systematic and unified study of the SFs in these planes via a state of the art ab initio technique. The four planes are visualized in figure 4.1 with their associated  $\langle \mathbf{a} \rangle$  and  $\langle \mathbf{c} + \mathbf{a} \rangle$  in red. Possible stable SFs are identified on the  $\gamma$ -surfaces and an all atom relaxation method is used to get the real stable SFs. The results invite to a further discussion of  $\langle \mathbf{c} + \mathbf{a} \rangle$  dislocation dissociation and cross-slip mechanism.

### 4.1.1 Vitek's method for $\gamma$ -surface calculations

In order to identify the possible stable SFs, we carry out à la Vitek  $\gamma$ -surface calculations. In this method, [56], a rigid translation is applied to the upper half block of a crystal in order to create a generalised-SF (GSF). The atoms are allowed to relax only in the direction perpendicular to the fault plane. We use a slab model with two surfaces in a supercell whose form is fixed. The excess energies for each GSF are then obtained by the usual following equation where  $A$  is the interfacial area:

$$\gamma = \frac{E_{slab-GSF} - E_{slab}}{A} \quad (4.1)$$

The energies are ab initio calculated via density functional theory using the VASP software with the PAW method, the GGA-PBE functional, and a Methfessel-Paxton smearing [134, 135, 132, 139, 137, 149]. Our slabs are made of 20 atomic layers for basal plane, 24 layers for prism plane, 24 layers for  $\pi_1$  plane and 12 layers for  $\pi_2$  plane. We obtain four  $\gamma$ -surfaces which are presented in figure 4.2-4.5. From local energy minima which can be identified in these  $\gamma$ -surfaces, we get five possible meta-stable SFs which are presented in table 4.1. Their stabilities now need to be checked with relaxation of atoms in  $x - y - z$  direction.

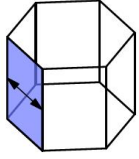
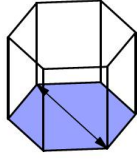
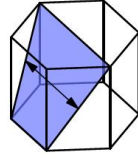
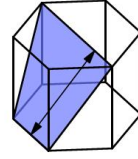
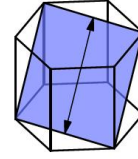
Slip Modes				
$\{10\bar{1}0\}\langle 11\bar{2}0\rangle$ P(a)	$\{0001\}\langle 11\bar{2}0\rangle$ B(a)	$\{10\bar{1}1\}\langle 11\bar{2}0\rangle$ $\Pi_1\langle a\rangle$	$\{10\bar{1}1\}\langle 11\bar{2}3\rangle$ $\Pi_1\langle c+a\rangle$	$\{11\bar{2}2\}\langle 11\bar{2}3\rangle$ $\Pi_2\langle c+a\rangle$
				

Figure 4.1: Slip systems, the arrow on the plane indicates a slip direction [39]. Cf. section 1.1.2.1.

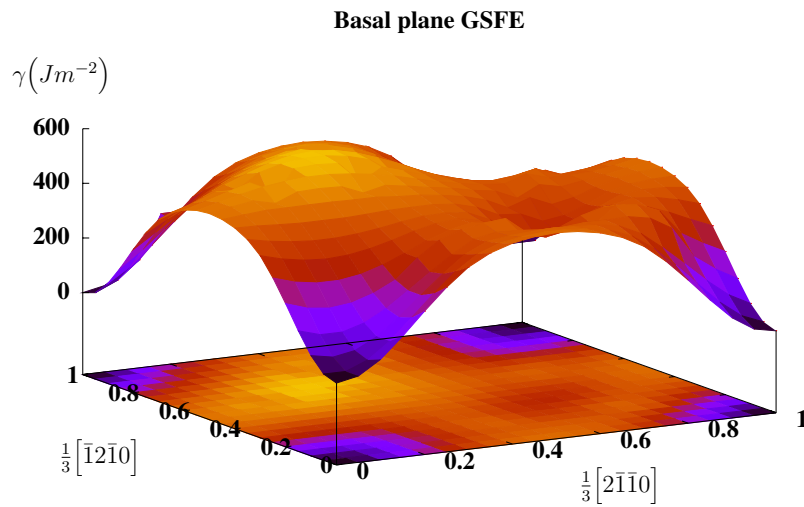


Figure 4.2:  $\gamma$ -surfaces of basal plane

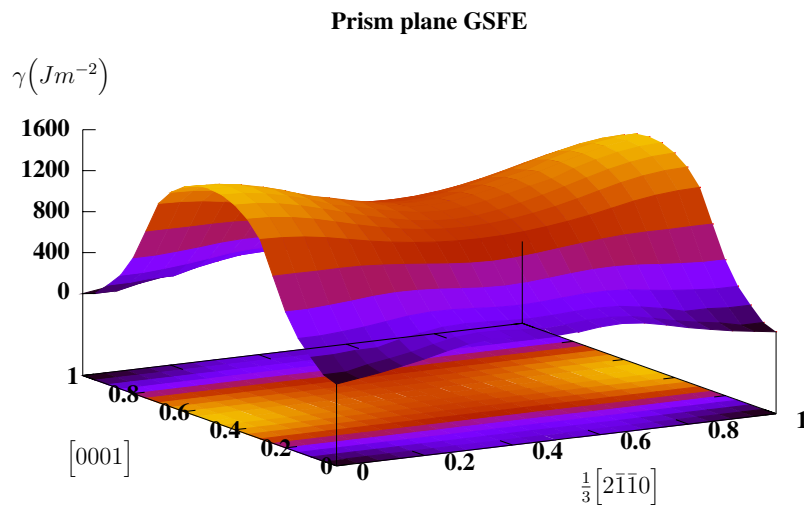
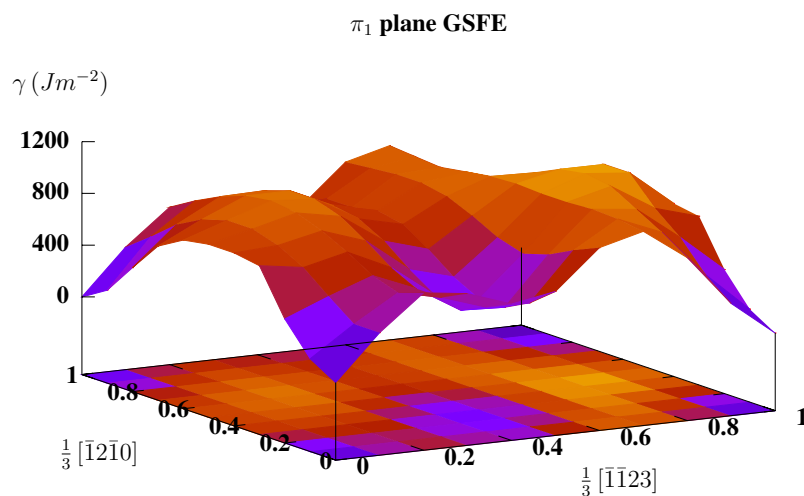
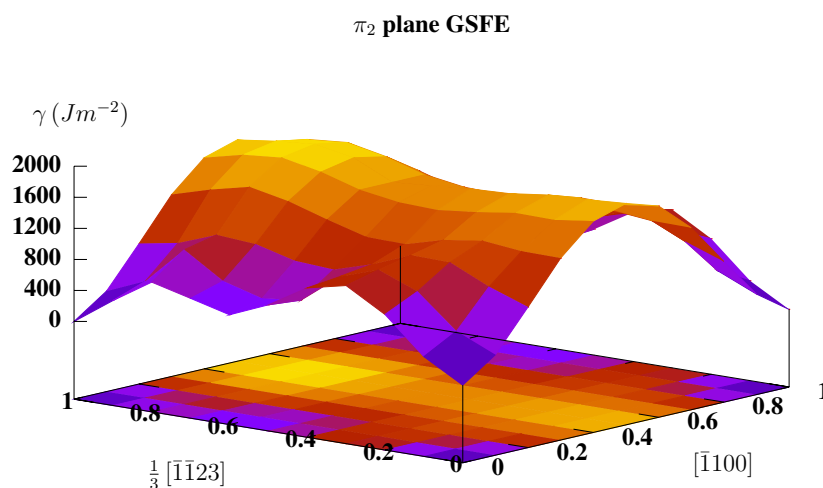


Figure 4.3:  $\gamma$ -surfaces on Prism plane



Figure 4.4:  $\gamma$ -surfaces on  $\pi_1$  planeFigure 4.5:  $\gamma$ -surfaces on  $\pi_2$  planeTable 4.1: Possible SFs identified by  $\gamma$ -plots

Slip Plane	Slip direction	SF	SFE ( $mJ/m^2$ )	Other SFEs
Basal $\{0001\}$	$\langle 10\bar{1}0 \rangle$	$\frac{1}{3}\langle 10\bar{1}0 \rangle$ ( $I_2$ )	309	292 [41], 287 [42], 259 [43]
Prism $\{10\bar{1}0\}$	$\langle \mathbf{a} \rangle$	$\frac{1}{6}\langle \bar{1}2\bar{1}0 \rangle$	213	220 [41], 250 [43]
$\pi_1$ $\{10\bar{1}1\}$	$\eta_1$	$\frac{1}{4}\langle 10\bar{1}\bar{2} \rangle$	243	(240-Zr[45])
$\pi_1$ $\{10\bar{1}1\}$	$\langle \mathbf{c} + \mathbf{a} \rangle$	$0.15\langle \bar{1}\bar{1}23 \rangle$	444	
$\pi_2$ $\{11\bar{2}2\}$	$\langle \mathbf{c} + \mathbf{a} \rangle$	$\frac{1}{5}\langle \bar{1}\bar{1}23 \rangle$	416	

$\eta_1$  is the direction of twinning dislocation of  $\{10\bar{1}1\}$  twin.

### 4.1.2 New stacking faults and twinning-assisted SF formation

The atoms in the slab model containing each of the presumed five SFs are relaxed in all three directions. The basal and prism SFs remain stable with exactly the same structures and energies. Other results are partly given in table 4.2. Both the  $\frac{1}{4}\langle 10\bar{1}\bar{2}\rangle$  and the  $0.15\langle \bar{1}\bar{1}23\rangle$  SFs on the  $\pi_1$  plane identified by Vitek's method in Section 2 relax to a unique SF which is  $0.215\langle 10\bar{1}\bar{2}\rangle$  and has a much lower energy. The  $\frac{1}{5}\langle \bar{1}\bar{1}23\rangle$  SF also relaxes to a lower energy  $0.19\langle \bar{1}\bar{1}23\rangle$  SF. We do reproduce the stable SF found by Chaari et al. on the  $\pi_1$  plane [44]. Note that this SF is not detected by the Vitek's construction. The  $0.215\langle 10\bar{1}\bar{2}\rangle$  energy is the smallest one in  $\alpha$ -Ti (table 4.2). Its atomic structure is shown in figure 4.6, together with the structure found in [44] for the sake of comparison. Both SFs on  $\pi_1$  plane correspond to  $\{10\bar{1}1\}$  nanotwin structures at the faulted area. The new  $0.215\langle 10\bar{1}\bar{2}\rangle$  SF corresponds to a  $\{10\bar{1}1\}$  nanotwin AB which leads to a significant decrease of the SFE, just as the simple  $\{111\}$  SF in a face centred cubic metal can be seen as made of two close  $\{111\}$  twin boundaries (TBs). Indeed, the  $\{10\bar{1}1\}$  TB energy turns out to be only 92 mJ/m<sup>2</sup>. Similar twin-assisted SF structures do not take place in the  $\pi_2$  plane because the associated TB energy is much higher, viz. 384 mJ/m<sup>2</sup>.

Since  $0.19\langle \bar{1}\bar{1}23\rangle = 0.57\langle \mathbf{c} + \mathbf{a}\rangle$ , the  $\alpha$  factor of the following dissociation model on the  $\pi_2$ - $\{11\bar{2}2\}$  plane

$$\langle \mathbf{c} + \mathbf{a}\rangle = \alpha\langle \mathbf{c} + \mathbf{a}\rangle + (1 - \alpha)\langle \mathbf{c} + \mathbf{a}\rangle \quad (4.2)$$

is 0.57 instead of 0.5 found with empirical potentials [46, 47].

Table 4.2: Final stable SFs and associated twins in pyramidal planes.  $\mathbf{b}_{TD}$  is the direction of twinning dislocation of the  $\{10\bar{1}1\}$  twin.

Slip Plane	Slip direction	SF	SFE (mJ/m <sup>2</sup> )
$\pi_1 \{10\bar{1}1\}$	$\eta_1$	$0.215\langle 10\bar{1}\bar{2}\rangle$	134
$\pi_2 \{11\bar{2}2\}$	$\langle \mathbf{c} + \mathbf{a}\rangle$	$0.19\langle \bar{1}\bar{1}23\rangle$	297
$\pi_1 \{10\bar{1}1\}$	$\frac{1}{2}\langle \mathbf{a}\rangle - \frac{1}{2}\langle \mathbf{b}_{TD}\rangle$	$\frac{1}{2}\langle \bar{1}2\bar{1}0\rangle - 0.0384\langle 10\bar{1}\bar{2}\rangle$	205      227 [44]
Associated Twins	twinning-dislocation		$\gamma_{TB}$ (mJ/m <sup>2</sup> )
$\pi_1 \{10\bar{1}1\}$		$0.0768\langle 10\bar{1}\bar{2}\rangle$	92
$\pi_2 \{11\bar{2}2\}$		$0.1427\langle \bar{1}\bar{1}23\rangle$	384

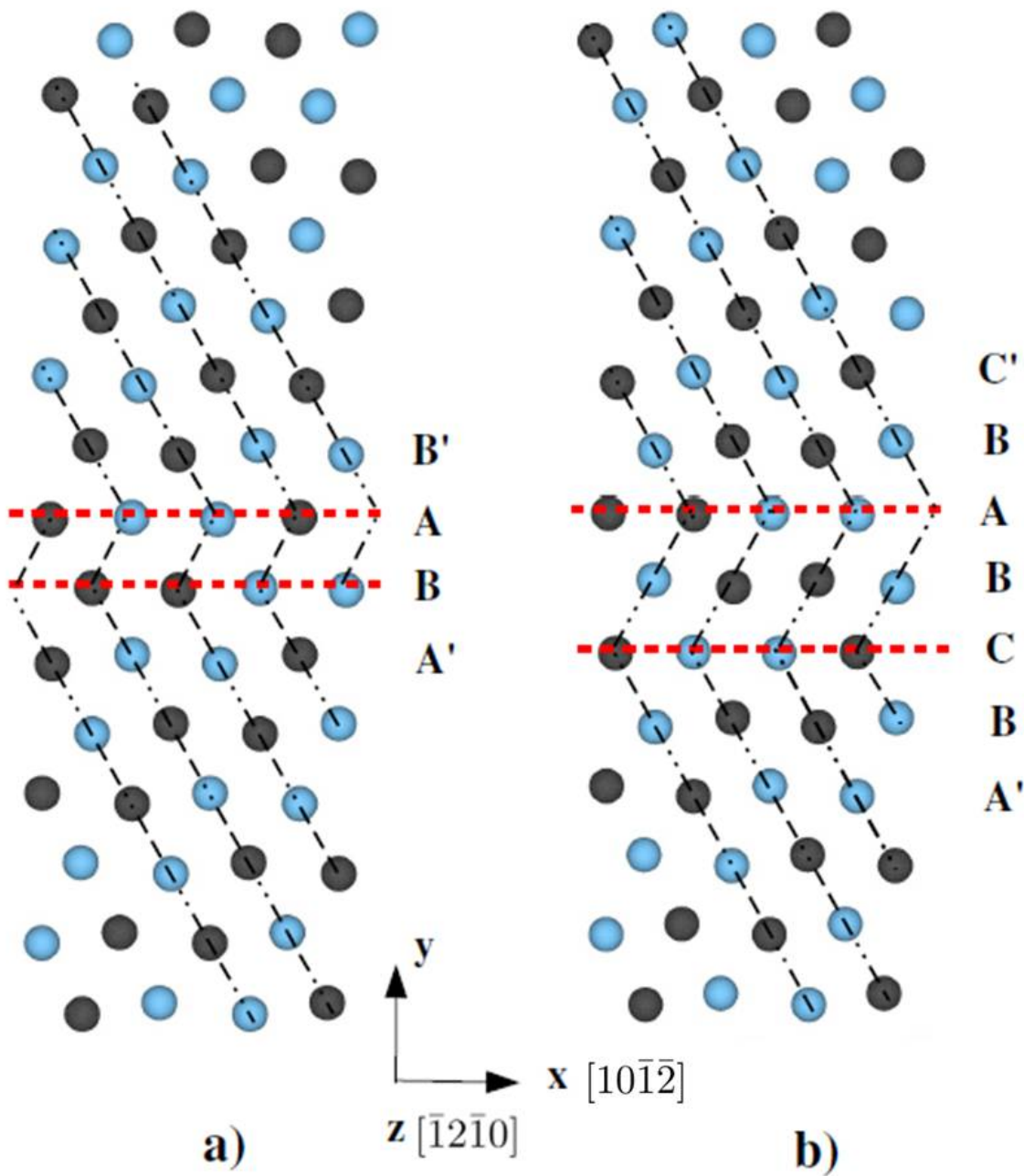


Figure 4.6: Two  $\{10\bar{1}1\}$  Twin-assisted SFs on  $\pi_1$ . Left figure is related to the  $0.215\langle 10\bar{1}2 \rangle$  partial dislocation; right figure corresponds to  $\frac{1}{2}\langle \mathbf{a} \rangle - \frac{1}{2}\langle \mathbf{b}_{TD} \rangle$  partial dislocation found in [44].

### 4.1.3 Discussion

From our simulations above, the former conclusions of the  $\langle \mathbf{c} + \mathbf{a} \rangle$  screw dislocation dissociation into two equivalent  $\frac{1}{2}\langle \mathbf{c} + \mathbf{a} \rangle$  dislocations must be reconsidered. We propose a two step mechanism which is visualized in figure 4.7 and given in the

following two step equation:

$$\begin{aligned} \langle \mathbf{c} + \mathbf{a} \rangle &= 0.57 \langle \mathbf{c} + \mathbf{a} \rangle_{\pi_2} + 0.43 \langle \mathbf{c} + \mathbf{a} \rangle_{\pi_1} \\ 0.43 \langle \mathbf{c} + \mathbf{a} \rangle_{\pi_1} &= 0.215 \eta_1 + 0.215 \langle \mathbf{a} \rangle \end{aligned} \quad (4.3)$$

where  $\eta_1$  is the twinning direction vector of the  $\{10\bar{1}1\}$  twin, viz.  $\langle 10\bar{1}\bar{2} \rangle$ . A  $\langle \mathbf{c} + \mathbf{a} \rangle$  screw dislocation dissociates to two partial dislocations with a SF ribbon in between, and the second partial dissociates to two partials in the  $\pi_1$ - $\{10\bar{1}1\}$  plane for  $0.215\eta_1$  and  $\pi_1$  or prismatic plane for  $0.215\langle \mathbf{a} \rangle$ , one along the  $\eta_1$  direction and another one along the  $\langle \mathbf{a} \rangle$  direction on the  $\pi_1$  plane.

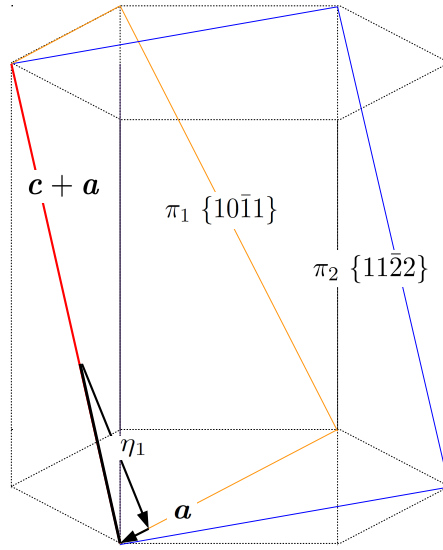


Figure 4.7: A possible  $\langle \mathbf{c} + \mathbf{a} \rangle$  screw dislocation dissociation mechanism.

This scheme is currently only based on SF calculations. In order to check its validity, a further direct study of the  $\langle \mathbf{c} + \mathbf{a} \rangle$  screw dislocation dissociation is necessary and is ongoing although it requires a large amount of atoms. Comparing with the traditional cross-slip hypothesis on only  $\pi_1$  and  $\pi_2$  planes [46, 55], there may exist a more complicated cross-slip phenomenon on all the four slip planes ( $\pi_1$ ,  $\pi_2$ , prism and basal plane). Since the empirical potential do not predict well the SFs found by our DFT calculations, the cross-slip study can only be done with a nudged elastic band method, still very heavy in DFT. This kind of work should hopefully become attainable thanks to the rapid development of computational capacities.

## 4.2 $\langle c+a \rangle$ screw dislocation core dissociation

In order to investigate the possible  $\langle c+a \rangle$  dissociation mechanism,  $\langle c+a \rangle$  screw dislocation core construction is necessary. Two core positions, A and B in figure 4.8, are tested as centre for the atomic displacements (dislocation line) imposed in the outer cylinder according to elasticity theory. With the cylinder radius I chose, it gives 412 atoms in the box with core A and 413 atoms in the box with core B.

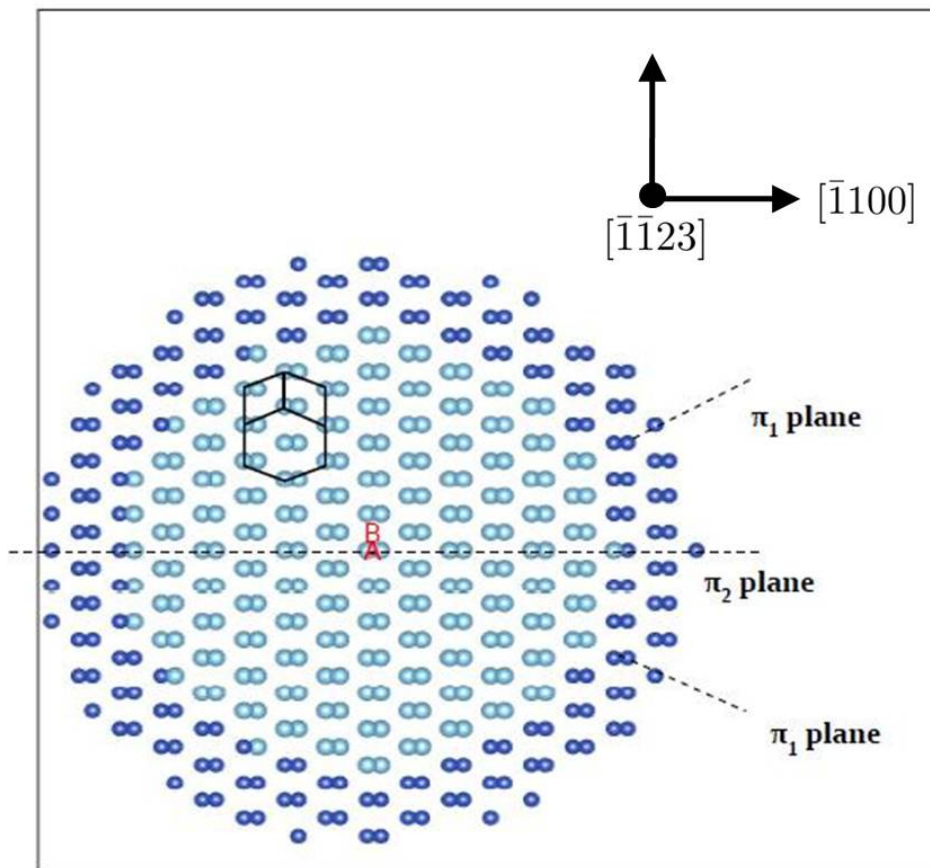


Figure 4.8: The  $\langle c+a \rangle$  screw dislocation visualized with two central core positions A and B for the application of  $u_z$  [eq. 2.22]. Direction perpendicular to  $\pi_2$  plane is  $[11\bar{2}\frac{2}{\Lambda^2}]$  with  $\Lambda^2 = (2/3)(c/a)^2$ . Cf. section 2.2.5.

After DFT relaxation, a Vitek's difference displacement map (DDmap) of the relaxed configuration is drawn with a DDmap program I wrote with Mapple.

The DDmaps are presented in figures 4.9- 4.10.

Unlike the  $\pi_1$  plane dissociation observed by Minonishi using a Lennard-Jones potential (lj56) potential (see section 1.1.2.2.3), but similarly to the dissociation

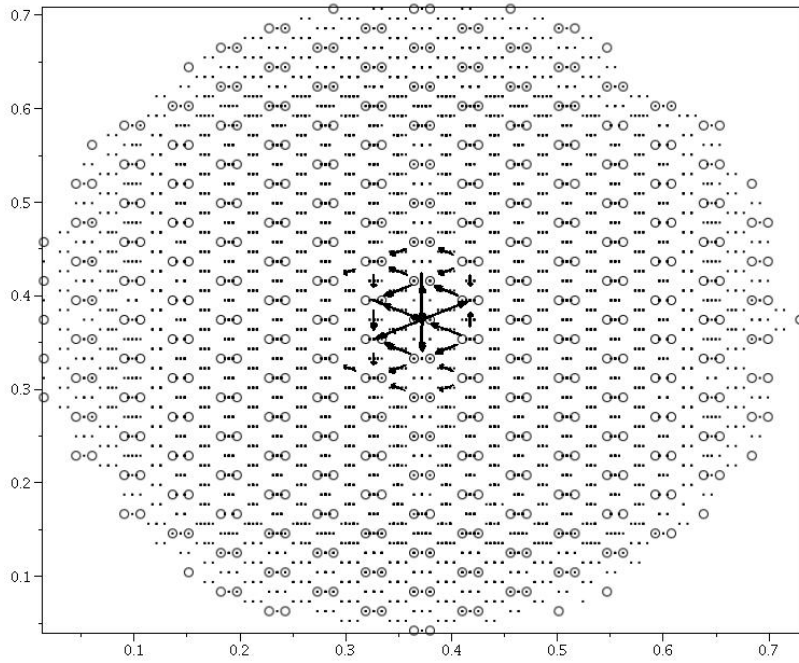


Figure 4.9: DDmap of the ‘A-positioned’  $\langle c+a \rangle$  screw dislocation core after relaxation. (All dots in this DDmap are artefacts from my DDmap generation program. Id. fig. 4.9.)

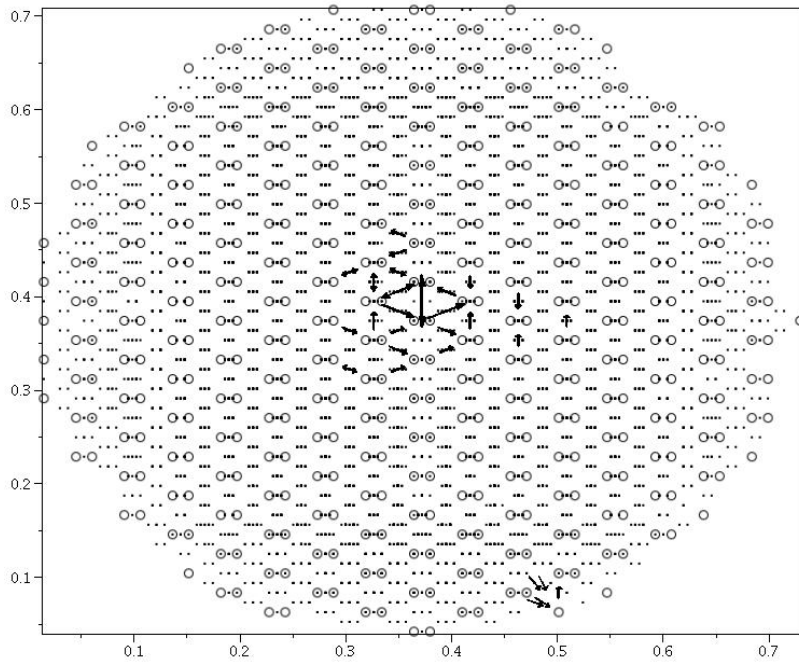


Figure 4.10: DDmap of the ‘A-positioned’  $\langle c+a \rangle$  screw dislocation core after relaxation. The small arrows presented in the boundary should be the results of surface effects.

configuration of Liang & Bacon [52] using a better ti12 or n56 potential (figure 4.11), my DFT simulations show the non-planar core spreading on  $\pi_1$ ,  $\pi_2$  and prismatic plane planes. Compared with the A position relaxed DDmap, the B position DDmap spreads more on the  $\pi_1$  and  $\pi_2$  planes and less on the vertical ( $1\bar{1}00$ )

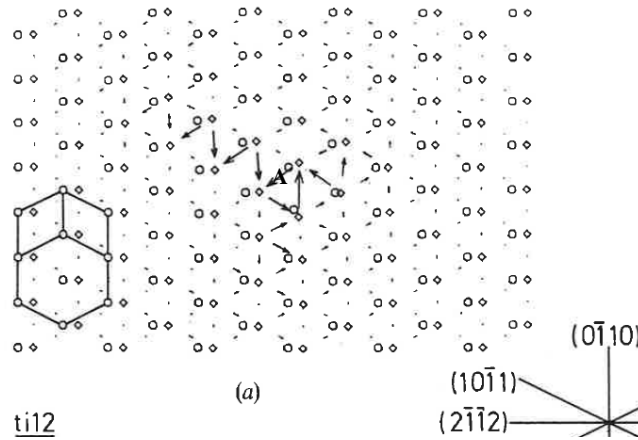


Figure 4.11:  $\langle \mathbf{c} + \mathbf{a} \rangle$  screw dislocation core dissociation in  $\pi_1$ ,  $\pi_2$  and prismatic planes obtained using a *ti12* potential with a dislocation line position at A [52].

plane. But neither the A nor the B configuration give a clear core dissociation. A large  $0.57\langle \mathbf{c} + \mathbf{a} \rangle$  screw partial dislocation dissociated on  $\pi_2$  is not observed.

All the atoms being allowed to relax in the periodic screw dislocation direction, the influence from the boundary condition can be thought of as being minimal. Thus, these simulations should give a good approximation for the screw core relaxation. The reason why we do not get a dissociation on  $\pi_1$ ,  $\pi_2$  and prismatic plane with expected partial dislocation as proposed by our SF calculations may be explained by the fact that, as revealed by our previous stacking fault calculations, the dissociation mechanism is more complex than a simple splitting to 2 partial dislocations. It could be 3 parts. Thus, such a  $\langle \mathbf{c} + \mathbf{a} \rangle$  screw dislocation dissociation may not be easy to obtain by direct relaxation from an initially perfect core (see the  $\langle \mathbf{a} \rangle$  screw dislocation core spreading case shown in section 4.4). A pre-extended dislocation core configuration as shown in the simulation of Minonishi et al. [46] or some external perturbations may be required.

### 4.3 H and O interaction with SFs

Plasticity of Ti is mainly controlled by the  $\langle \mathbf{a} \rangle$  screw dislocation glide. As shown by many DFT-based screw dislocation core simulations on hcp metals (Ti [41], Zr [23], Mg), the prismatic screw dislocation core  $\langle \mathbf{a} \rangle$  can dissociate to two closely related partials  $1/2 \langle \mathbf{a} \rangle$ , separated by a narrow SF.  $\langle \mathbf{a} \rangle$  or  $\langle \mathbf{c} + \mathbf{a} \rangle$  dislocation associated SFs are also observed in empirical potential simulations. It is thus

important to study the effect of H or O on them from a energetic point of view. This will be useful for a rough estimation of the H/O effects on core structure.

### 4.3.1 Segregation of H and O to stacking faults

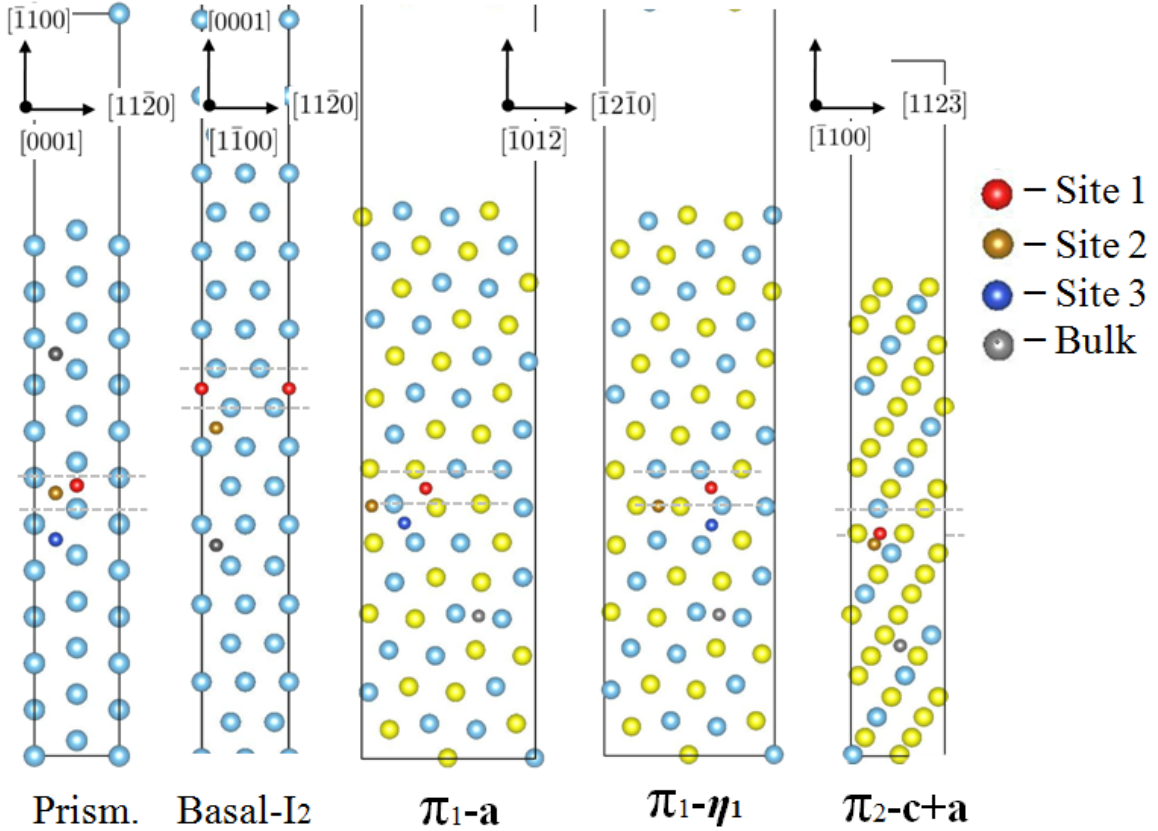


Figure 4.12: Segregation sites for H and O near SFs

First of all, in order to study the effect of H and O on SFs, we carry out segregation energy calculations. All deformed octahedral sites on or near the SFs are investigated. According to their distances to the SFs, they are named site 1 (closest to SF), site 2 and site 3 (far from SF), site 2 are closer than site 3, except for the site 2 of the prism fault for which it is also a on-SF-site. Their positions with respect to SFs are shown in figures 4.12. For each site, super-cells of different sizes are used in order to check the sign and value of  $E_{seg}$  when it is favourable. table 4.3 gives the segregation energies for these sites.

The segregation energies are small, which sounds reasonable for interstitial rather than substitutional segregation near SFs. From table 4.3, we start by discussing the  $\langle a \rangle$  screw dislocation associated SFs.

For the prismatic fault: O does not segregate to site 1, it segregates to the site 2 only with the box 1x1. It segregates to the site 3, but it seems that the segregation



Table 4.3: Segregation energies for H and O in different Octa sites near each SFs.  $\mathbf{b}_{TD}$  is the direction of twinning dislocation of the  $\{10\bar{1}1\}$  twin

SF	Size	$E_{seg}$ O (eV)			$E_{seg}$ H (eV)		
		Site 1	Site 2	Site 3	Site 1	Site 2	Site 3
Prism. $\langle \mathbf{a} \rangle$	1x1	2.0	-0.019	-0.068	0.761	-0.047	0.041
	2x2	3.183	0.097	-0.008	0.792	-0.031	0.041
	3x3	2.473	0.124	-0.001	0.802	-0.026	0.016
$\pi_1$	1x1	-0.083	0.120	-0.078	0.02	-0.103	0.020
$0.5\mathbf{a}-0.5\mathbf{b}_{TD}$	2x1	-0.098	0.025				
Basal	1x1	0.123	-0.006		-0.245	-0.168	
$I_2$	2x2	-0.01	-0.058		-0.251	-0.164	
	3x3	0.009	-0.053		-0.279	-0.170	
$\pi_1$	1x1	-0.015	0.123	-0.095	0.06	-0.052	-0.005
$0.215\langle \mathbf{c}+\mathbf{a} \rangle$	2x2	0.195	0.165	-0.033	0.066	-0.054	-0.002
$\pi_2$	1x1	0.394	0.393		-0.124	-0.122	
$0.57\langle \mathbf{c}+\mathbf{a} \rangle$	2x2	0.373	0.545		-0.134	-0.134	

will not happen for a box larger than 3x3 according to the tendency. H segregates neither to the site 1 nor the site 3, while it segregates to site 2 with all the 3 sizes.

They show that oxygen normally does not segregate to prismatic SF and H has only a small segregation ability ( $E_{seg}$  lower than 50 meV) to this SF.

For the important  $0.5\mathbf{a}-0.5\mathbf{b}_{TD}$  SF in  $\pi_1$  plane, O segregates to sites 1 and 3 while H segregates only to site 2. The segregation energies on this SF are more important than those on the prismatic SF, which suppose a more important interaction between H and O with this SF on  $\pi_1$  plane.

For the secondary glide system associated basal  $I_2$  SF, O segregates mainly to site 2 and H segregates to both sites 1 and 2. The large  $E_{seg}$  of H indicates a possible large effect on the basal glide system.

For the  $\langle \mathbf{c}+\mathbf{a} \rangle$  screw dislocation associated SFs, in the case of  $0.215\langle \mathbf{c}+\mathbf{a} \rangle$  on  $\pi_1$  plane, O mainly segregates to the site 3 and H mainly to site 2.

In the case of  $0.57\langle \mathbf{c}+\mathbf{a} \rangle$  on  $\pi_2$  plane, O does not segregate while H strongly segregates to sites 1 and 2. This indicates a possibly large influence of H on the  $\pi_2$  plane glide.

We can conclude that except for O in prism &  $\pi_2$  SF cases, O/H will closely influence the SF and thus the core structures. Segregation energy calculation on screw dislocation core  $\langle \mathbf{a} \rangle$  on prism and  $\pi_1$  plane will be done in the section 4.5.

### 4.3.2 Effects of H and O on stacking fault energies

We can go further to see the SFE variations in presence of the H/O in different sites. The sites now investigated are not limited to the segregation sites because the velocity of a passing dislocation is much larger than H and O diffusion velocities. The SF may be formed in presence of O/H in non-segregated sites as H or O may not have time to diffuse to other sites [8, 12].

SFEs values in presence of H and O in site 1, 2, 3 with different concentrations are shown in table 4.4. These values are compared to the SFEs obtained from a pure Ti supercell (column 6)

Table 4.4: SFE values in presence of H and O in different octahedral sites near SFs and with different concentrations

SF	Size	SFE with O (mJ/m <sup>2</sup> )				SFE with H (mJ/m <sup>2</sup> )		
		X-Y	Site 1	Site 2	Site 3	bulk	Site 1	Site 2
Prism. $\langle \mathbf{a} \rangle$	1x1	2586	190	132	213	1107	149	206
	2x2	944	244	213	213	448	204	213
	3x3	695	231	206	213	363	199	208
$\pi_1$ 0.5a-0.5b <sub>TD</sub>	1x1	170	275	172	205	209	145	132
	2x1	209	249	208	205			
Basal $I_2$	1x1	546	265		309	-237	-72	
	2x2	298	273		309			
	3x3	294	279		309	234	260	
$\pi_1$ 0.215 $\langle \mathbf{c} + \mathbf{a} \rangle$	1x1	137	209	96	134	165	107	132
	2x2	193	185	134	134	153	121	135
$\pi_2$ 0.57 $\langle \mathbf{c} + \mathbf{a} \rangle$	1x1	554	554		297	257	258	
	2x2	381	406		297	308	308	

The  $\Delta SFE$  induced by H and O depends linearly on the H and O's segregation energies to SFs. Their relations are explained by the following equations. As defined in section 2.29, the segregation energy with an O in site  $i$  is expressed by:

$$E_{seg}(O) = E_{TiO}^{SF}(O \text{ in site } i) - E_{TiO}^{SF}(O \text{ in bulk}) \quad (4.4)$$

and SFE variation in presence of an oxygen can be determined by the equation:

$$\begin{aligned}\Delta\gamma(O) &= \gamma(TiO) - \gamma(Ti) \\ &= \frac{E_{TiO}^{SF}(O \text{ in site } i) - E_{TiO}(O \text{ in site } i)}{A} - \frac{E_{Ti}^{SF} - E_{Ti}}{A}\end{aligned}\quad (4.5)$$

When an oxygen is in a bulk-environment octahedral site which is far away from the SF, it is supposed to have no influence on SFE. We thus have:

$$\frac{E_{Ti}^{SF} - E_{Ti}}{A} = \frac{E_{TiO}^{SF}(O \text{ in bulk}) - E_{TiO}(O \text{ in bulk})}{A}\quad (4.6)$$

Since the total energies of TiO system are the same for a O in site  $i$  or in bulk site when there is no more defect in Ti supercell, we have:

$$E_{TiO}(O \text{ in site } i) = E_{TiO}(O \text{ in bulk})\quad (4.7)$$

We thus have:

$$\Delta\gamma(O) = \frac{E_{seg(O)}}{A}\quad (4.8)$$

Let us summarize the effects of O on prismatic SFs: When the material is in its equilibrium state, O segregates to the sites discussed above. When the material is under stress and the glide system is activated, under this dynamical process, O may either decrease the SFE or increase it, whether it happens to be in a favourable or non favourable site, with  $\Delta\gamma(O) = E_{seg(O)}/A$ . Let us take the example of O in site 1 of a prism SF, since the plasticity of  $\alpha$ -Ti is mainly controlled by the prismatic glide, the presence of oxygen prevents the formation of a meta-stable SF during the dislocation glide process and thus hardens the  $\alpha$ -Ti material, which is in qualitative agreement with experimental observations [123, 11]. And the O effects is mainly related to the dynamical process.

For the effects of H on SFs: Under dynamical process, the effect of H is uncertain, It depends on the energy barrier of the transition path from site 1 to site 2 (in the prismatic SF case). H in site 1 will increase the SFE. If it can easily move from site 1 to site 2, H will slightly decrease the SFE. Furthermore, as the H solubility limit in alpha Ti is 20 wt.ppm at ambient temperature, dislocation glide has much less chance to meet a H than an O. The effect of H on dynamical process should be small. At equilibrium, H segregates to site 1 of basal SF  $I_2$  and  $\pi_2$  plane SF and to site 2 of prismatic plane SF and  $\pi_1$  plane SFs. We conclude that the effects

of H is mainly related to the equilibrium state and should be further investigated by a real dislocation core simulation.

#### 4.4 $\langle a \rangle$ screw dislocation core

I tested supercell sizes  $N\sqrt{3}a \times Nc \times 1a$  boxes with an N from 5 to 8 in order to find an adequate size for a reliable screw core simulation. The core structures after relaxation are visualized in DDmap. See figure 4.13.

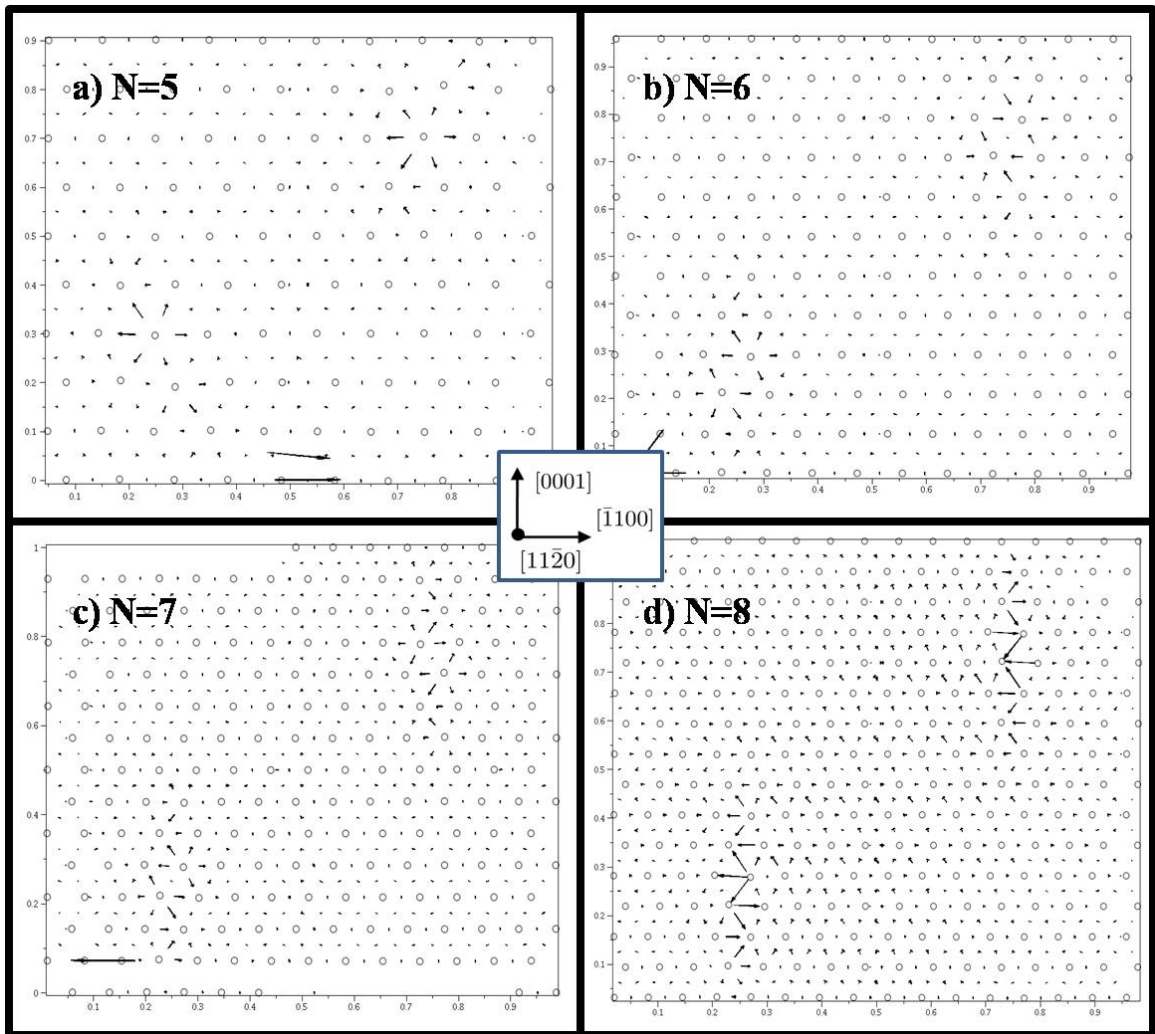


Figure 4.13: dipole supercell size tests with  $N= 5, 6, 7$  and  $8$

A prismatic dissociation is finally found with  $N=8$  after a relaxation with all the forces on atoms converged to  $2 \text{ meV}/\text{\AA}$ . A more stable pyramidal plane dissociation of the  $\langle a \rangle$  screw dislocation core are recently discovered [41, 24]. However, this structure does not easily show up when the DFT relaxation starts from a perfect core configuration. With some slightly different initial configurations (slightly

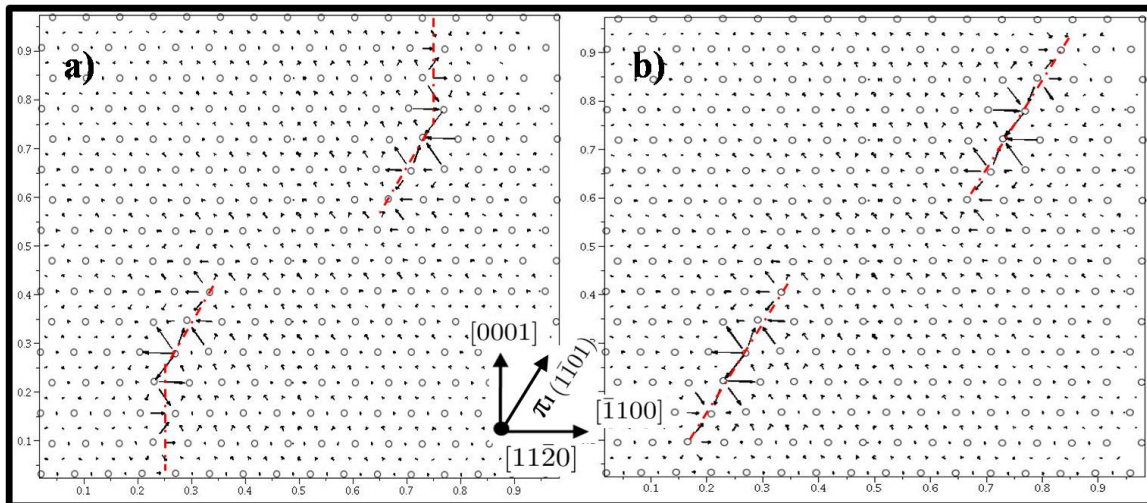


Figure 4.14: a) Prism- $\pi_1$  plane mixed dissociation; b)  $\pi_1$  plane dissociation.

changed elastic constants), we got some prism- $\pi_1$  mixed dissociation, they are shown in figure 4.14.

By pre-extending the dislocation core partially to the  $\pi_1$  plane, the  $\pi_1$  plane dissociation is eventually obtained for both cores of the dipole. The energy difference between a prism and a  $\pi_1$  plane dissociation is  $15 \text{ meV}/\text{\AA}$ . It is three times larger than the  $4.7 \text{ meV}/\text{\AA}$  obtained in the calculation of Clouet et al. [24]. This may be related to the differences in the modelling and optimisation algorithms used in the ab initio softwares to simulate large boxes (e.g. considerations of semi-core and of smearing of the electronic occupancies applied for metals).

## 4.5 H and O effects on $\langle \mathbf{a} \rangle$ screw dislocation core

### 4.5.1 H and O effects on prismatic plane spreading $\langle \mathbf{a} \rangle$ screw dislocation core

I want to study the effects of H and O on the gliding-motion the  $\langle \mathbf{a} \rangle$  screw dislocation. Knowing from Clouet et al.'s recent studies that the  $\langle \mathbf{a} \rangle$  screw dislocation glides in the unlocked prismatic plane dissociated configuration, it is the effects of H and O on this prismatic plane dissociated configuration that I am first going to study, in section 4.5.1. I also study the effects of H and O on the pyramidal  $\pi_1$  plane dissociated configuration in section 4.5.2.

Octahedral interstitial sites are spotted in figure 4.15, in and around the prismatic plane along which the  $\langle \mathbf{a} \rangle$  screw dislocation is dissociated in its unlocked mode. These sites are numbered from 0 to 13, possibly doubled or even quadrupled due to obvious symmetry considerations. The 0 site corresponds to the original dislocation line position.

With the x and y directions indicated in figure 4.15, viz.  $[\bar{1}100]$  and  $[0001]$ , I use  $8\sqrt{3}a \times 8c \times n_z a$  boxes, with  $n_z=1$  and 2 (and 216 and 512 titanium atoms, respectively), to study the one atom, H or O, interstitial segregation energies at several sites, thus studying two different concentrations along the screw dislocation line. These segregation energies are given in the following table 4.5.

The first line in this table, noted  $0_{2c}$ , corresponds to a first study with one H/O put in each core of the supercell which actually contains two cores in the Clouets S arrangement (see section 2.2.6 of chapter 2). There are thus two formally equivalent sites “0”, with  $n_z=1$  and four with  $n_z=2$ . In that first study, I use  $n_z=2$  and I put one H, or one O, in each core, thus giving  $Ti_{512}H_2$  and  $Ti_{512}O_2$  systems to relax. After relaxation, the unlocked prismatic configurations have both spontaneously evolved towards a pyramidal  $\pi_1$  configurations (see the corresponding DDmaps in figure 4.16). Remember that in the pure Ti case, such an evolution does not spontaneously occur, so that we can attribute this spontaneous evolution to the effect of H and O. One may thus think that when an  $\langle \mathbf{a} \rangle$  screw gliding dislocation in the unlocked prismatic configuration meets an H or an O, it may be turned into the locked pyramidal configuration. This should strengthen  $\alpha$ -Ti. In the case of oxygen, a similar result has already been obtained by Chaari in her PhD thesis work [128].

I now put one H or one O at only one of the two possible cores in the supercells, thus considering  $Ti_N H_1$  and  $Ti_N O_1$  boxes, with  $N=216$  ( $n_z=1$ ) or 512 ( $n_z=2$ ). When one H is put in a “0” site, the corresponding core evolves toward the  $\pi_1$  dissociation (see fig. 4.16b), while the other core, which is far enough in our 8x8 box, remains in its prismatic configuration. The final nearest neighbours environment for the hydrogen atom is no longer octahedral: it is surrounded by only five Ti atoms, at distances equal to, in Å, 1.91, 1.94, 2.02, 2.03 and 2.04. This occurs whether  $n_z=1$  or 2. When one O is put in a “0” site, the corresponding cores evolve towards a combined (mixed) prismatic- $\pi_1$  spreading character (the other core remains prismatic). For O in “0” site, if  $n_z=1$ , the O environment remains octahedral (with distances equal to 2.04, 2.04, 2.04, 2.10, 1.18 and 2.20 Å). If  $n_z=2$ , the O atom moves to a new nearby octahedral environment (with

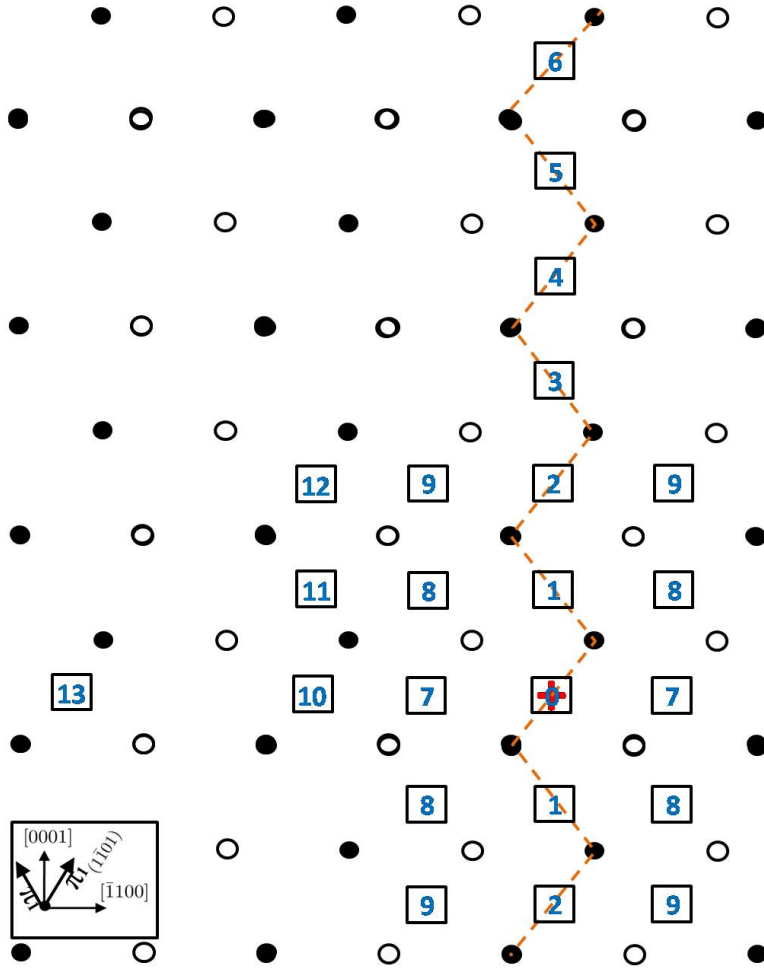


Figure 4.15: Octa sites around the prismatic plane dissociated dislocation.

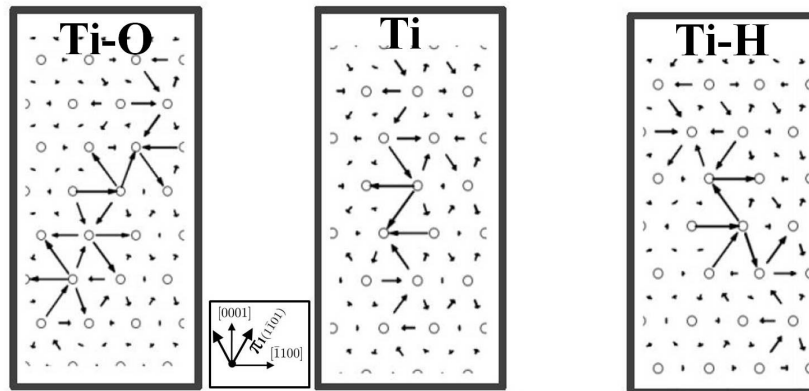


Figure 4.16:  $Ti_{512} - H/O$  : Core structure changes induced by the presence of H/O in site 1 (the central core position)

distances equal to 2.04, 2.04, 2.10, 2.11, 2.11 and 2.15 Å), see figure 4.17 i. Thus, the concentration of O, between  $n_z=1$  and  $n_z=2$ , strongly affects its behaviour with respect to a prismatic  $\langle a \rangle$  screw core, whereas the behaviour of H does not seem to depend on its concentration, between  $n_z=1$  and  $n_z=2$  (we cannot yet consider  $n_z=3, 4, \dots$ ). This is certainly due to the strong O-O interaction in  $\alpha$ -Ti observed

in the solute-solute interaction section in chapter 3, see table 3.11. The H-H interaction was observed to be much less important. For the sake of illustration, I give in figure 4.17 the DDmaps of the core spreading configurations after relaxation for  $Ti_{512}H_1$  and  $Ti_{512}O_1$  boxes for seven different sites, viz. the “13” bulk-like site which induces almost no change, and six sites at and close to the central dislocation line position, “0”, “1”, “2”, “7” and “8” (see figure 4.15). H and O in sites 0 and 1 induce a spontaneous evolution of the prismatic core to a  $\pi_1$  configuration or to a combined prismatic- $\pi_1$  character. One O in site 1 has a similar effect. The other cases do not induce significant changes. Given the favourable segregation energies of H for several sites around the central core position, hydrogen may form Cottrell atmospheres around prismatic plane dissociated  $\langle \mathbf{a} \rangle$  screw dislocations.

Table 4.5: Segregation energies of H and O in the sites near the prismatic core (meV).

Site	H		O	
	$n_z = 1$	$n_z = 2$	$n_z = 1$	$n_z = 2$
$0_{2c}$		-292		+21
0	-209	-239	0	-33
1	-137	-160	+30	+2
2	-127	-108	-52	+13
3	-133		+3	
4	-122		-39	
5	-70		0	
6	-59		-10	
7	+7	+13	+8	-20
8	-106	-20	0	+1
9	-144	-155	+33	+2
10	-35		+26	

#### 4.5.2 H and O effects on $\pi_1$ plane spreading $\langle \mathbf{a} \rangle$ screw dislocation core

As in 4.5.1, octahedral interstitial sites are spotted, in figure 4.18, in and around the  $\pi_1$  plane along which the  $\langle \mathbf{a} \rangle$  screw dislocation is dissociated in its locked mode. These sites are numbered from 0 to 7. The 0 site which corresponds to the original dislocation line position. Site 7 corresponds to a bulk-like site. I only consider  $8 \times 8 \times 1$   $Ti_{256}H_1$  and  $Ti_{256}O_1$  boxes. One H in sites 0, 2 or 4 induces the  $\pi_1$  plane dissociated configuration to evolve to a combined (mixed) prismatic- $\pi_1$  spreading



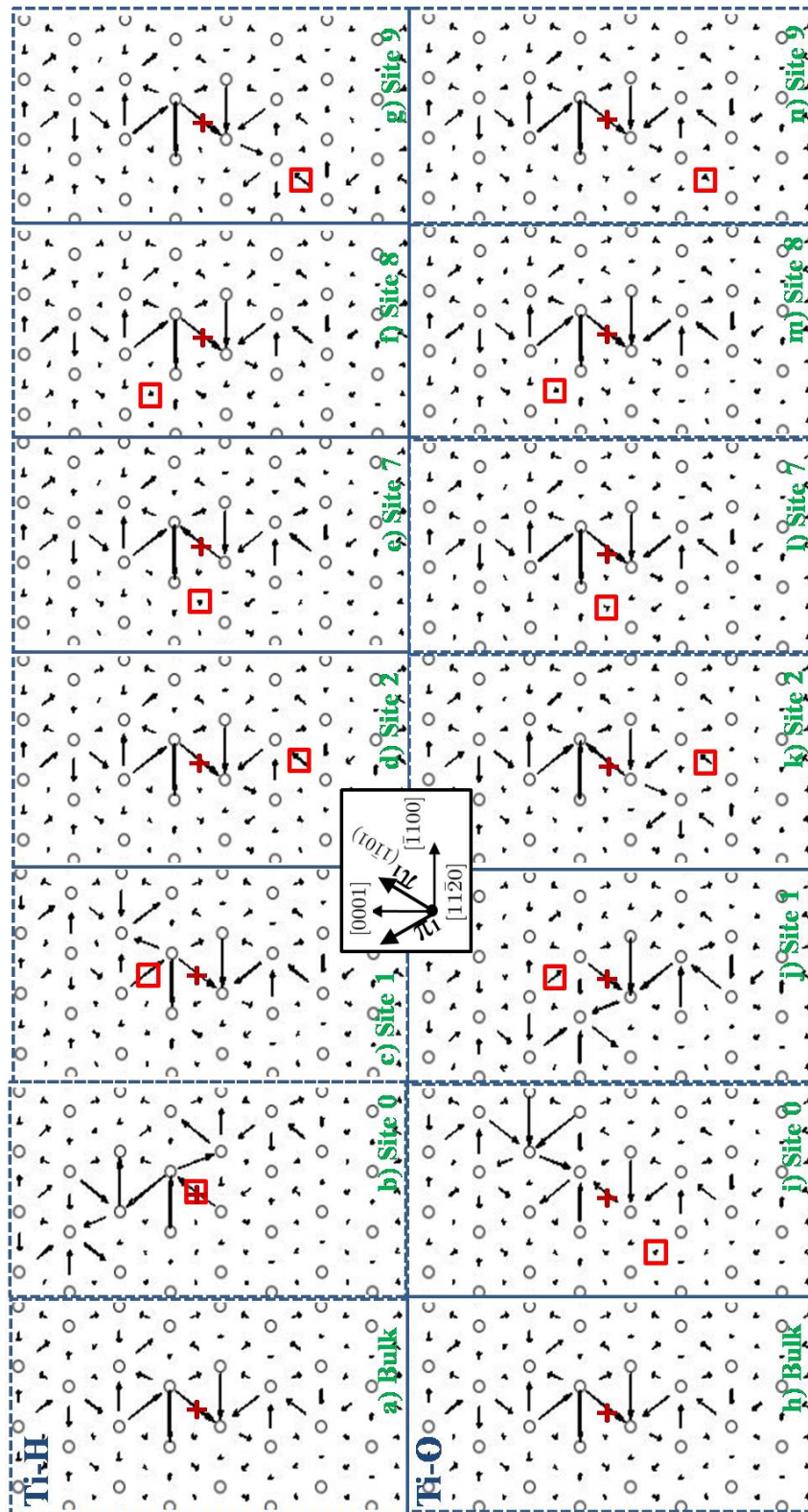


Figure 4.17: Core structure changes induced by the presence of H/O in site 0-1 and site 7-9. The “+” sign indicates the core position. “red square” sign indicates the solute position after relaxation.

character. One O in sites 0 and 1 has the same effect. Again, a similar effect was observed by Chaari in her PhD thesis work for an O near the  $\pi_1$  core [128]. The core structure transformation to a mixed prismatic- $\pi_1$  spreading character may facilitate the unlocking to a  $\pi_1$  configuration. Segregation energies for sites 0, 1, 2 and 4 are given in table 4.6.

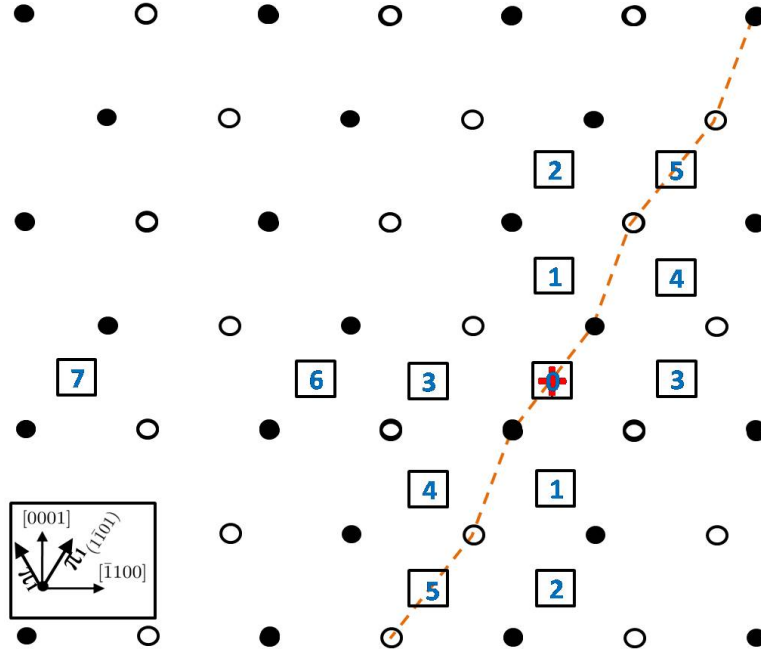


Figure 4.18: Six Octa sites around the  $\pi_1$  plane dissociated dislocation.

Segregation energies of H and O on site 0, 1, 2, 4 for a  $Ti_{256}H_1$  cell are given in table 4.6.

Table 4.6: Segregation energies of H and O in the sites near the  $\pi_1$  core (meV).

	Site 0	Site 1	Site 2	Site 4
H	-141	-90	+40	-34
O	-31	+30	-106	-3

## 4.6 H and O effects on $\langle a \rangle$ screw dislocation glide

### 4.6.1 $\langle a \rangle$ screw dislocation glide in pure Ti

The climbing-image NEB (CI-NEB) method [179] can be used to estimate the Peierls potential, for a stable  $\pi_1$  dislocation from one configuration to the next nearest stable  $\pi_1$  configuration. Two well relaxed  $\pi_1$  cores separated by one half

of the lattice vector  $\mathbf{c}$  are first obtained. They can be called ‘0c’ and ‘0.5c’. Only three intermediate images are then linearly interpolated from these two stable configurations to form a five point chain. The CI-NEB resulting MEP is given in figure 4.19, with the red curve extrapolated with a simple spline interpolation. As we only used a five point chain, it is probably safer to only consider the energy barrier and not to try to evaluate a Peierls stress. The energy barrier is  $18 \text{ meV}/\text{\AA}$ . As the ‘0c’ and ‘0.5c’ positions are in a same prismatic plane, this move can be called a ‘ $\pi_1$  core - prism glide’ move.

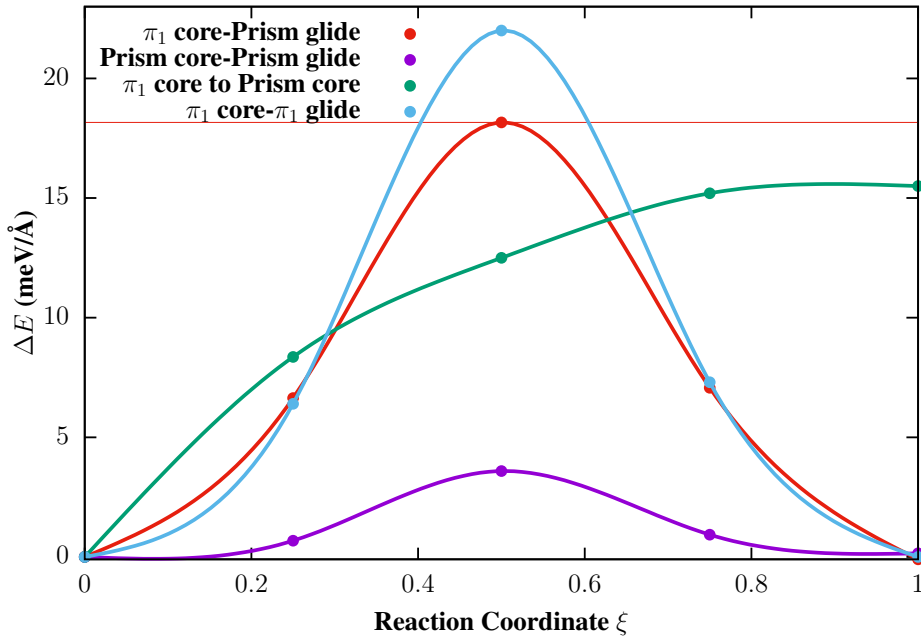


Figure 4.19: Four minimum energy paths (MEPs) for various moves of an  $\langle a \rangle$  screw dislocation core. See text for details.

One may similarly look for the MEP for a prismatic core from ‘0c’ position to a next nearest ‘0.5c’ position and call this move a ‘prism core - prism glide’ move. The obtained Peierls potential is given in the same figure 4.19, with the purple curve. The energy barrier is  $3.6 \text{ meV}/\text{\AA}$ . I note in passing that this  $3.6 \text{ meV}/\text{\AA}$  value is nine times larger than the value obtained by Clouet et al. [24] As already mentioned, see section 4.4, this may be due to differences in modelling and in optimisation algorithms used in the ab initio softwares to simulate large metallic boxes (e.g. consideration of semi-core electrons, and smearing values applied to metallic electronic occupancies) since we are the limits of accuracy of the DFT calculations.

One may also look for the MEP static structural transformation from a  $\pi_1$  core to a prismatic core and call this a ‘ $\pi_1$  core to prism core’. The corresponding MEP is given in green in figure 4.19. An energy of  $15.5 \text{ meV}/\text{\AA}$ , is needed for this

transformation, which is smaller than the energy required for the direct ‘ $\pi_1$  core - prism glide’. It indicates that, in order to glide easily in a prismatic plane, a  $\pi_1$  core to a prismatic core transformation is more likely to happen than the ‘ $\pi_1$  core - prism glide’. This core structure transformation has already been discussed by Clouet et al. [24] and is related to the ‘unlocking’ procedure, The reverse core structure transformation is called the ‘locking’ procedure.

One may also look for the MEP for a ‘ $\pi_1$  core -  $\pi_1$  glide’ move, i.e. for the move of a  $\pi_1$  core at  $0\mathbf{v}$  to a  $\pi_1$  core at  $0.5\mathbf{v}$  position with  $\mathbf{v} = \frac{1}{2}[\bar{1}106]$ , from site ‘0’ to site ‘5’ in figure 4.18 (also see figure 1.10 in the Literature Review chapter 1, taken from Clouet et al., then from  $\xi=-2$  to  $\xi=0$ ). The obtained MEP again looks like a Peierls potential path and is given in light blue in figure 4.19. Its value is 22.1 meV/Å (Clouet et al.’s value is 11.4 meV/Å). It is the highest value from the three calculated Peierls barriers. It could be interesting to study the ‘prism core -  $\pi_1$  glide’ minimal energy path.

#### 4.6.2 $\langle \mathbf{a} \rangle$ screw dislocation glide with H and O solute

In order to estimate the effects of H and O on the dislocation glide on prismatic plane,  $Ti_{256}H_1$  and  $Ti_{256}O_1$  supercells are selected for calculations.

A scenario is proposed (see down-part of figure 4.20): Let us assume that a prismatic spread  $\langle \mathbf{a} \rangle$  screw core (red ‘+’ symbols in figure) approaches an H atom in a frontal way. The H atom is at a given octahedral site at a given time, as for instance the position chosen as a snapshot in figure 4.20 (the H symbol in the black square). If the screw core keeps on moving left on the prismatic plane with respect to the H atom, one can look for its minimal energy path between successive relaxed configurations corresponding to a ‘prism core - prism glide’ in presence of an H in the dislocation-core-located prismatic plane. This, in principle because of Galileo, is equivalent to moving the H atom upwards from site 0 to site 1 then to site 2 and so on in figure 4.15 even if my proposed scenario actually corresponds to the reverse. The successive MEPs for this scenario are shown in the upper part of figure 4.20.

These MEPs in presence of a H in figure 4.20 are compared to the case where H is extremely far away from the dislocation. This is the red curve shown between  $\xi=8$  and  $\xi=9$ . Its presence does not mean that dislocation glide happens in this area, it is put here just to be compared to other MEPs affected by a H. It is used

in the same way in figure 4.21- 4.22). The dashed line between two solid points means that NEB calculation is not performed for dislocation glide in this area.

For each integer value of the reaction coordinate  $\xi$ , there are always two calculations made, and thus two corresponding solid points in figure 4.20. They correspond to calculations for the dislocation core in formally two crystallographically equivalent positions, viz.  $0.5c$  as the final configuration of one MEP, and  $0c$  as the starting configuration of the next MEP. Ideally, the global path should be continuous and symmetrical with respect to  $\xi=0$ . This is not true in these simulations, see the divergence of the two solid points at  $\xi$  equal to 1 and 3, for example. Also, checking for symmetry, I did not get symmetrical MEPs, it means that some of these MEPs are not reliable, probably due to instability problems in the DFT-NEB algorithms containing many titanium atoms and only one hydrogen atom in unstable positions.

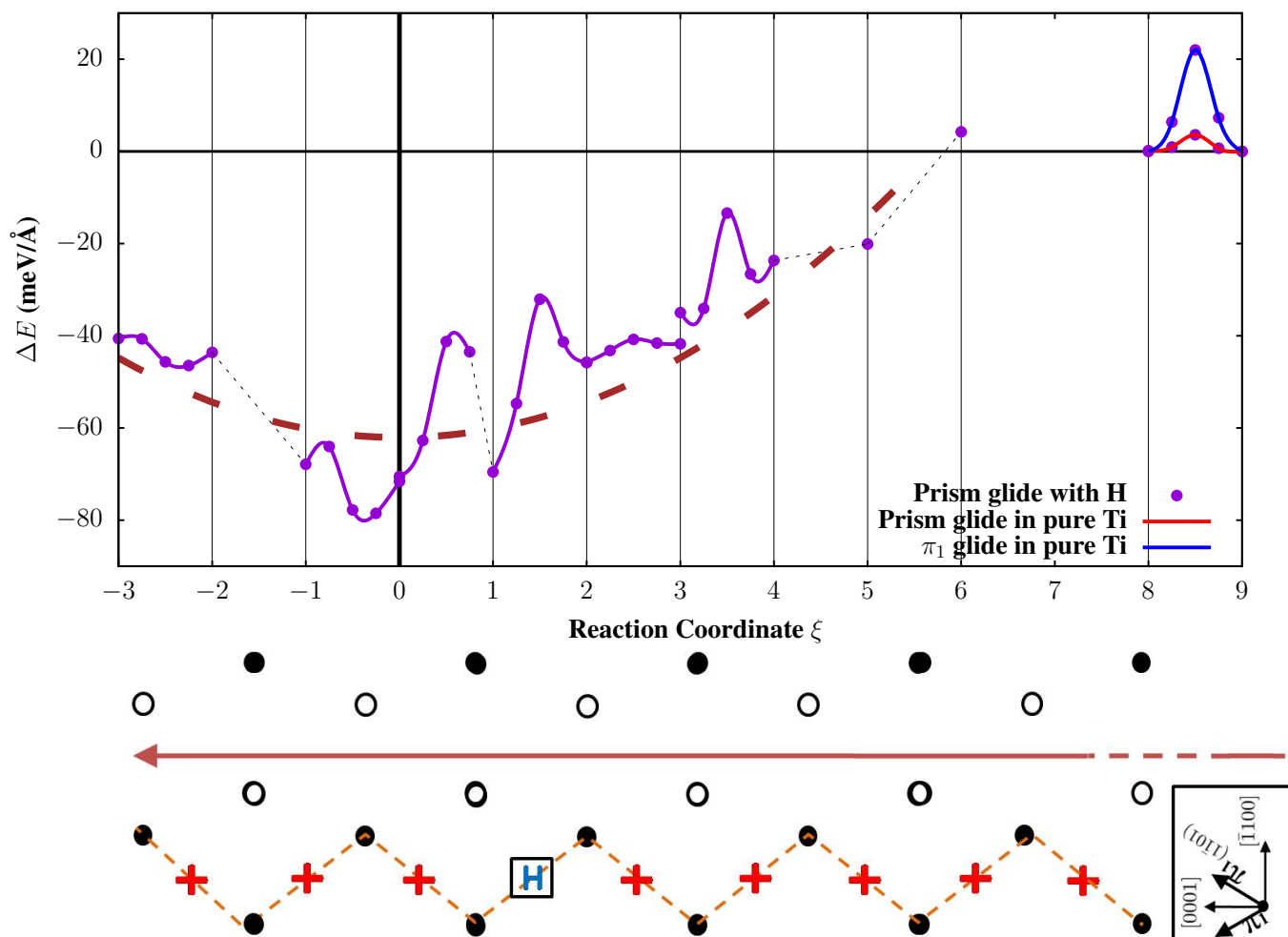


Figure 4.20: Up: MEP for a prismatic dislocation glide with H in dissociated plane; Down: Visualization of a prismatic dislocation glide with respect of a interstitial solute in an octahedral site. See text for critical comments.

The MEPs in figure 4.20 go down when the dislocation gets closer to H. This corresponds to the large segregation energies of H in the sites at the prismatic core (see table 4.5 together with figure 4.15). The presence of an H at one of these sites rather naturally increases the dislocation Peierls energy(ies), with non symmetrical profiles locally, due to the fact that the closer to the centre of the core the larger the segregation energy of H (table 4.5). The barrier energies are not the same when going from right to left than from left to right. Again, these conclusions should be re-checked since some of MEPs shown in figure 4.20 present a large uncertainty.

In the case of oxygen, see figure 4.21, the very large Peierls energy barrier I obtained, 284 meV/Å, even if not accurate, is largely above all the energy barriers obtained in the previous section and it is likely that the moving prism core will cross-slip in order to avoid the oxygen atom. The prism core will probably transform into a  $\pi_1$  core and perform a ‘ $\pi_1$  core -  $\pi_1$  glide’. A cross-slip must happen in this case and the dislocation glide is blocked in the pyramidal plane ( $\pi_1$ ). This could explain the oxygen induced dynamic strain ageing phenomena. Hydrogen segregates more strongly to the core of the  $\langle \mathbf{a} \rangle$  screw dislocation than oxygen and probably more rapidly since it diffuses faster. Yet, it is much less present in Ti than oxygen (probably ten times at ambient temperature, about four times at elevated temperature, e.g. 600°C, but with an O content up to 33at.%) and it has a lightly attractive interaction with oxygen. One may thus understand that it has a complex but probably softening role on  $\alpha$ -titanium in presence of oxygen.

When a dislocation moves near a hydrogen or an oxygen, the H and O are in a site near the dislocation but not in the prismatic glide plane, their effects on prismatic glide are shown in figure 4.22.  $\xi=0$  and 1 corresponds to site 7 and site 8, the two closest sites of the dislocation core centre. H increases largely the Peierls barrier of pure Ti because of its large influence on dislocation core, which is observed with DDmap when it is in the site 8 (corresponding here  $\xi=1$ ). Oxygen increases slightly the Peierls barrier of Ti compared its effects with its presence on glide plane. For H and O in other octahedral positions farther than the site 7 and 8, Their effects on dislocation glide should be less important. (Note that the cusps at  $\xi=0$  and  $\xi=1$  are unphysical. They are simply due to the fact that the spline fitting does not include points beyond the [0,1] range).

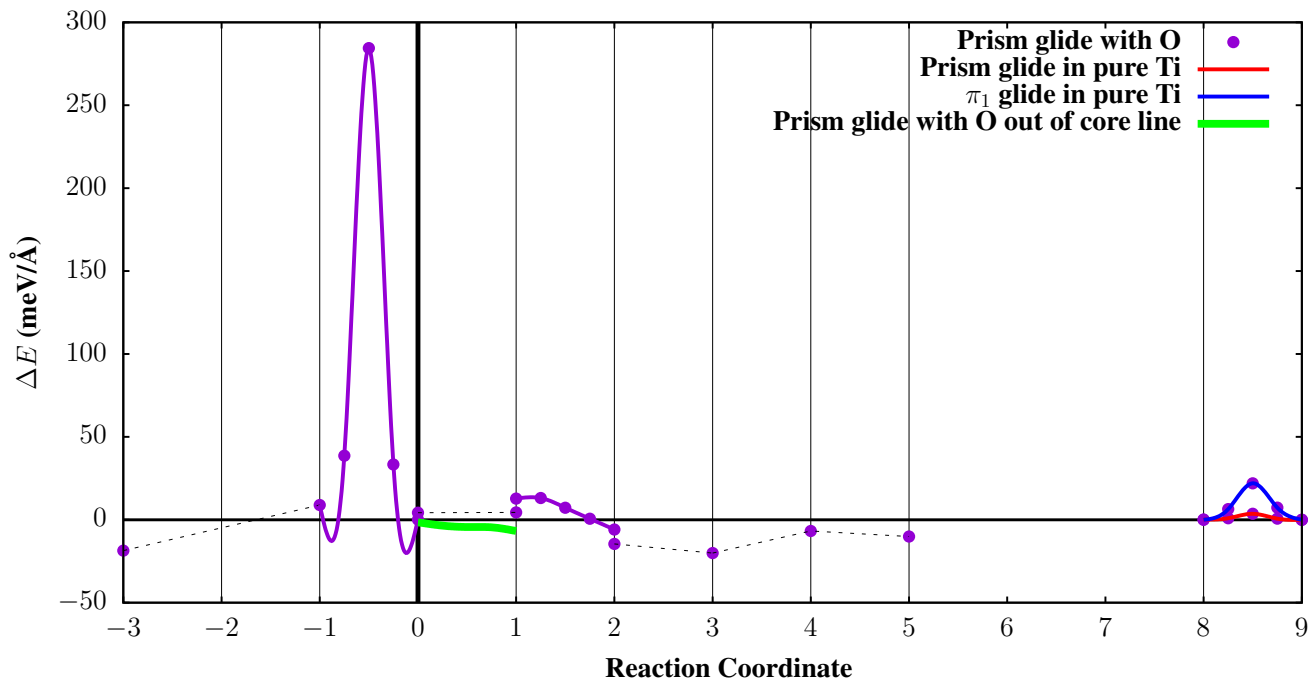


Figure 4.21: Peierls energy barrier for a prismatic dislocation glide with O in dissociated plane

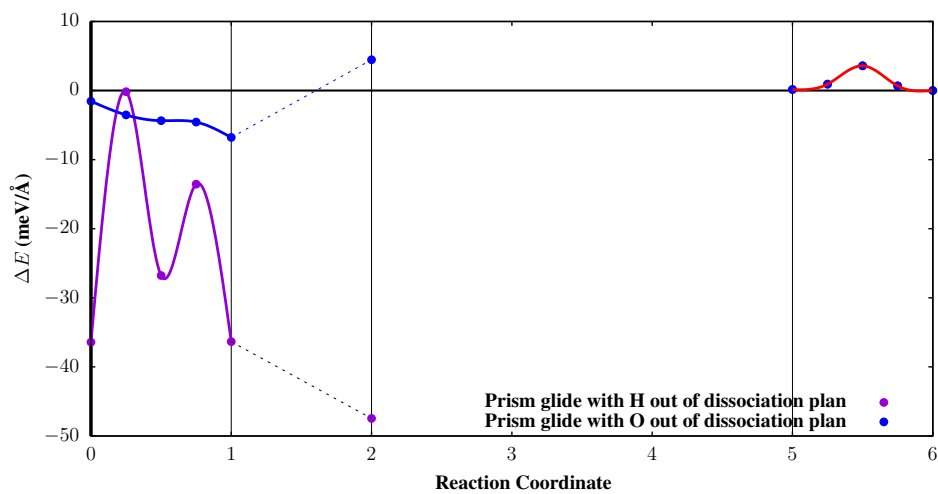


Figure 4.22: MPEs for a prismatic dislocation glide with H/O out of the dislocation core spreading plane.

# Chapter 5

## Results III: H and O effects on TB and on TD

This chapter is to study the effects of hydrogen and oxygen on some important twin boundaries and on the  $\{10\bar{1}2\}$  twinning disconnection.

It is divided into 4 parts:

Twin Boundaries in  $\alpha$ -Ti.

H and O effects on TBs

TBs under deformation in presence of H and O.

H and O effects on TD.



## 5.1 Twin boundaries in $\alpha$ -Ti

The three mechanical, or deformation, twins most easily found in  $\alpha$ -Ti, as well as in other hexagonal metals with a low axial ratio, may be simply labelled  $\{10\bar{1}2\}$ ,  $\{11\bar{2}1\}$ , and  $\{11\bar{2}2\}$  and will be described below, as well as for the  $\{10\bar{1}1\}$  twin.

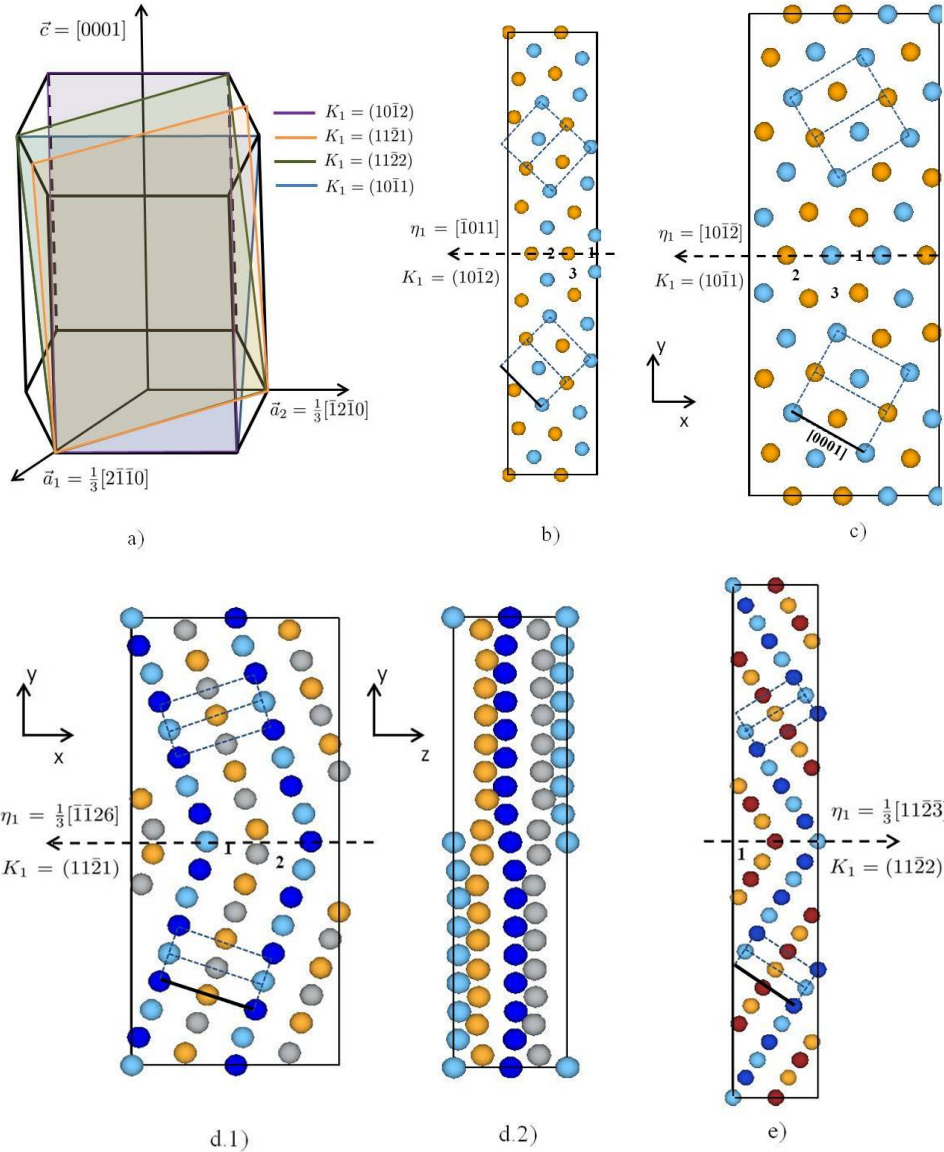


Figure 5.1: The four  $K_1$  planes and the corresponding relaxed atomic twin structures studied in this paper, shown projected on to their shear planes  $S$ . See table 5.1 and the text for further details. The  $\eta_1$  given here give the actual periodicities. The numbers 1, 2 and 3 indicate the interstitial sites used in Sections 4 and 6. The black bold bars correspond to the  $[0001]$   $c$ -axis in the lower parts considered as the matrix parts in Sections 5 and 6. For all four considered TBs, the  $c$ -axis belong to the  $S$  shear planes.

The ninth column in table 5.1 gives the TB energies  $\gamma$  of the four TBs obtained in this work. It is calculated with the usual equation, given just below, from the

Table 5.1: Twinning crystallographic elements  $K_1$ ,  $\eta_2$ ,  $K_2$ ,  $\eta_1$ ,  $S$ , shear magnitude  $s$ , Kihô, Bilby and Crocker's index  $q$ , inter  $K_1$  plane distance  $d_1$ , energy  $\gamma$ , expansion(contraction)  $\delta$ , periodic area  $A$ , Mügge's type [183] after atomic relaxation, Friedel's virtual inverse coincidence lattice site index  $\Sigma$ , and **c**-type (Tension or Compression, along **c**) for the  $\{10\bar{1}2\}$ ,  $\{11\bar{2}1\}$ ,  $\{11\bar{2}2\}$  and  $\{10\bar{1}1\}$  TBs in  $\alpha$ -Ti (with  $c/a = 1.585$ , or  $\sqrt{5/2}$  for the  $\Sigma$ s).  $d_1$  and  $\delta$  are in Å,  $A$  is in Å<sup>2</sup>,  $\gamma$  is in mJ/m<sup>2</sup>. The relaxed atomic structures are given in 5.1.

$K_1$	$\eta_2$	$K_2$	$\eta_1$	$S$	$s$	$q$	$d_1$	$\gamma$	$\delta$	$A$	M-type	$\Sigma$	<b>c</b> -type
$\{10\bar{1}2\}$	$\langle 10\bar{1}1 \rangle$	$\{\bar{1}012\}$	$\langle \bar{1}011 \rangle$	$\{1\bar{2}10\}$	0.178	4	1.709	299	-0.08	20.06	I,II	11	T
$\{11\bar{2}1\}$	$\langle 11\bar{2}0 \rangle$	(0001)	$\langle \bar{1}\bar{1}26 \rangle$	$\{\bar{1}100\}$	0.631	2	1.394	257	-0.06	49.19	II	11	T
$\{11\bar{2}2\}$	$\langle 22\bar{4}3 \rangle$	$\{11\bar{2}4\}$	$\langle 11\bar{2}\bar{3} \rangle$	$\{\bar{1}100\}$	0.215	6	1.236	384	+0.18	27.73	I	7	C
$\{10\bar{1}1\}$	$\langle 30\bar{3}2 \rangle$	$\{10\bar{1}\bar{3}\}$	$\langle 10\bar{1}\bar{2} \rangle$	$\{1\bar{2}10\}$	0.096	8	2.221	92	+0.07	30.86	I,II	13	C

difference in energies between an optimised box containing  $N$  atoms with two TBs and a box containing  $N$  atoms with no structural defect. The normalising factor  $A$  is the periodic surface in the TB plane. Convergence is ensured with respect to the distance between the two TBs contained in the periodic box (i.e. the box length perpendicular to the TB planes):

$$\gamma = \frac{E_{Box+TB} - E_{Box}}{2A}$$

These TBs experience only small expansion/contraction  $\delta$  values (given by the following volume difference equation), except for the highest energy one.

$$\delta = \frac{V_{Box+TB} - V_{Box}}{2A}$$

The virtual inverse coincidence lattice site (i.e. nodal site) index  $\Sigma$ , the Friedel's index (see [186] and [187]), is calculated with Grimmer's formula, approximating the  $c/a$  ratio for Ti to its close value  $\sqrt{5/2}$  [188]. It can also be evaluated by direct inspection from the dichromatic patterns with this  $c/a$  ratio. Finally, the inverse of  $A$  gives the two-dimensional common nodal density at the TB plane.

These TBs can also be considered as special tilt grain boundaries (GBs) with specially low energies and simple atomic structures which do not involve any dislocation cores and can thus be called coherent twin boundaries by contrast with other more GBs [189].

The energies of these four TBs do not seem to be correlated with any other property listed in table 5.1. The  $\{10\bar{1}1\}$  TB has the smallest energy and smallest shear

magnitude. Yet, it is only observed under high compressive strain or at high temperature. This clearly indicates that neither the interface excess energy nor the shear magnitude are determinant factors for the occurrence of mechanical twins in titanium (nor in other hcp metals). The  $\{10\bar{1}1\}$  TB actually has the highest Kihô Bilby and Crocker's  $q$  index [86, 87] among the four TBs. This index corresponds to the number of nodal  $K_1$  planes crossed by  $\eta_2$  (taken as primitive translation vector), and thus relates to the possible difficulty or easiness of the actual twinning mechanisms even if it still lacks important atomistic details when the atomic basis is not elementary, as it is the case for hcp metals, see [88, 185, 89]. Let us note that a given TB can be thought of as being obtainable via different deformation, or twinning, modes. These modes correspond to different shear magnitudes  $s$  and  $q$  indices. Another twinning mode is possible for the  $\{10\bar{1}1\}$  TB, with  $\eta_2 = \langle 01\bar{1}0 \rangle$  [184] which has a smaller  $q=2$  but a larger  $s=1.09$ . The twinning mode given in table 5.1 is the one indicated in [190]. In the case of the  $\{11\bar{2}2\}$  TB, a twinning mode with  $\eta_2 = \langle 5, 5, \bar{1}0, 6 \rangle$  would give a very small  $s=0.004$  but with a rather huge  $q=42$  which, however, only concerns atomic shuffles. No one has yet ever seen a twinning process in situ in a real metal but twins corresponding to very small  $s$  have never been observed. Mendelson [191] advised to apply minimum energies shear-strain and small atomic shuffling criteria in choosing the most likely twin mode on each twin plane.

Let us note that the low energy of the  $\{10\bar{1}1\}$  TB may explain the occurrence of two-layer micro-twins in the pyramidal stacking fault structure minimisation [44].

## 5.2 H and O effects with TBs

### 5.2.1 Segregation

All deformed octahedral sites on or near the TBs are investigated. They are marked in figures 5.1b, c, d.1 and e. table 5.2 gives the segregation energies for these sites.

The  $z$  period is  $a$  for the  $\{10\bar{1}2\}$  and  $\{10\bar{1}1\}$  TBs, and  $a\sqrt{3}$  for the  $\{11\bar{2}1\}$  and  $\{11\bar{2}2\}$  TBs. For each site, super-cells of different sizes are thus used in order to check the sign and value of  $E_{seg}$  when it is favourable. The  $x$  period for the last TB is only  $a\sqrt{1 + (c/a)^2} \sim 1.87a$  so that we also checked a double  $x$  double  $z$  period for that TB. The segregation energies are small, which sounds reasonable

Table 5.2: Segregation energies (in meV) for one H or one O at selected interstitial sites as shown in figure 5.1. Checks on box sizes are  $d$ :  $n_z$  and  $n_x$  denote the  $z$  and  $x$  period multiplicity respectively.

		H			O		
Twin	$n_z$	Site1	Site2	Site3	Site1	Site2	Site3
{10 $\bar{1}$ 2}	1	881	-85	-27	1506	-97	180
	2	-54	-129	-6	72	-88	371
	3	-39	-127	-28	-39	-88	364
{10 $\bar{1}$ 1}	1	-6	17	-54	-3	-40	-39
	2	3	26	-60	-40	8	-63
	3	-6	15	-69	-40	17	-69
{11 $\bar{2}$ 1}	1	-149	-151		97	-43	
	2	-154	-127		128	-45	
{11 $\bar{2}$ 2}	1	-129			96		
	2	-114			145		
	$n_x = 2$	-120			479		

for interstitial segregation at mechanical twin boundaries, as opposed to substitutional segregation [129, 72]. O and H segregate to all four TBs except for O to the {11 $\bar{2}$ 2} TB. The sites with largest segregation energies are: for both O and H, site 2 of {10 $\bar{1}$ 2}, site 3 of {10 $\bar{1}$ 1}, and site 2 of {11 $\bar{2}$ 1}; sites 1 of {11 $\bar{2}$ 1} and {11 $\bar{2}$ 2} TBs for H. H segregates more than O to the {10 $\bar{1}$ 2}, {11 $\bar{2}$ 1} and {11 $\bar{2}$ 2} TBs. These tendencies do not depend on the super-cells sizes in  $x$  and  $z$ . Periodic substitutional solutes segregations have been observed experimentally, e.g. in magnesium [129]. We thereafter consider  $1x - 1z$  periodic segregation in the smallest super-cells.

## 5.2.2 Atomic and electronic structures

Let us look at the atomic structures of the TBs, when one solute atom, O or H, is put in its correspondingly most segregating site. They are shown in figure 5.2 where the differences of charge density caused by the solute are also visualised.

Comparing the atomic structures in figures 5.2a and b with figures 5.1b and c, one can say that the {10 $\bar{1}$ 2} and {10 $\bar{1}$ 1} TB structures are well preserved for both O and H cases. The segregated solute at site 2 of the {10 $\bar{1}$ 2} TB respects its symmetrical environment, and site 3 of the {10 $\bar{1}$ 1} TB corresponds to a large octahedral

site, larger than in bulk environment, so that an interstitial atom segregated there does not induce much global structural changes. By contrast, comparison of figures 5.2c.1 and 5.2 5.2c.2 with figure 5.1d.1 shows that the  $\{11\bar{2}1\}$  TB structure is strongly modified by H/O segregation. In the case of O, for instance, the segregated site which was a strongly deformed octahedral site in the pristine  $\{11\bar{2}1\}$  TB structure is nearly restored in shape by the oxygen atom, figure 5.2c.3, at the expense of a strong distortion of the global TB structure.

figures 5.2 also display the charge density differences caused by O or H at the four TBs, as defined by the following equation:

$$\rho_{diff} = \rho_{Ti-solute} - \rho_{Ti} - \rho_{solute}$$

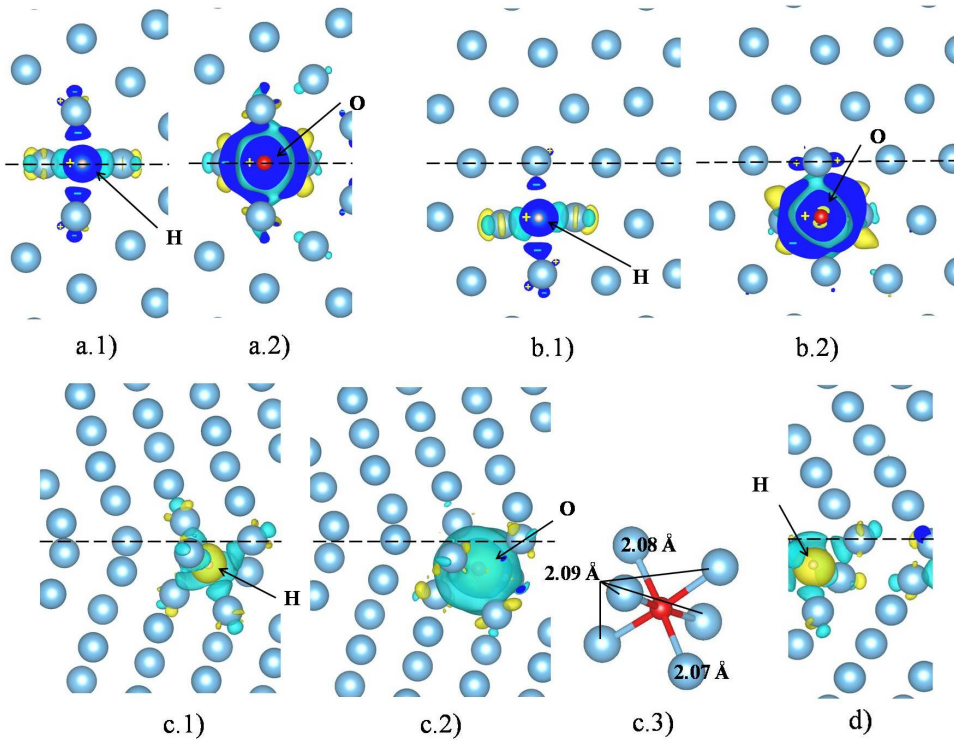


Figure 5.2: Atomic structures and charge density differences of the four TBs,  $\{10\bar{1}2\}$ ,  $\{10\bar{1}1\}$ ,  $\{11\bar{2}1\}$  and  $\{11\bar{2}2\}$ , in presence of one H (pink) or one O (red), as indicated by black arrows, initially put at the corresponding most segregating sites (see table 5.2 together with figures 5.1). figure 5.2c.3 explicitly shows the O atom and its nearly perfectly restored immediate neighbourhood in the  $\{11\bar{2}1\}$  TB, see Section 4.2. Oxygen does not segregate at the  $\{11\bar{2}2\}$  TB, see table 5.2.

In units of one electron per cubic Bohr radius, we chose to represent charge density difference isosurfaces of +0.002, the yellow surfaces, and isosurfaces corresponding to a -0.002 depletion, the blue-green surfaces. For the sake of comparison, the charge density is about 0.035 in the middle of a Ti-Ti metallic bond and excess isosurfaces up to +0.02 exist near the solute nuclei. The isosurfaces are actually

3-dimensional surfaces. The dark blue area correspond to cross s of these +0.002 and -0.002 isosurfaces, with "+" or "-" signs to distinguish them. O solutes are surrounded by much larger excess +0.002 isosurfaces than H solutes, corresponding to larger electronic charge transfer from Ti to O than from Ti to H. This is in good agreement with what can be expected from the electronegativity scaling between Ti, H, and O, viz. roughly 1.4, 2.2 and 3.4 respectively in Pauling units. Said otherwise, the Ti-H and Ti-O bonds do appear to be fairly ionic, with a stronger interaction between Ti and O than between Ti and H.

Figure 5.3 shows a series of total electronic densities of states (DOS) locally projected on a Ti atom first neighbouring a segregating site as indicated before. Besides the differences between the different TBs, the character of the metallic band is always preserved. The O atom has a larger influence than the H atom, in agreement with the previous charge density difference analyses. The local DOS levels in the [-6,0] eV below the Fermi level are slightly lowered, which implies a lowering of the metallic cohesive strength for these Ti atoms. The lost occupied band states are transferred into hybridized  $O_{2p}$ -Ti or  $H_{1s}$ -Ti states located in the [-8,-6] eV range, which correspond to the Ti-O and Ti-H interactions. The stronger effect occurs for the  $\{10\bar{1}2\}$  TB which has the lowest  $x$  and  $z$  periods, thus leading to an electronic band formation in these directions for periodic segregation.

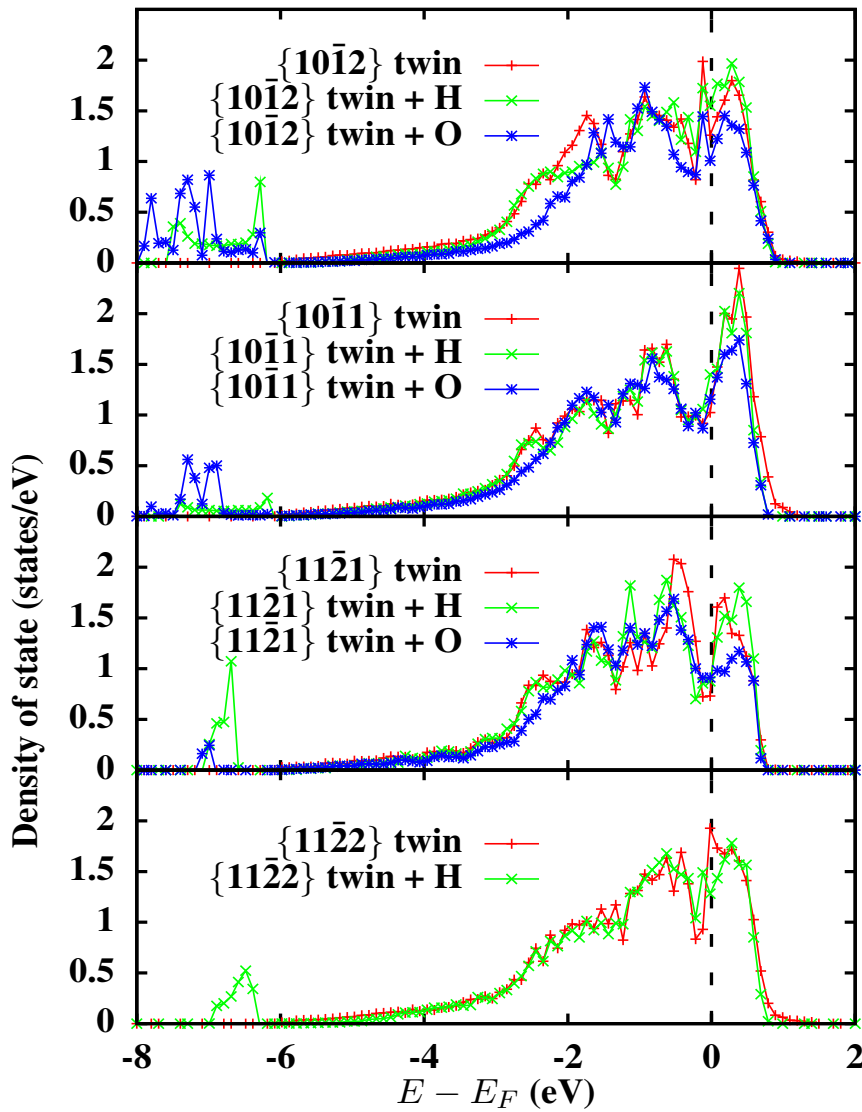


Figure 5.3: Local DOSs on one Ti atom at each of the four TBs, pure Ti TBs, and with one segregated H or O. The Ti atom is first neighbouring a most segregating interstitial site.

## 5.3 TBs under deformation in presence of H/O

### 5.3.1 Twin boundary *c*-axis deformations

In order to investigate and compare the TB behaviour under deformation, series of elongation-contraction tests are carried out along the *c*-axis of the matrix-lower (or Castor, as Pollux' twin in Roman-Greek mythology, to follow Crocker and Bilby and Charles Frank) part of each TB structure shown in figure 5.1, first of all for perfect  $\alpha$ -Ti (null twin). The theoretical stress-strain curves are obtained under both rigid and relaxation modes. The rigid mode means that neither relaxation of

atomic positions nor of the super-cell is allowed. The relaxation mode is equivalent to a total relaxation except for the extended or contracted super-cell dimension [174]. We start with a first analysis of the four TB behaviour in pure titanium, and we will go into further details to examine the effects of segregated H or O in the next section.

Figure 5.4.a corresponds to rigid mode tests which give information about the interplanar binding forces along the  $c$ -axis. We observe only very small variations of such  $c$ -axis rigid ultimate tensile stresses (UTSs, the maximal stress values) compared with the perfect  $\alpha$ -Ti case. The stress-strain curve for the  $\{10\bar{1}1\}$  twin, which has the smallest twinning shear magnitude  $s$ , is very similar to the one in bulk material. The other three TBs have comparable rigid strain-stress curves and, for instance, their equal presence decreases by about 10% the necessary stress to get a  $c$ -axis rigid 20% elongation. It is important to recall, however, that these rigid tests do not take care of the Poisson effect.

Figure 5.4.b corresponds to the full relaxation mode tests. By contrast with the previous mode, the presence of a TB dramatically reduces the relaxed theoretical UTS of the material. The violent drops of stresses actually correspond to the disappearance (failure) of the twin structures. Again, the  $\{10\bar{1}1\}$  twin follows most closely the perfect  $\alpha$ -Ti stress-strain curve, with only a 7% decrease of the UTS, failing at an about 35% elongation. The  $\{11\bar{2}1\}$  TB fails much before, a little before a 20% elongation (with a UTS more than halved), while the  $\{10\bar{1}2\}$  and  $\{11\bar{2}2\}$  TBs fail almost immediately at the beginning of these tensile tests. More deformation tests are realised below elongations of 4% and until 4% contraction. The results are shown in the figure 5.4.c. For these small deformations, pure  $\alpha$ -Ti has a symmetric behaviour under compression or tension. The  $\{10\bar{1}2\}$  and  $\{11\bar{2}2\}$  TB start to fail under 2% contraction and 1.5% elongation. The  $\{10\bar{1}2\}$  TB, which corresponds to the most widely observed twin structure, and the  $\{11\bar{2}2\}$  TB are thus clearly the most prone to failure under  $c$ -axis deformation. This can only be due to their detailed atomic structures and does not seem to be explainable by any parameter given in table 5.1, even if one can notice that they have highest excess energies  $\gamma$  together with relatively small shear magnitudes  $s$ . They embody only two different atoms per periodic TB area, see figure 5.1, when  $\{10\bar{1}1\}$  has four and  $\{11\bar{2}1\}$  has six (allowing for a physically non-zero planar thickness). The  $\{10\bar{1}1\}$  TB has the lowest energy and may thus be thought to be hard to destabilize. Another possible reason for the stability of the  $\{10\bar{1}1\}$  TB may be related to the fact that, according to the Bilby and Crocker scheme, its detwinning requires the shuffling of 7/8 of all its atoms in the core region of a zonal



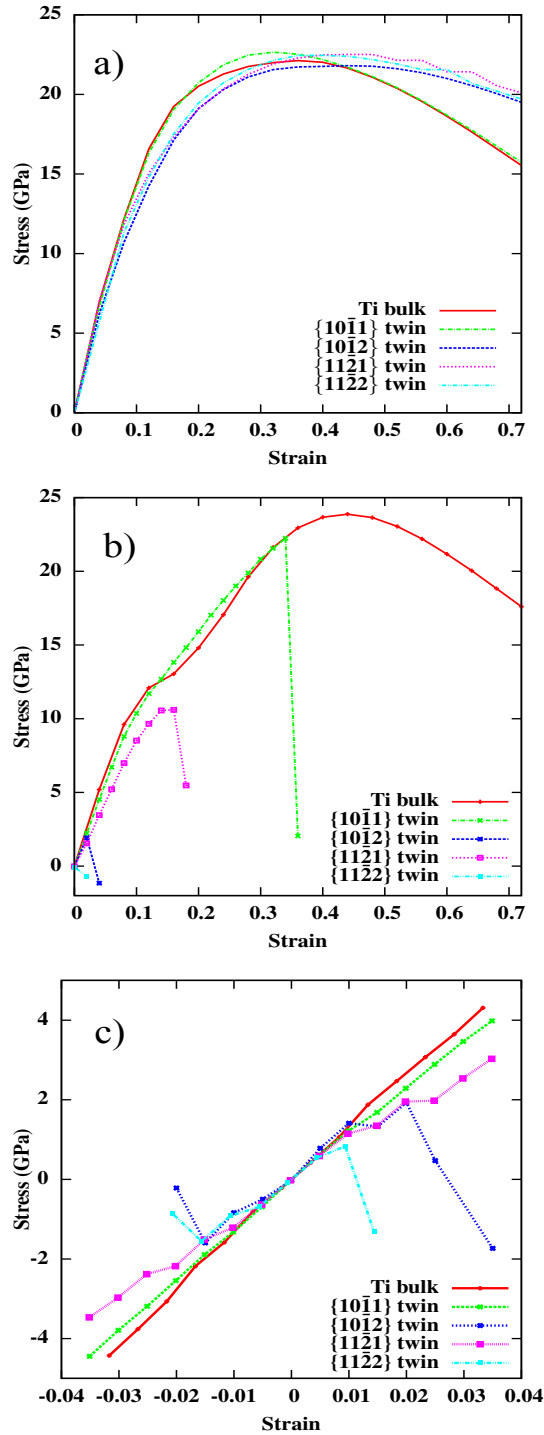


Figure 5.4: Stress-Strain curves for the four *TBs* for theoretical tests along *c*-axis. The figure 5.4.a corresponds to the non-relaxation tensile test; figure 5.4.b corresponds to relaxation tensile test; figure 5.4.c is related to deformation tests between -4% and 4%.

As for the other figures, lines are only guides to the eye.

twin dislocation [6, 81]. Experimentally, the  $\{10\bar{1}2\}$  twin grows more easily than the  $\{10\bar{2}2\}$  twin. Here we considered these twins independently, in independent boxes so that the competition between different twins can not appear. In that

case, it appears that the  $\{10\bar{2}2\}$  bi-crystal behaves qualitatively as the  $\{10\bar{1}2\}$  bi-crystal. The  $\{11\bar{2}1\}$  TB which has twice higher an energy starts some local atomic rearrangement at small deformations but these rearrangement occur mainly in the direction perpendicular to the  $K_1$  plane. As this  $\{11\bar{2}1\}$  twin is a type II twin, shuffling in the direction perpendicular to the shear plane  $S$  is needed to suppress the twin structure. The  $c$  direction being parallel to that shear plane, no perpendicular stress component is directly produced. The  $\{11\bar{2}1\}$  twin structure is thus not easily destabilized, until large deformations when perpendicular shuffling eventually occurs.

### 5.3.2 Twin boundary $c$ -axis deformations in presence of O/H

The same type of numerical tests on tension and compression are carried out with either an O or a H atom at the most segregating site of the considered TBs. Strain-stress results are shown in figure 5.5. The energy variations  $\Delta E$  with respect to zero strain states are also calculated and are shown in figure 5.6. We first consider the  $\{10\bar{1}2\}$  and  $\{11\bar{2}2\}$  TBs, then the more resistant  $\{10\bar{1}1\}$  and  $\{11\bar{2}1\}$ . Figures 5.7 and 5.8 show the evolution of the atomic structures via their charge densities for one TB of each one of these two groups, viz.  $\{10\bar{1}2\}$  and  $\{10\bar{1}1\}$ .

For the  $\{10\bar{1}2\}$  twin, a change in the variation of stress vs. strain takes place between 1.5% and 2.5% of elongation or of contraction for the pure twin structure (figure 5.5.a). This is confirmed by the decreases of the total energy in the same strain ranges  $(+(1.5-2.5\%))$  and  $-(1.5-2.5\%)$  shown in figure 5.6.a. These changes correspond to a local rearrangement of the atoms of the TB plane which gets tilted as indicated by the central tilted dashed line in figure 5.7.1 at a 2.5% elongation. The pure  $\{10\bar{1}2\}$  twin structure thus starts to be lightly destabilised after 1.5% of elongation or of contraction. The stress continues to decrease for elongations beyond 2.5% (figure 5.5.a). A steeper descent of total energy is observed in the same strain range in figure 5.6.a. These stronger changes correspond to a global rearrangement of all the atoms as can be seen in figure 5.7.1 at the 3.5% elongation. In this structure, the up and down parts of the simulated box have the same crystallographic structure as indicated by the rectangular cells in red. The twin structure  $\{10\bar{1}2\}$  has disappeared at a 3.5% elongation.

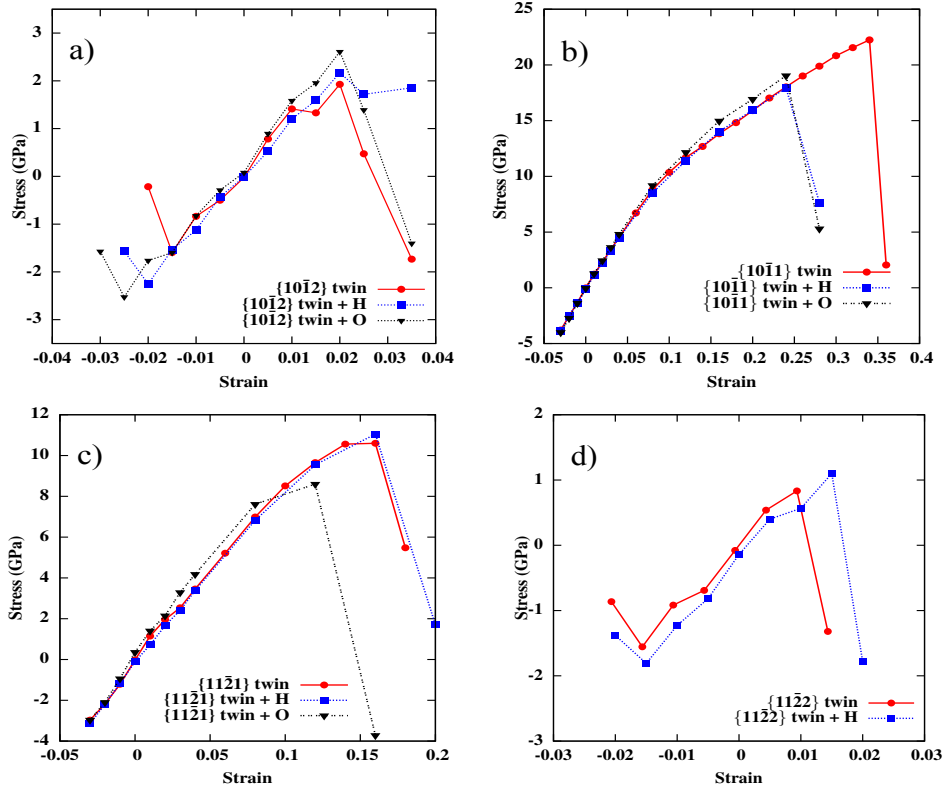


Figure 5.5: *c*-axis stress-strain values for the four TBs for pure Ti, and with segregated O or H, until failures.

These weakening/transforming effects are slightly retarded, by 0.5% to 1%, in presence of a segregated oxygen, which means an enhanced resistance to failure for the  $\{10\bar{1}2\}$  TB. figures 5.5.a and 5.6.a indicate that hydrogen also retards these effects, with a twinned structure still maintained at a 3.5% elongation (figure 5.7.3). Figures 5.5.d and 5.6d indicate a similar effect for O at the  $\{11\bar{2}2\}$  TB.

The O and H solute play a complex role for the  $\{10\bar{1}2\}$  and  $\{11\bar{2}2\}$  twin boundaries because these TBs are very unstable with respect to *c*-axis deformation, at just a few percents of deformation, so that the energy variations at stake are very small and comparable to the segregation energies of O and H, of the order of 0.1 eV (which is also of the same order of magnitude than the TB energies themselves). Although this does not imply that these segregated TBs should become more stable with respect to small *c*-deformation, it is a possibility, and it indeed seems to be the case for these two TBs, especially for H.

Let us now discuss the  $\{10\bar{1}1\}$  and  $\{11\bar{2}1\}$  twin boundaries. Since they have a similar behaviour under *c*-deformation, only the evolution of the atomic structure of  $\{10\bar{1}1\}$  TB under elongation is shown in figure 5.8. Figures 5.5b and 5.5.c show that O decreases the *c*-UTS of these two TBs. H also does it for the  $\{11\bar{2}1\}$ . As

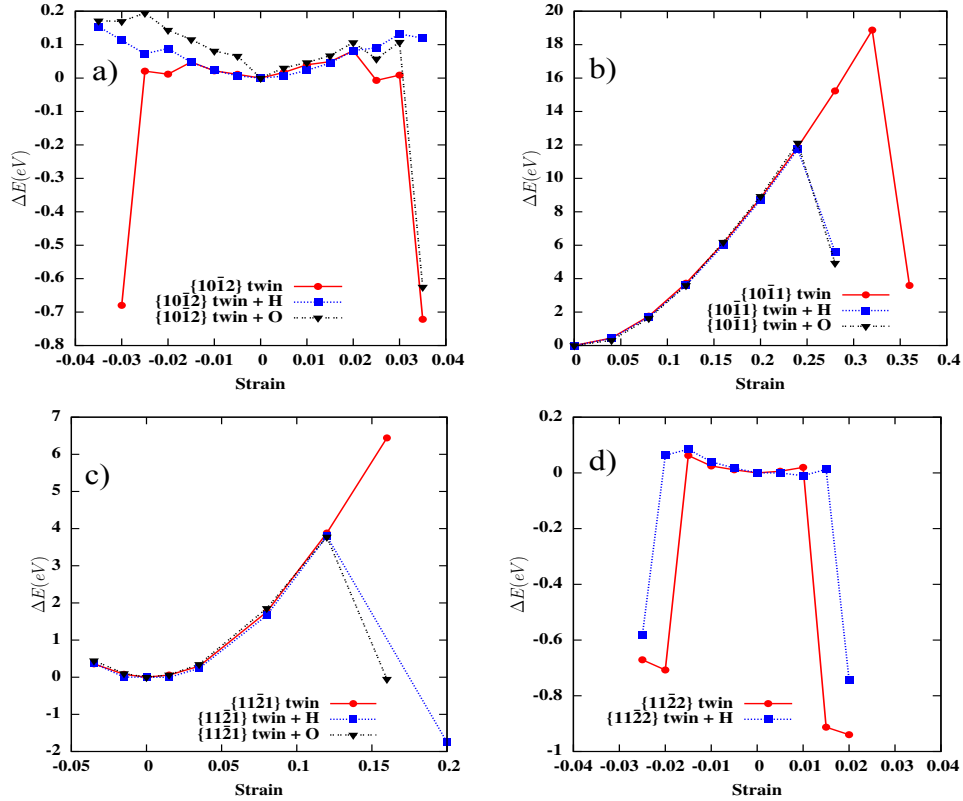


Figure 5.6: Total energy variations versus  $c$ -axis deformation, for pure Ti and with segregated O/H, until failures.

illustrated in figure 5.8 for the  $\{10\bar{1}1\}$  TB, the local atomic perturbation caused by the presence of a segregated O or H slowly increases with the elongation rate, eventually causing an advanced and disruptive failure of the whole structure, albeit still at an important elongation rate corresponding to a very large stress (figures 5.5b and 5.5.c) by experimentalists standards.

One can also see from figures 5.5 that, before failure, the  $c$ -stress-strain curves tend to be stiffer with an O, softer with a H, than in the pure case. Carrying out calculations of the elastic constants on various supercells with simple crystallographic orientations, like a  $3ax3ax2c$  supercell for instance, with one interstitial O or one interstitial H, we similarly found that the presence of an O increases the elastic stiffness coefficient, especially the  $C_{33}$  one by about 10%, while the presence of a H lightly decreases them, with respect to pristine titanium.

### 5.3.3 Twin boundary deformations perpendicular to $K_1$

The strain-stress curves in figure 5.9 are for the case when the Poisson effect is taken into consideration, while those in figure 5.10 do not take it into account. When we consider the Poisson effect, the  $\{10\bar{1}1\}$  TB is always the most stable TB. The stabilities of the  $\{10\bar{1}2\}$  and the  $\{11\bar{2}2\}$  TBs increase to 12%. The lack of  $\eta_1$  direction shear stress in this kind of deformation make these twin structures more stable. The stability of the  $\{11\bar{2}1\}$  TB decreases to 8%. This may be related to a increase of  $z$ -direction stress which is more favorable for shuffling occurring in the  $z$ -direction, knowing that it is the shuffling process which is responsible for  $\{11\bar{2}1\}$  twin structure transtion.

Without consideration of the Poisson effect, the curves in figure 5.10 show that the  $\{10\bar{1}2\}$  TB is the most unstable TB. It fails under a 4% elongation. The three other twin structures remain more stable than the Poisson effect is taken into account (figure 5.9). The constraints on the twin plane dimension probably explain the enhancement of stabilities of these twins.

Three different deformation methods are used in above sections. The  $\{10\bar{1}2\}$  TB is the most unstable under all three methods while  $\{10\bar{1}1\}$  is the most stable. The results obtained from these three deformation methods show that the twin structure stabilities depend on their intrinsic structural characters and also the deformation modes applied.

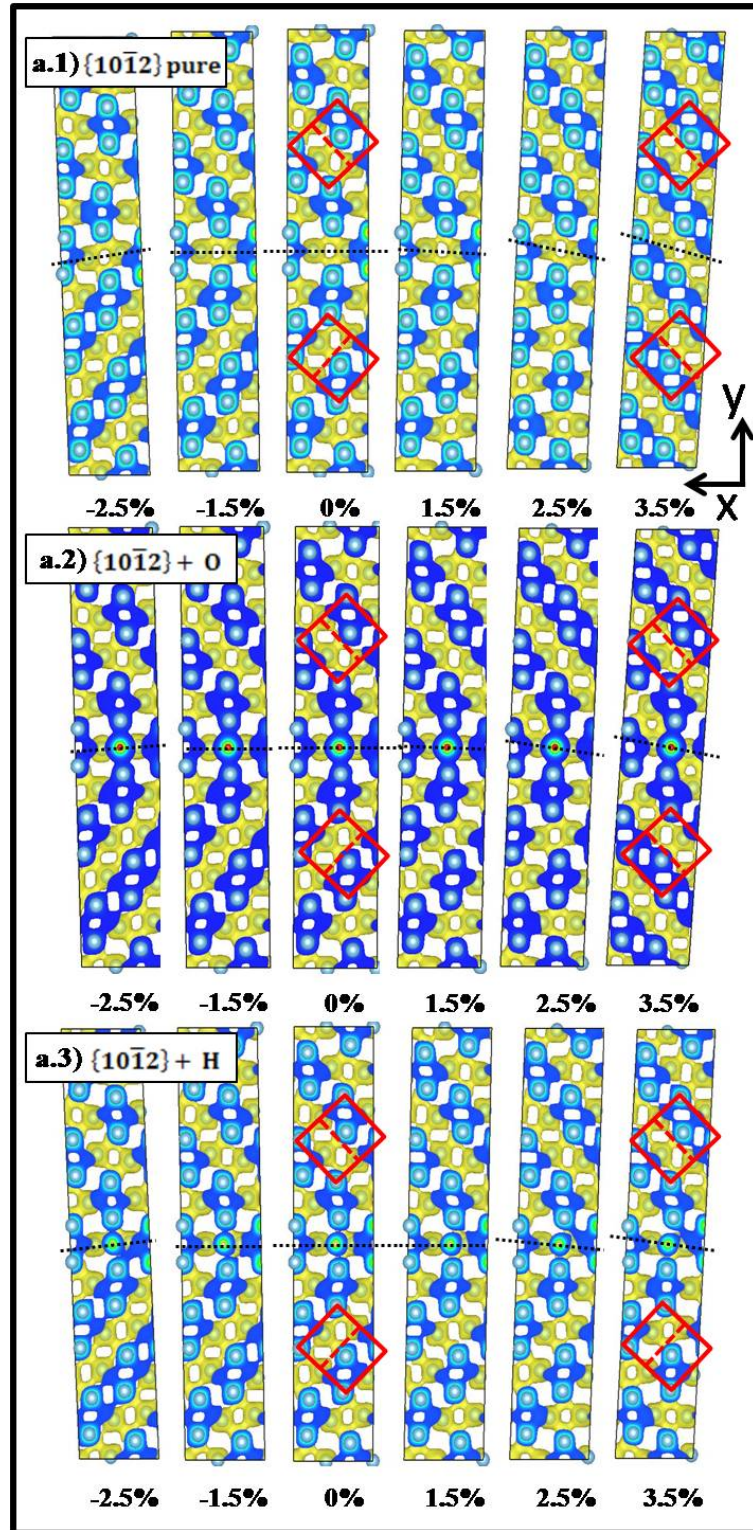


Figure 5.7: Evolution of charge density - atomic structure of  $\{10\bar{1}2\}$  under *c*-axis deformation, pure titanium and with the presence of one segregated *O* (red) or *H* (pink) solute. Isosurfaces of  $0.03 e/(\text{Bohr radius})^3$  are visualised in yellow except when they cut a *z*-plane in blue. Direction *z* is reversed compared to figure 5.1. The light blue contours of *Ti* atoms do not appear when an *O* is segregated because charge density goes up to 1.13 instead of only 0.2 with a *H*. The directions of deformation are the dashed lines in the rectangles in red in the lower parts of the twinned structures at 0% deformation.



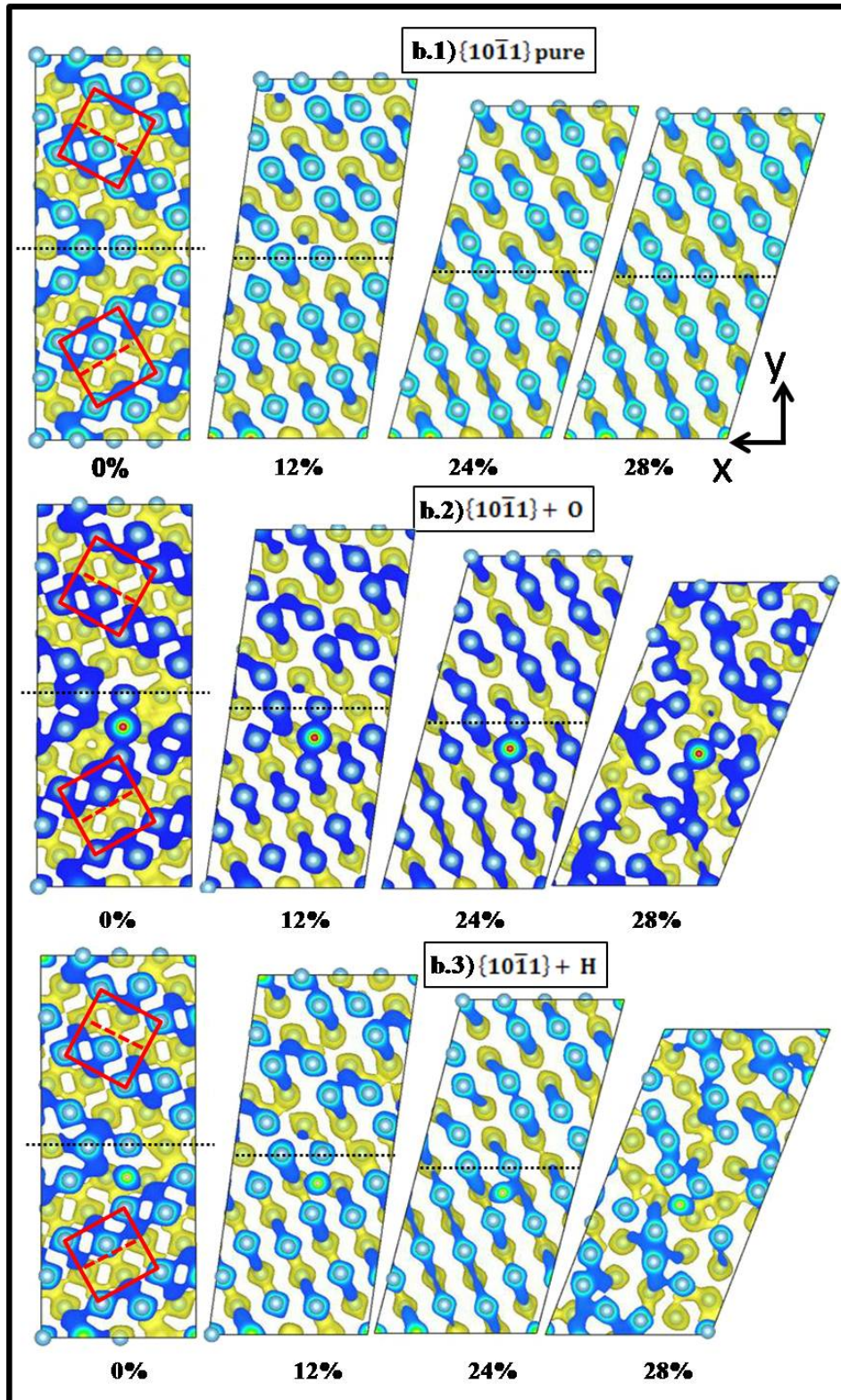


Figure 5.8: Evolution of charge density - atomic structure of  $\{10\bar{1}1\}$  under  $c$ -axis deformation, pure titanium and with the presence of one segregated O (red) or H (pink) solute.

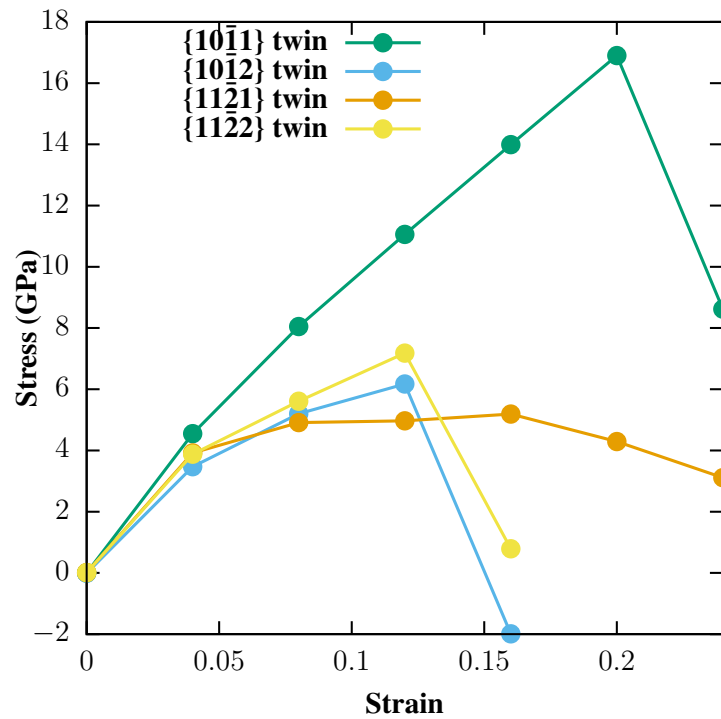


Figure 5.9: Twin boundary under deformations along perpendicular direction in pure Ti

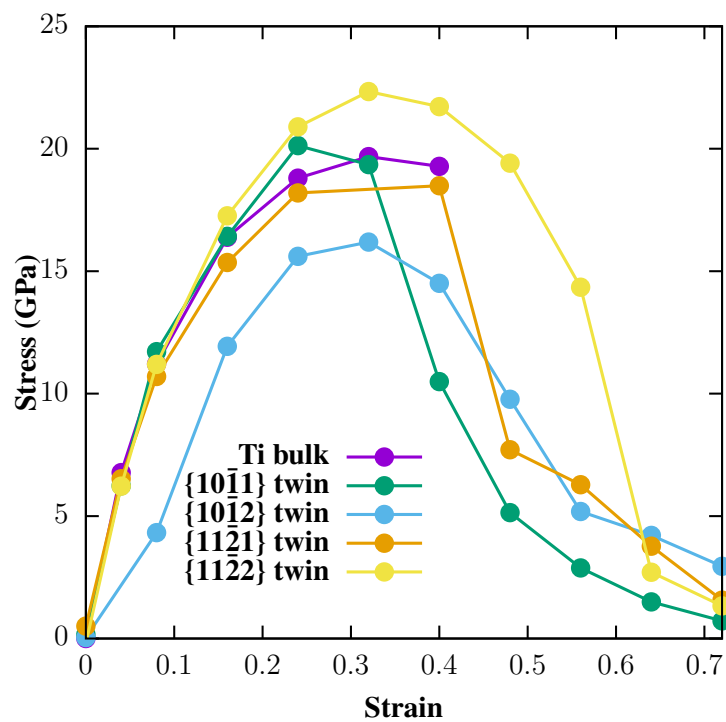


Figure 5.10: Twin boundary under deformations along perpendicular direction with Kozyama method in pure Ti



## 5.4 H and O effects on twinning disconnection $\{10\bar{1}2\}$

In order to calculate the segregation energy of different sites near a TD, 7 sites are chosen. They are visualised in figure 5.11. The most segregating sites on the TB are also shown in figure 5.11

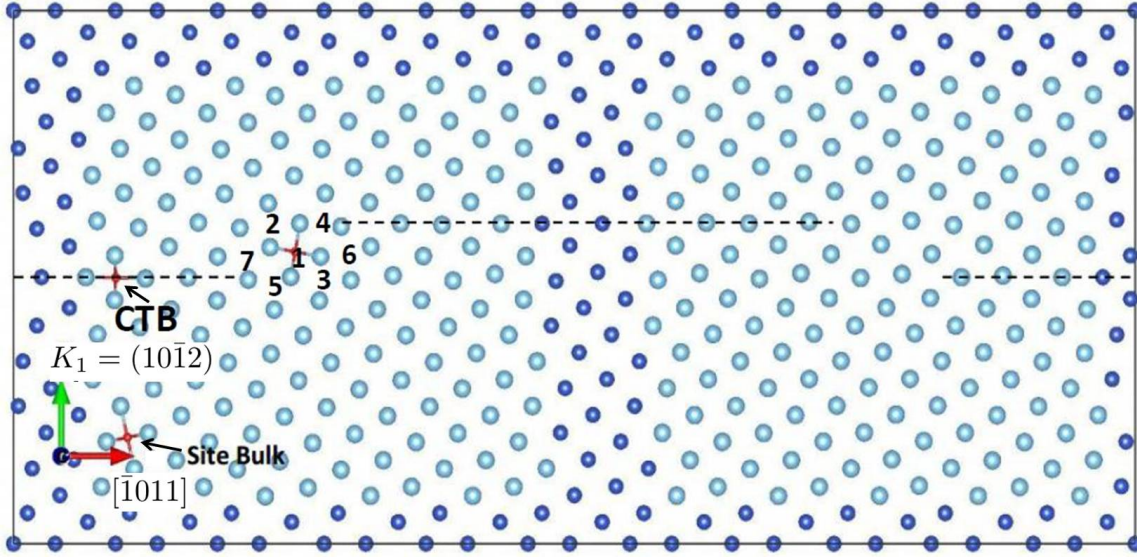


Figure 5.11: The sites near a relaxed TD core.

Their segregation energies compared to the one on TB are shown in the table 5.3.

Table 5.3: Segregation energy of H/O on the site near the TD core. \* Values are obtained from TB segregation calculation

Site	H (meV)	O (meV)
CTB-1	-107	-74
CTB-1*	-85	-97
CTB-2*	881	720
Site 1	-27	249
Site 2	-106	-39
Site 3	-114	-61
Site 4	-112	-69
Site 5	-126	-86
Site 6	28	334
Site 7	-11	193

Compared to segregation energy on TB, H prefers to segregate to the site 3, 4 and 5 near TD core and O prefers to segregate to the site 5. However, the energy differences between the most segregating sites on TBs or near TD core are very small (less than 20 meV), this indicates that H and O may segregate more or less equally to these sites.

Another result come from the table 5.3 is that the site 1, 6, 7, which are in the layer of TD, have a large positive energy which means a large instability of the configuration when a H or O is in these sites, which may change a lot the core structure.

### 5.4.1 Conclusions

It is worth keeping in mind the several limitations of current DFT studies: our elongation tests remain ideal in the sense that they are done at zero K, thus with no atomic dynamics, and our boxes contain no bulk or twin dislocations. They are size limited and correspond to a fifty percent presence of twins. Yet, from our comparative DFT calculations on the twin boundaries associated to the three most commonly found twins in pure  $\alpha$ -titanium, viz.  $\{10\bar{1}2\}$ ,  $\{11\bar{2}1\}$ ,  $\{11\bar{2}2\}$ , together with the  $\{10\bar{1}1\}$  which is also observed under more severe conditions and has the lowest energy, we can conclude that:

1. The energies of these four mechanical TBs is not correlated to any of the crystallographical parameters used to describe them. Neither these energies nor the usually taken shear magnitudes  $s$  explain the frequencies of these twins in deformed titanium. The Kihô Crocker Bilby index  $q$  is also involved. Yet, both  $s$  and  $q$  depend on the twinning mode assumed for a given twin. This has been known for a long time (see for instance Mendelson [191]) and we are just confirming it.
2. For deformations along the  $c$ -axis, all four TBs decrease the theoretical Ultimate Tensile Stress of titanium when all atoms relaxation and the Poisson effect are taken into account. Specially, the most common  $\{10\bar{1}2\}$ , and the  $\{11\bar{2}2\}$  TB structures fail for deformation as low as 1 or 2%.
3. Three different deformation methods are used in above sections. The  $\{10\bar{1}2\}$  TB is always the most unstable while  $\{10\bar{1}1\}$  is the most stable. The results

obtained from the three deformation methods show that the twin structure stabilities depend on their intrinsic structural characters and also the deformation modes applied.

4. Oxygen and hydrogen segregate to all four TBs, except O to  $\{11\bar{2}2\}$ .
5. The presence of segregated oxygen and hydrogen enhances the  $\{10\bar{1}2\}$  and  $\{11\bar{2}2\}$  TB limited stability under *c*-axis deformation. They decrease the  $\{10\bar{1}1\}$  TB stability under high deformation and so does O for the  $\{11\bar{2}1\}$  TB.

A twinning disconnection dipole model is proposed which allows the simulation of a TD in a size limited supercell. TB and TD segregation energies of H and O are measured in the TB and the TD in such a  $\{10\bar{1}2\}$  dipole model. For the TB, the segregation energies are similar to those obtained in case of a pristine TB model, showing the validity of this model. Further segregation energy calculations show that H and O should distribute more or less homogeneously to the TD core and the  $\{10\bar{1}2\}$  TB, with only a slight preference to the TD core although not at the interstitial sites of the atomic layer related to the disconnection step itself.

# Conclusions

In this work, I studied the influences of hydrogen or oxygen solute on extended defects in  $\alpha$ -titanium by ab initio DFT calculations.

A preliminary result is that the  $\alpha$  and  $\omega$  structures of Ti at zero K and zero pressure have almost the same energy, with a slight preference for the  $\omega$  structure, not changed when the zero point vibration energy contribution is taken into account. The energy differences are smaller for zirconium, and at the limits of current DFT calculations. These results have been obtained with PAW\_PBE potentials, with 4 explicit as well as with 12 explicit valence electrons. Although both hexagonal, these structures have different atomic local environment and can be considered as stable at zero pressure, in agreement with experiments (for Ti).

Other main results can be presented in three parts:

— In a first part, the effects of H or O on various properties of titanium without extended defects are first presented. Coupling electronic energy calculations with zero point energy calculations, the octahedral interstitial site is found to be energetically more favorable site for a H as well as for an O atom. Calculations with different H or O concentrations in  $\alpha$ -Ti show that the presence of H increases the hexagonal lattice parameter  $a$ , the  $c/a$  ratio and the cell volume while O has a more anisotropic effect: it increases the  $c/a$  ratio but decreases the lattice parameter  $a$  and the cell volume. The Ti-O bond formation enthalpy is about twice larger than its Ti-H counterpart, pointing to a stronger Ti-O than Ti-H interaction. The presence of H decreases the shear modulus  $G$  and Young's modulus  $E$  of  $\alpha$ -Ti while O has an opposite and stronger effect on  $G$ ,  $E$  and the bulk modulus  $B$ . H increases the  $B/G$  ratio (Pugh's plasticity criterion), thus makes  $\alpha$ -Ti intrinsically more ductile. It also shows a significant non-monotonic influence on  $B/G$  ratio with respect to its concentration, while the presence of oxygen makes  $\alpha$ -Ti less ductile. Using a nudged elastic band method, the migration energy of a H from an octahedral to a tetrahedral site is found to be around 0.5 eV. For an

O octahedral-octahedral site migration, it is more than three times larger along the  $\mathbf{c}$ -axis and twice larger again in the basal plane. The H-H, H-O, and O-O interactions in  $\alpha$ -Ti shows that the O-O interactions are stronger than the H-H interactions. H-O interaction is always attractive. These interaction energies get very small, less than 10 meV, when the solutes are more than 9 Å apart.

— In a second part, stacking-faults (SF) and screw dislocation cores are studied first without, then with H and O. Vitek's  $\gamma$ -surfaces are measured within all the possible slip planes of  $\alpha$ -Ti, namely the basal, prismatic,  $\pi_1$ , and  $\pi_2$  planes. Five SFs are found. Performing further all-direction relaxations on all atoms, only the prismatic and basal SFs remain stable. Two new SFs are found:  $0.57\langle\mathbf{c} + \mathbf{a}\rangle$  on  $\pi_2$  and  $0.215\langle 1\bar{1}02\rangle$  on  $\pi_1$  plane. Together with the  $1/2\langle\mathbf{a}\rangle - 0.0384\langle\bar{1}102\rangle$  SF on  $\pi_1$  plane recently found in the literature, such stable SFs are related to the low formation energy of the  $\{10\bar{1}1\}$  twin boundary. The two new SFs discovered on  $\pi_1$  and  $\pi_2$  plane satisfy the condition for a  $\langle\mathbf{c} + \mathbf{a}\rangle$  screw core dislocation dissociation in a surprising threefold form:  $\langle\mathbf{c} + \mathbf{a}\rangle = 0.57\langle\mathbf{c} + \mathbf{a}\rangle_{\pi_2} + 0.215\langle\bar{1}102\rangle_{\pi_1} + 0.215\langle\mathbf{a}\rangle$ , which may reveal a new cross-slip mechanism in  $\alpha$ -Ti. In order to check this proposition, a  $\langle\mathbf{c} + \mathbf{a}\rangle$  screw core is built. The core tends to spread in the  $\pi_2$ ,  $\pi_1$  and prismatic planes as mentioned above. But a complete 3-part dissociation as supposed is not found, which may mean that such a dissociation is not easily obtainable in limited size simulations from an initially perfect dislocation core. The segregation energies of H and O are measured in different sites near the SFs. H segregates to all SFs, especially to the basal and the  $0.57\langle\mathbf{c} + \mathbf{a}\rangle_{\pi_2}$  ones. O does not segregate to  $0.57\langle\mathbf{c} + \mathbf{a}\rangle_{\pi_2}$ , it almost does not to the prismatic SF and it slightly does to the other SFs. As segregation to SF means a decrease of the SF energy, the presence of O may make the SF formation energetically more difficult, contrary to H case. H and O are then tested with different concentrations in octahedral sites of the core region of the  $\langle\mathbf{a}\rangle$  screw dislocation. H strongly segregates to the core region with segregation energies varying up to 300 meV. O's segregation energies are small, below 60 meV. The strong segregation energies of H in multiple sites near core region suggest that a Cottrell atmosphere may form near the dislocation core. Both H and O in these sites can change the metastable gliding prismatic dissociation to a  $\pi_1$  plane or a prism- $\pi_1$  plane mixed configuration. The Peierls energy barriers are measured with H or O at different sites of the  $\langle\mathbf{a}\rangle$  screw dislocation core in order to estimate these solute effects on its glide. The Peierls energy barrier is extremely increased when an O is present in the core position, more than ten times higher than the barrier for  $\pi_1$  plane glide. A cross-slip must happen in this case and the dislocation glide is blocked in the pyramidal plane

( $\pi_1$ ). This could explain the oxygen induced dynamic strain ageing phenomena. Hydrogen segregates more strongly to the core of the  $\langle \mathbf{a} \rangle$  screw dislocation than oxygen and probably more rapidly since it diffuses faster. Yet, it is much less present in Ti than oxygen (probably ten times at ambient temperature, about four times at elevated temperature, e.g. 600°C, but with an O content up to 33at.%) and it has a lightly attractive interaction with oxygen. One may thus understand that it has a complex but probably softening role on  $\alpha$ -titanium in presence of oxygen.

— Finally, twin boundary (TB) structures and energies, TB deformations, and a twinning disconnection (TD) are studied, first without then with H and O. Among the four mechanical TBs investigated, viz.  $\{10\bar{1}2\}$ ,  $\{10\bar{1}1\}$ ,  $\{11\bar{2}1\}$  and  $\{11\bar{2}2\}$  TBs, the  $\{10\bar{1}1\}$  TB has the smallest energy while the  $\{11\bar{2}2\}$  has the largest one. For deformations along the  $\langle \mathbf{c} \rangle$ -axis, all four TBs decrease the theoretical ultimate tensile stress of titanium. The structures of most commonly found TB, viz.  $\{10\bar{1}2\}$ , and of the  $\{11\bar{2}2\}$  TB fail for deformation as low as 1% or 2%. The  $\{11\bar{2}1\}$  and the  $\{10\bar{1}1\}$  TBs are much more resistant. Three different deformation methods proposed in the literature are tested. The results show that the TB structural stabilities depend not only on their intrinsic characters at the atomistic level but also on the deformation mode applied. H and O segregate to all four TBs, except O to  $\{11\bar{2}2\}$ . The presence of segregated oxygen and hydrogen enhances the  $\{10\bar{1}2\}$  and  $\{11\bar{2}2\}$  TB limited stability under  $\langle \mathbf{c} \rangle$ -axis deformation. They decrease the  $\{10\bar{1}1\}$  TB stability under high deformation and so does O for the  $\{11\bar{2}1\}$  TB. A twinning disconnection dipole model is proposed which allows the simulation of a TD in a size limited supercell. TB and TD segregation energies of H and O are measured in the TB and the TD in such a  $\{10\bar{1}2\}$  dipole model. For the TB, the segregation energies are similar to those obtained in case of a pristine TB model, showing the validity of this model. Further segregation energy calculations show that H and O should distribute more or less homogeneously to the TD core and the  $\{10\bar{1}2\}$  TB, with only a slight preference to the TD core although not at the interstitial sites of the atomic layer related to the disconnection step itself.



# Bibliography

- [1] A.D. McQuillan, M.K. McQuillan, Titanium, Butterworths, London, 1956
- [2] G. Lütjering, J.C. Williams, Titanium, 2nd Ed., Springer, Berlin, 2007
- [3] D. Banerjee, J.C. Williams, Perspectives on Titanium Science and Technology, Acta Mater. 61 (2013) 844-879
- [4] T.M. Flynn, Cryogenic Engineering, 2nd Ed., Dekker, New York, 2004
- [5] P.G. Partridge, The crystallography and deformation modes of hexagonal close-packed metals, Metallurgical reviews 12 (1967) 169-194
- [6] M.H. Yoo, Slip, Twinning, and Fracture in Hexagonal Close-Packed Metals, Metallurgical Transactions A 12 (1981) 409-418
- [7] Biget, M. P., and G. Saada, Low-temperature plasticity of high-purity  $\alpha$ -titanium single crystals, Phil. Mag. A 59 (1989) 747-757
- [8] H. Conrad, Effect of interstitial solutes on the strength and ductility of titanium, Progress in Materials Science 26 (1981) 123-403
- [9] S. Naka, L.P. Kubin, C. Perrier, The plasticity of titanium at low and medium temperatures, Phil. Mag. A 63 (1991) 1035-1043
- [10] Q. Yu, L. Qi, T. Tsuru, R. Traylor, D. Rugg, J.W. Morris Jr., M. Asta, D.C. Chrzan, A.M. Minor, Origin of dramatic oxygen solute strengthening effect in titanium, Science 347 (2015) 635-639
- [11] B. Barkia, Viscoplasticité à l'ambiante du titane en relation avec ses teneurs en oxygène et hydrogène, PhD thesis, École polytechnique, 2014
- [12] P.G. Oberson, Z.W. Wyatt, S. Ankem, Modeling interstitial diffusion controlled twinning in alpha titanium during low-temperature creep, Scripta Materialia 65 (2011) 638-641



- [13] D.S. Shih, M.I. Robertson, H.K. Birnbaum, Hydrogen embrittlement in  $\alpha$  Titanium: in situ TEM studies, *Acta Met.* 36 (1988) 111-124
- [14] O.N. Senkov, J.J. Jonas, Effect of Phase Composition and Hydrogen Level on the Deformation Behavior of Titanium-Hydrogen Alloys, *Met. Mat. Trans.* 27 (1996) 1869-1876
- [15] J.P. Couzinié, B. Barkia, V. Doquet, I. Guillot, Influence of Hydrogen and Oxygen Content on the Mechanical Behavior of Zr at 300°C and Ti at 20°C, *Int. Hydrogen Conference*, Jackson Lake: United States (2012) chap. 44
- [16] B. Barkia, V. Doquet, J.P. Couzinié, I. Guillot, Room-temperature creep and stress relaxation in commercial purity titanium - Influence of the oxygen and hydrogen contents on incubation phenomena and aging-induced rejuvenation of the creep potential, *Mat. Sci. Eng. A* 264 (2015) 79-89
- [17] F.H. Beck, *Effect of Hydrogen on the Mechanical Properties of Titanium and Its Alloys*, Ohio State, University of Columbus, 1975
- [18] G.Y. Gao, S.C. Dexter, Effect of hydrogen on creep behavior of Ti-6Al-4V alloy at room temperature, *Met. Trans. A* 18 (1987) 1125-1130
- [19] H.K. Birnbaum, P. Sofronis, Hydrogen-enhanced localized plasticity mechanism for hydrogen-related fracture, *Mat. Sci. Eng. A*, Vol 176, (1994), Pages 191-202
- [20] A. Marchenko, *Rupture différée dans le titane non allié en tenant compte des teneurs en hydrogène et en oxygène*, PhD Thesis at École des Mines Paris, 2015
- [21] F. Mignot, V. Doquet, C. Sarrazin-Baudoux, Contributions of internal hydrogen and room-temperature creep to the abnormal fatigue cracking of Ti6246 at high  $K_{max}$ , *Materials Science and Engineering A* 380 (2004) 308-319
- [22] O.N. Senkov, J.J. Jonas, Dynamic strain aging and hydrogen-induced softening in alpha titanium, *Met. Mat. Trans. A* 27 (1996) 1877-1887
- [23] E. Clouet, Screw dislocation in zirconium: An *ab initio* study, *Phys. Rev. B* 86 (2012) 144104 (11pp)
- [24] E. Clouet, D. Caillard, N. Chaari, F. Onimus, D. Rodney, Dislocation locking versus easy glide in titanium and zirconium, *Nat. Mat.* 14 (2015) 931-936

- [25] D. Clayton, Handbook of Isotopes in the Cosmos. Hydrogen to Gallium. Cambridge University Press, Cambridge, 2003
- [26] S.K. Sikka, Y.K. Vohra, R. Chidambaram, Omega phase in materials, Prog. Mater. Sci. 27 (1982) 245-310
- [27] Y.K. Vohra, P.T. Spencer, Novel  $\gamma$ -phase of Titanium Metal at Megabar Pressures, Phys. Rev. Lett. 86 (2001) 3068-3071
- [28] Y. Akahama, H. Kawamura, T. Le Bihan, New  $\delta$  (Distorted-bcc) Titanium at 220 GPa, Phys. Rev. Lett. 87 (2001) 275503 (4pp)
- [29] Z.G. Mei, S. Shang, Y. Wang, Z.K. Liu, Density-functional study of the pressure-induced phase transition in Ti at zero Kelvin, Phys. Rev. B 79 (2009) 134102 (6pp)
- [30] L. Huang, B. Grabowski, E. McEniry, D.R. Trinkle, J. Neugebauer, Importance of coordination number and bond length in titanium revealed by electronic structure investigations, Phys. Status Solidi B 252 (2015) 1907-1924
- [31] A. Dewaele, V. Stutzmann, J. Bouchet, F. Bottin, F. Occelli, M. Mezouar, High pressure-temperature phase diagram and equation of state of titanium, Phys. Rev. B 91 (2015) 134108 (10pp)
- [32] V. Trinité, Etude théorique des phases du titane, PhD Thesis at the École polytechnique, 2008
- [33] J. Zhang, Y. Zhao, R.S. Hixson, G.T. Gray III, L. Wang, W., Utsumi, S. Hiroki, H. Takanori, Experimental constraints on the phase diagram of titanium metal, J. Phys. Chem. Solids 69 (2008) 2559-2563
- [34] S. Nishitani, H. Kawabe, M. Aoki, First-principles calculations on bcc-hcp transition of titanium, Mater. Sci. Eng., A 312 (2001) 77-83
- [35] E.Yu. Tonkov, High Pressure Phase transformations: A Handbook, vol. 2, Gordon and Breach Science, Philadelphia, 1992
- [36] G.W. Groves, A. Kelly, Independent Slip Systems in Crystals, Phil. Mag. 8 (1963) 877-887
- [37] J.P. Hirth, J. Lothe, Theory of Dislocations in Crystals, 2nd Edition, Wiley, New York, 1982

- [38] A. Kelly, K. Knowles, *Crystallography and Crystal Defects*, 2nd Edition, Wiley, New York, 2012
- [39] M. Battaini, *Deformation behavior and twinning mechanisms of commercially pure titanium alloys*, PhD thesis, Monash University, 2008
- [40] A. Roth, *Étude multi-échelles de l'hétérogénéité et de l'anisotropie de la déformation plastique : cas des aciers TWIP et du Ti- $\alpha$* . PhD thesis, Université de Lorraine, 2014
- [41] M. Ghazisaeidi, D. Trinkle, Core structure of a screw dislocation in Ti from density functional theory and classical potentials, *Acta Mater.* 60 (2012) 1287-1292
- [42] X. Wu, R. Wang, S. Wang, Generalized-stacking-fault energy and surface properties for HCP metals: A first-principles study (with wrong indices!!!) *Appl. Surf. Sci.* 256 (2010) 3409-3412
- [43] M. Benoit, N. Tarrat, J. Morillo, Density functional theory investigations of titanium  $\gamma$ -surfaces and stacking faults, *Modelling Simul. Mater. Sci. Eng.* 21 (2013) 015009
- [44] N. Chaari, E. Clouet, D. Rodney, First-Principle Study of Secondary Slip in Zirconium, *Phys. Rev. Lett.* 112 (2014) 075504 (5pp)
- [45] C. Domain, *Simulations atomiques ab initio des effets de l'hydrogène et de l'iode dans le zirconium*, PhD Thesis, Université Lille 1, 2002
- [46] Y. Minonishi, S. Ishioka, M. Koiwa, S. Morozumi, M. Yamaguchi, The core structure of  $1/3\langle\bar{1}\bar{1}23\rangle\{11\bar{2}2\}$  screw dislocations in h.c.p. metals, *Phil. Mag. A* 44 (1981) 1225-1237
- [47] J.R. Morris, J. Scharff, K.M. Ho, Y.Y. Ye, M.H. Yoo, Prediction of a  $\{1122\}$  hcp stacking fault using a modified generalized stacking-fault calculation, *Phil. Mag. A* 76 (1997) 1065-1077
- [48] Y. Minonishi, S. Ishioka, M. Koiwa, S. Morozumi, M. Yamaguchi, The core structure of  $1/3\langle\bar{1}\bar{1}23\rangle\{11\bar{2}2\}$  edge dislocations in h.c.p. metals, *Phil. Mag. A* 43 (1981) 1017-1026
- [49] Y. Minonishi, S. Ishioka, M. Koiwa, S. Morozumi, M. Yamaguchi, The core structure of a  $1/3\langle\bar{1}\bar{1}23\rangle\{11\bar{2}2\}$  edge dislocation under applied shear stresses in an h.c.p. metals, *Phil. Mag. A* 45 (1982) 835-850

- [50] Y. Minonishi, S. Ishioka, M. Koiwa, S. Morozumi, Motion of a  $1/3\langle\bar{1}\bar{1}23\rangle\{11\bar{2}2\}$  screw dislocation in a model h.c.p. lattice, *Phil. Mag. A* 46 (1982) 761-770
- [51] D.J. Bacon, M.H. Liang, Computer simulations of dislocation cores in h.c.p. metals. I. Interatomic potentials and stacking fault stability, *Phil. Mag. A* 53 (1986) 163-179
- [52] D.J. Bacon, M.H. Liang, Computer simulations of dislocation cores in h.c.p. metals. II. Core structure in unstressed crystals, *Phil. Mag. A* 53 (1986) 181-204
- [53] M.H. Liang, D.J. Bacon, Computer simulations of dislocation cores in h.c.p. metals. III. The effect of applied shear strain, *Phil. Mag. A* 53 (1986) 205-220
- [54] J.R. Morris, K.M. Ho, K.Y. Chen, G. Rengarajan, M.H. Yoo, Large-scale atomistic study of core structures and energetics of  $\langle\mathbf{c}+\mathbf{a}\rangle\{11\bar{2}2\}$  dislocations in hexagonal close packed, *Model. Simul. Mater. Sci. Eng.* 8 (2000) 25-35
- [55] M. H. Yoo, J. R. Morris, K. M. Ho, S. R. Agnew, Nonbasal Deformation Modes of HCP Metals and Alloys: Role of Dislocation Source and Mobility, *Metal. Mat. Trans. A* 33 (2002) 813-822
- [56] V. Vitek, Intrinsic Stacking Faults in Body-centred Cubic Crystals, *Phil. Mag.* 28 (1968) 773-786
- [57] N. Tarrat, M. Benoit, J. Morillo, Core structure of screw dislocations in hcp Ti: an ab initio DFT study, *Int. J. Mat. Res.* 100 (2009) 329-332
- [58] V. Bulatov, W.Cai, Computer simulation of dislocation, Oxford university press, Oxford, 2006
- [59] B. Legrand, Relations entre la structure électronique et la facilité de glissement dans les métaux hexagonaux compacts, *Phil. Mag. A* 49 (1984) 171-174
- [60] B. Legrand, Structure du cœur des dislocations vis  $1/3\langle 1120\rangle$  dans le titane, *Phil. Mag. A* 52 (1985) 83-97
- [61] N. Tarrat, M. Benoit, D. Caillard, L. Ventelon, N. Combe, J. Morillo, Screw dislocation in hcp Ti: DFT dislocation excess energies and metastable core structures, *Modelling Simul. Mater. Sci. Eng.* 22 (2014) 055016

- [62] S. Farenc, D. Caillard, A. Couret, An in situ study of prismatic glide in  $\alpha$  titanium at low temperatures, *Acta Metall. Mater.* 41 (1993) 2701-2709
- [63] R. Peierls, The size of a dislocation, *Proc. Phys. Soc.* 52 (1940) 34-37
- [64] F.R.N. Nabarro, Dislocations in a simple cubic lattice, *Proc. Phys. Soc.* 59 (1947) 256-272
- [65] D. Caillard, J.L. Martin, *Thermally Activated Mechanisms in Crystal Plasticity*, Pergamon Press, 2003
- [66] N. Itoh, M. Ogaya, S. Ishiyama, T. Matsushita, Y. Hayashi, M. Koike, Press formability of commercial pure titanium at warm working temperatures. *Titanium 80, Science and Technology, Proceedings of the 4th International Conference on Titanium, Vol. 4* (1980) 2523-2529
- [67] M.-J. Philippe, C. Esling, B. Hocheid, Role of Twinning in Texture Development and in Plastic Deformation of hexagonal Materials, *Textures and Microstructures* 7 (1988) 265-301.
- [68] Y.B. Chun, S.H. Yu, S.L. Semiatin, S.K. Hwang, Effect of deformation twinning on microstructure and texture evolution during cold rolling of CP-titanium, *Mater. Sci. Eng. A* 398 (2005) 209-219
- [69] A.A. Salem, S.R. Kalidindi, R.D. Doherty, Strain hardening of titanium: role of deformation twinning, *Acta Mater.* 51 (2003) 4225-4237
- [70] Ph. Komninou, Th. Kehagias, Th. Karakostas, J.G. Antonopoulos, T. Braisaz, G. Nouet, A. Serra, Electron Microscopy of Defects in Hexagonal Materials, in *Multiscale Phenomena in Plasticity*, J. Lépinoux et al. (eds.), Kluwer 2000 (pp. 215-226)
- [71] N.E. Paton, W.A. Backofen, Plastic Deformation of Titanium at Elevated Temperatures, *Met. Trans.* 1 (1970) 2839-2847
- [72] A. Kumar, J. Wang, C.N. Tomé, First-principles study of energy and atomic solubility of twinning-associated boundaries in hexagonal metals, *Acta Mater.* 85 (2015) 144-154 (with a very distorted figure 1, and a wrongly noted z for that figure.)
- [73] J.R. Morris, Y.Y. Kee, M.H. Yoo, First-principle examination of the  $(10\bar{1}2)$  twin boundary in hcp metal, *Phil. Mag.* 85 (2005) 233-238.

- [74] M. Ghazisaeidi, D.R. Trinkle, Interaction of oxygen interstitials with lattice faults in Ti, *Acta Mater.* 76 (2014) 82-86
- [75] N. Lane, S.I. Simak, A.S. Mikhaylushkin, I.A. Abrikosov, L. Hultman, M.W. Barsoum, First-principles study of dislocations in hcp metals through the investigation of the  $(11\bar{2}1)$  twin boundary, *Phys. Rev. B* 84 (2011) 184101 (7pp)
- [76] J.R. Morris, Y.Y. Kee, M. Ho, C.T. Chan, M.H. Yoo, Structures and energies of compression twin boundaries in hcp Ti and Zr, *Phil. Mag. A* 72 (1995) 751-753
- [77] Y.C. Wang, D.H. Ping, D.X. Li, H.Q. Ye, A high-resolution transmission electron microscopy study of the  $\{10\bar{1}1\}$  twin-boundary structure in alpha-Ti, *Phil. Mag. Lett.* 74 (1996) 367-373
- [78] S. Lay, G. Nouet, HREM Study of the  $(01\bar{1}2)$  Twin Interface in Zinc, *Phil. Mag.* 70 (1994) 261-275
- [79] Th. Braisaz, P. Ruterana, G. Nouet, A. Serra, High-resolution electron microscopy study of the  $(10\bar{1}2)$  twin and defects analysis in deformed polycrystalline alpha titanium, *Phil. Mag. Lett.* 74 (1996) 331-338
- [80] A. Serra, D.J. Bacon, Computer simulation of twin boundaries in the h.c.p. metals, *Phil. Mag. A* 54 (1986) 793-804
- [81] A. Serra, R.C. Pond, D.J. Bacon, Computer simulation of the structure and mobility of twinning dislocations in H.C.P. metals, *Acta metall. mater.* 39 (1991) 1469-1480
- [82] I.J. Beyerlein, X.Zhang, A. Misra, Growth Twins and Deformation Twins in Metals, *Annu. Rev. Mater. Res.* 44 (2014) 329-363
- [83] R.J. McCabe, G. Proust, E.K. Cerreta, A. Misra, Quantitative analysis of deformation twinning in zirconium, *Int. J. Plast.* 25 (2009) 454-472
- [84] I.J. Beyerlein, J. Wang, M.R. Barnett, C.N. Tomé, Double twinning mechanisms in magnesium alloys via dissociation of lattice dislocations, *Proc. R. Soc. A* 468 (2012) 1496-1520
- [85] M. Knezevic, I.J. Beyerlein, D.W. Brown, T.A. Sisneros, C.N. Tomé, A polycrystal plasticity model for predicting mechanical response and texture evolution during strain-path changes: application to beryllium, *Int. J. Plast.* 49 (2013) 185-198

- [86] H. Kihô, The Crystallographic Aspect of the Mechanical Twinning in Metals, *J. Phys. Soc. Japan* 9 (1954) 739-747
- [87] B.A. Bilby, A.G. Crocker, The Theory of the Crystallography of Deformation Twinning, *Proc. R. Soc. A* 288 (1965) 240-255
- [88] J.W. Christian, S. Mahajan, Deformation twinning, *Prog. Mater. Sci.* 39 (1995) 1-157
- [89] H.A. Khater, A. Serra, R.C. Pond, Atomic shearing and shuffling accompanying the motion of twinning disconnections in Zirconium, *Phil. Mag.* 93 (2013) 1279-1298
- [90] E. Orowan, Dislocations and mechanical properties, in *Dislocations in Metals*, ed. M Cohen, Am. Inst. Mining Metall. Eng., New York, 1954, pp.69-195
- [91] S. Mendelson, Dislocation dissociations in hcp metals, *J. Appl. Phys.* 41 (1970) 1893-1910
- [92] J. Wang, R.G. Hoagland, J.P. Hirth, L. Capolungo, I.J. Beyerlein, C.N. Tomé, Nucleation of a  $\{10\bar{1}2\}$  twin in hexagonal-close-packed crystals, *Scr. Mater.* 61 (2009) 903-906
- [93] N. Thompson, D.J. Millard, Twin formation in cadmium, *Phil. Mag.* 43 (1952) 422-440
- [94] A. Le Lann, A. Dubertret, A development of Kronbergs model for  $\{10\bar{1}2\}$  twins in H.C.P. metals. Extension to  $\{11\bar{2}2\}$  twins, *Phys. Status Solidi* 51 (1979) 497-507
- [95] J. Wang, S.K. Yadav, J.P. Hirth, C.N. Tomé, I.J. Beyerlein, Pure-shuffle nucleation of deformation twins in hexagonal-close-packed metals, *Mater. Res. Lett.* 1 (2013) 126-132
- [96] A. Serra, D.J. Bacon, A new model for  $\{10\bar{1}2\}$  twin growth in HCP metals, *Phil. Mag.* 73 (1996) 333-343
- [97] B. Xu, L. Capolungo, D. Rodney, On the importance of prismatic/basal interfaces in the growth of  $\{10\bar{1}2\}$  twins in hexagonal close-packed crystals, *Scr. Mater.* 68 (2013) 901-904
- [98] A. Ostapovets, A. Serra, Characterization of the matrix-twin interface of a  $\{10\bar{1}2\}$  twin during growth, *Phil. Mag.* 94 (2014) 2827-2839

- [99] L. Capolungo, I.J. Beyerlein, C.N. Tomé, Slip-assisted twin growth in hexagonal close-packed metals, 60 (2009) 32-35
- [100] A. Serra, D.J. Bacon, R.C. Pond, The Crystallography and Core Structure of Twinning Dislocations in H.C.P. Metals, *Acta metall.* 36 (1988) 3183-3203
- [101] R.C. Pond, D.J. Bacon, A. Serra, Interfacial structure of  $\{10\bar{1}1\}$  twins and twinning dislocations in titanium, *Phil. Mag. Lett.* 71 (1995) 275-284
- [102] A. Serra, D. J. Bacon, On the Generation of Twinning Dislocations in HCP Twin Boundaries, *Materials Science Forum*, 207-209 (1996) 553-556
- [103] A. Serra, D.J. Bacon, Modelling the motion of  $\{11\bar{2}2\}$  twinning dislocations in the HCP metals, *Mat. Sci. Eng. A* 400-401 (2005) 496-498
- [104] A. Serra, D.J. Bacon, Computer simulation of screw dislocation interactions with twin boundaries in H.C.P. metals, *Acta metall. mater.* 43 (1995) 4465-4481
- [105] A. Serra, D.J. Bacon, Interaction of a moving  $\{10\bar{1}2\}$  twin boundary with perfect dislocations and loops in a hcp metal, *Phil. Mag.* 90 (2010) 845-861
- [106] M. Ghazisaeidi, L.G. Hector Jr., W.A. Curtin, First-principles core structures of  $\langle c+a \rangle$  edge and screw dislocations in Mg, *Acta Materialia* 80 (2014) 278-287
- [107] R. A. Johnson and J. R. Beeler, in *Interatomic Potentials and Crystalline Defects*, edited by J. K. Lee, AIME, New York, 1981 (pp. 165-177)
- [108] G. V $\acute{e}$ rit $\acute{e}$ , C. Domain, C.-C. Fu, P. Gasca, A. Legris, F. Willaime, Self-interstitial defects in hexagonal close packed metals revisited: Evidence for low-symmetry configurations in Ti, Zr, and Hf, *Phys. Rev. B* 87 (2013) 134108 (6pp)
- [109] R. G. Hennig, D. R. Trinkle, J. Bouchet, S. G. Srinivasan, R. C. Albers, and J. W. Wilkins, Impurities block the  $\alpha$  to  $\omega$  martensitic transformation in titanium, *Nat. Mat.* 4 (2005) 129-133
- [110] H.H. Wu, D.G. Trinkle, Direct diffusion through interpenetrating networks: oxygen in titanium, *Phys. Rev. Lett.* 107 (2011) 045504
- [111] R. Khoda-Bakhsh, D.K. Ross, Determination of the hydrogen site occupation in the  $\alpha$  phase of zirconium hydride and in the  $\alpha$  and  $\beta$  phases of titanium hydride by inelastic neutron scattering, *J. Phys. F* 12 (1982) 15-24



- [112] R. Hempelmann, D. Richter, B. Strizker, Optic phonon modes and superconductivity in  $\alpha$  phase (Ti, Zr)-(H, D) alloys, *J. Phys. F* 12 (1982) 79-86
- [113] Q. Xu, A. Van der Ven, First-principles investigation of metal-hydride phase stability: The Ti-H system, *Phys. Rev. B* 76 (2007) 064207 (12pp)
- [114] C.P. Liang, H.R. Gong, Fundamental influence of hydrogen on various properties of  $\alpha$ -titanium, *Int. J. Hydrogen Energy* 35 (2010) 3812-3816
- [115] D. Connétable, J. Huez, É. Andrieu, C. Mijoule, First-principles study of diffusion and interactions of vacancies and hydrogen in hcp-titanium, *J. Phys. Cond. Matter* 23 (2011) 405401 (14pp)
- [116] J. L. Murray, H. A. Wriedt, The O-Ti (Oxygen-Titanium) system, *Journal of Phase Equilibria*, 8 (1987) 148-165
- [117] S. Weismann and A. Shrier, in *The Science Technology and Application of Titanium*, Eds. R.I. Jaffee, N.E. Promisel, Pergamon Press, New York, 1970 (pp.441-451)
- [118] N.E. Paton, B.S. Hickman, D. Leslie, Behavior of hydrogen in alpha-phase Ti-Al Alloys, *Metall. Trans. 2* (1971) 2791-2796
- [119] R. Vitt, K. Ono, Hydrogen solubility in alpha titanium. *Metall. Trans. 2* (1971) 608-609
- [120] F. Cardarelli, *Materials Handbook*, second Edition, Springer, 2008
- [121] L. Köster, L. Bangert, M. Evers, Über das dampfungsverhalten von wasserstoffbeladenem titan, *Zeits. f. Metallkunde* 47 (1956) 564-570
- [122] Y. Lu and P. Zhang, First-principles study of temperature-dependent diffusion coefficients: Hydrogen, deuterium, and tritium in  $\alpha$ -Ti, *J. Appl. Phys.* 113 (2013) 193502 (5pp)
- [123] S. Naka, Étude des mécanismes de déformation plastique à basse température de monocristaux de phase  $\alpha$ , PhD Thesis, Université de Paris Sud (Orsay) 1983
- [124] G. Elssner, V. Krohn and O. Ruano, Härtung der IVa-Metalle durch interstitiell gelosten Sauerstoff und Stickstoff, *Zeits. f. Metallkunde* 67 (1976) 311-317
- [125] R.L. Fleischer, in *The Strengthening of Metals*, Ed. D. Peckner, Reinhold Publ. Corp., New York, 1964, p.93

- [126] M. Šob, Sessile Splittings of Screw Dislocations in HCP Metals, *Phys. Stat. Sol. (a)* 24 (1974) K133-136
- [127] M. Šob, J. Kratochvíl, F. Kroupa, Theory of strengthening of alpha titanium by interstitial solutes, *Czech. J. Phys. B* 25 (1975) 872-890
- [128] N. Chaari, Modélisation ab initio de la plasticité dans les métaux hexagonaux: zirconium et titane purs et effet de l'oxygène. PhD Thesis at CEA, Saclay, 2015
- [129] J.F. Nie, Y.M. Zhu, J.Z. Liu, X.Y. Fang, Periodic segregation of solute atoms in fully coherent twin boundaries, *Science* 340 (2013) 957-960
- [130] J. Pokluda, M. Černý, M. Šob, Y. Umeno, Ab initio calculations of mechanical properties: Methods and applications, *Prog. Mat. Sci.* 73 (2015) 127-158
- [131] G. Kresse, J. Hafner, *Ab initio* molecular dynamics for liquid metals, *Phys. Rev. B* (1993) 558-561
- [132] G. Kresse, J. Furthmüller, Efficiency of ab initio total-energy calculations for metals and semiconductors using a plane-wave set, *Comp. Mater. Sci.* 6 (1996) 15-50
- [133] M. Martin, *Electronic Structure: Basic Theory and Practical Methods*, Cambridge University Press, 2004
- [134] P. Hohenberg, W. Kohn, Inhomogeneous Electron Gas, *Phys. Rev. B* 136 (1964) 864-871
- [135] W. Kohn, L.J. Sham, Self-Consistent Equations Including Exchange and Correlation Effects, *Phys. Rev.* 140 (1965) A1133-1138
- [136] D.M. Ceperley, B.J. Alder, Ground state of the electron gas by a stochastic method, *Phys. Rev. Lett.* 45 (1980) 566-569
- [137] J.P. Perdew, K. Burke, M. Ernzerhof, Generalized Gradient Approximation Made Simple, *Phys. Rev. Lett.* 77 (1996) 3865-3868
- [138] J.P. Perdew, Y. Wang, Accurate and simple analytic representation of the electron-gas correlation energy, *Phys. Rev. B* 45 (1992) 13244-13249
- [139] P. Blöchl, Projector augmented-wave method, *Phys. Rev. B* 50 (1994) 17953-17978

- [140] Experiment at 4K by H. Dammak, LSI, École Polytechnique, 2004, private communication
- [141] E.S. Fisher C.J. Renken, Single-Crystal Elastic Moduli and the hcp  $\rightarrow$  bcc Transformation in Ti, Zr, and Hf, *Phys. Rev.* 135 (1964) A482-494
- [142] A. De Crecy, A. Bourret, S. Naka, A. Lasalmonie, High resolution determination of the core structure of  $1/311\bar{2}0\{100\}$  edge dislocation in titanium, *Phil. Mag. A* 47 (1983) 245-254
- [143] B. Legrand, Relations entre la structure électronique et la facilité de glissement dans les métaux hexagonaux compacts, *Phil. Mag. B* 49 (1984) 171-184
- [144] H.J. Monkhorst, J.D. Pack, Special points for Brillouin-zone integrations, *Phys. Rev. B* 13 (1976) 5188-5192
- [145] G. Kress, M. Marsman, J. Furthmüller, VASP the GUIDE, Universität Wien Juin 1, 2012
- [146] L. Hung, C. Huang, I. Shin, G.S. Ho, V.L. Lignères, E.A. Carter, Introducing PROFESS 2.0: A parallelized, fully linear scaling program for orbital-free density functional theory calculations, *Comput. Phys. Comm.* 181 (2010) 2208-2209
- [147] A. van de Walle, G. Ceder, The effect of lattice vibrations on substitutional alloy thermodynamics, *Rev. Mod. Phys.* 74 (2002) 11-45
- [148] D. Alfè, PHON: A program to calculate phonons using the small displacement method, *Computer Physics Communications* 180 (2009) 2622-2633
- [149] M. Methfessel, A.T. Paxton, High-precision sampling for Brillouin-zone integration in metals, *Phys. Rev. B* 40 (1989) 3616-3621
- [150] W. Voigt, *Lehrbuch der Kristallphysik*, Teubner, Leipzig, 1910
- [151] J.F. Nye, *Physical Properties of Crystals: Their Representation by Tensors and Matrices*, Clarendon, Oxford, 1957 & 1982
- [152] G. Grimvall, *Thermophysical Properties of Materials*, North Holland, Amsterdam, 1986
- [153] K.B. Panda, K.S. Ravi Chandran, Determination of elastic constants of titanium diboride (TiB<sub>2</sub>) from first principles using FLAPW implementation of the density functional theory, *Comput. Mater. Sci.* 35 (2006) 134-150

- [154] P. Kwasniak, M. Muzyk, H. Garbacz, K.J. Kurzydowski, Influence of oxygen content on the mechanical properties of hexagonal Ti - First principles calculations, *Mat. Sci. Eng. A* 590 (2014) 74-79
- [155] J.D. Eshelby, W.T. Read, W. Shockley, Anisotropic Elasticity with Applications to Dislocation Theory, *Acta Met.* 1 (1953) 251-259
- [156] A.N. Stroh, Dislocations and Cracks in Anisotropic Elasticity, *Phil. Mag.* 3 (1958) 625-646
- [157] A.N. Stroh, Steady-state problems in anisotropic elasticity, *J. Math. Phys.* 41 (1962) 77-103
- [158] Y. Minonishi, S. Ishioka, M. Koiwa, S. Moberg, The structure of  $\{11\bar{2}1\}$  twin boundaries in H.C.P. crystals, *phys. stat. sol. a* 71 (1982) 253-258
- [159] O. Hardouin Duparc, M. Torrent, A New Type of Periodic Boundary Condition Useful for High-Temperature Atomistic Simulations of Grain Boundaries: Applications in Semiconductors, *Interface Sci.* 2 (1994) 7-16
- [160] J. Wang, L. Liu, C. N. Tomé, S. X. Mao, S. K. Gong, Twinning and Detwinning via Glide and Climb of Twinning Dislocations along Serrated Coherent Twin Boundaries in Hexagonal-close-packed Metals, *Mat. Res. Lett.* 1 (2013) 81-88
- [161] C.D. Barrett, H. El Kadiri, The roles of grain boundary dislocations and disclinations in the nucleation of  $\{10\bar{1}2\}$  twinning, *Acta Mater.* 70 (2014) 1-15
- [162] C.D. Barrett, H. El Kadiri, Impact of deformation faceting on  $\{10\bar{1}2\}$ ,  $\{10\bar{1}1\}$  and  $\{10\bar{1}3\}$  embryonic twin nucleation in hexagonal close-packed metals, *Acta Mater.* 70 (2014) 137-161
- [163] J.C. Jamieson, Crystal Structures of Titanium, Zirconium, and Hafnium at High Pressures, *Sciences* 140 (1963) 72-73
- [164] J. Spreadborough, J. Christian, The Measurement of the Lattice Expansions and Debye Temperatures of Titanium and Silver by X-ray Methods, *Proc. Phys. Soc.* 74 (1959) 609-615
- [165] C. Stassis, D. Arch, B.N. Harmon, N. Wakabayashi, Lattice dynamics of hcp Ti, *Phys. Rev. B* 19 (1979) 181-188

- [166] A. Heiming et al. Phonon dispersion of the bcc phase of group-IV metals. II. bcc zirconium, a model case of dynamical precursors of martensitic transitions *Phy. Rev. B* 43 (1991) 10948-10962
- [167] J. Goldak, L.T. Lloyd, C.S. Barrett, Lattice Parameters, Thermal Expansions, and Grüneisen Coefficients of Zirconium, 4.2 to 1130K, *Phy. Rev.* 144 (1966) 478-484
- [168] B. Olinger, J.C. Jamieson, Zirconium: phases and compressibility to 120 kilobars, *High Temp.-High Press.* 5 (1973) 123-131
- [169] A. Heiming, W. Petry, J. Trampenau, M. Alba, C. Herzig, H.R. Schober, G. Vogl, Phonon dispersion of the bcc phase of group-IV metals. II. bcc zirconium, a model case, of dynamical precursors of martensitic transitions, *Phy. Rev. B* 43 (1991) 10948-10962
- [170] C. Domain, A. Legris, *Ab initio* atomic-scale determination of point-defect structure in hcp zirconium, *Phil. Mag.* 85 (2005) 569-575
- [171] C. Varvenne, O. Mackain, L. Proville, E. Clouet, Hydrogen and vacancy clustering in zirconium, *Acta Mat.* 102 (2016) 56-69
- [172] J. Garcés, P. Vajda, H ordering in hcp MH systems (M=Sc, Y, Ti, Zr), *International Journal of Hydrogen Energy* 35 (2010) 6025-6030
- [173] A. Clementi, D.L. Raimondi, W.P. Reinhardt, Atomic Screening Constants from SCF Functions. II. Atoms with 37 to 86 Electrons, *J. Chem. Phys.* 47 (1967) 1300-1307
- [174] M. Sob, L.G. Wang, V. Vitek, Theoretical tensile stress in tungsten single crystals by full-potential first-principles calculations, *Mater. Sci. Eng. A* 234-236 (1997) 1075-1078
- [175] O.N. Senkov, M. Dubois, J.J. Jonas, Elastic moduli of titanium-hydrogen alloys in the temperature range 20°C to 1100°C, *Metall. Mater. Trans. A* 27 (1996) 3963-3970
- [176] S.F. Pugh, Relations between the elastic moduli and the plastic properties of polycrystalline pure metals, *Phil. Mag.* 45 (1954) 823-843
- [177] B. Sun, S.F. Li, I. Hisashi, U. Junko, K. Katsuyoshi, Fabrication of high-strength Ti materials by in-process solid solution strengthening of oxygen via P/M methods, *Mater. Sci. Eng. A* 563 (2013) 95-100

- [178] S. Firstov, V. Kulikovskiy, T. Rogul, R. Ctvrtlik, Effect of small concentrations of oxygen and nitrogen on the structure and mechanical properties of sputtered titanium films, *Surf. Coat. Technol.* 206 (2012) 3580-3585
- [179] G. Henkelman, B.P. Uberuaga, H. Jónsson, A climbing image nudged elastic band method for finding saddle points and minimum energy paths, *J. Chem. Phys.* 113 (2000) 9901-9904
- [180] G.H. Vineyard, Frequency factors and isotope effects in solid state rate processes, *J. Phys. Chem. Solids* 3 (1957) 121-127
- [181] S. Ishioka, M. Koiwa, Diffusion coefficient in crystals with multiple jump frequencies, *Phil. Mag. A* 52 (1985) 267-277
- [182] A. Abbasi, A. Dick, T. Hickel, J. Neugebauer, First-principles investigation of the effect of carbon on the stacking fault energy of Fe-C alloys, *Acta Mat.* 59 (2011) 3041-3048
- [183] O. Mügge, Ueber homogene Deformationen (einfache Schiebungen) an dem triklinen Doppelsalzen  $\text{BaCdCl}_4 \cdot 4\text{aq.}$ , *Neues Jahrbuch für Mineralogie B-B6* (1889) 274-304
- [184] E.O. Hall, *Twinning*, Butterworths, London, 1954
- [185] J.W. Christian, *The Theory of Transformations in Metals and Alloys*, Third Ed., Pergamon Press, Amsterdam, 2002
- [186] G. Friedel, Contribution à l'étude géométrique des macles, *Bull. Soc. Franç. Minér.* 43 (1920) 246-294
- [187] O. Hardouin Duparc, A review of some elements in the history of grain boundaries, centered on Georges Friedel, the coincident site lattice and the twin index, *J. Mat. Sci.* 46 (2011) 4116-4134
- [188] S. Hagège, G. Nouet, Géométrie des relations d'orientation dans la symétrie hexagonale. Dimension de la coïncidence, *Acta Cryst. A* 45 (1989) 217-227
- [189] J. Wang, I.J. Beyerlein, Atomic structures of symmetric tilt grain boundaries in hexagonal close packed (hcp) crystals, *Modelling Sim. Mater. Sc. Eng.* 20 (2012) 024002 (22pp)
- [190] R.E. Reed-Hill, A study of the  $\{10\bar{1}1\}$  and  $\{10\bar{1}3\}$  twinning modes in magnesium, *Trans. Met. Soc. AIME* 218 (1960) 554-558

- [191] S. Mendelson, Zonal Dislocations and Twin Lamellae in h.c.p. Metals, *Mat. Sci. Eng. A* 4 (1969) 231-242

# List of Figures

1.1	a) The conventional hexagonal cell of the $\alpha$ -Ti structure; b) The primitive cell of the hexagonal $\omega$ -Ti structure. In figure b, all balls should have the same size (in first approximation). The 'sticks' have no physical meaning. . . . .	6
1.2	Phase diagram of titanium, determined by Tonkov in 1992 [35] and by Zhang et al. in 2008 [33] . . . . .	7
1.3	Slip systems. The arrow in a given plane indicates a slip direction [39]. . . . .	8
1.4	Frequency of slip modes under a transverse tensile for a T60 sample. Barkia's PhD thesis 2014 [11]. . . . .	9
1.5	The fixed boundary method . . . . .	11
1.6	The flexible boundary method . . . . .	11
1.7	Clouet's quadrupolar configuration [23]: an extended dipole method. (a) and (b) represent two quadrupolar configurations with different periodic dislocation arrangements. . . . .	12
1.8	$\langle \mathbf{a} \rangle$ screw dislocation core structure with one specific dislocation line position, only the screw components are shown with DD map [61] . . . . .	12
1.9	$\langle \mathbf{a} \rangle$ screw dislocation core spreads to the $\pi_1$ plane [41]. . . . .	13
1.10	$\langle \mathbf{a} \rangle$ screw dislocation core gliding on $\pi_1$ plane ( $\xi = -2 \sim 0$ ), on prismatic plane ( $\xi = 1 \sim 5$ ) and the cross slip ( $\xi = 0 \sim 1$ ) [24]. The various dislocation core structures are shown in the bottom part of the figure, b, c, d, e. . . . .	14
1.11	Possible $\langle \mathbf{c} + \mathbf{a} \rangle$ screw dislocation core dissociation proposed by Minonishi et al. [50] in which the 1.11c and 1.11e are actually observed in their simulations. The figure 1.11c corresponds to the relaxed core structure from a initially perfect dislocation core and the 1.11e are obtained from a pre-extended $\langle \mathbf{c} + \mathbf{a} \rangle$ screw dislocation core . . . . .	15
1.12	$\langle \mathbf{c} + \mathbf{a} \rangle$ screw dislocation core dissociation in $\pi_1$ , $\pi_2$ and prismatic planes obtained using a ti12 potential with a dislocation line position at A [52]. . . . .	15
1.13	Peierls potential profile. $\Delta E_p$ is the Peierls energy barrier and $\tau_p$ is the Peierls stress. . . . .	16
1.14	Crystallographic elements of twinning. The unit cell defined by $\eta_1, \eta_2$ and S is homogeneously sheared to the unit cell in twin defined by $\eta'_1, \eta'_2$ and S. Figure from [6]. . . . .	18



1.15	Schematic presentation of a TD [89]. . . . .	19
1.16	Basic processes for twin development: a) nucleation, b) propagation and c) thickening (yellow regions). The twin thickness $t$ is the spacing between two adjacent twin boundaries (TBs). The bottom blue region is one grain, and the top blue region is another grain with a different crystallographic orientation. $\theta$ corresponds to the orientation of the parent grain, and $\theta_t$ is the orientation of the twin. The red dashed lines are the glide planes. The bold black symbols represent twinning dislocations [82]. . . . .	20
1.17	The octahedral interstitial atom is shown in red and the tetrahedral interstitial atom is shown in pink. One has $\mathbf{a} = [2\bar{1}10]$ , $\mathbf{b} = [\bar{1}2\bar{1}0]$ and $\mathbf{c} = [0001]$ . . . . .	21
1.18	H's limit of solubility in the Octa interstitial site [119]. . . . .	22
1.19	Basal and perpendicular diffusivities of H (and of deuterium (D) and of tritium (T)), functions of temperature T, in $\alpha$ -Ti, figure from [122]. . . . .	23
1.20	Diffusion of O in $\alpha$ -Ti by Wu and Trinkle [110] (Analytical Model) vs. experimental results. . . . .	24
1.21	Effect of oxygen on the yield stress of Ti wire specimens with a 'bamboo' structure. Data from Elssner, Krohn and Ruano [124]. . . . .	25
1.22	A) dislocations in 3D before and after deformation in Ti-0.1wt%O, B) dislocations in 3D before and after deformation in Ti-0.3wt%O. . . . .	26
1.23	The cross-slip mechanism of an $\langle \mathbf{a} \rangle$ screw dislocation induced by an oxygen, as proposed by Yu et al. [10] . . . . .	27
1.24	a) Initial DD map with a oxygen is placed in central core position; b) DD map after relaxation [128]. . . . .	27
1.25	Serration on Stress-Strain curve under a mechanical jump test [11] . . . . .	28
1.26	Abnormal peaks at the front of two TD direction strain-stress curves related to O- $\langle \mathbf{c} + \mathbf{a} \rangle$ interaction [11]. . . . .	28
1.27	Effect of hydrogen content on the critical resolved shear stress for prism slip of Ti.[17] . . . . .	29
1.28	Fracture toughness $K_{max}$ for T40 and T60 as a function of H concentration [20]. . . . .	29
1.29	a) Geometric analysis of O in a bulk site or two near $\{10\bar{1}2\}$ TB sites. Values in parenthesis are distances before relaxation in Å. After relaxation, octahedral site in TB1 and TB2 approach those in bulk environment. b) electronic density of states for oxygen s and p states at each site. Site 0 is the bulk octahedral site. Attractive and repulsive sites show shifts in the oxygen states, but not changes in broadening [74]. . . . .	30
1.30	a) Shear added to perfect crystal to form a $\{10\bar{1}2\}$ twin in $\langle \bar{1}10\bar{1} \rangle$ direction; b) Arrows give the shuffles required to move the atoms in B-type sites (red) to either the B-(red) or C-type sites (green) in the twinned lattice. Reorientation of the lattice will eliminate the octahedral sites (marked with an X) where an oxygen atom could reside. [12]. . . . .	31

2.1	DOS of Ti with 4e or 12e . . . . .	40
2.2	Band structures of Ti with 4e or 12e . . . . .	40
2.3	Procedures of a self-consistent calculation to obtain the KS ground state in VASP [145] . . . . .	42
2.4	Possible configurations for the study of interstitial-interstitial atom interaction. a) <b>c</b> -axis projection; b) <b>a</b> direction projection . . . . .	47
2.5	Schematic presentation of a GSF characterized by the fault vector $\mathbf{v}_{GSF}$ . . . . .	49
2.6	The $\langle \mathbf{c} + \mathbf{a} \rangle$ screw dislocation visualised with two central core positions A and B for the application of $u_z$ [eq. 2.22]. Direction perpendicular to $\pi_2$ plane is $[11\bar{2}\frac{2}{\Lambda^2}]$ with $\Lambda^2 = (2/3)(c/a)^2$ . . . . .	50
2.7	$\langle \mathbf{a} \rangle$ screw dislocation core construction. . . . .	52
2.8	$\langle \mathbf{a} \rangle$ screw dislocation core dipole model. Continuous model and atomic model. . . . .	53
2.9	Schema of deformation tests done on twin structures. a) deformation direction is perpendicular to each $K_1$ plane; b) deformation direction is the <b>c</b> -axis direction of the matrix part. . . . .	54
2.10	TD model by Ghazisaeidi et al. for Mg-solute interaction [106]. . . . .	55
2.11	The TD dipole model. . . . .	55
2.12	Segregation sites for H and O near SFs . . . . .	56
3.1	The phonon dispersion curves of $\alpha$ -Ti. $12e-05$ used for the PAW potential. . . . .	58
3.2	The phonon dispersion curves of $\omega$ -Ti. $12e-05$ used for the PAW potential. . . . .	59
3.3	The octahedral interstitial atom is shown in red, the tetrahedral interstitial atom is shown in pink. $\mathbf{a} = [2\bar{1}\bar{1}0]$ , $\mathbf{b} = [\bar{1}2\bar{1}0]$ and $\mathbf{c} = [0001]$ . . . . .	60
3.4	The phonon dispersion curves of the supercell Ti36H with H in the octahedral interstitial site. In figure 3.4-3.7, following a usual mode of representation, the ‘negative’ frequencies correspond to imaginary frequencies coming from negative eigenvalues. . . . .	62
3.5	The phonon dispersion curves of the supercell Ti36H with H in the tetrahedral interstitial site (see note at the end of this 3.2 section). . . . .	63
3.6	The phonon dispersion curves of the supercell Zr36H with H in the octahedral interstitial site. . . . .	63
3.7	The phonon dispersion curves of the supercell Zr36H with H in the tetrahedral interstitial site. . . . .	64
3.8	Local titanium position changes induced by (yellow titanium) or by O (purple titanium) in octahedral site, compared with original positions (blue). The solute, H or O, is in red. Configuration with a $4 \times 4 \times 3$ supercell. . . . .	66
3.9	Charge transfer between Ti and H atom in the plane containing four nearest Ti atoms and one H. The scale is from -0.005 (deep blue) to 0.02 (red) $e/Bohr^3$ . . . . .	67

3.10	Charge transfer between Ti and O atom in the plane containing four nearest Ti atoms and one O. The scale is from -0.005 to 0.02 $e/Bohr^3$ . . . . .	68
3.11	DOS of Ti in presence of H or O . . . . .	69
3.12	Possible configurations for solute-solute interaction in two different interstitial sites a) <b>c</b> -axis projection; b) <b>a</b> direction projection. . . . .	69
3.13	B/G ratio of Ti-H and Ti-O system. The polycrystalline Ti is intrinsically brittle for a B/G value less than 1.75 according to Pugh's plasticity criterion. . . . .	73
3.14	Elastic constant calculation for Ti-H system . . . . .	74
3.15	Elastic constant calculation for Ti-O system . . . . .	75
3.16	Elastic modulus surface of a) pure Ti; b) Ti <sub>36</sub> H; c) Ti <sub>36</sub> O. The unit for the three box axis is GPa. . . . .	76
3.17	The Octa to Tetra site migration of H in $\alpha$ -Ti . . . . .	77
3.18	The c-axis and basal plane migration of O in $\alpha$ -Ti . . . . .	77
4.1	Slip systems, the arrow on the plane indicates a slip direction [39]. Cf. section 1.1.2.1. . . . .	81
4.2	$\gamma$ -surfaces of basal plane . . . . .	81
4.3	$\gamma$ -surfaces on Prism plane . . . . .	81
4.4	$\gamma$ -surfaces on $\pi_1$ plane . . . . .	82
4.5	$\gamma$ -surfaces on $\pi_2$ plane . . . . .	82
4.6	Two $\{10\bar{1}1\}$ Twin-assisted SFs on $\pi_1$ . Left figure is related to the $0.215\langle 10\bar{1}\bar{2} \rangle$ partial dislocation; right figure corresponds to $\frac{1}{2}\langle \mathbf{a} \rangle - \frac{1}{2}\langle \mathbf{b}_{TD} \rangle$ partial dislocation found in [44]. . . . .	84
4.7	A possible $\langle \mathbf{c} + \mathbf{a} \rangle$ screw dislocation dissociation mechanism. . . . .	85
4.8	The $\langle \mathbf{c} + \mathbf{a} \rangle$ screw dislocation visualized with two central core positions A and B for the application of $u_z$ [eq. 2.22]. Direction perpendicular to $\pi_2$ plane is $[11\bar{2}\frac{2}{\sqrt{2}}]$ with $\Lambda^2 = (2/3)(c/a)^2$ . Cf. section 2.2.5. . . . .	86
4.9	DDmap of the 'A-positioned' $\langle c + a \rangle$ screw dislocation core after relaxation. (All dots in this DDmap are artefacts from my DDmap generation program. Id. fig. 4.9.) . . . . .	87
4.10	DDmap of the 'A-positioned' $\langle c + a \rangle$ screw dislocation core after relaxation. The small arrows presented in the boundary should be the results of surface effects. . . . .	87
4.11	$\langle \mathbf{c} + \mathbf{a} \rangle$ screw dislocation core dissociation in $\pi_1$ , $\pi_2$ and prismatic planes obtained using a ti12 potential with a dislocation line position at A [52]. . . . .	88
4.12	Segregation sites for H and O near SFs . . . . .	89
4.13	dipole supercell size tests with N= 5, 6, 7 and 8 . . . . .	93
4.14	a) Prism- $\pi_1$ plane mixed dissociation; b) $\pi_1$ plane dissociation. . . . .	94
4.15	Octa sites around the prismatic plane dissociated dislocation. . . . .	96
4.16	$Ti_{512} - H/O$ : Core structure changes induced by the presence of H/O in site 1 ( the central core position) . . . . .	96

4.17	Core structure changes induced by the presence of H/O in site 0-1 and site 7-9. The “+” sign indicates the core position. “red square” sign indicates the solute position after relaxation. . . . .	98
4.18	Six Octa sites around the $\pi_1$ plane dissociated dislocation. . . . .	99
4.19	Four minimum energy paths (MEPs) for various moves of an $\langle \mathbf{a} \rangle$ screw dislocation core. See text for details. . . . .	100
4.20	Up: MEP for a prismatic dislocation glide with H in dissociated plane; Down: Visualization of a prismatic dislocation glide with respect of a interstitial solute in an octahedral site. See text for critical comments. . . . .	102
4.21	Peierls energy barrier for a prismatic dislocation glide with O in dissociated plane . . . . .	104
4.22	MPEs for a prismatic dislocation glide with H/O out of the dislocation core spreading plane. . . . .	104
5.1	The four $K_1$ planes and the corresponding relaxed atomic twin structures studied in this paper, shown projected on to their shear planes $S$ . See table 5.1 and the text for further details. The $\eta_1$ given here give the actual periodicities. The numbers 1, 2 and 3 indicate the interstitial sites used in Sections 4 and 6. The black bold bars correspond to the $[0001]$ $\mathbf{c}$ -axis in the lower parts considered as the matrix parts in Sections 5 and 6. For all four considered TBs, the $\mathbf{c}$ -axis belong to the $S$ shear planes. . . . .	106
5.2	Atomic structures and charge density differences of the four TBs, $\{10\bar{1}2\}$ , $\{10\bar{1}1\}$ , $\{11\bar{2}1\}$ and $\{11\bar{2}2\}$ , in presence of one H (pink) or one O (red), as indicated by black arrows, initially put at the corresponding most segregating sites (see table 5.2 together with figures 5.1). figure 5.2c.3 explicitly shows the O atom and its nearly perfectly restored immediate neighbourhood in the $\{11\bar{2}1\}$ TB, see Section 4.2. Oxygen does not segregate at the $\{11\bar{2}2\}$ TB, see table 5.2. . . . .	110
5.3	Local DOSs on one Ti atom at each of the four TBs, pure Ti TBs, and with one segregated H or O. The Ti atom is first neighbouring a most segregating interstitial site. . . . .	112
5.4	center . . . . .	114
5.5	$\mathbf{c}$ -axis stress-strain values for the four TBs for pure Ti, and with segregated O or H, until failures. . . . .	116
5.6	Total energy variations versus $\mathbf{c}$ -axis deformation, for pure Ti and with segregated O/H, until failures. . . . .	117

5.7	Evolution of charge density - atomic structure of $\{10\bar{1}2\}$ under $\mathbf{c}$ -axis deformation, pure titanium and with the presence of one segregated O (red) or H (pink) solute. Isosurfaces of $0.03 e/(Bohrradius)^3$ are visualised in yellow except when they cut a $z$ -plane in blue. Direction $z$ is reversed compared to figure 5.1. The light blue contours of Ti atoms do not appear when an O is segregated because charge density goes up to 1.13 instead of only 0.2 with a H. The directions of deformation are the dashed lines in the rectangles in red in the lower parts of the twinned structures at 0% deformation. . . . .	119
5.8	Evolution of charge density - atomic structure of $\{10\bar{1}1\}$ under $\mathbf{c}$ -axis deformation, pure titanium and with the presence of one segregated O (red) or H (pink) solute. . . . .	120
5.9	Twin boundary under deformations along perpendicular direction in pure Ti . . . . .	121
5.10	Twin boundary under deformations along perpendicular direction with Kohyama method in pure Ti . . . . .	121
5.11	The sites near a relaxed TD core. . . . .	122

# List of Tables

1.1	Deformation modes of $\alpha$ -Ti. . . . .	8
1.2	Critical resolved shear stress (CRSS) in two $\alpha$ -Ti samples, normalised to their prismatic CRSS, Barkia's PhD thesis 2014 [11]. . .	8
1.3	Stacking-faults studied in the literature. $\mathbf{b}_{TD}$ is the twinning dislocation associated to the $\{10\bar{1}1\}$ twin. . . . .	9
1.4	Twinning crystallographic elements $K_1, \eta_2, K_2, \eta_1, S$ , shear magnitude $s = \frac{1}{2}  e\vec{\eta}_1  /  \vec{\eta}_2 $ , Kihô, Bilby and Crocker's index $q$ , and $\mathbf{c}$ -type (Tension or Compression, along $\mathbf{c}$ ) for the $\{10\bar{1}2\}$ , $\{11\bar{2}1\}$ , $\{11\bar{2}2\}$ and $\{10\bar{1}1\}$ TBs (with $\gamma=c/a < 1.633$ ). . . . .	18
2.1	Comparison between 4e and 12e PAW-PBE potential for various properties in $\alpha$ -Ti. Also see section 3.4 and table 3.10 for the elastic constants. . . . .	39
2.2	Titanium elastic constants (GPa) in the standard and in the new Cartesian frames. . . . .	52
3.1	Lattice parameters and electronic total energies of $\alpha, \omega$ and $\beta$ phases of Ti, calculated at 0 K and 0 Pa, with experimental values . . . . .	58
3.2	Energy differences (in meV) between the $\alpha$ and the $\omega$ phases of Ti, not including and including $\Delta$ ZPEs . . . . .	59
3.3	Lattice parameters and electronic total energies of $\alpha, \omega$ and $\beta$ phases of Zr . . . . .	60
3.4	Energy differences (in meV) between the $\alpha$ and $\omega$ phases of Zr not including and including ZPEs . . . . .	60
3.5	Formation energy differences between Octa and Tetra sites for H and O in Ti. ISIF=3 means that the form and volume of supercell are relaxed, and they are fixed when ISIF=2. The octahedral site is favoured if $E_{Octa} - E_{Tetra}$ is negative: $E_{Octa} < E_{Tetra}$ ) . . . . .	61
3.6	Stability of interstitial sites for H in $\alpha$ -Ti. $\Delta F_f$ is the free energy difference with ZPE taken into account. . . . .	62
3.7	Formation energy differences between Octa and Tetra site for H and O in Zr . . . . .	62
3.8	Effects of one H and one O in various hcp titanium cells. The $\delta X$ values are relatively $\Delta X/X$ variations, given in %, see text. Atomic position optimisations are converged to 0.1 meV, with the 4e PAW potential with Encut=300 eV. . . . .	65

3.9	O-O, H-H and O-H interaction energies (in meV). Distances are in (Å). Box size is $4 \times 4 \times 3$ . . . . .	70
3.10	Elastic Constants (GPa) of pure Ti: comparison . . . . .	71
3.11	Elastic Constants (GPa) of Ti-H system . . . . .	72
3.12	Elastic Constants (GPa) of Ti-O system . . . . .	73
4.1	Possible SFs identified by $\gamma$ -plots . . . . .	82
4.2	Final stable SFs and associated twins in pyramidal planes. $\mathbf{b}_{TD}$ is the direction of twinning dislocation of the $\{10\bar{1}1\}$ twin. . . . .	83
4.3	Segregation energies for H and O in different Octa sites near each SFs. $\mathbf{b}_{TD}$ is the direction of twinning dislocation of the $\{10\bar{1}1\}$ twin	90
4.4	SFE values in presence of H and O in different octahedral sites near SFs and with different concentrations . . . . .	91
4.5	Segregation energies of H and O in the sites near the prismatic core (meV). . . . .	97
4.6	Segregation energies of H and O in the sites near the $\pi_1$ core (meV).	99
5.1	Twinning crystallographic elements $K_1, \eta_2, K_2, \eta_1, S$ , shear magnitude $s$ , Kihô, Bilby and Crocker's index $q$ , inter $K_1$ plane distance $d_1$ , energy $\gamma$ , expansion(contraction) $\delta$ , periodic area $A$ , Mügge's type [183] after atomic relaxation, Friedel's virtual inverse coincidence lattice site index $\Sigma$ , and $\mathbf{c}$ -type (Tension or Compression, along $\mathbf{c}$ ) for the $\{10\bar{1}2\}$ , $\{11\bar{2}1\}$ , $\{11\bar{2}2\}$ and $\{10\bar{1}1\}$ TBs in $\alpha$ -Ti (with $c/a = 1.585$ , or $\sqrt{5/2}$ for the $\Sigma$ s). $d_1$ and $\delta$ are in Å, $A$ is in Å <sup>2</sup> , $\gamma$ is in mJ/m <sup>2</sup> . The relaxed atomic structures are given in 5.1. .	107
5.2	Segregation energies (in meV) for one H or one O at selected interstitial sites as shown in figure 5.1. Checks on box sizes are d: $n_z$ and $n_x$ denote the $z$ and $x$ period multiplicity respectively. . . . .	109
5.3	Segregation energy of H/O on the site near the TD core. * Values are obtained from TB segregation calculation . . . . .	122









**Titre :** Simulation *ab initio* des défauts étendus du Ti- $\alpha$  en présence d'interstitiels H et O

**Mots clés :** Ti, calculs *ab initio*, fautes d'empilement, cœur de dislocation, mâtage, ségrégation.

**Résumé :** La thèse est divisée en trois parties. Dans la première partie le site interstitiel octaédrique du Ti- $\alpha$  est trouvé être le site énergétiquement le plus favorable pour un H ou un O. La présence d'H augmente le volume tandis que O a un effet inverse. La présence d'H diminue le module de cisaillement G et le module de Young E, la présence d'O a un effet opposé. La présence d'H augmente le rapport B/G alors que O le diminue. Deux nouvelles fautes d'empilement sont trouvées dans la deuxième partie. Un mécanisme de dissociation triple du cœur de la dislocation vis  $\langle c + a \rangle$  est proposé et étudié. La présence d'O rend sans doute la formation des fautes d'empilement énergétiquement plus difficile, contrairement au cas d'H. Pour la dislocation vis  $\langle a \rangle$ , H et O induisent une dissociation dans le plan  $\pi_1$  ou vers une configuration prism- $\pi_1$  mixte. Les barrières d'énergie de Peierls mesurées avec O dans différents sites et avec différentes concentrations montrent que O rend le glissement de la dislocation beaucoup plus difficile. Du glissement dévié devrait être induit dans ce cas. H ségrège plus fortement que O au cœur de la dislocation vis  $\langle a \rangle$  mais a un léger effet attractif avec O et il est moins présent que O dans le Ti, ce qui explique probablement pourquoi l'effet de H sur la plasticité du Ti  $\alpha$  est un problème complexe. Finalement, la macle la plus observée,  $\{10\bar{1}2\}$ , et la macle  $\{11\bar{2}2\}$  ne résistent pas à une déformation de plus de 1% ou 2% selon l'axe **c**. La présence de H ou O ségrégés améliorent la stabilité des macles  $\{10\bar{1}2\}$  et  $\{11\bar{2}2\}$ . Un modèle de dipôle de dislocations de mâtage (TD) est proposé. H et O peuvent se distribuer de manière plus ou moins homogène au joint et niveau de la TD mais pas dans les sites interstitiels de la couche atomique liée à la TD.

**Title:** *Ab initio* simulation of extended defects of  $\alpha$ -Ti in presence of interstitial atoms H/O

**Keywords:** Ti, *ab initio* calculation, stacking faults, dislocation core, twinning, segregation.

**Abstract:** This thesis is divided into three parts. In a first part, the octahedral interstitial site of  $\alpha$ -Ti is found energetically more favorable for a H or an O atom. The presence of H decreases the shear modulus G and Young's modulus E of  $\alpha$ -Ti while O has an opposite and stronger effect. H increases the B/G ratio while O decreases it. In a second part two new stacking faults are found. A  $\langle c + a \rangle$  screw dislocation 3-part dissociation mechanism is proposed and studied. The presence of O may make the stacking faults formation energetically more difficult, contrary to the H case. For the  $\langle a \rangle$  screw dislocation, both H and O in core sites change the metastable gliding prismatic dissociation to  $\pi_1$  plane or to a prism- $\pi_1$  plane mixed configuration. According to our measurements of Peierls energy barriers with O at different sites and concentrations, O makes the gliding much more difficult. Cross-slip should happen in that case. H segregates more strongly than O to  $\langle a \rangle$  screw cores but has a slightly attractive interaction with O and is less present than O in Ti, which probably explains why the effect of H on the plasticity of  $\alpha$ -Ti is a complex issue. In the last part, the  $\{10\bar{1}2\}$  and  $\{11\bar{2}2\}$  twin boundaries (TB) structures are shown to fail for deformations as low as 1% or 2% along the **c**-axis. The  $\{11\bar{2}1\}$  and  $\{10\bar{1}1\}$  TBs are much more resistant. The presence of segregated H and O enhances the  $\{10\bar{1}2\}$  and  $\{11\bar{2}2\}$  TB limited stability. A twinning disconnection (TD) dipole model is proposed and applied to  $\{10\bar{1}2\}$  case. Segregation energy calculations show that H and O should distribute more or less homogeneously to the TD core and the TB, with only a slight preference to the TD core although not at the interstitial sites of the atomic layer related to the disconnection step itself.